PB88-140702

Mechanical Response of Unidirectional Boron/Aluminum under Combined Loading

Virginia Tech Center for Composite Materials and Structures, Blacksburg

Prepared for

National Aeronautics and Space Administration
Hampton, VA

Oct 87

PB88-140702

CCMS-87-06
VPI-E-87-17

VIRGINIA TECH

CENTER FOR COMPOSITE MATERIALS AND STRUCTURES

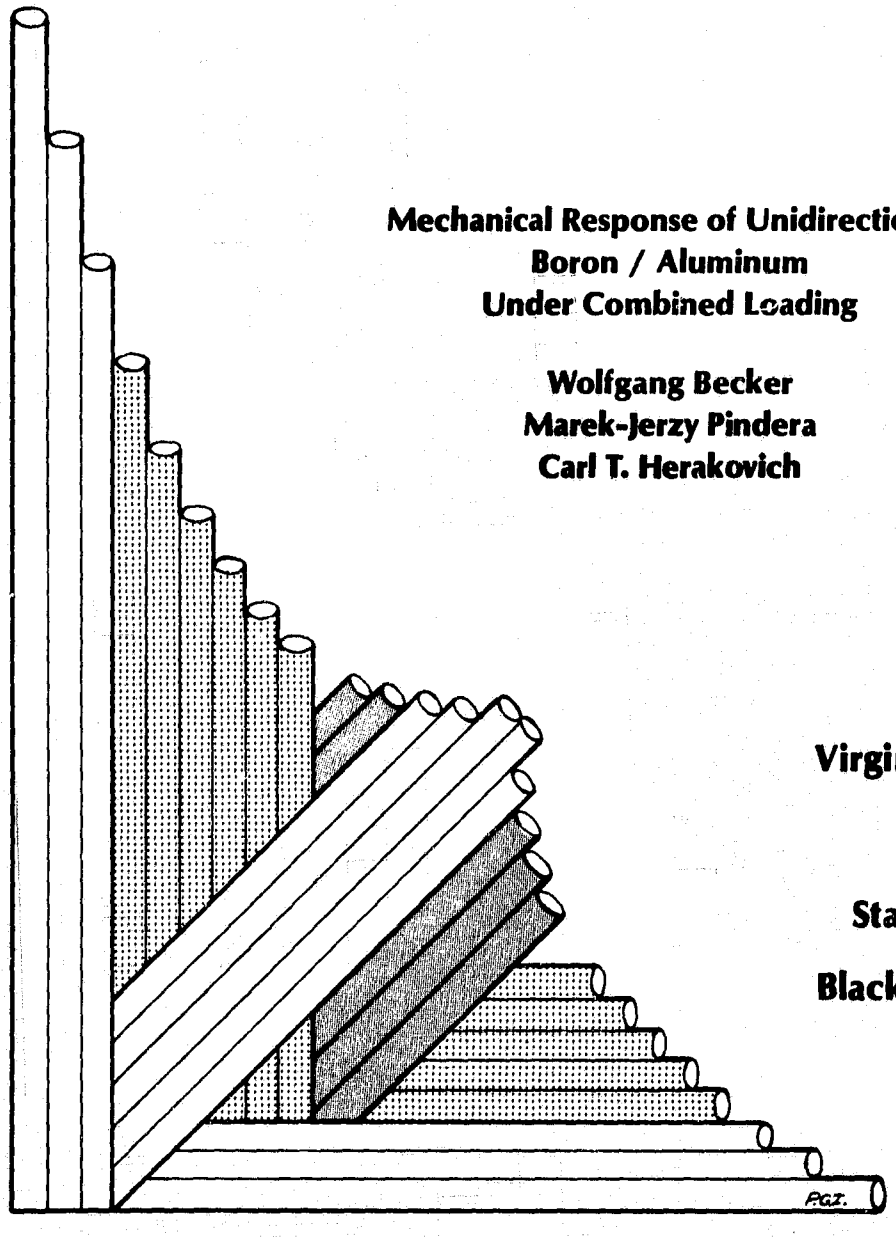

Mechanical Response of Unidirectional Boron / Aluminum Under Combined Loading

Wolfgang Becker
Marek-Jerzy Pindera
Carl T. Herakovich

Virginia Polytechnic Institute and State University

Blacksburg, Virginia 24061

BIBLIOGRAPHIC DATA SHEET	1. Report No. CCMS-87-06; VPI-E-87-17	2.	3. Recipient's Accession No. PB88 140702/AS
4. Title and Subtitle MECHANICAL RESPONSE OF UNIDIRECTIONAL BORON/ALUMINUM UNDER COMBINED LOADING			5. Report Date Oct 1987 6.
7. Author(s) W. Becker, M-J Pindera, C. T. Herakovich			8. Performing Organization Rept. No. VPI-E-87-17
9. Performing Organization Name and Address Dept Engineering Science & Mechanics Virginia Polytechnic Institution & State University Blacksburg, Virginia 24061			10. Project/Task/Work Unit No. 11. Contract/Grant No. MAT 87-001
12. Sponsoring Organization Name and Address Center for Innovative Technology Hallmark Building, Suite 201 13873 Park Center Road Herndon, Virginia 22071			13. Type of Report & Period Covered 14.

15. Supplementary Notes

16. Abstracts

Three test methods were employed to characterize the response of unidirectional Boron / Aluminum metal matrix composite material under monotonic and cyclic loading conditions, namely: Iosipescu Shear, Off-Axis Tension and Compression. The characterization of the elastic and plastic response includes the elastic material properties, yielding and subsequent hardening of the unidirectional composite under different stress ratios in the material principal coordinate system. The elastic response is compared with the prediction of the transformation theory, based on the far field stress $\bar{\sigma}_{xx}$, the Pagano-Halpin Model, and finite element analysis. Yield loci generated for different stress ratios are compared for the three different test methods, taking into account residual stresses and specimen geometry. Subsequently, the yield locus for in-plane shear is compared with the prediction of an analytical, micromechanics model. The influence of the scatter in the experimental data on the predicted yield surface is also analyzed. Lastly, the experimental material strengths in tension and compression are correlated with the Maximum Stress and the Tsai-Wu failure criterion.

17. Key Words and Document Analysis. 17a. Descriptors

Unidirectional Boron/Aluminum, test methods, off-axis tension test, off-axis compression test, Iosipescu shear test, material characterization, clastoplastic response, yielding, strain-hardening, stress-interaction, micromechanics model

17b. Identifiers/Open-Ended Terms

17c. COSATI Field/Group

18. Availability Statement	19. Security Class (This Report)	21. No. of Pages
unlimited	UNCLASSIFIED	321
	20. Security Class (This Page) UNCLASSIFIED	22. Price

College of Engineering
Virginia Polytechnic Institute and State University
Blacksburg, Virginia 24061

October 1987

CCMS-87-06
VPI-E-87-17

Mechanical Response of Unidirectional Boron / Aluminum Under Combined Loading

Wolfgang Becker[1]
Marek-Jerzy Pindera[2]
Carl T. Herakovich[3]

Department of Engineering Science & Mechanics

Prepared for:

Center for Innovative Technology
Hallmark Building, Suite 201
13873 Park Center Road
Herndon, Virginia 22071

---

1 Graduate Student, Department of Engineering Science & Mechanics

2 Assistant Professor, Department of Engineering Science & Mechanics

3 Professor, Department of Engineering Science & Mechanics

Mechanical Response Of Unidirectional

Boron / Aluminum

Under Combined Loading

(ABSTRACT)

Three test methods were employed to characterize the response of unidirectional Boron / Aluminum metal matrix composite material under monotonic and cyclic loading conditions, namely: Iosipescu Shear, Off-Axis Tension and Compression. The characterization of the elastic and plastic response includes the elastic material properties, yielding and subsequent hardening of the unidirectional composite under different stress ratios in the material principal coordinate system. The elastic response is compared with the prediction of the transformation theory, based on the far field stress $\overline{\sigma}_{xx}$, the Pagano-Halpin Model, and finite element analysis. Yield loci generated for different stress ratios are compared for the three different test methods, taking into account residual stresses and specimen geometry. Subsequently, the yield locus for in-plane shear is compared with the prediction of an analytical, micromechanics model. The influence of the scatter in the experimental data on the predicted yield surface is also analyzed. Lastly, the experimental material strengths in tension and compression are correlated with the Maximum Stress and the Tsai-Wu failure criterion.

Acknowledgements

This work was supported by the Center for Innovative Technology through Grant MAT 87-001. The authors are grateful for this financial support and the material supplied by NASA Langley Research Center.

Thanks are also due to Messers J. Michael Starbuck and Gaurang N. Choksi for their assistance with the testing and finite element analysis.

Table of Contents

List of Tables

List of Illustrations

1.0 INTRODUCTION

The search for new and advanced materials for structural applications has always been a major task for researchers, analysts, and designers. Special and unique problems in structural design require the use of special and unique materials. Fiber-reinforced composite materials are an example of these new advanced materials. Composites enlarge the choice of materials to the designer for various applications, such as tailoring procedures for airplanes, cars, or other structures. By changing the stacking sequence and fiber orientations of the laminate, for instance, the same type of material can be taylored for a large number of special geometrical applications.

The increase in the number of useable composite systems available today is a result of various research projects taking place all over the world. Combining different fibers with different matrix materials has resulted in a large number of new and unique material systems possessing new and unique properties. The use of these newly developed materials, on the other hand, requires a thorough and complete study of the material response in the elastic (linear) and plastic (nonlinear) range. Anisotropic materials like composites, with their complex and direction-dependent material response characteristics under different loading conditions, require deeper and more sophisticated analysis than homogeneous, isotropic materials such as alloys and steels.

1.1 Literature Review

The amount of experimental information available in the open literature on the elastoplastic behavior of metal matrix laminae is rather limited. Viswanathan, Davis, and Herakovich [1, 2] studied the tensile and compressive behavior of borsic/aluminum composite laminates. In this investigation, monotonic and cyclic off-axis tension and compression tests were performed and yielding as well as strain-hardening characteristics were analyzed. In 1976, Pipes et al [3] studied the acoustic emission response of metal matrix composites, following the work of Kreider and Prewo [4]. In the course of the above investigation, the authors carried out monotonic off-axis tension tests for various off-axis orientations of unidirectional boron/aluminum coupons. Subsequently, they compared the strength obtained from the off-axis tension tests with several failure criteria. However, the character of the observed elastoplastic response was not discussed in detail. Kennedy, Herakovich, and Tenney [5-7] studied the influence of temper conditions and cyclic loading on the nonlinear behavior of boron/aluminum laminates. As a part of their investigation, monotonic and cyclic tension and compression tests on six different laminates were performed. In 1977 Shuart and Herakovich [8] studied the tensile and compressive response of 0° and 90° boron/aluminum laminae and angle- and cross-ply laminates, using the off-axis tension test and different compression test methods. A subsequent study [9] carried out by the same authors focused on the Poisson's Ratio for metal matrix composite laminates.

In France, Bunsell and Nguyen [10] developed a technique to measure the radial strength of large diameter elastic fibers and applied it to boron fiber composites such as boron/aluminum. This study demonstrated the influence of splitting of large boron fibers on the composite strength. Recently, Johnson [11] published a report on "Fatigue Damage Accumulation in various Metal Matrix Composites". The major part of this report focused on matrix dominated fatigue damage, as it occurs in boron/aluminum composites.

Theoretical studies on boron/aluminum systems were performed by Shorshorov et al [12] in the USSR in 1981, addressing the effect of interfacial strength on the strength of the aluminum-boron composite. In 1983, Datta and Ledbetter [13] developed a mathematical model for the evaluation of the elastic constants of fiber-reinforced boron/aluminum. Recently, Aboudi [14, 15] developed extensive models for evaluating elastic constants as well as viscoplastic behavior for two-phase composite systems. Dvorak et al [16, 17] developed different models for characterizing the behavior of composite materials in the elastoplastic region. General information on metal matrix composites, such as fiber and matrix properties, manufacturing processes etc., can be found in the book by Lynch and Kershow [18] on "Metal Matrix Composites" published in 1972.

1.2 Objectives and Thesis Outline

Metal matrix composite materials are one of the first continuous fiber-reinforced composites ever studied [11]. The high manufacturing costs, as well as the high cost of the individual components however, were major drawbacks in the early days of composite materials. In addition, the requirement for special equipment needed for post-processing of these metal matrix composites (MMC) (special grinder, diamond saw, etc.), limited their use. Recently, interest in MMC has revived due to their advantages over the more common polymer-based composites. Besides such features as high stiffness-to-weight and strength-to-weight ratio common to all advanced composites, the MMC exhibit several other desirable material characteristics. MMC are known for their better environmental tolerance to moisture, corrosion and temperature, as well as better impact and lightning damage resistance [11]. Likewise, the transverse modulus, transverse strength, and interlaminar strength of MMC is higher than that of resin matrix composites, especially in the case of boron/aluminum composites. The major advantage of MMC however, is the higher melting point of the matrix, combined with the small coefficient of thermal expansion (CTE) along the fiber

direction. This results in higher thermal dimensional stability, opening new temperature ranges for composite materials which had been previously reserved for steels and ceramics. This is particularly important in space applications where the materials are exposed to high temperature changes and radiation.

The present investigation was carried out in order to provide the analyst and designer with the basic and essential information for subsequent investigations of the response of laminated composites, both in the linear and nonlinear region. The objective of this study was the characterization of the linear and nonlinear mechanical response of unidirectional boron/aluminum under combined loading conditions (biaxial state of stress). The knowledge of the constitutive response of unidirectional composites is a requirement for characterizing the response of multidirectional laminates.

In order to achieve the above goal, three different test methods were used, namely: off-axis tension, off-axis compression, and Iosipescu shear.

The tensile response of 0°, 90° and five off-axis configurations was characterized using the off-axis tension test (Section 2.2). An optimized specimen geometry was used in conjunction with a specially designed tensile test fixture [19], and the experimental results were corrected for end-constraint effects. The compressive response of 0°, 90° and four off-axis configurations was characterized with the aid of a newly designed compression test fixture (Section 2.3). The advantages and disadvantages of this fixture are discussed in Section 2.3.1.3. Correction procedures for the off-axis compression test results follow in Section 2.3.3. In the off-axis tests, different stress ratios were obtained along the principal material directions by varying the fiber orientation of the specimen. The different stress ratios changed the in-plane state of stress and resulted in stress-interaction effects in the plastic region.

For the characterization of the elastic response of the unidirectional composite, the elastic material properties were evaluated experimentally in tension and compression for different fiber orientations

and compared with several theoretical predictions. Iosipescu shear tests (Section 2.4) were also performed in order to provide additional data on the in-plane shear modulus G_{12}, in-plane shear strength and failure strains. 0°, 90°, and three off-axis configurations were tested using the 'Wyoming' Iosipescu shear test fixture and an optimized specimen whose geometry was based on an extensive finite element analysis. Finite element analysis was used for the correction of the experimental results.

Characterization of the plastic response included the evaluation of the yield point in tension and compression for various on- and off-axis configurations. Also, subsequent hardening was analyzed, including permanent strain accumulation, dissipation, and other plastic phenomena, as a function of fiber orientation. An attempt was made to provide data on material hardening for the development of hardening rules based on a power law expression. The functional form of the plastic stress-strain response was presented graphically for the various on-and off-axis configurations. A further objective of this investigation was to provide failure stresses and strains for the boron/aluminum system. The experimentally evaluated failure stresses of the composite in tension and compression were compared with the maximum stress and the Tsai-Wu failure criterion. Also, the different failure modes for the three different test methods and the different fiber orientations were analyzed.

The experimental results on in-plane yielding were compared with an analytical micromechanics model (Chapter 5) employed to predict the yield surface of the boron/aluminum composite. The influence of the scatter in the experimental results on the shape of the predicted yield surface was subsequently analyzed.

All experimental results obtained from the three different test methods are presented in Chapter 3 (apparent values) and in Chapter 4 (corrected values), and compared with theoretical predictions. Summary, conclusions and recommendations are given in Chapter 6. The appendices contain the individual test results in the form of tables and diagrams. Also included in the appendices are the

individual finite element results along with the results of a quantitative analysis of residual thermal stresses in the coupons due to the manufacturing process.

1.3 Constituent Properties and Material Fabrication

The composite used for the present investigation contained 0.0056 inch-diameter boron fibers imbedded uniformly in a 6061 0T aluminum alloy (Figure 1). The material properties of the fiber and matrix are given in Table 1. The fiber properties were taken from [3, 18], the matrix properties are a result of additional tests on pure 6061 0T aluminum (monotonic tension test results). Both fiber and matrix are assumed to be isotropic.

Table 1. Constituent Properties

Fiber Properties	Matrix Properties
E^f = 55.00 (msi)	E^m = 10.00 (msi)
G^f = 22.92 (msi)	G^m = 3.75 (msi)
ν^f = 0.20	ν^m = 0.31

The boron fibers were synthesized by chemical vapor deposition from the reduction of boron thricloride on a tungsten filament at 1100 to 1300 °C or 2000 to 2350 °F. The presence of the tungsten core inside the boron fiber is evident in Figure 1.

Figure 1. Tungsten Core in Boron Fiber (275 X)

Fabrication of the composite was accomplished by first wrapping a foil of 6061 0T aluminum alloy around a mandrel. The foil was than sprayed with a resin matrix (polystyrene) in a volatile solvent (xylene) before and after winding boron fibers onto the drum. In order to form the laminate, the plies were heat treated at 400 °C (750 °F) for one hour to exhaust the resin binder. Immediately after the heat treatment, the plies were subjected to a high-pressure bonding, to preserve the fibers and the foils. The high-pressure bonding is carried out at 520 °C (975 °F) and 5000 psi or (35 MPa) for one-half hour, followed by a slow cooling process of the entire laminate to room temperature. The manufacturing process resulted in a nearly prefect fiber spacing in the matrix, as shown in Figures 2 and 3. Figure 3 also shows that the laminate consists of 8 layers. The quoted thickness of the aluminum layer at the top and the bottom of the composite is 0.002 inch and the thickness of the aluminum between each layer is 0.0018 inch, based on information provided by DWA Composite Specialty Inc., Chatworth, CA. California.

Figure 2. Boron / Aluminum Composite (135 X)

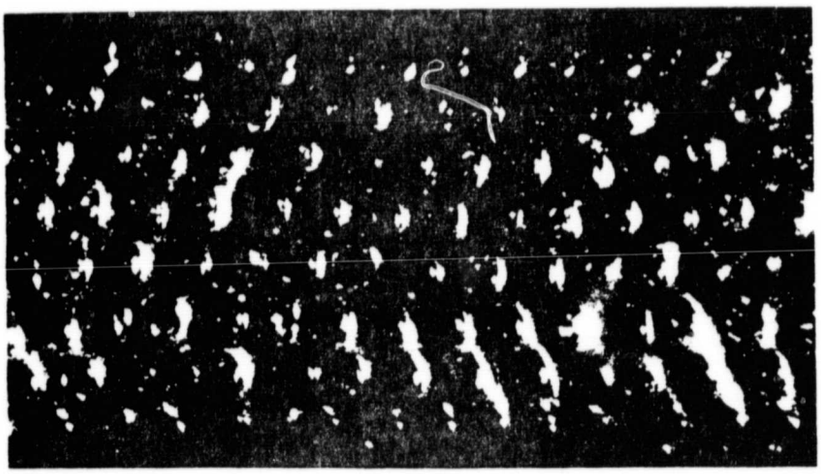

Figure 3. Entire 8 - Ply Lamina (40 X)

2.0 TEST METHODOLOGY

2.1 General Test Description

In order to characterize the linear and nonlinear response of the uniaxial boron/aluminum composite system, three test methods were employed; namely : off-axis tension, off-axis compression, and Iosipescu shear. All tests were performed on a displacement-controlled UTS testing machine at an approximate strain rate of 0.75% per minute. All specimens were been instrumented with TML FRA-2-11 rosettes, oriented at 0°, 45°, and 90° with respect to the specimens' axes. In addition, the off-axis tension and compression specimens were instrumented with a TML FLA-2-11 uniaxial (0°) gage mounted back-to-back with the rosette to correct for possible bending of the specimen during testing. The amount of bending for the off-axis tension tests and the Iosipescu shear tests was negligibly small; however, bending played an important role in the off-axis compression test (Section 2.4). The acquisition of the data was accomplished with the aid of a signal conditioning unit (Vishay 2120), consisting of amplifiers and Wheatstone Bridges, which was connected to an IBM-XT personal computer data acquisition system. Five data sweeps per second per channel were acquired in the course of performing the various tests. The tests were fully automated and controlled by the IBM-XT personal computer, using "MATPAC" and "MATPAC2"

software packages developed at Virginia Tech. One-half of the Iosipescu shear tests was performed using a MINC data acquisition system (see Appendix C), but this system was subsequently rejected due to the limited number of acquired data sweeps per second (only up to 1 sweep per second) and its sensitivity to outside electronical noise. The results of these tests are listed in the tables in Appendix C for completeness, but remain questionable.

All test data were corrected for misalignment of strain gages using photographs and/or a Nicon (type 104) microscope. Additionally, the data were corrected for bending, as mentioned before, and transverse sensitivity effects. The fiber orientations measured from fracture angles were employed in the data reduction.

All specimens were cut from a 12 inches x 21 inches panel using a high-speed diamond saw, and were subsequently ground to the specified dimensions. The nominal panel thickness was 0.055 in which corresponds to a 8-ply lay-up, with the fibers nearly perfectly spaced in the matrix (Figures 1, 2, and 3). The fiber volume fraction was 46 %. All tests have been performed at ambient conditions. The specimen geometries for the off-axis tension, the off-axis compression, and the Iosipescu shear tests are shown in Figure 4.

A) Off - Axis Tension Test Specimen

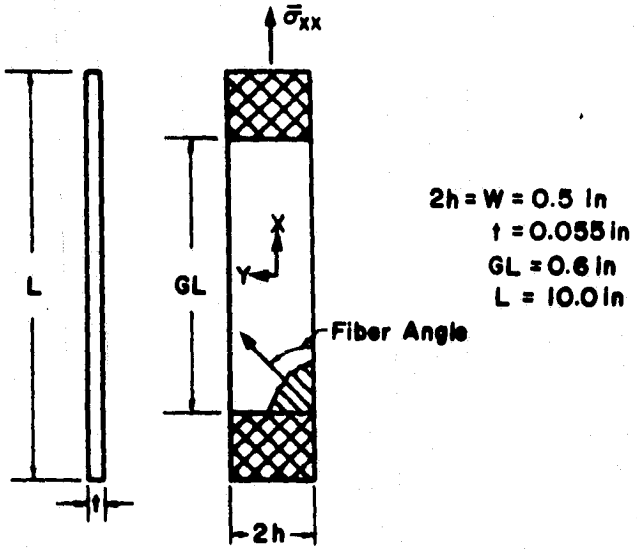

B) Off - Axis Compression Test Specimen

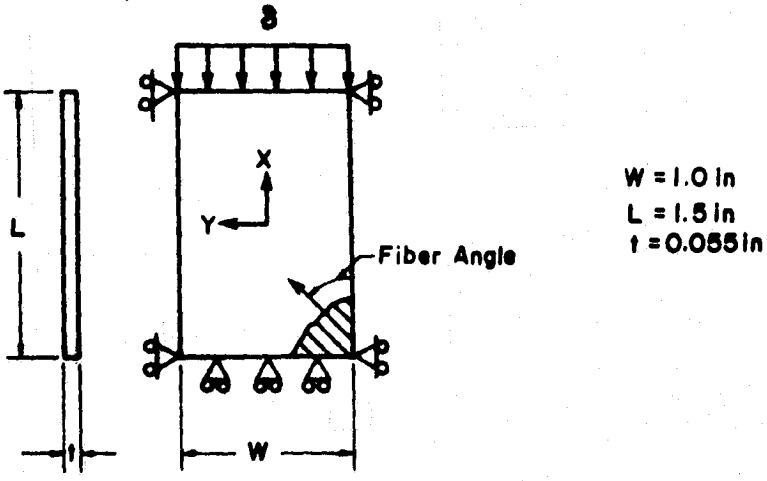

C) Iosipescu Shear Test Specimen

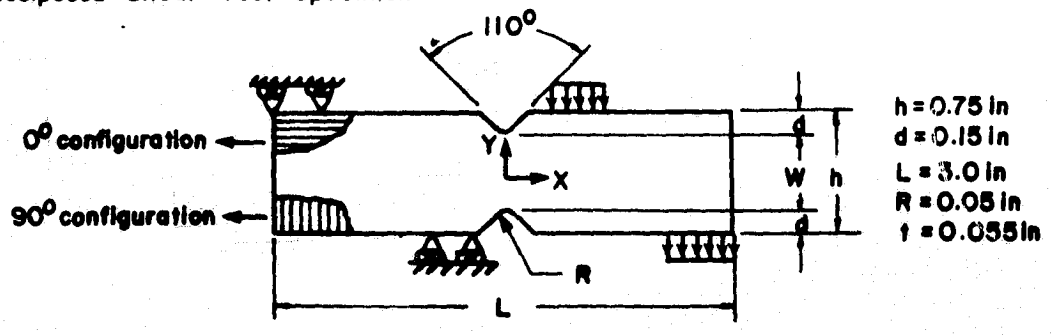

Figure 4. Specimen Geometries and Boundary Conditions

2.2 *Off-Axis Tension Test*

2.2.1 General Information

2.2.1.1 Test Procedure

The monotonic off-axis tension test is the most widely used test for the characterization of the linear and nonlinear in-plane mechanical response of uniaxial composites. Data on in-plane elastic constants (E_{11}, E_{22}, ν_{12}, and G_{12}), subsequent hardening, and failure can be obtained from this test. Additionally, cyclic tests may be performed in order to further characterize the nonlinear response with regard to hardening, dissipation, and material consistency. The wide range of applications and the advantages of the off-axis tension test are well documented in the literature [19-25].

The 0° and 90° tensile coupons are sufficient for the complete characterization of the in-plane elastic constants E_{11}, E_{22}, ν_{12} and ultimate strength parameters X_t, Y_t and S. One additional off-axis test yields data on the remaining in-plane shear modulus G_{12}. Due to the end-constraint effect caused by the shear coupling phenomonon in off-axis specimens (Section 2.2.3), the 45° off-axis coupon provides the most accurate value of G_{12} [19, 21, 22]. However, the in-plane ultimate shear strength $\tau_{12}^{u/l}$ cannot be estimated from this configuration.The studies cited showed that the 10° off-axis coupon provides a better estimate of the ultimate in-plane shear strength $\tau_{12}^{u/l}$. On the other hand, the 10° off-axis test is very sensitive to end-constraint effects. Consequently, if the specimen geometry is not optimized, this test may provide an inaccurate value for the in-plane shear modulus G_{12}. An explicit discussion of the end-constraint effect and its influence on the test data is provided in Section 2.2.3 .

In order to gain a broad understanding of the material response of the considered boron/aluminum system, and in view of the limited amount of test material available, the following off-axis tension test matrix was chosen :

Table 2. Off-Axis Tension Test Matrix

Fiber Orientation	Loading Type / Number of Tests	
	monotonic	cyclic
0°	2	1
10°	2	1
15°	1	1
30°	2	1
45°	2	1
60°	2	1
90°	2	1

2.2.1.2 Specimen Geometry and Instrumentation

All off-axis tensile coupons had the same, optimized geometry (Section 2.2.3). They were 10 inches long and 0.5 inches wide. The grip length at each end of the specimen was 2 inches in order to prevent the coupon from slipping in the grips. This resulted in an aspect ratio (i.e. gage length/gage width) of 12. This aspect ratio was sufficiently high to provide a nearly uniform stress distribution in the test section even for low off-axis orientations.

The coupons were instrumented with a TML FRA-2-11 strain gage rosette (0°, 45°, 90°) and a TML FLA-2-11 uniaxial strain gage (0°) mounted back-to-back centered in the center of the specimen.

2.2.1.3 Test Fixture

End-constraint effects due to the gripping of a specimen always influence the actual state of stress in the specimen. Due to the rigid clamping of the ends of an off-axis coupon, an additional moment and shear force are introduced into the specimen, resulting in a nonuniform displacement field and stress distribution in the gage section (Figure 5). The nonuniformity of the stresses must be taken into account for the the correct interpretation of the test results.

The test fixture used to perform the uniaxial off-axis tension tests (Figure 6), was designed to reduce the influence of the end-constraint effects on the stress distribution in the gage section [19]. By allowing the grips to rotate in the x-y plane, the additional moment can be reduced significantly. Friction between grips and fixture still remained, although lubricants were used.

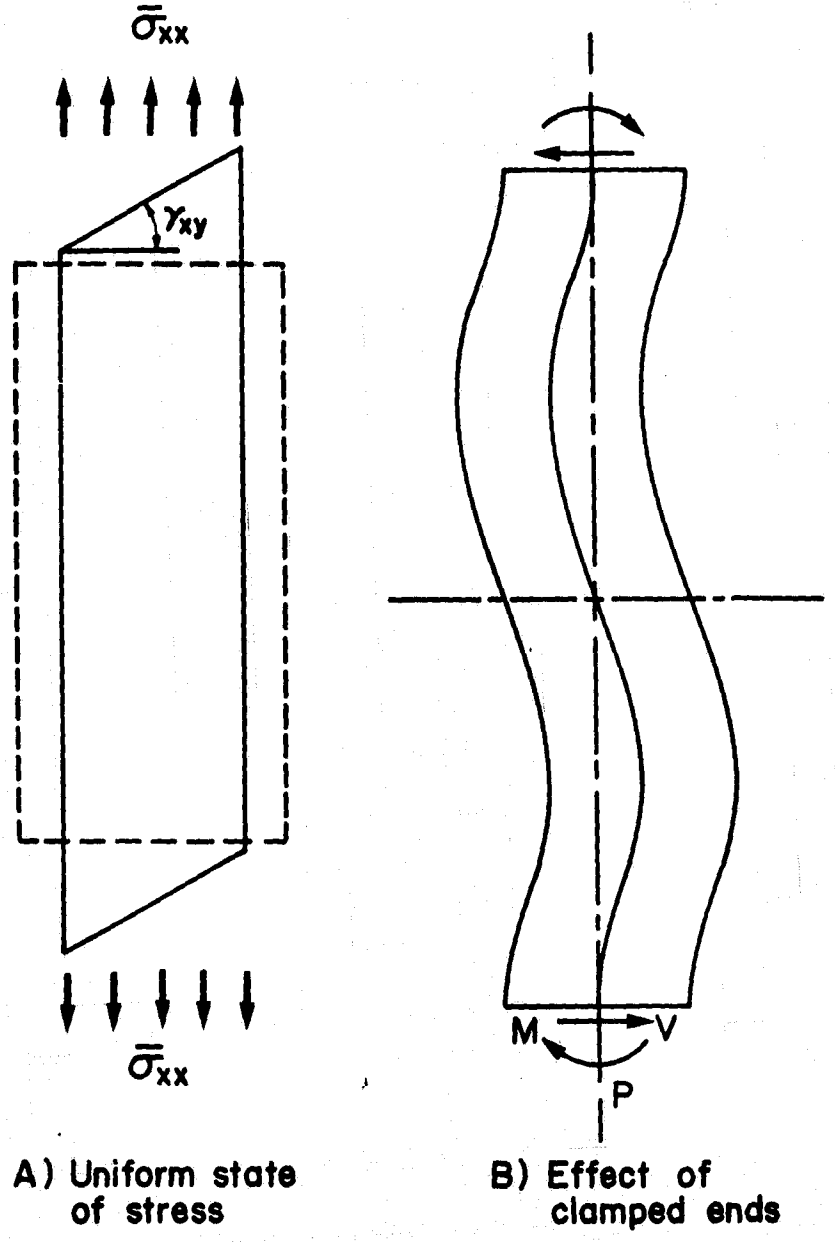

Figure 5. End Constraint Effect: Reference: [19]

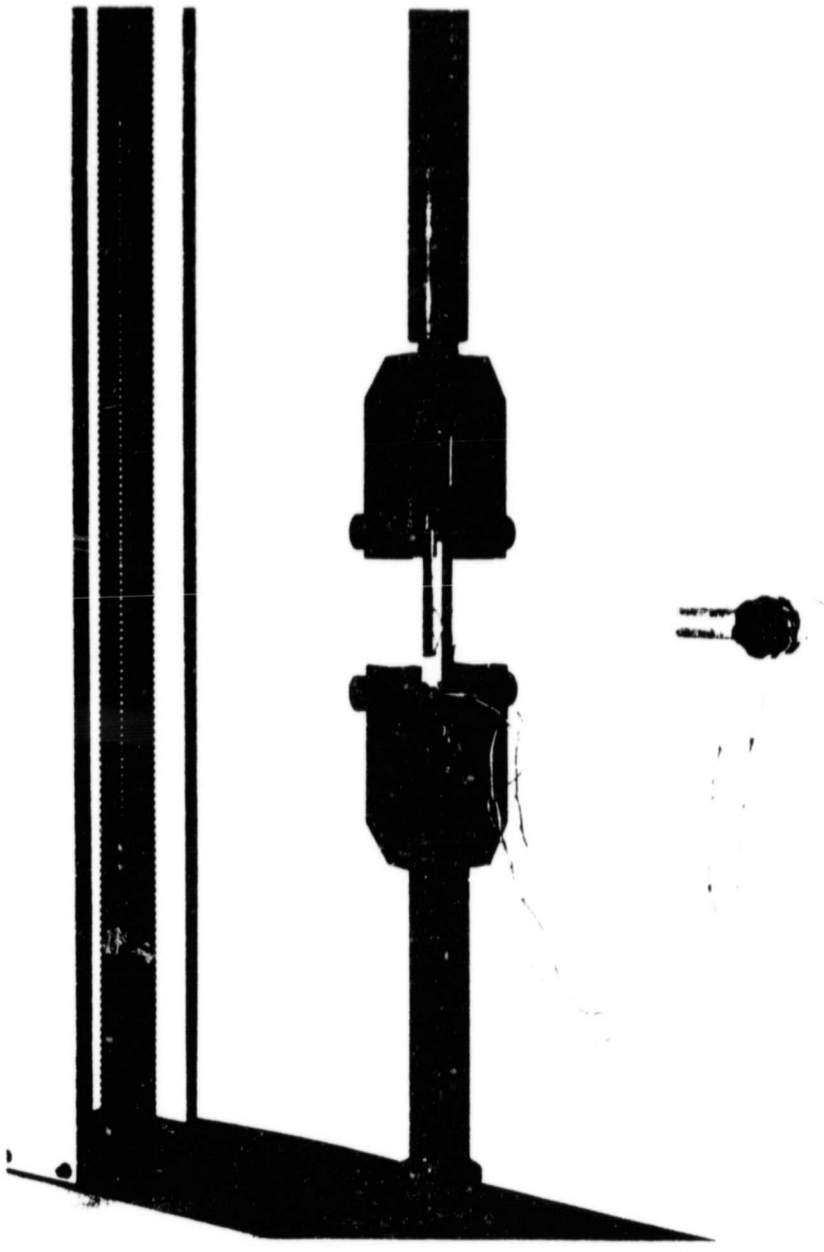

Figure 6. Uniaxial Tension Test Fixture & Specimen

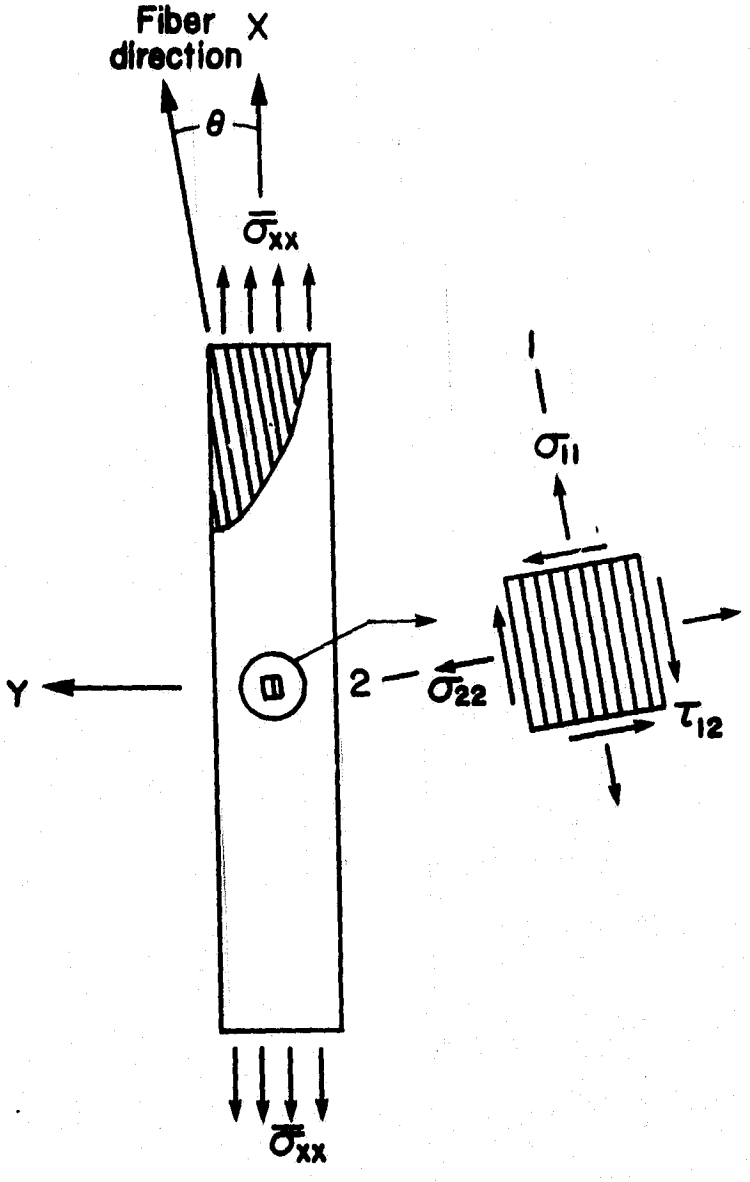

Figure 7. Typical Off-Axis Specimen

2.2.2 Stress Field

All results from the unidirectional off-axis tension tests are based on the assumption that the stress is uniformly distributed in the test section. The average tensile stress in the specimen is defined as follows:

$$\bar{\sigma}_{xx} = \left(\frac{1}{2h}\right) \int_{-h}^{h} \sigma_{xx}\, dy = \frac{P}{A} \tag{2.1}$$

where

h = half-width of the specimen

P = axial applied load

A = cross-section area

Therefore, the stress field in the principal material coordinate system, based on the far field stress $\bar{\sigma}_{xx}$ only, can be obtained as follows :

$$\begin{bmatrix} \sigma_{11}^{*} \\ \sigma_{22}^{*} \\ \tau_{12}^{*} \end{bmatrix} = \begin{bmatrix} \cos^2\theta & \sin^2\theta & 2\cos\theta\sin\theta \\ \sin^2\theta & \cos^2\theta & -2\cos\theta\sin\theta \\ -\cos\theta\sin\theta & \cos\theta\sin\theta & \cos^2\theta - \sin^2\theta \end{bmatrix} \begin{bmatrix} \bar{\sigma}_{xx} \\ 0 \\ 0 \end{bmatrix} \tag{2.2}$$

and results in :

$$\begin{aligned} \sigma_{11}^{*} &= \cos^2\theta\, \bar{\sigma}_{xx} \\ \sigma_{22}^{*} &= \sin^2\theta\, \bar{\sigma}_{xx} \\ \tau_{12}^{*} &= -\sin\theta\cos\theta\, \bar{\sigma}_{xx} \end{aligned} \tag{2.3}$$

where θ denotes the angle between global and principal material directions (Figure 7) and * denotes apparent uncorrected stresses.

2.2.2.1 *Off-Axis Test*

In the off-axis tension test, unidirectional coupon behaves effectively as an anisotropic (monoclinic) material. Axial loading of such an anisotropic system results in a shear deformation ($\gamma_{xy} \neq 0$) as shown in Figure 5A. If the ends of the off-axis specimen are rigidly clamped, and the coupon is prevented from rotating, the specimen tends to deform nonuniformly, as shown in Figure 5B. In addition to the axial load, a moment and a shear force are introduced at the ends of the specimen contributing to the nonuniform stress field in the test section. This effect is referred to in the literature as the end-constraint effect [19, 25]. The end-constraint effect is a function of specimen geometry (aspect ratio), material properties, and fiber orientation. In order to obtain accurate experimental results, correction procedures must be applied by evaluating the influence of all parameters mentioned above. A procedure for the correction of the off-axis tension test results is given in Section 2.2.3 .

2.2.2.2 *On-Axis Test*

For the on-axis tests (0° or 90°) the end-constraint effects are negligibly small, since the deformation is nearly uniform under axial loading. The shear angle γ_{xy} is zero. Consequently, no additional moments and forces are introduced into the specimen. All deformations are a result of the axial load only. Therefore the stress field in the principal material direction can be simplified in the following manner.

0° TEST	90° TEST	
$\sigma_{11}^{*} = \bar{\sigma}_{xx}$	$\sigma_{11}^{*} = 0$	
$\sigma_{22}^{*} = 0$	$\sigma_{22}^{*} = \bar{\sigma}_{xx}$	(2.4)
$\tau_{12}^{*} = 0$	$\tau_{12}^{*} = 0$	

2.2.3 Stress Ratios

By varying the off-axis angle θ and applying a uniform average stress (eqn. 2.1), different in-plane stress ratios $\frac{\sigma_{11}^{*}}{\sigma_{11}^{*}}$, $\frac{\sigma_{22}^{*}}{\sigma_{11}^{*}}$, and $\frac{\tau_{12}^{*}}{\sigma_{11}^{*}}$ are obtained in the specimen. The influence of the different stress ratios on the material response can be seen in the high extent of stress-interaction in the plastic region. The deviation from the pure plastic in-plane response for various off-axis configurations due to different states of stress in the test section is referred to in the open literature as the stress-interaction effect [19]. The extent of stress-interaction for unidirectional boron/aluminum will be discussed in Chapter 3.1.

Based on eqn. 2.3, the various stress ratios can be calculated in the following manner:

$$\frac{\sigma_{22}^{*}}{\sigma_{11}^{*}} = \frac{\sin^2\theta}{\cos^2\theta} = \tan^2\theta \qquad (2.5)$$

$$\frac{\tau_{12}^{*}}{\sigma_{11}^{*}} = -\frac{\sin\theta\cos\theta}{\cos^2\theta} = -\tan\theta \qquad (2.6)$$

For the off-axis orientations shown in Table 2, the different stress ratios obtained in the specimen are presented in Table 3.

Table 3. Stress Ratios for Off-Axis Tests

Fiber Orientation	In-Plane Stress Ratios		
	$\frac{\sigma'_{11}}{\sigma'_{11}}$	$\frac{\sigma'_{22}}{\sigma'_{11}}$	$\frac{\tau'_{12}}{\sigma'_{11}}$
10°	1.0	0.031	0.176
15°	1.0	0.072	0.268
30°	1.0	0.333	0.577
45°	1.0	1.000	1.000
60°	1.0	3.000	1.732

2.2.4 Correction of the Tension Test Results

The end-constraint effect was first discussed by Pagano and Halpin [25]. Inclusion of the shear stress component that results from the end effects leads to the following relationship between the in-plane strains and stresses in test section of the specimen:

$$\begin{bmatrix} \varepsilon_{xx} \\ \varepsilon_{yy} \\ \gamma_{xy} \end{bmatrix} = \begin{bmatrix} \bar{S}_{11} & \bar{S}_{12} & \bar{S}_{16} \\ \bar{S}_{12} & \bar{S}_{22} & \bar{S}_{26} \\ \bar{S}_{16} & \bar{S}_{26} & \bar{S}_{66} \end{bmatrix} \begin{bmatrix} \sigma_{xx} \\ 0 \\ \tau_{xy} \end{bmatrix} \tag{2.7}$$

Pagano and Halpin used the above form of constitutive equation in conjunction with an assumed form of the displacement field to estimate the error in the determination of the off-axis Young's

Modulus E_{xx} (0). The extent of the error was characterized by the ratio $\frac{E_{xx}}{E^*_{xx}}$ which was derived by Pagano and Halpin using local stresses at the mid-point of the text section, where * indicates an apparent modulus. In the above, $\bar{S}_{ij}$ are the transformed compliances in the laminate coordinate system, and σ_{xx} and τ_{xy} are functions of the applied center line strain, material properties and specimen geometry. By relating σ_{xx} and τ_{xy} to the average laminate stress in the loading direction ($\bar{\sigma}_{xx}$), it was shown subsequently by Pindera and Herakovich [19] that the Young's Modulus E_{xx} and the Poisson's ratio ν_{xy} can be related to their apparent laminate values E^*_{xx} and ν^*_{xy} in the following manner:

$$\frac{E_{xx}}{E^*_{xx}} = \frac{1-\eta}{1-\frac{2}{3}\eta} \tag{2.8}$$

$$\frac{\nu_{xy}}{\nu^*_{xy}} = \frac{1+\beta\frac{\bar{S}_{16}}{\bar{S}_{11}}}{1+\beta\frac{\bar{S}_{26}}{\bar{S}_{12}}} \tag{2.9}$$

where

$$\beta = -\frac{6\left(\frac{h}{l}\right)^2\frac{\bar{S}_{16}}{\bar{S}_{11}}}{1+6\left(\frac{h}{l}\right)^2\frac{\bar{S}_{66}}{\bar{S}_{11}}} \tag{2.10}$$

and η is defined as:

$$\eta = -\frac{6\left(\frac{h}{l}\right)^2\left(\frac{\bar{S}_{16}}{\bar{S}_{11}}\right)^2}{1+6\left(\frac{h}{l}\right)^2\frac{\bar{S}_{66}}{\bar{S}_{11}}} \tag{2.11}$$

with ℓ and h being gage length and half-width of the specimen, respectively.

In the same investigation, Pindera and Herakovich developed a procedure for the accurate determination of the in-plane shear modulus G_{12} from the off-axis tension test. Relating the apparent in-plane shear stress in the principal material direction to the average applied axial stress

$$\tau_{12}^{*} = -\bar{\sigma}_{xx} \sin\theta \cos\theta \tag{2.12}$$

they obtained the following relationship between G_{12} and its corresponding, apparent laminate value G_{12}^{*}.

$$\frac{G_{12}}{G_{12}^{*}} = \frac{\tau_{12}}{\tau_{12}^{*}} = \frac{1}{1 - \frac{2}{3}\eta}\left[1 - \beta\frac{(\cos^2\theta - \sin^2\theta)}{\sin\theta\cos\theta}\right] \tag{2.13}$$

A subsequent thorough study and comparison of equations (2.8), (2.9), and (2.13) with experimental results [19] revealed that the end-constraint effect may result in a significantly greater error in the determination of G_{12} that E_{xx} or ν_{xy}. The extent of the error is a function of the aspect ratio $\ell/2h$, the ratio of anisotropy (E_{11}/E_{22}) and the fiber orientation. It is significantly greater for G_{12} than E_{xx} in the low off-axis fiber orientation range. These conclusions resulted in a specimen optimization procedure which iteratively minimizes the error between the actual and apparent values of the elastic moduli for small off-axis orientations by increasing the aspect ratio to its lowest suitable value.

For the investigated boron/aluminum system, an aspect ratio of 12 is sufficient to minimize the error in the determination of the material properties. This is primarily due to the fact that the ratio of the longitudinal and transverse Young's Modulus (E_{11}/E_{22}) is only 1.6. In comparison to other composite systems (e.g. graphite/aluminum: E_{11}/E_{22} = 16.7, boron/epoxy: E_{11}/E_{22} = 10.0) this ratio is small.

A complete comparison between theoretical predictions of the elastic moduli as a function of the fiber orientation based on the far field stress only, the Pagano-Halpin model, and experimental re-

sults is shown in Section 3.1 . It will be conclusively demonstrated that the uniaxial off-axis tension test is the most accurate and simplest test method to determine the tensile in-plane elastic constants (E_{11}, E_{22}, ν_{12}, and G_{12}), subsequent hardening, and ultimate values such as σ_{xx}^{ult}, ε_{xx}^{ult} , and ε_{yy}^{ult}, when the specimen geometry is properly optimized.

2.3 *Off-Axis Compression Test*

2.3.1 General Description

2.3.1.1 Test Procedure

Unlike the off-axis tension test, the off-axis compression test is far more complicated in its procedure, specimen preparation, and interpretation of the test results. In order to determine the compressive properties of a composite system, numerous test procedures have been developed [8, 26, 27, 28]. In general, the major problem associated with compression testing is the elimination of buckling of the specimen inside the test fixture. Other parameters such as specimen misalignment, eccentricity of the applied load, and end-constraint effects also must be considered. Each of these parameters can influence the stress field in the test section and lead to incorrect interpretation of test results.

At least three different types of compression test procedures, requiring their own unique test fixtures, have been developed to overcome the problems mentioned above [21]. The unsupported

coupon test method attempts to solve these problems by using a short coupon with a completely unsupported gage section. The load can be either applied directly at the end of the specimen or by shear action using end tabs (IITRI specimen) [8]. The disadvantage of this method is the very short gage section, which makes it difficult to instrument the coupon and which may introduce significant end effects. The second method is the so-called supported coupon test. Here, a relatively long gage section is fully supported along the unloaded edges. Similar to the unsupported coupon test method, the load can be introduced by shear action using end tabs, or directly at the end of the specimen. By far the most complicated and most expensive test method is that using sandwich beam constructions, in which the specimen is imbedded and loaded either in three or four point bending, or edgewise in compression. This test method requires a costly and time consuming preparation of the specimen. A combination of the three test methods is also possible. Shuart and Herakovich [8] imbedded an IITRI specimen in a honeycomb sandwich beam construction and loaded it edgewise and in four point bending.

Based on the above information, the author decided on a supported coupon test method, using a newly designed test fixture (Section 2.3.1.3.) developed at Virginia Tech [21]. Taking into account the limited amount of test material and the capability of the test fixture, the following off-axis compression test test matrix was employed:

Table 4. Off-Axis Compression Test Matrix

Fiber Orientation	Loading Type / Number of Specimen	
	monotonic	cyclic
0°	2	1
10°	2	1
15°	1	0
30°	2	0
45°	1	0
90°	3	0

2.3.1.2 Specimen Geometry and Instrumentation

All off-axis compression test specimens were 1.5 inches long and 1.0 inch wide. In the process of optimizing the specimen geometry the critical buckling load was calculated using an orthotropic plate solution with all four edges simply supported [21]. The coupons were instrumented with a TML FRA-2-11 rosette oriented at 0°, 45°, and 90° and a TML FLA-2-11 uniaxial gage oriented at 0°, mounted back-to-back in the middle of the specimen. The specimen geometry of the off-axis compression test specimen is shown in Figure 4.

2.3.1.3 Test Fixture

The fixture used in this investigation consists of two major parts as shown in Figure 8. The top plate consists of the top grip and four linear bearings and the bottom plate consists of the bottom

grip and four guide pins on which the bearings slide up and down. This assemblage, combined with the use of alignment shims in the grip area, guarantees perfect alignment of the two grips with respect to each other. Therefore, eccentricity and misalignment problems were solved by requiring small tolerances for the manufacturing and subsequent cutting of the specimen. This can be assured using diamond saw and grinder for the fabrication of the specimens.

The specimen is loaded at the ends (top and bottom) and fully supported by four cylindrical side support pins, preventing out-of-plane deformation at the unloaded edges. Grip size and the length of the side support pins are variable, which allows various specimen geometries to be tested. The specimen thickness can be varied by changing the size of the alignment shims. A major advantage of this test fixture is its capability of accommodating large specimens. The fairly long gage section facilitates mounting of strain gages. No tabbing of the end of the specimen is necessary. Also, the stress concentration due to the Poisson's effect at the grips is reduced and the in-plane boundary condition are better defined (Section 2.3.3), using four thin, quarter-circular pieces to prevent side-ways deformation of the specimen in the grip areas.

Beside the small machining tolerances imposed on the geometry of the specimens, another limitation of this fixture is its initial response to the applied axial load. An accurate study of the initial loading portion showed that the load was initially introduced directly into the test fixture and not into the specimen, due to friction inside the bearings. Using a correction procedure based on the comparison of stress-strain and strain-strain with stress-time and strain-time diagrams, the real initial portion could be identified and meaningful results were obtained (see Section 2.3.3).

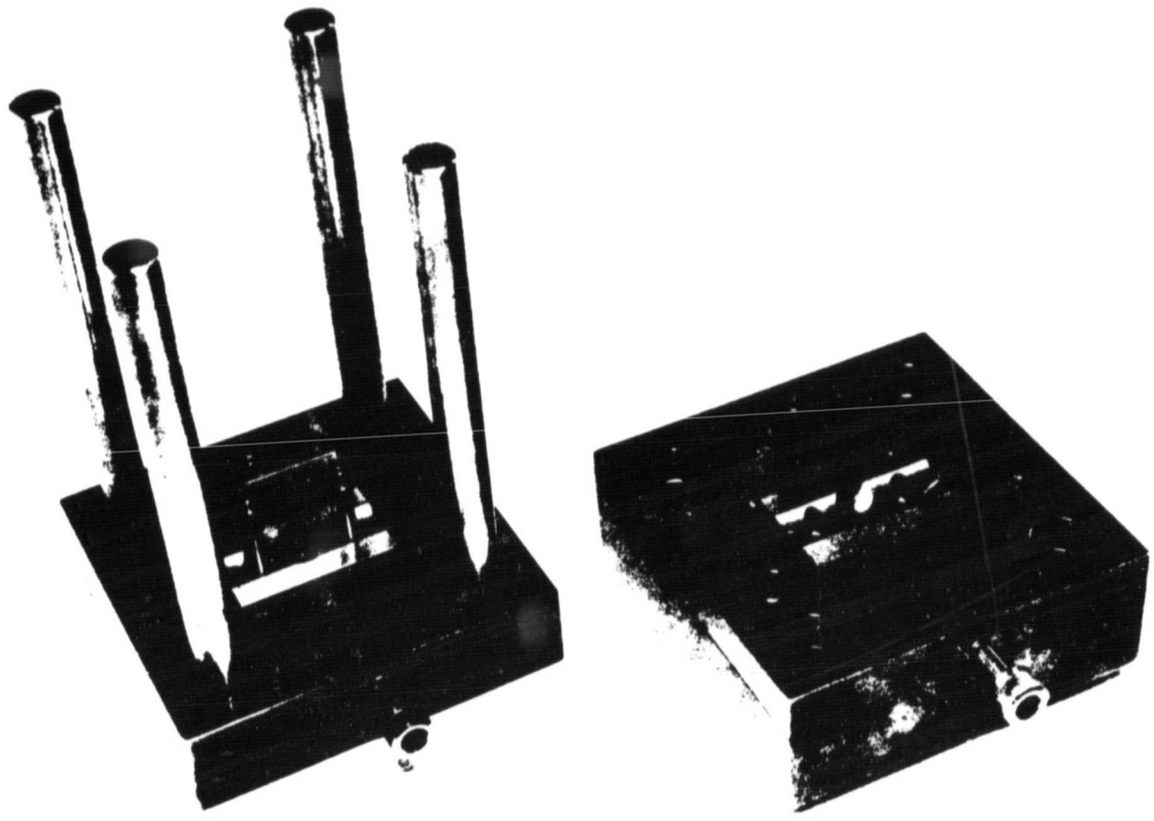

Figure 8. Off-Axis Compression Test Fixture & Specimen

2.3.2 Stress Field

The stress field in the off-axis compression specimen was obtained in the same manner as for the off-axis tension test. Based on the assumption of uniform stress in the gage section (eqn. 2.1) an apparent stress field in the principal material coordinate system was calculated as a function of the far field stress ($\bar{\sigma}_{xx}$) only. Consequently, the stress field in a compression specimen can be calculated in a similar fashion as for the tensile specimen using equation (2.3) and (2.4).

2.3.2.1 Off-Axis Test

As mentioned in the case of the off-axis tension test, the end-constraint effects and the resulting shear coupling influence the actual state of stress in the gage section. These effects are more significant for the off-axis compression specimens than for the off-axis tension coupons, due to the small aspect ratio (specimen length / specimen width) of the compression specimen. The small aspect ratio also influences the load introduction into the specimen. In the case of the off-axis tension coupons with an aspect ratio of 12, only the 0° coupon has fibers running from the top to the bottom grip, whereas in the case of the off-axis compression specimens with an aspect ratio of 1.5, fibers run from the top to the bottom grip in 0°, 10°, 15°, 30° orientations. This influences not only the stress distribution in the gage section by affecting the end-constraints, but it may also influence yielding and failure, as discussed in Chapter 3. In order to obtain meaningful results which take into account the actual state of stress in the gage section, a correction procedure must be applied.

2.3.2.2 *On-Axis Test*

The above mentioned end-constraint effects can be neglected for the on-axis compression tests, as in the case of the tension tests. Since loading of the specimen does not produce rotation of the specimen's ends, no additional shear force and moment are introduced. Disregarding the influence of local and global buckling, the state of stress in the test section remains undisturbed and nearly uniform. Therefore, the actual stress field can be expressed using eqn. (2.4).

2.3.3 Stress Ratios

Since the stress field in off-axis compression coupons is calculated in the same manner as for the off-axis tension test, the stress ratios for the various off-axis configurations are the same in tension and compression. Therefore the different stress ratios for the off-axis compression test specimens are given in Table 3.

2.3.4 Correction of the Test Results

For the off-axis compression test, several effects influence the state of stress in the gage section. In order to obtain meaningful results for the actual elastic and plastic response of the boron/aluminum system, several correction procedures must be applied to the measured apparent data.

As mentioned previously, it was observed that the load was introduced initially into the test fixture and not into the specimen. By plotting axial strain versus time and axial stress versus time, it could be determined how much load was introduced into the fixture. A typical set of plots for one individual test is given in Figures 9 and 10. A subsequent study of this issue revealed that the amount

of load which was initially introduced into the fixture was independent of the fiber orientation and therefore could be considered independent of the actual material response. The amount of this load was approximately 190 pounds (3.5 ksi). The exact amount for each individual test was determined on the basis of individual stress vs. time and strain vs. time plots. The results presented in Chapter 3 were obtained by subtracting the amount of stress carried by the fixture itself for each individual test from the stress measured in the experiments. It is believed that the the load was not released back into the specimen during the test, since no change in the strain or stress rate had been observed.

The second phenomenon effect which influences the stress distribution in the gage section is the end-constraint effect. For the off-axis compression test the influence of the end constraints on the stress field in the test section is more significant than for the off-axis tension test due to the small aspect ratio of the compression specimens (1.5 instead of 12), as mentioned previously. In order to characterize the effect of the end constraints on the stress distribution in the off-axis compression test specimen, two different correction procedures were applied.

The Pagano-Halpin model and the Pindera-Herakovich correction were used for the off-axis compression tests in order to evaluate the error between the actual and apparent (experimental) values. The reader is referred to equations (2.8), (2.9), and (2.13). In order to confirm the theoretical predictions based on the Pagano-Halpin model, an additional finite element analysis was performed. Comparison of the finite element analysis results and test data (Chapter 3.2) demonstrates that the Pindera-Herakovich correction methodology predicts well the amount of error between the apparent and actual elastic moduli even for very small aspect ratios in the case of compressive loading.

The finite element analysis was performed using the FORTRAN code "ANFRAC", developed at Virginia Tech [29]. This code is based on a standard displacement formulation using six-noded, isoparametric elements and was developed for modeling anisotropic materials. The mesh used for the analysis of stress and strain distribution in the off-axis compression coupon is shown in Figure 11. It consists of 240 elements and 525 nodes. In order to model the actual gripping condi-

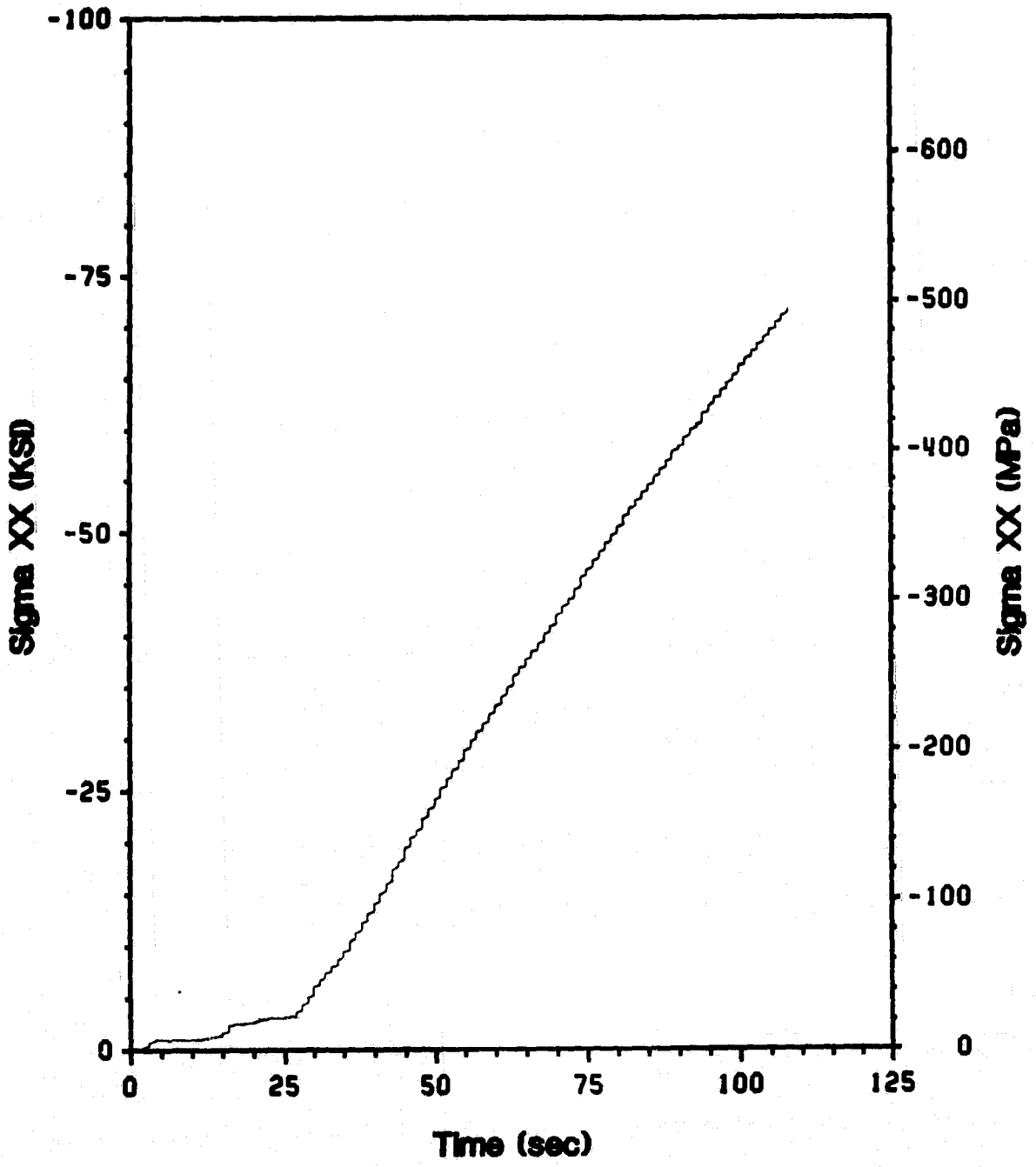

Figure 9. Time History of a 30° Off-Axis Compression Test ($\bar{\sigma}_{xx}$)

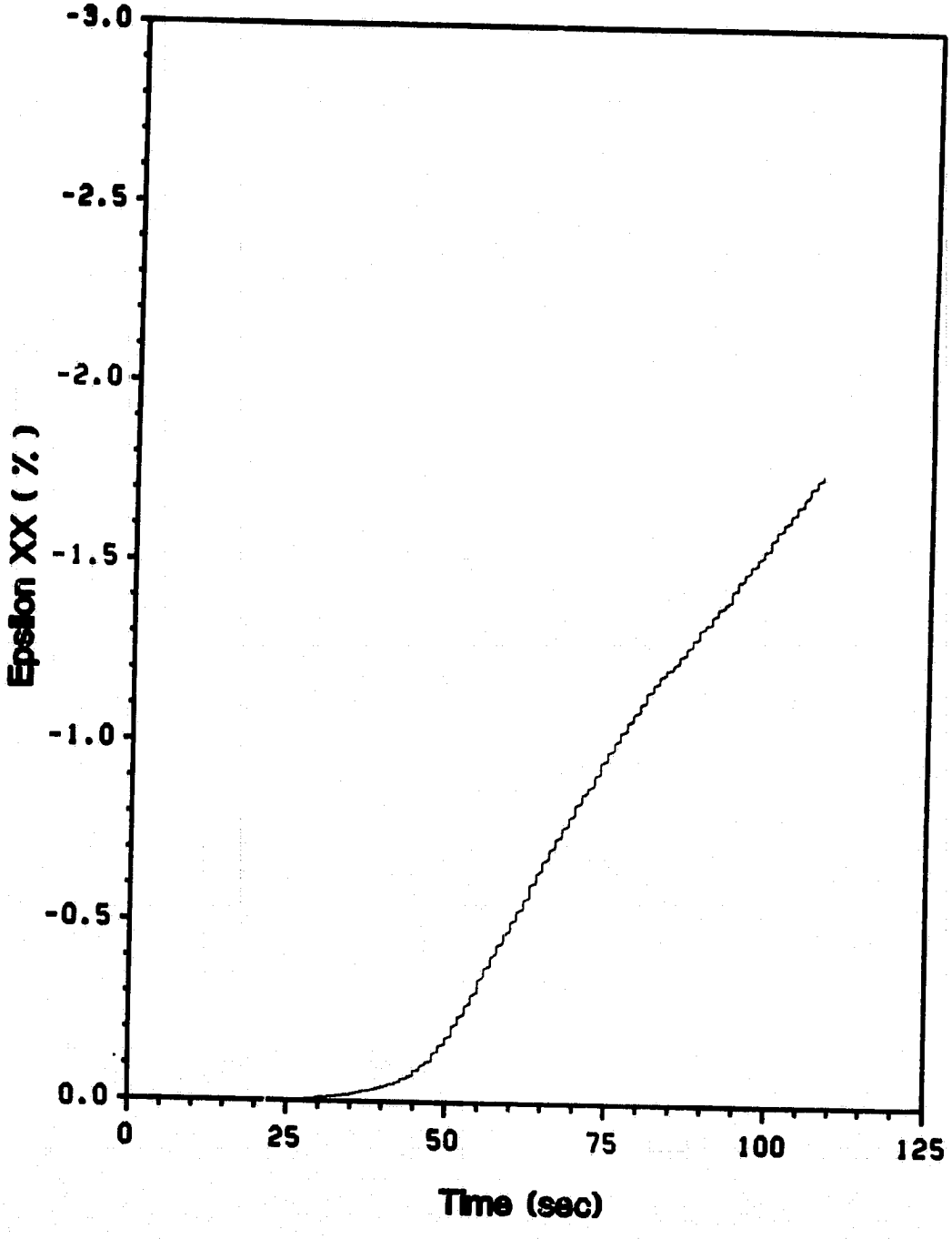

Figure 10. Time History of a 30° Off-Axis Compression Test (ε_{xx})

tions and the influence of the end-constraint effects on the stress distribution in the compression coupon, two different sets of boundary conditions were used. These were: 1.) fully clamped, and 2.) simply supported at one node in the y-direction. These boundary conditions simulated the stiffest and softest possible responses of the compression specimens. The material input data for the finite element analysis are the off-axis compression test results (E_{11}, E_{22}, ν_{12}^{com}), shown in Table 10. The value for the in-plane shear modulus was taken from the 45° off-axis tension test, since it is believed that it provides the most accurate value of G_{12} [21].

The first set of boundary conditions, which was chosen to simulate the stiffest response, fully constrained the specimen at the top and at the bottom grip. In the finite element code the x- and y-displacements were fixed for the 21 bottom nodes and the y-displacements were fixed for the 21 top nodes. Additionally, in order to model the loading, a constant negative displacement in the x-direction was specified for the 21 top nodes. The second set of boundary conditions, simulating the softest possible response, simply supported the specimen only at two points in the y-direction and constrained it in the x-direction. This was modeled in the finite element analysis by fixing the x-displacements for the 21 bottom nodes, specifying a constant negative displacement in the x-direction for the 21 top nodes, and additionally fixing the right bottom and the left top node in the y-direction. Results and correlation between the two theoretical predictions and the experimental results are given in Section 3.2. The individual results of the finite element analysis are presented in Appendix D.

All stresses in the finite element analysis were normalized with respect to the average shear stress (eqn. 2.1) in order to perform a quantitative, elastic analysis of the stress distribution in the gage section of the off-axis compression specimen.

The in-plane shear modulus G_{12} is much more affected by the end-constraints than any other elastic constant. It can further be stated that correction of the apparent values of the Young's Modulus E_{xx} (θ) and Poison's Ratio $\nu_{xy}(\theta)$ was not necessary due to the small difference between theoretical predictions based on the far field stress $\bar{\sigma}_{xx}$ only, the Pagano-Halpin prediction and the experimental

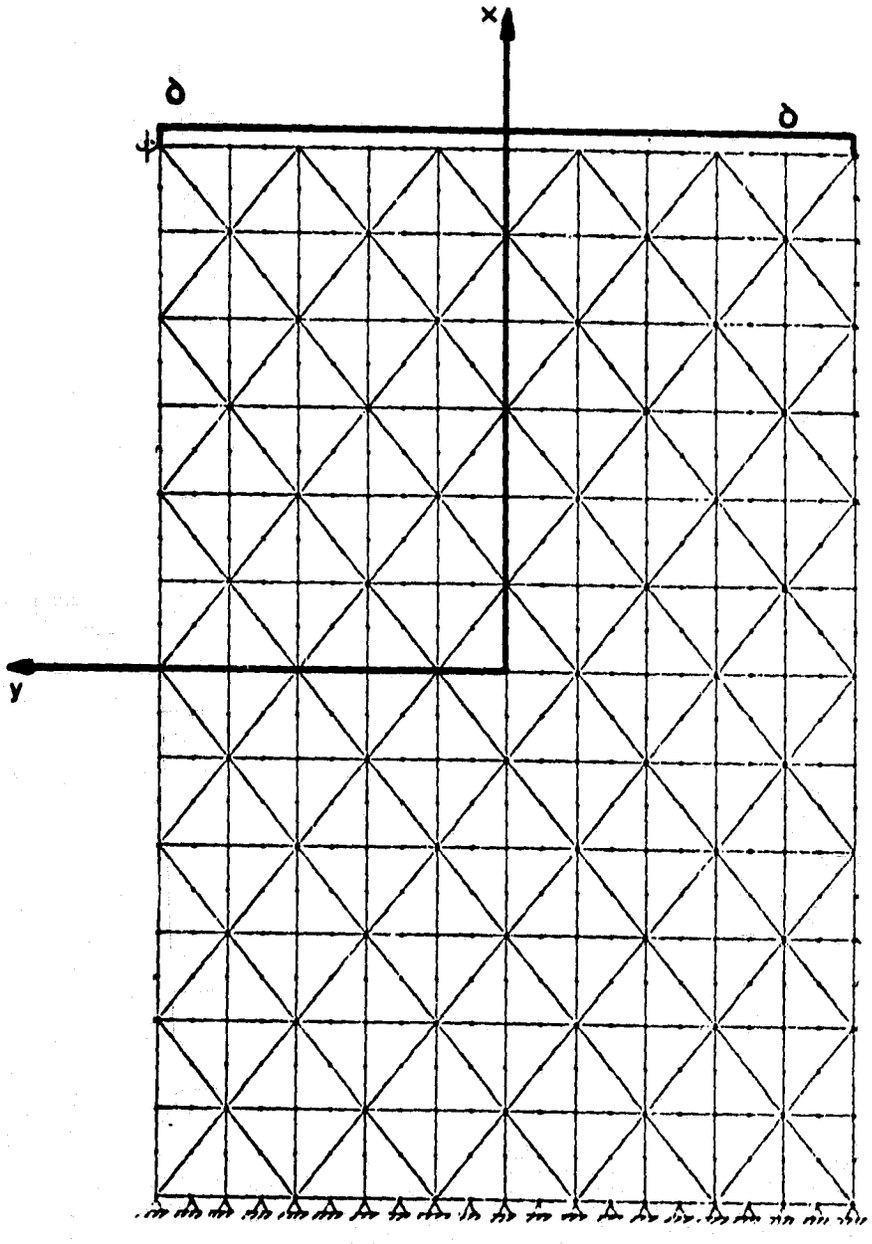

Figure 11. FEM Mesh for the Off-Axis Compression Test Specimen

results. However, since the in-plane shear modulus G_{12} is very sensitive to the end-constrains in the fixture, especially for small off-axis configurations, a correction procedure to evaluate the actual in-plane shear modulus in compression is essential.

A procedure similar to that used for the off-axis tension test was applied to the off-axis compression test. The procedure incorporates the transformation theory and the results from the finite element analysis. The in-plane shear stress in the principal material direction can be expressed in terms of the laminate stresses in the following manner:

$$\tau_{12} = - \sin\theta\cos\theta\sigma_{xx} + \sin\theta\cos\theta\sigma_{yy} + (\cos^2\theta - \sin^2\theta)\tau_{xy} \qquad (2.14)$$

Consequently, the ratio indicating the amount of error between the actual and apparent in-plane shear modulus can be obtained in a similar manner as obtained for the Pagano-Halpin model by relating the actual in-plane shear stress τ_{12} (eqn. 2.14) to the apparent in-plane shear stress τ^*_{12} (eqn 2.3). This results in the following expression:

$$\frac{G_{12}}{G^*_{12}} = \frac{\tau_{12}}{\tau^*_{12}} = \frac{\sigma_{xx}}{\bar{\sigma}_{xx}} - \frac{\sigma_{yy}}{\bar{\sigma}_{xx}} - \frac{(\cos^2\theta - \sin^2\theta)}{\sin\theta\cos\theta}\frac{\tau_{xy}}{\bar{\sigma}_{xx}} \qquad (2.15)$$

The ratios $\frac{\sigma_{xx}}{\bar{\sigma}_{xx}}$, $\frac{\sigma_{yy}}{\bar{\sigma}_{xx}}$, and $\frac{\tau_{xy}}{\bar{\sigma}_{xx}}$ are obtained from the finite element analysis of the stress distribution along the center-line of the specimen (see Appendix D).

The test results also were corrected for bending. In the case of the off-axis compression tests, bending of the specimen was significant and influenced the recorded material response. Since two 0° strain gages were mounted on each specimen in a back-to-back fashion, two separate strain readings were recorded for each individual test. The axial strains reported in this investigation are the arithmetical mean of both strain readings, front and back, following eqn. (2.16) shown below.

$$\bar{\varepsilon}_{xx} = \frac{\varepsilon_{xx}^{front} + \varepsilon_{xx}^{back}}{2} \tag{2.16}$$

The amount of bending for the other two test methods was negligibly small and therefore not explicitly mentioned.

2.4 *Iosipescu Shear Test*

2.4.1 General Description

2.4.1.1 Test Procedure

The third method used to characterize the linear and nonlinear response of the boron/aluminum composite system was the Iosipescu shear test. This test method was used for the determination of the in-plane shear modulus G_{12} , the ultimate in-pane shear strength τ_{12}^{ult} and the ultimate in-plane shear strain γ_{12}^{ult}. The unique specimen geometry (Figure 4) and fixture design (Figure 12) result in a state of stress in the test section, which is close to a state of pure shear. The unique specimen geometry is the result of a thorough study by Walrath and Adams [30-33] using finite element analysis, and was originally studied by Bergner and Herakovich [34]. The test fixture used for the current project is a modified version recently developed by Walrath and Adams [32]. Application and verification of the Iosipescu shear test procedure was discussed by Walrath and Adams [29-34] for various composite systems. Swanson et al [35] compared the Iosipescu shear test with the torsion tube, a more traditional method for the determination of the in-plane shear modulus G_{12}.

Pindera et al [36] subsequently showed that if the test results of an Iosipescu shear test were interpreted correctly, using correction procedures, accurate results can be obtained. The correction of the Iosipescu shear test results was based on finite element analysis, taking into account the nonuniform stress distribution in the test section (Section 2.4.3). Very good correlation between off-axis tension test results and corrected Iosipescu shear test results was obtained in the above investigation.

The Iosipescu shear test program consisted of monotonic and cyclic tests outlined in Table 5.

Table 5. Iosipescu Shear Test Matrix

Fiber Orientation	Loading Type / Number of Specimen	
	monotonic	cyclic
0°	4	2
75°	2	0
80°	4	2
85°	4	1
90°	3	0

2.4.1.2 Specimen Geometry and Instrumentation

The Iosipescu specimen geometry is shown in Figure 4. The specimen is 3.0 inches long and 0.75 inches wide with two 110° V-notches centered in the middle of the loaded edges. The nominal specimen thickness is 0.055 inches and corresponds to an 8-ply lay-up.

All Iosipescu shear specimens were instrumented with TML FRA-2-11 rosettes oriented at 0°, -45°, and -90°. Experience showed that uniaxial gages needed to correct for bending of the specimen

during the test were not necessary for the Iosipescu shear specimens. For this reason only rosettes mounted on the front of the specimens were used.

2.4.1.3 Test Fixture

The modified version of the Iosipescu shear test fixture, proposed by Walrath and Adams, is shown in Figure 12. This fixture consists of two major parts, the left and right grip assemblies. The left grip assembly is attached to the bottom plate with a guide pin in the right back corner of the bottom plate, and the right grip assembly, which is connected to the moving part of the testing machine, contains a linear bearing and slides up and down on the guide pin. This bearing, guide-pin combination assures axial application of the load in the test (V-notch) area. Thin, ductile aluminum inserts were used between grips and specimen to guarantee a more uniform load introduction into the specimen and therefore a reduction of the high stress concentration at the edges.

After fixing the bottom plate using c-clamps, the fixture could be used for reversed cyclic tests, applying positive and negative shear stresses. Results of these reversed cyclic tests are presented in Appendix C.2.

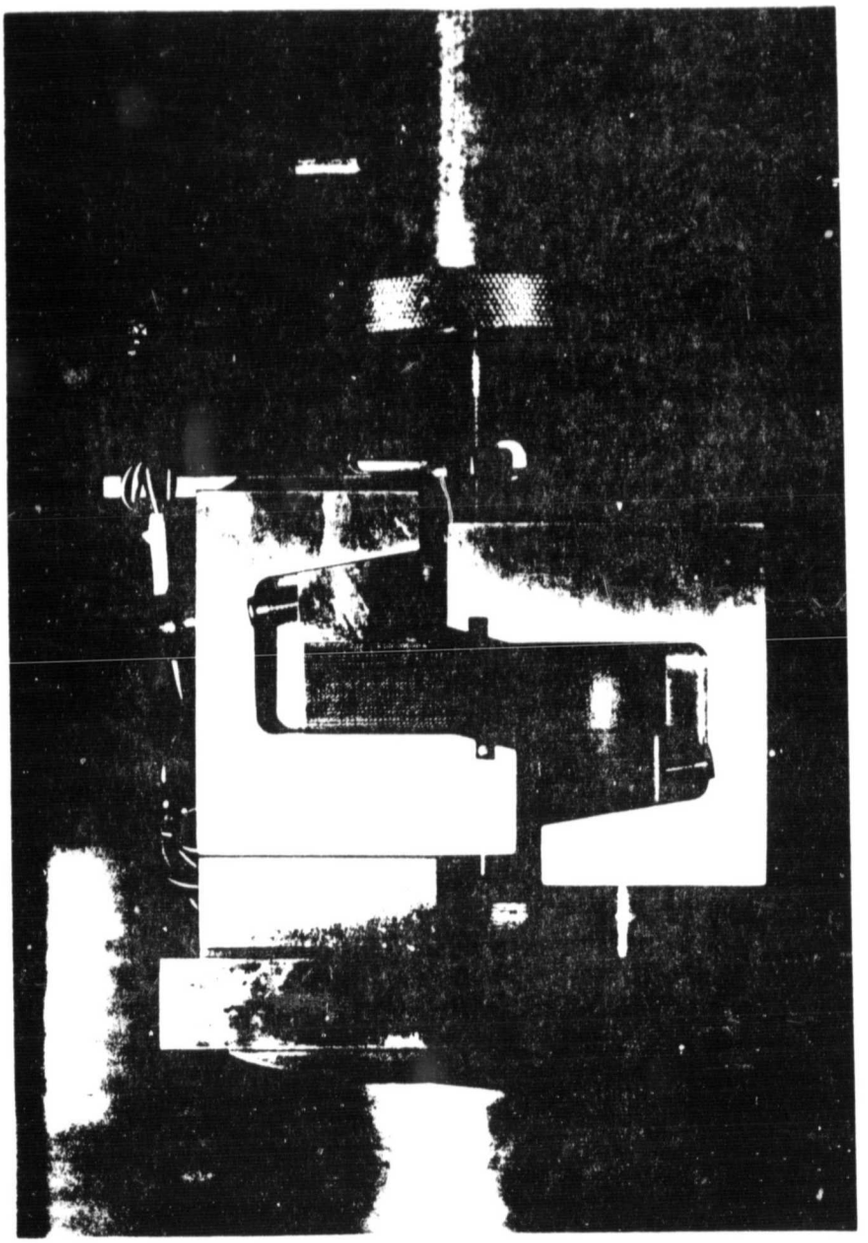

Figure 12. Iosipescu Test Fixture & Specimen

2.4.2 Stress Field

2.4.2.1 Off-Axis Test

The average shear stress in the notched section of the Iosipescu specimen is calculated as follows :

$$\bar{\tau}_{xy} = \frac{1}{w} \int_{-w/2}^{w/2} \tau_{xy}\, dy = \frac{P}{A_n} \tag{2.17}$$

where

w = width in the notched section

P = applied axial load

A_n = cross section area in the notched section

σ_{xx} and σ_{yy} are assumed to be zero in the test section. Consequently, using the transformation theory, the stresses in the principal material directions can be obtained as follows,

$$\begin{bmatrix} \sigma^*_{11} \\ \sigma^*_{22} \\ \tau^*_{12} \end{bmatrix} = \begin{bmatrix} \cos^2\theta & \sin^2\theta & 2\cos\theta\sin\theta \\ \sin^2\theta & \cos^2\theta & -2\cos\theta\sin\theta \\ -\cos\theta\sin\theta & \cos\theta\sin\theta & \cos^2\theta - \sin^2\theta \end{bmatrix} \begin{bmatrix} 0 \\ 0 \\ \bar{\tau}_{xy} \end{bmatrix} \tag{2.18}$$

which results in the following apparent material principal stresses,

$$\begin{aligned} \sigma^*_{11} &= 2\sin\theta\cos\theta\,\bar{\tau}_{xy} \\ \sigma^*_{22} &= -2\sin\theta\cos\theta\,\bar{\tau}_{xy} \\ \tau^*_{12} &= (\cos^2\theta - \sin^2\theta)\,\bar{\tau}_{xy} \end{aligned} \tag{2.19}$$

where θ indicates the angle between global and principal material coordinate system.

2.4.2.2 On-Axis Test

The stress field in an on-axis Iosipescu specimen (i.e. 0° or 90° orientation) can be simplified in a similar manner as for the off-axis tension test. Assuming a uniform stress distribution in the gage section, the stress field in the Iosipescu coupon reduces to :

0° TEST	90° TEST
$\sigma_{11}^{*} = 0$	$\sigma_{11}^{*} = 0$
$\sigma_{22}^{*} = 0$	$\sigma_{22}^{*} = 0$
$\tau_{12}^{*} = \bar{\tau}_{xy}$	$\tau_{12}^{*} = -\bar{\tau}_{xy}$

(2.20)

In reality, however, the shear stress distribution in the test section of on-axis and off-axis Iosipescu specimens is not uniform. The nonuniform shear stress distribution is a result of the unique specimen geometry and the manner of load introduction. Thus, correction procedures must be applied in order to obtain an accurate value of the in-plane shear modulus G_{12}. The stress distributions in the test section of the Iosipescu specimens employed in the present investigation are given in Appendix E.

2.4.3 Stress Ratios

For the Iosipescu shear test, different stress ratios were obtained using the average shear stress assumption (eqn. 2.17). Based on eqn. (2.18) and (2.19), the stress ratios can be calculated in the following manner.

$$\frac{\tau_{12}^{*}}{\sigma_{11}^{*}} = \frac{(\cos^2\theta - \sin^2\theta)}{2\sin\theta\cos\theta} \qquad (2.21)$$

The different stress ratios for the off-axis configurations (75°, 80°, and 85°) are listed in Table 5.

Table 6. Stress Ratios for Iosipescu Shear Tests

Fiber Orientation	In-Plane Stress Ratios		
	$\frac{\sigma_{11}^{*}}{\sigma_{11}^{*}}$	$\frac{\sigma_{22}^{*}}{\sigma_{11}^{*}}$	$\frac{\tau_{12}^{*}}{\sigma_{11}^{*}}$
75°	1.0	-1.0	-1.732
80°	1.0	-1.0	-2.748
85°	1.0	-1.0	-5.671

2.4.4 Correction of the Test Results

Since the stress distribution in the Iosipescu shear test specimen is nonuniform, the use of an average shear stress $\bar{\tau}_{xy}$ eqn. (2.17) in the post-processing calculation yields only data on the apparent in-plane shear modulus G_{12}^{*}. It can be shown that the ratio $\tau_{xy}/\bar{\tau}_{xy}$, where τ_{xy} is the local stress at the point where the shear strain γ_{xy} is measured, corresponds to the ratio G_{12}/G_{12}^{*} in the case of the on-axis specimens. This ratio indicates the error introduced in the determination of the in-plane shear modulus using the average shear stress assumption for the post-processing calculations. The use of the average stress assumption is common practice in material testing. The ratio of G_{12}/G_{12}^{*} can be used as a correction factor, correcting for stress nonuniformity along the center line (x = 0.0) of the specimen.

The FORTRAN code "ANIFRAC" was also used for the finite element analysis of the stress distribution in an Iosipescu coupon. The mesh employed for the analysis, shown in Figure 12, contains 468 elements and 1001 nodes. The boundary conditions, simulating experimental conditions, are also shown in Figure 12. The input values for the finite element analysis were taken from the off-axis tension test (E_{11},E_{22}, ν_{12}, G_{12}). The input value for the in-plane shear modulus G_{12}, in particular, was taken from the 45° off-axis tension test. The resulting stresses were normalized with respect to the average shear stress $\bar{\tau}_{xy}$, eqn. (2.17), in order to compare the magnitudes of the in-plane stresses in the gage section.

For the on-axis tests (0°, 90°), the ratio $\tau_{xy}/\bar{\tau}_{xy}$ is directly related to the ratio of the actual and apparent in-plane shear modulus G_{12} /G^*_{12}, since for on-axis configurations $|\tau_{xy}| = |\tau_{12}|$. For off-axis configurations however, the stresses in the global coordinate system must be transformed to the principal material coordinate system. Applying the transformation theory, the in-plane shear stress τ_{12} can be expressed in terms of global stresses in the same way as was done for the off-axis compression tests (see eqn. (2.14)).

Relating the actual in-plane shear stress τ_{12} to the apparent in-plane shear stress τ^*_{12}, the following expression for the ratio of the actual and apparent in-plane shear moduli can be obtained :

$$\frac{G_{12}}{G^*_{12}} = \frac{\tau_{12}}{\tau^*_{12}} = -\frac{(\sin\theta\cos\theta)}{(\cos^2\theta - \sin^2\theta)}\frac{\sigma_{xx}}{\bar{\tau}_{xy}} + \frac{(\sin\theta\cos\theta)}{(\cos^2\theta - \sin^2\theta)}\frac{\sigma_{yy}}{\bar{\tau}_{xy}} + \frac{\tau_{xy}}{\bar{\tau}_{xy}} \quad (2.22)$$

Again, the ratios $\frac{\sigma_{xx}}{\bar{\tau}_{xy}}$, $\frac{\sigma_{yy}}{\bar{\tau}_{xy}}$, and $\frac{\tau_{xy}}{\bar{\tau}_{xy}}$ were obtained from the finite element analysis. The individual finite element results for the various on- and off-axis configurations are presented in Appendix E.

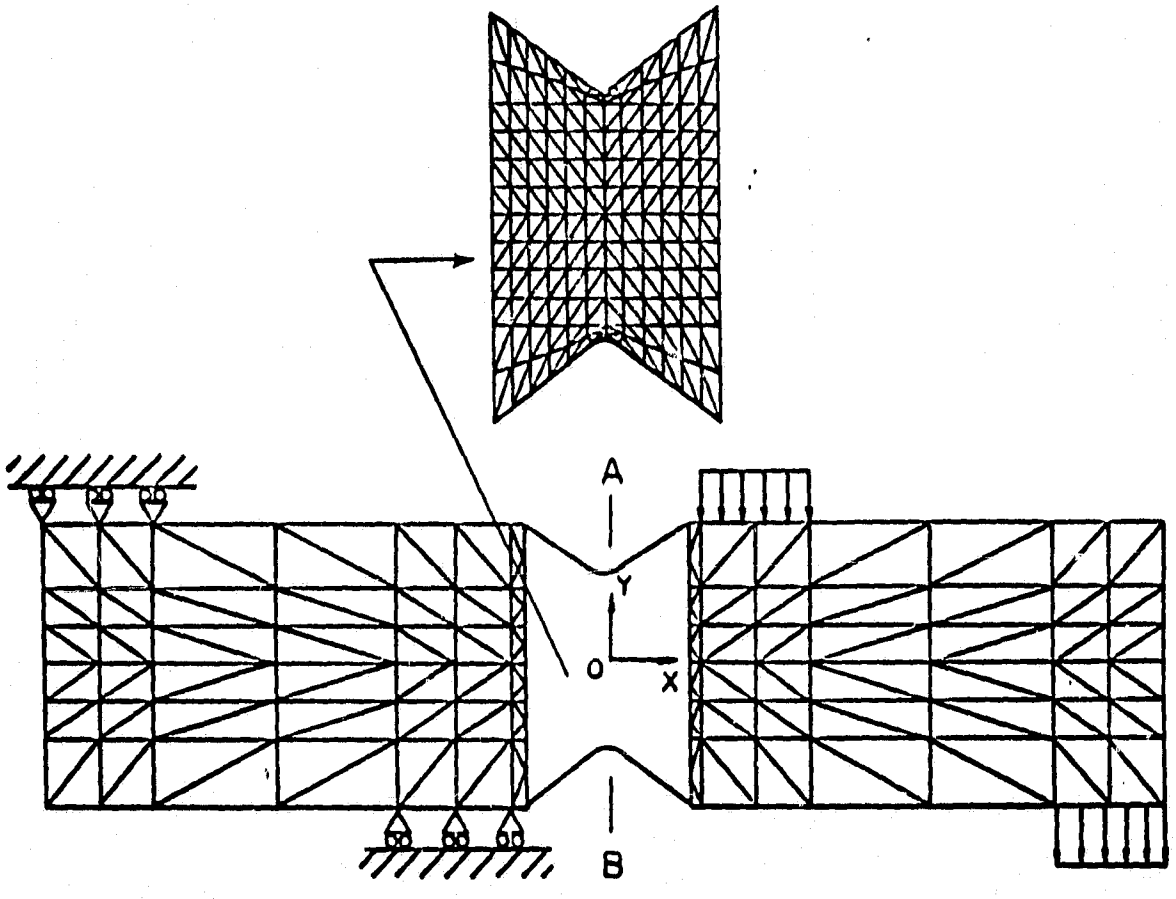

Figure 13. FEM Mesh for Iosipescu Specimen

3.0 EXPERIMENTAL RESULTS

The experimental results presented in this chapter are all apparent values. They were obtained assuming a uniform stress distribution in the gage section based on the average axial stress assumption (eqn. 2.1) and the average shear stress assumption (eqn. 2.16). The measured elastic constants are compared with the theoretical predictions of the transformation theory, neglecting the shear coupling effect due to end-constraints, the Pagano-Halpin model, taking into account the shear coupling effect, and the finite element analysis.

For the evaluation of the elastic properties the following definitions were used. The Young's Modulus E_{xx} (0) is defined as the ratio of the initial average axial stress $\overline{\sigma}_{xx}$ divided by the measured initial strain ε_{xx} (eqn. 3.1). Poisson's ratio $\nu_{xy}(0)$ is defined as the ratio of the measured negative initial transverse strain $-\varepsilon_{yy}$ divided by the measured initial longitudinal strain ε_{xx} (eqn. 3.2). The apparent in-plane shear modulus G'_{12} was obtained by dividing the initial apparent in-plane shear stress τ'_{12} by the measured initial in-plane shear strain γ_{12} (eqn. 3.3).

$$E_{xx}(\theta) = \frac{\overline{\sigma}_{xx}(\theta)}{\varepsilon_{xx}(\theta)} \tag{3.1}$$

$$\nu_{xy}(\theta) = \frac{-\varepsilon_{yy}(\theta)}{\varepsilon_{xx}(\theta)} \tag{3.2}$$

$$G^{*}_{12}(\theta) = \frac{\tau^{*}_{12}(\theta)}{\gamma_{12}(\theta)} \tag{3.3}$$

The expressions for the Young's Modulus and Poisson's ratio for an orthotropic lamina in the global coordinate system can be obtained by performing a transformation with respect to the off-axis angle θ (see Figure 4).

$$E_{xx}(\theta) = \frac{1}{\frac{1}{E_{11}}\cos^4\theta + \left(\frac{1}{G_{12}} - \frac{2\nu_{12}}{E_{11}}\right)\sin^2\theta\cos^2\theta + \frac{1}{E_{22}}\sin^4\theta} \tag{3.4}$$

$$\nu_{xy}(\theta) = E_{xx}(\theta)\left[\frac{\nu_{12}}{E_{11}}(\sin^4\theta + \cos^4\theta) - \left(\frac{1}{E_{11}} + \frac{1}{E_{22}} - \frac{1}{G_{12}}\right)\sin^2\theta\cos^2\theta\right] \tag{3.5}$$

The input values for equations (3.4) and (3.5) were taken from the 0° (E_{11}, ν_{12}) and 90° (E_{22}) on-axis tests and the 45° (G_{12}) off-axis tension test.

3.1 *Tension Test Results*

Typical results of the monotonic on- and off-axis tension tests are shown in Figures 14 and 15, where the global stress-strain and Poisson's responses are presented. Results of individual tests are given in Appendix A.1 . The scatter in the test results obtained from different specimens of the same

configuration was extremely small (less than 1 %), which justifies the presentation of only one representative plot for each orientation.

Transforming the global results shown in Figure 14 to the principal material directions, the in-plane material responses shown in Figures 16 - 18 are obtained. The in-plane longitudinal response was normalized with respect to E_{11}, whereas the in-plane transverse response was normalized with respect to the transverse Young' Modulus E_{22} .

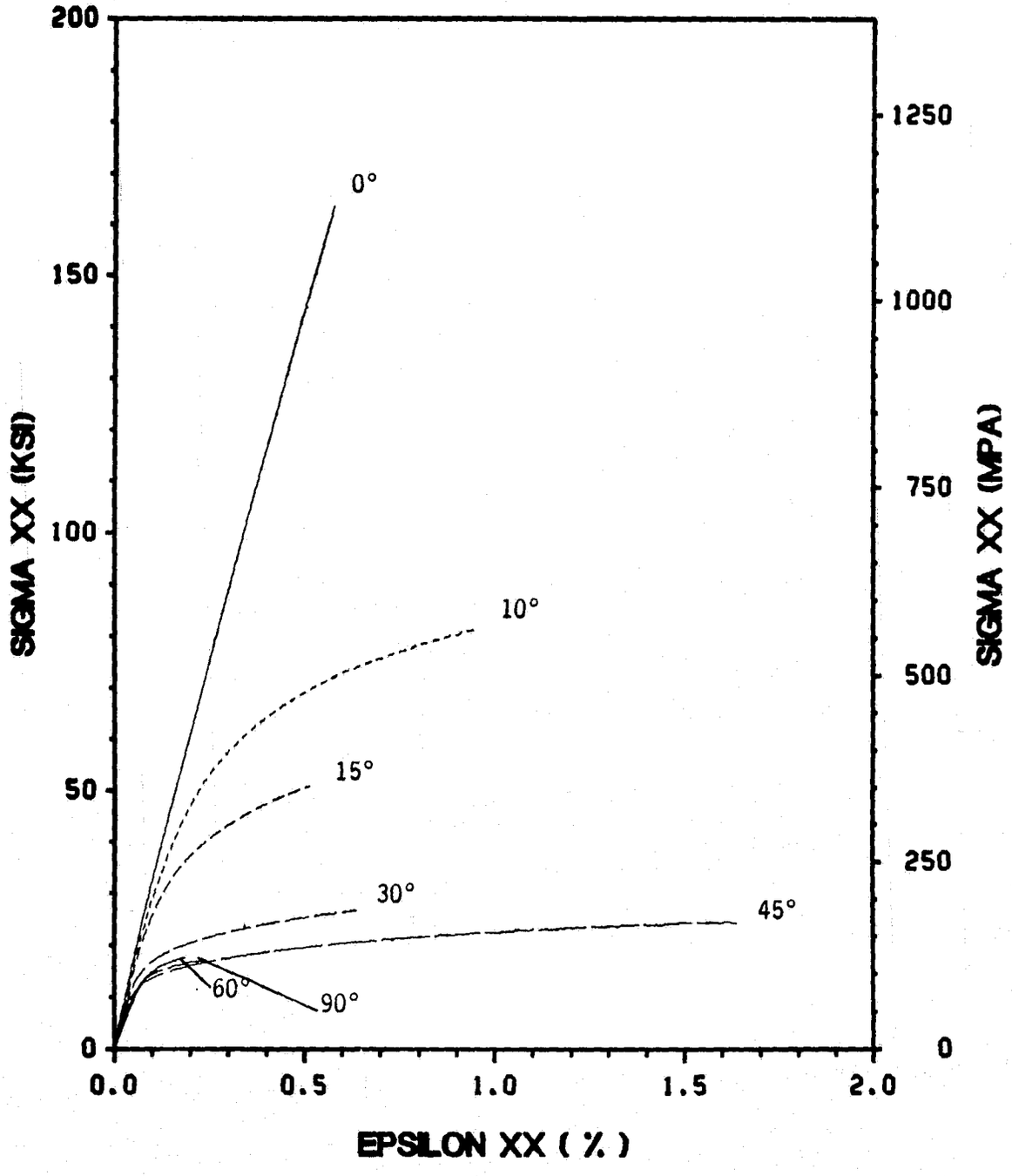

Figure 14. Global Tensile Stress - Strain Response

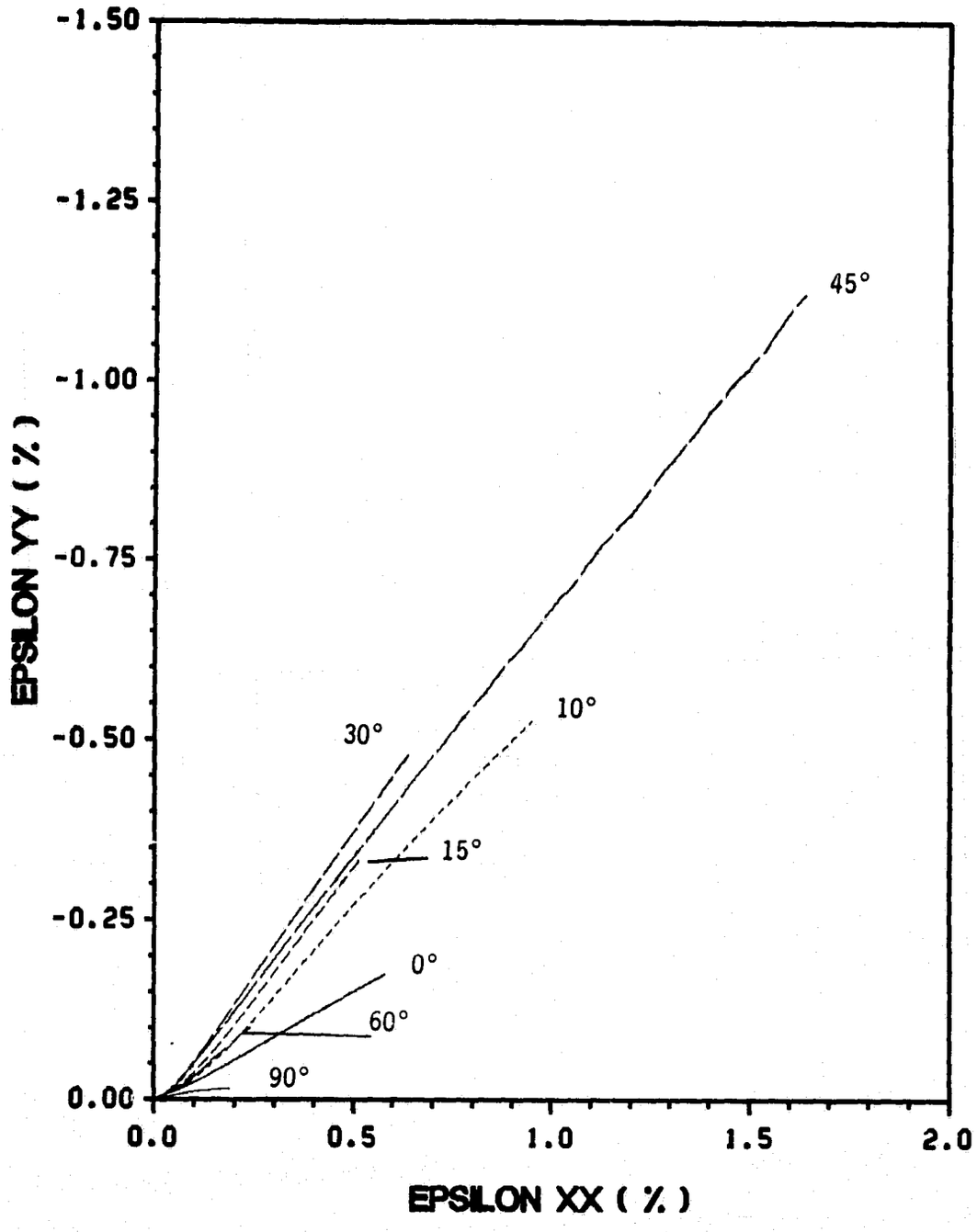

Figure 15. Global Tensile Poisson's response

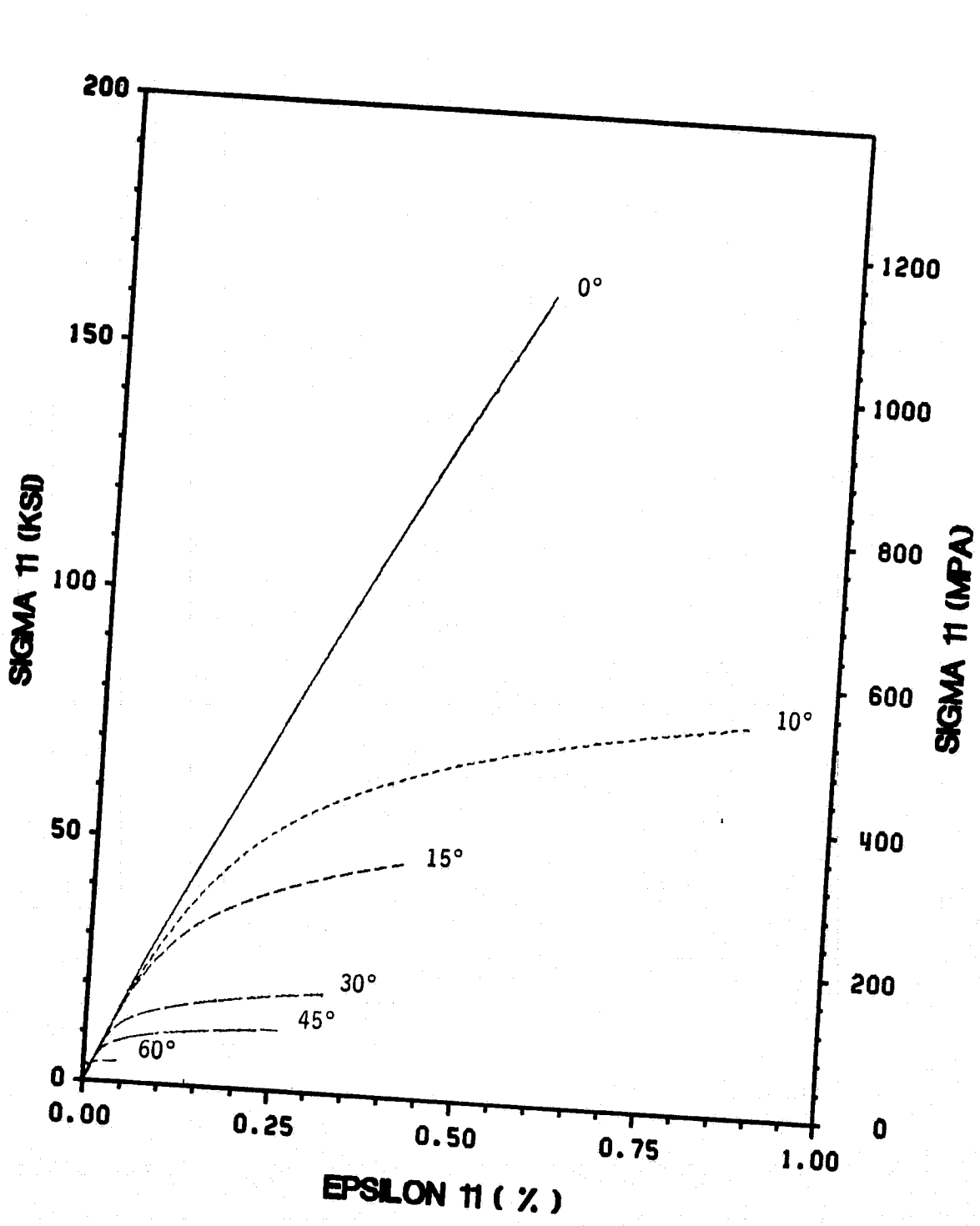

Figure 16. Normalized In-Plane Longitudinal Response

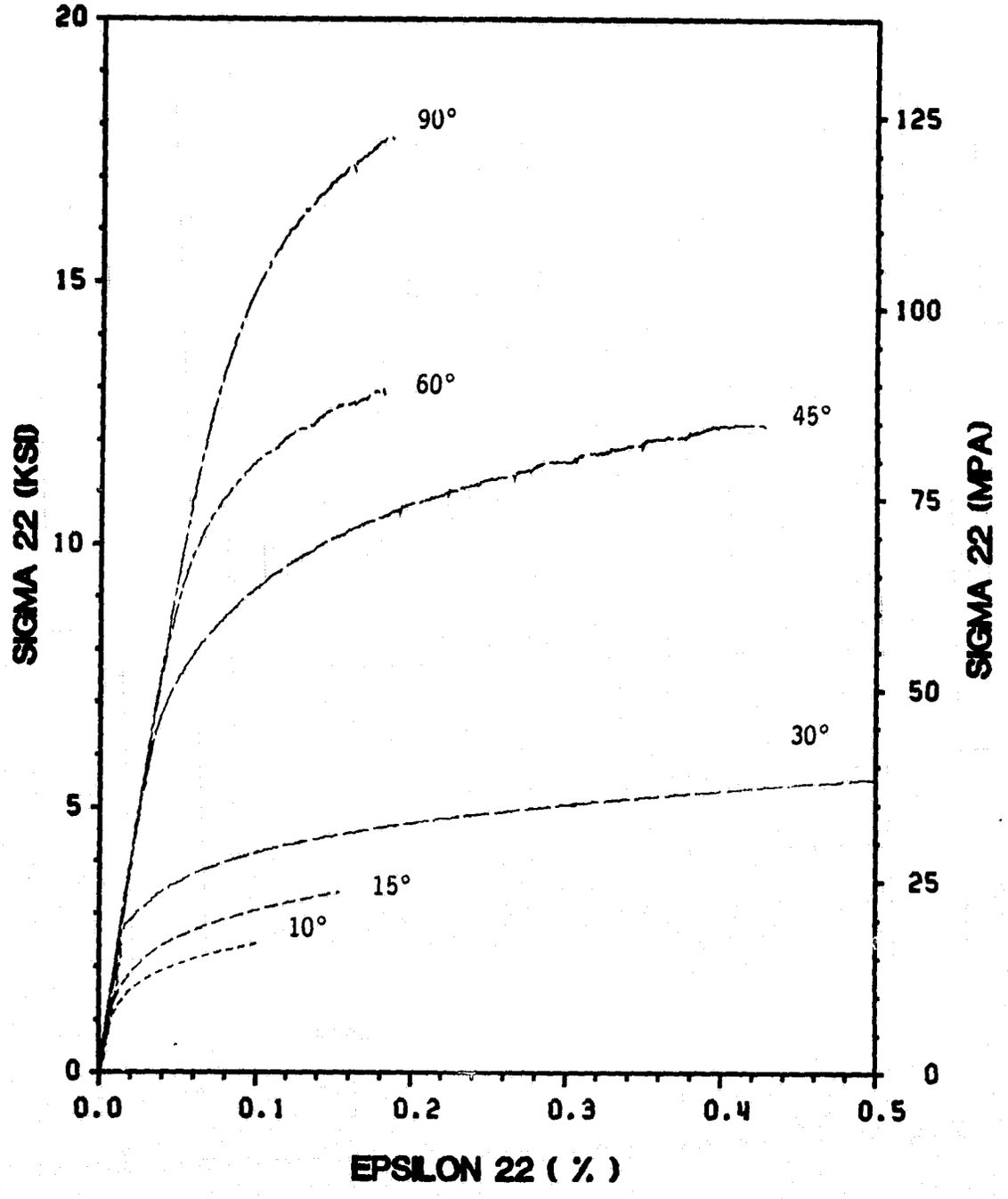

Figure 17. Normalized In-Plane Transverse Response

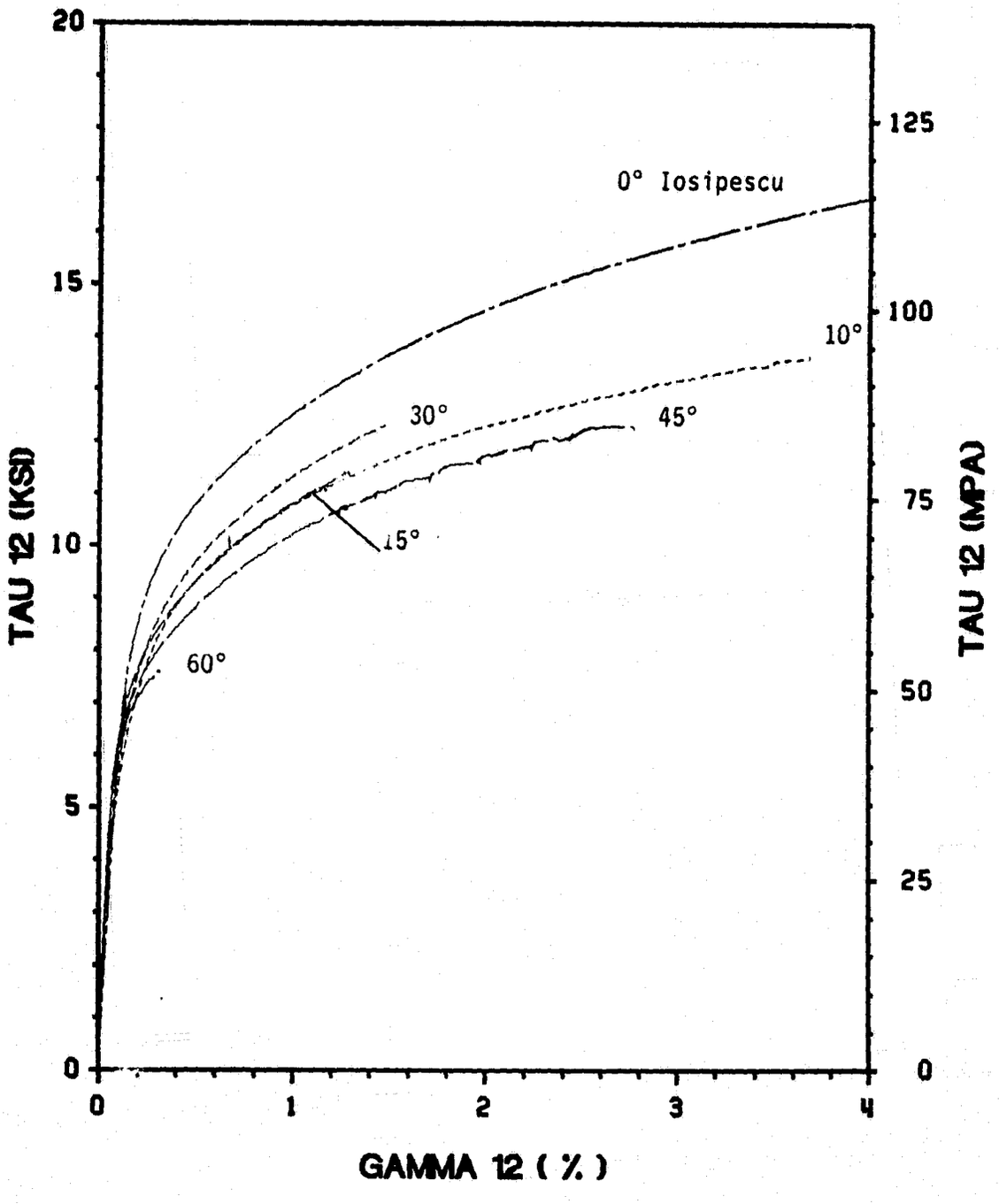

Figure 18. Tensile In-Plane Shear Response

3.1.1 Elastic Response

The average values of initial moduli obtained from the various off-axis configurations are summarized in Tables 7 and 8. Also included in the tables are the maximum stress and strain recorded at failure.

Table 7. Average Tensile Properties

Fiber Orientation 0	Elastic Modulus E_{xx}(msi)	Poisson's Ratio ν_{xy}	Ultimate Stress σ^{*}_{xx}(ksi)	Ultimate Strain ε_{xx}(%)
0°	32.93	0.237	187.5	0.826
10°	31.36	0.257	94.5*	1.688*
15°	30.64	0.272	66.8*	1.846*
30°	26.50	0.318	26.9	0.638
45°	22.03	0.317	25.0	1.708
60°	19.90	0.271	16.9	0.204
90°	20.21	0.150	17.1	0.184

* cyclic loading

Table 8. Average Shear Properties from Off-Axis Tension Test

Fiber Orientation θ	Shear Modulus G'_{12}(msi)	Ultimate Stress τ'_{12}(ksi)	Ultimate Strain γ_{12}(%)
10°	8.50	15.67*	5.513*
15°	8.41	16.08*	5.672*
30°	8.59	11.41	1.297
45°	8.35	12.46	2.806
60°	8.05	7.60	0.285

* cyclic loading

Comparison between apparent experimental results and theoretical predictions of the elastic moduli is given in Figures 19 - 21. Due to the fact that boron/aluminum is not highly anisotropic and the aspect ratio of the off-axis tension specimens is fairly high, no significant difference between the Pagano-Halpin prediction, which takes into account the shear coupling effect due to end-constraints, and the prediction based on the far field stress ($\bar{\sigma}_{xx}$) only, is observed.

For the global Young's Modulus $E_{xx}(\theta)$ (Figure 19), the correlation between experimental results and theoretical predictions is excellent. Six out of seven experimental values fall directly on top of the theoretical predictions.

The experimentally obtained Poisson's ratio ν_{xy} (θ), Figure 20, exhibits some scatter. The theoretical predictions are somewhat lower than the experimental values, but follow the same general trend. A remarkable result is the agreement between experiment and theory for the transverse value ν_{21}. It is generally recognized that the evaluation of the transverse Poisson's ratio is very difficult. High amount of scatter in the experimentally observed transverse Poisson's response of many advances composites is typical, which is a result of small failure strains. This affects the size of the initial region and makes it difficult to determine an initial transverse value. Small failure strains for

the 90° on-axis tests have been also noted in the present investigation. Nevertheless, the amount of scatter in the data presented in Figure 20 is fairly small. It is certainly reassuring that the difficult-to-satisfy relationship between longitudinal and transverse response (eqn. 3.6) holds for the obtained tensile experimental data.

$$\frac{\nu_{12}}{E_{11}} = \frac{\nu_{21}}{E_{22}} \tag{3.6}$$

The correlation of the measured apparent in-plane shear modulus G'_{12} and the prediction of the Pagano-Halpin model is also fairly good (Figure 21). For small off-axis orientations the difference between the actual and apparent value is very small. This result was expected, since the ratio of anisotropy (E_{11} / E_{22}) is very small and the aspect ratio of the off-axis tension coupons is fairly large. The poor correlation of the values obtained from the 60° off-axis test is not understood. It can be seen in Figure 21 that the use of the G_{12} value obtained from the 45° off-axis tension test as an input value for the theoretical analysis is justified. It can be shown analytically that the 45° off-axis coupon is virtually unaffected by the shear coupling effect and therefore gives the most accurate value of G_{12}. Considering the stress field in the gage section used by Pagano and Halpin, eqn. (2.7), the actual in-plane shear stress can be expressed in the following manner including the shear coupling effect.

$$\tau_{12} = - \sin\theta\cos\theta\sigma_{xx} + (\cos^2\theta - \sin^2\theta)\tau_{xy} \tag{3.7}$$

For the $\theta = 45°$, $\cos^2\theta = \sin^2\theta$ and the shear coupling term vanishes.

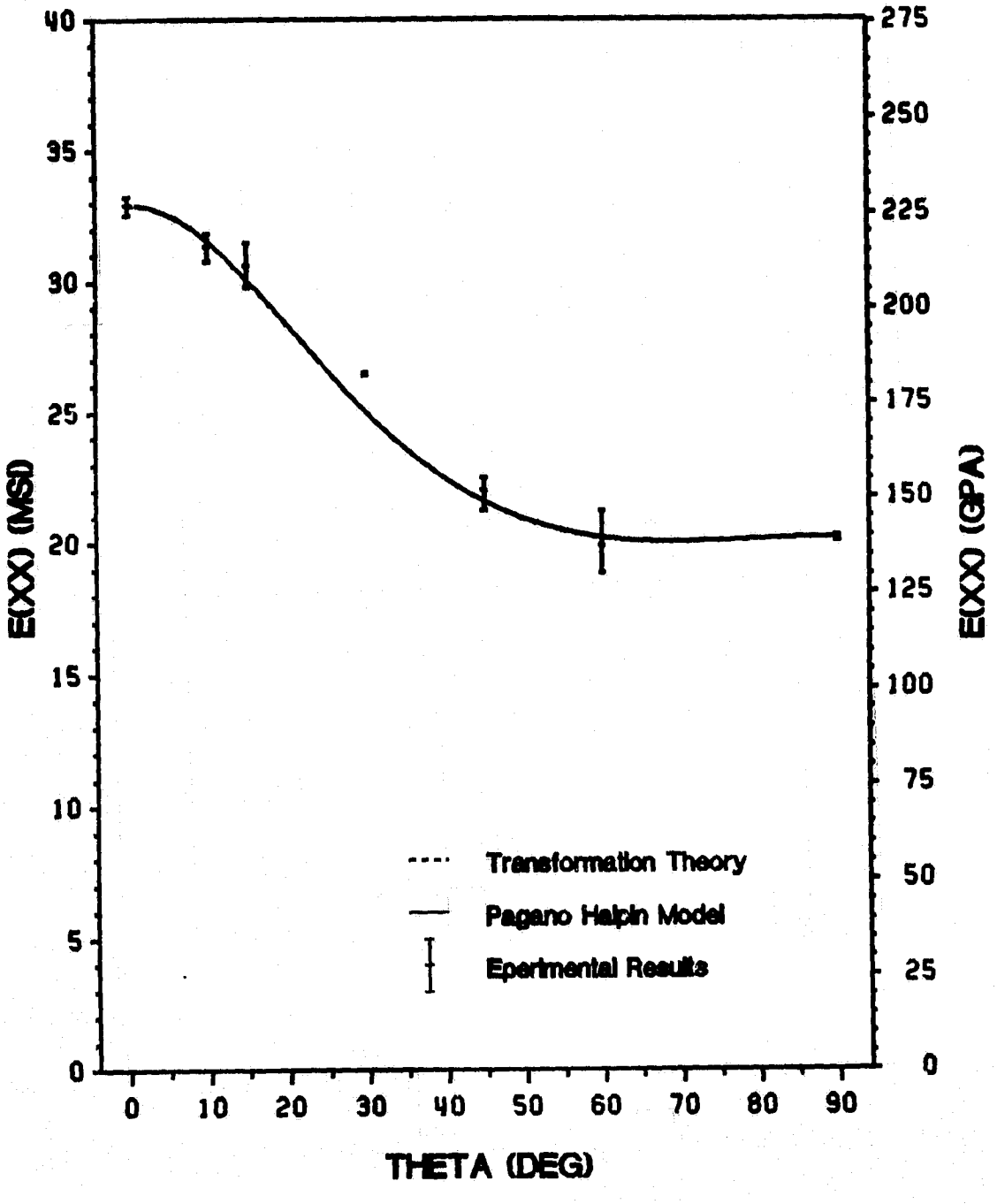

Figure 19. Global Tensile Young's Modulus E_{xx} (θ)

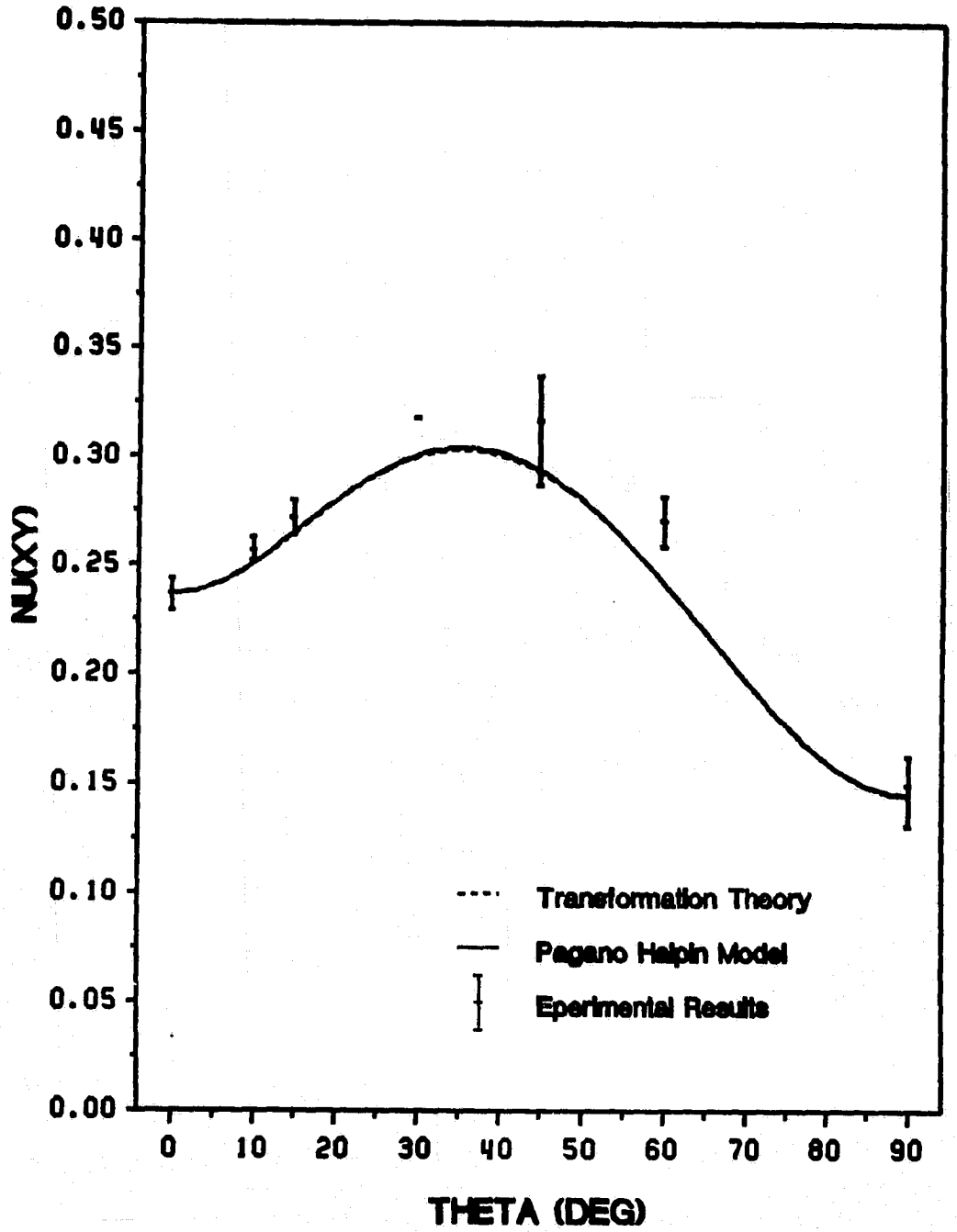

Figure 20. Global Tensile Poisson's ratio ν_{xy} (θ)

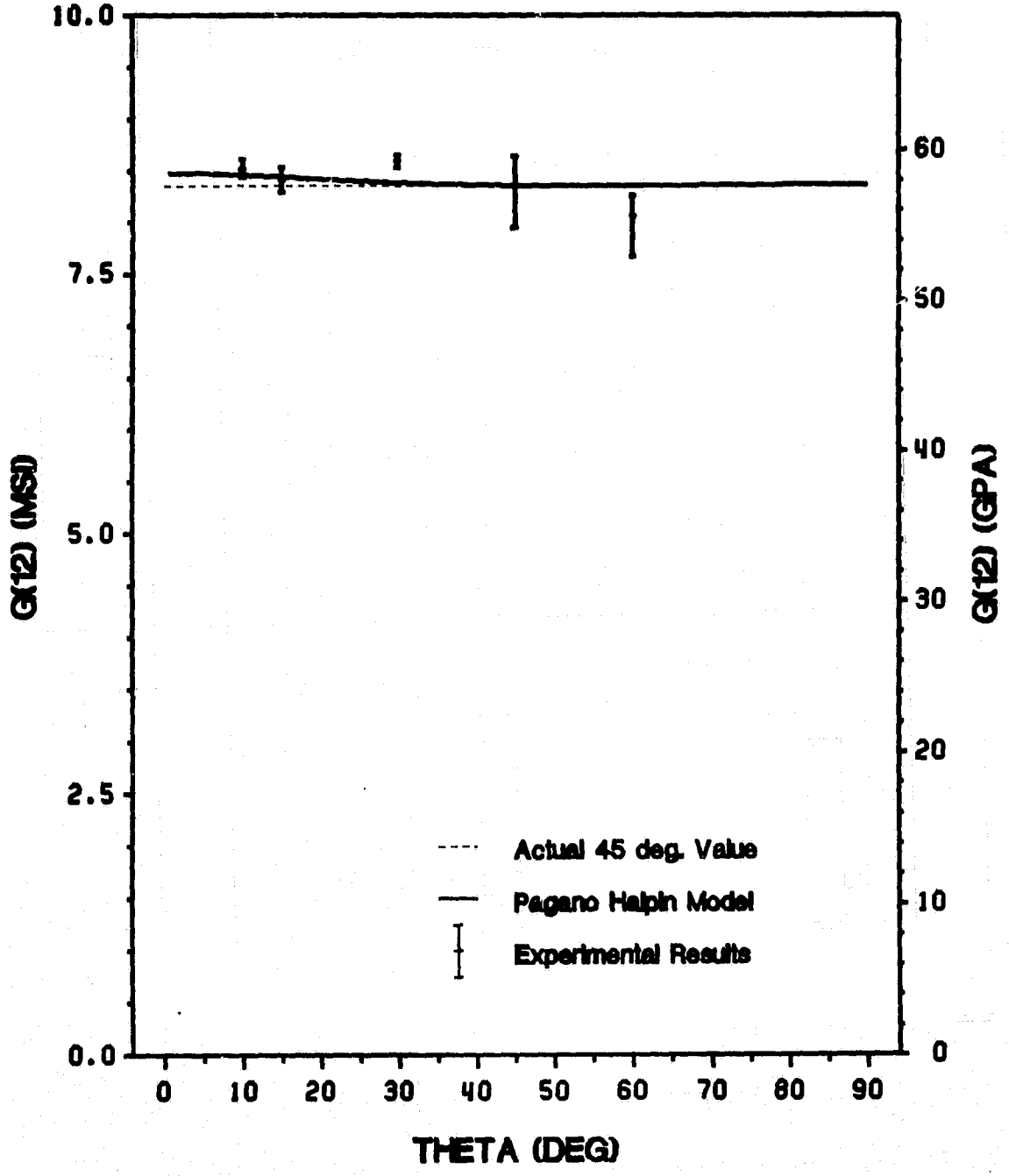

Figure 21. Apparent Tensile In-Plane Shear Modulus $G'_{12}(\theta)$

3.1.2 Plastic Response

Yielding

In order to determine the yield point for each individual test, three different methods were used. The yield point was defined as the proportional limit of the stress-strain or Poisson's responses. The first indication of nonlinearity from the initial linear curve of the tensile stress-strain response ($\bar{\sigma}_{xx}$ vs. ε_{xx}), the Poisson's response ($-\varepsilon_{yy}$ vs. ε_{xx}), and the in-plane shear response (τ'_{12} vs. γ_{12}) was defined as the initiation of yielding in the present study. Comparison between the yield loci obtained from the tensile response, Poisson's response, and the in-plane shear response for the average axial stress $\bar{\sigma}_{xx}$, the actual axial strain ε_{xx}, the apparent in-plane shear stress τ'_{12}, and the actual in-plane shear strain γ_{12} is presented in Figures 22 - 25. In these figures average values for each on- and off-axis configuration were plotted. In general, it can be said that the difference between the three different approaches for determining the yield point is small, with the in-plane shear response predicting generally the lowest yield stresses. The highest values are obtained from the tensile stress-strain response. The results of each individual test are given in Appendix A. The scatter for each on- and off-axis configuration is fairly small.

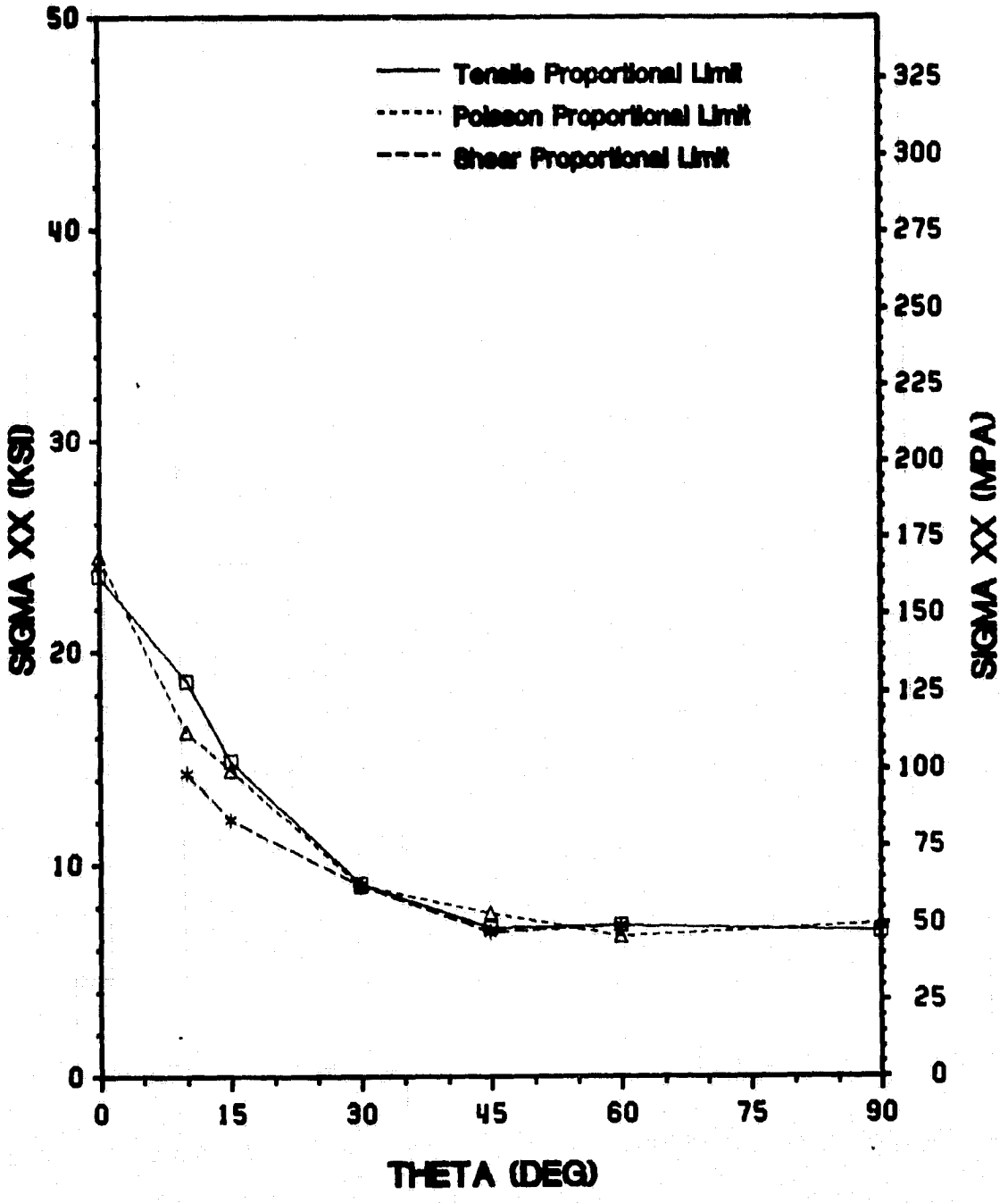

Figure 22. Apparent Axial Yield Stress in Tension $\overline{\sigma}^{y}_{xx}(\theta)$

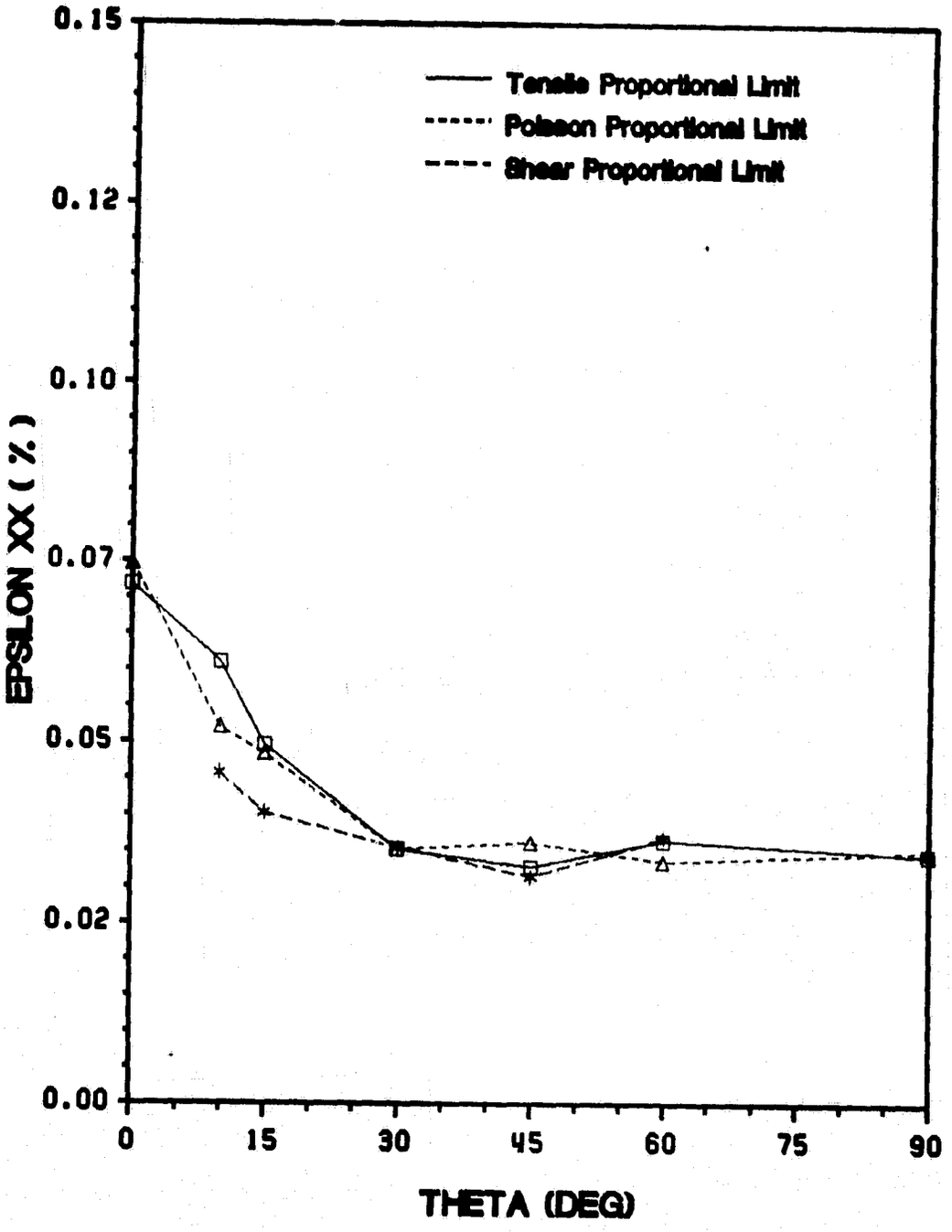

Figure 23. Axial Yield Strain in Tension $\varepsilon^{y}_{xx}(\theta)$

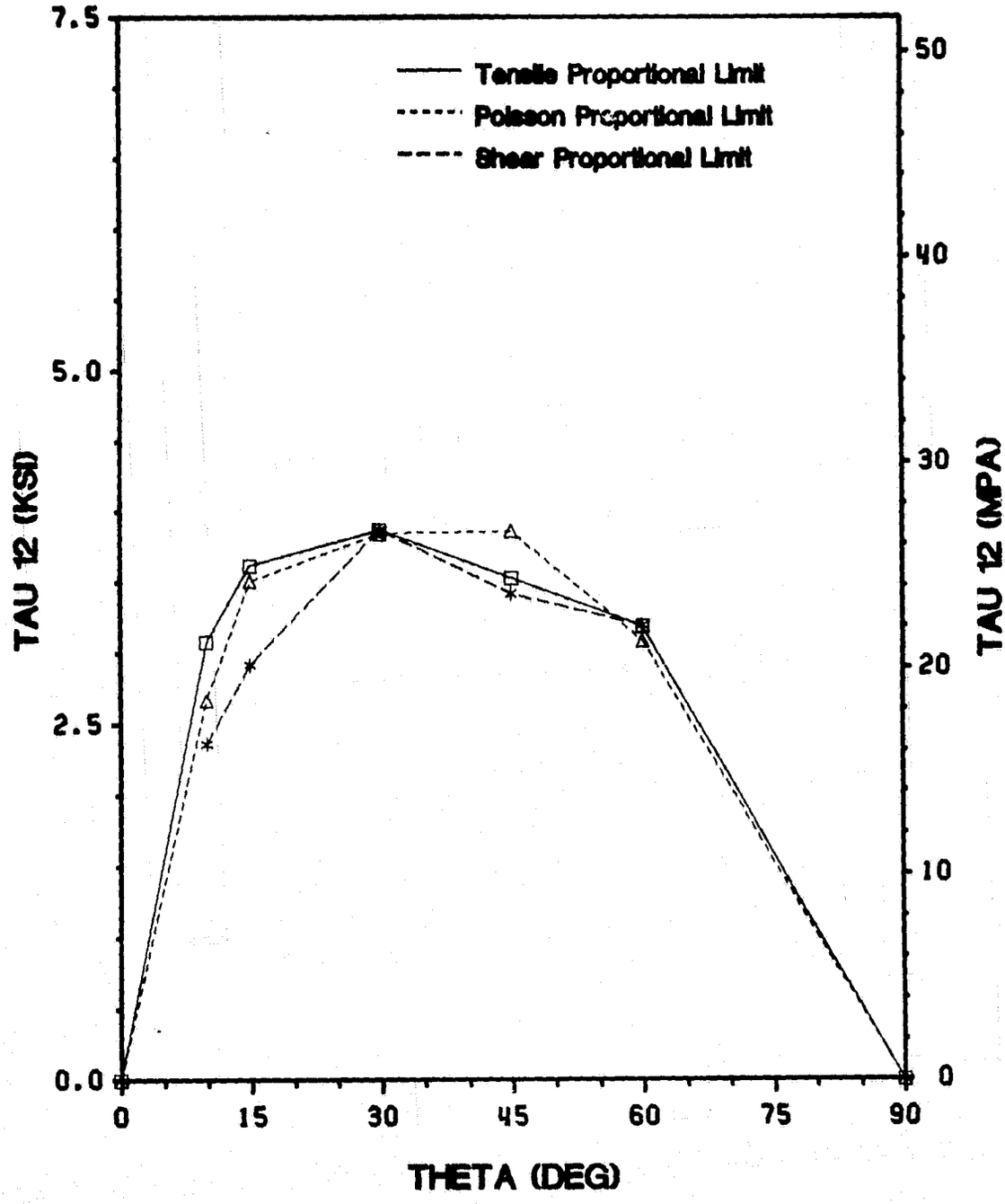

Figure 24. Apparent In-Plane Shear Yield Stress in Tension $\tau_{12}^{y}(\theta)$

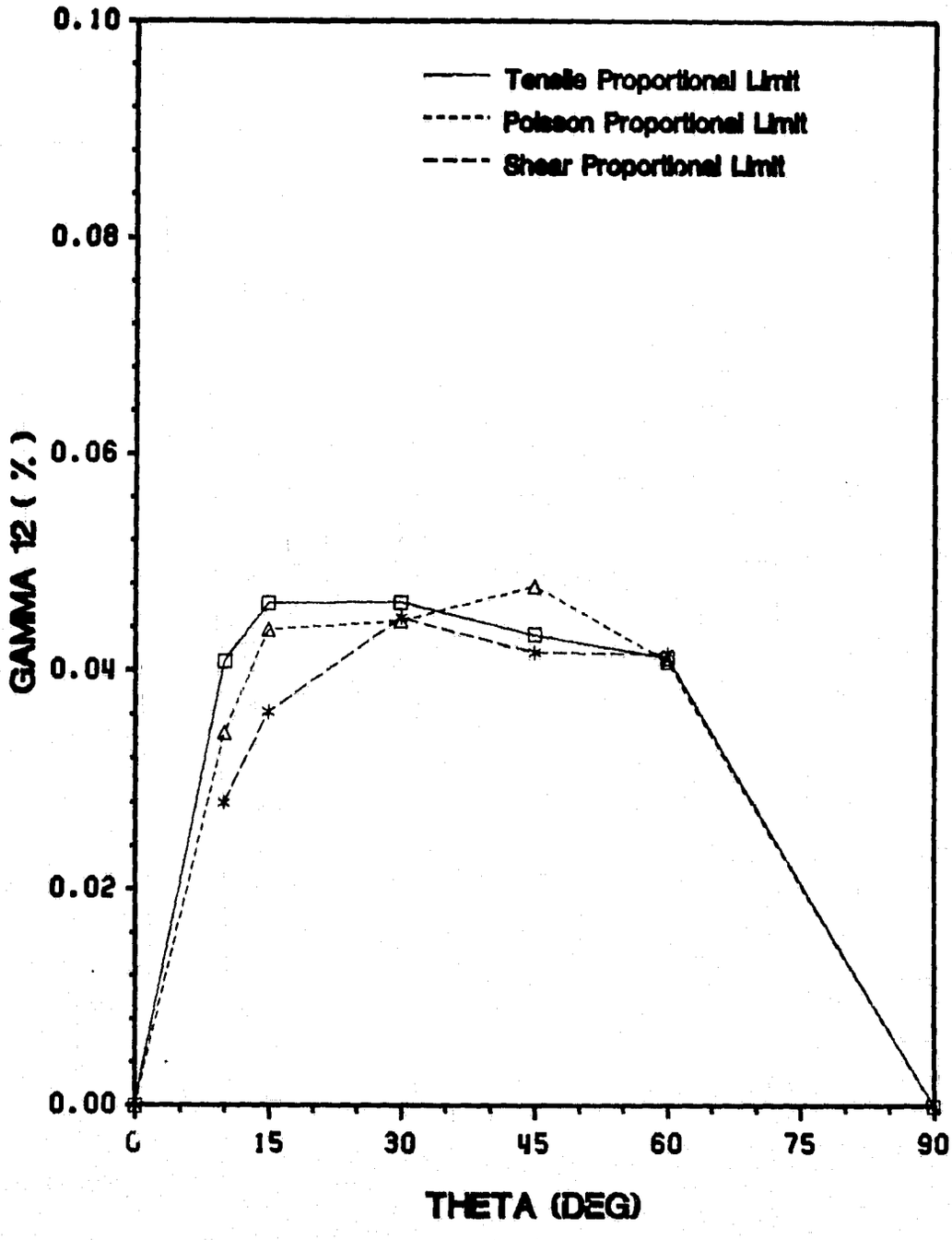

Figure 25. In-Plane Shear Yield Strain in Tension γ_{12}^{Y} (θ)

Subsequent Hardening

Monotonic Test

As shown in Figure 14, the nonlinear (plastic) response of boron/aluminum is a function of the fiber orientation. The amount and rate of material softening increases with increasing off-axis angle θ. The change in the off-axis angle θ results in a change of the in-plane stress ratios. The resulting stress-interaction effects for the various in-plane responses (σ_{11} vs. ε_{11}, σ_{22} vs. ε_{22}, and τ_{12} vs. γ_{12}) are well documented in Figures 16 - 18. It should be mentioned that the 10° and 15° off-axis tension coupons were not tested monotonically to failure due to grip slippage or strain gage malfunction. For these low off-axis coupons, the strain gages were not able to record the high plastic strain at failure. Consequently, the tests were stopped, the specimens were regaged and subsequently reloaded to failure.

As a first attempt to determine the functional form of the plastic response of boron/aluminum in the global and material principal coordinate systems, the global axial and in-plane longitudinal and transverse response as well as the in-plane shear response were plotted on a logarithmic scale (Figures 26 - 29). In these figures, only the plastic strains are presented. Recalling the following classical definition of the total strain,

$$\varepsilon_{ij}^{tot.} = \varepsilon_{ij}^{el.} + \varepsilon_{ij}^{pl.} \tag{3.16}$$

the global axial plastic strain can be expressed in the following manner,

$$\varepsilon_{xx}^{pl.} = \varepsilon_{xx}^{tot.} - \frac{\bar{\sigma}_{xx}}{E_{xx}} \tag{3.17}$$

where the one-dimensional Hooke's Law,

$$\sigma_{xx} = E_{xx}\,\varepsilon_{xx} \tag{3.18}$$

has been used.

The other plastic strain components (ε_{11}^{pl}, ε_{22}^{pl}, and γ_{12}^{pl}) were calculated in a similar fashion. The linearity of the curves in Figures 26 - 29 illustrates the possibility of approximating the plastic response of boron/aluminum by a power law expression, using the same power exponents for each global or in-plane response, but different coefficients depending on the different off-axis orientations. The coefficients represent the varying amount of stress-interaction. The only exception was the 0° test, where a bimodular hardening was observed.

For completeness, the result obtained from a typical 0° Iosipescu shear test was included in Figures 18 and 29. From Figure 29 it can be seen that the plastic response of a 0° Iosipescu shear test is very close to that observed in an off-axis tension test, but at a higher stress level. A complete comparison of the Iosipescu shear test and off-axis tension test results is given in Chapter 4.

The individual monotonic off-axis tension test results are given in Appendix A.1. The small amount of scatter in the results for each individual orientation forms a solid base for subsequent statements and conclusions.

The global Poisson's response exhibited some scatter for different tests of the same on- and off-axis configurations for high off-axis angles. The plastic response exhibited linear behavior for all orientations.

The in-plane shear response exhibits highly nonlinear behavior. This is especially true for small off-axis orientations (10°, 15°), where the high extent of nonlinearity and corresponding dissipation is seen. This leads to the conclusion that the nonlinear response of the entire lamina was influenced to a large extent by the intralaminar shear stress.

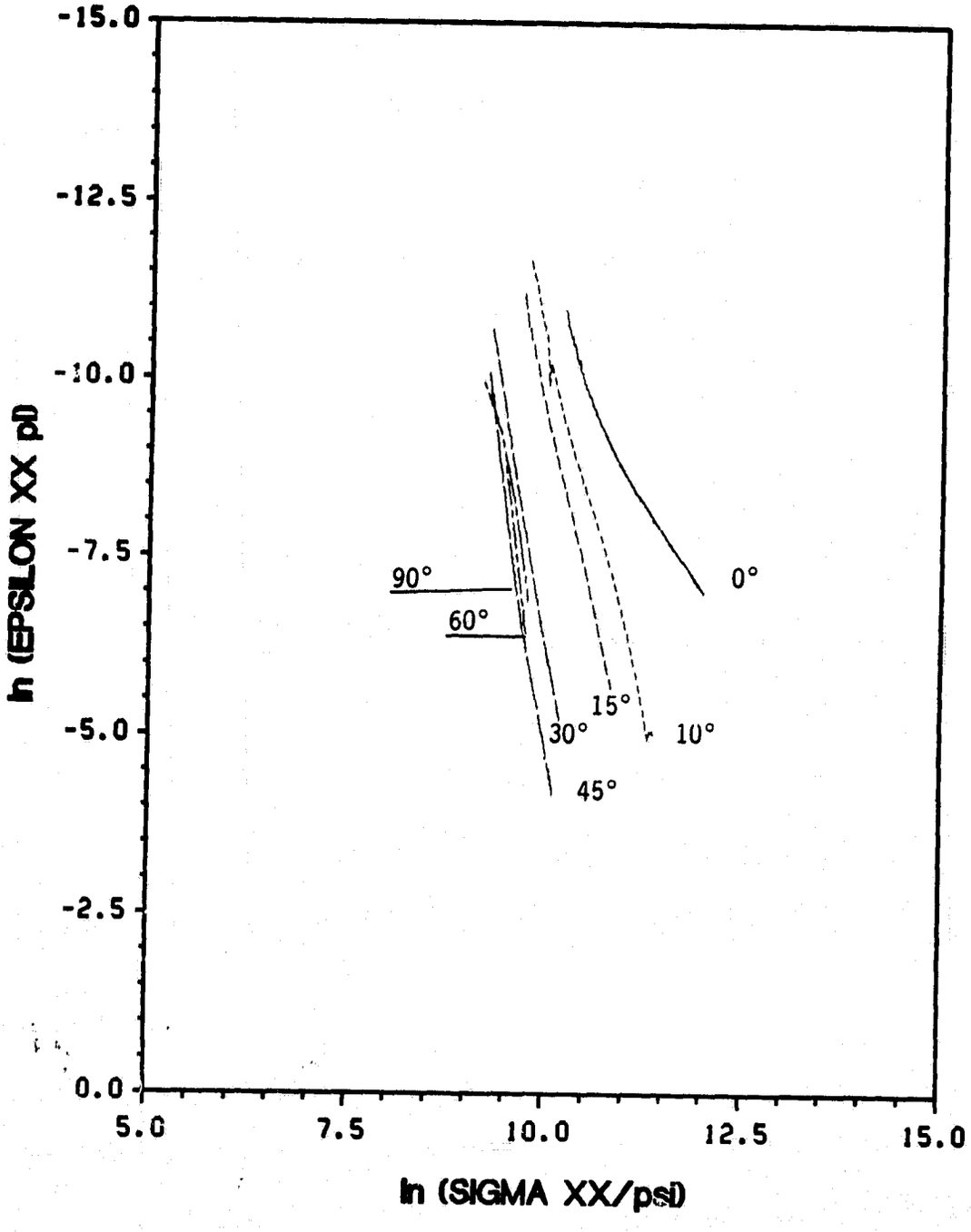

Figure 26. Functional Form of the Global Axial Response

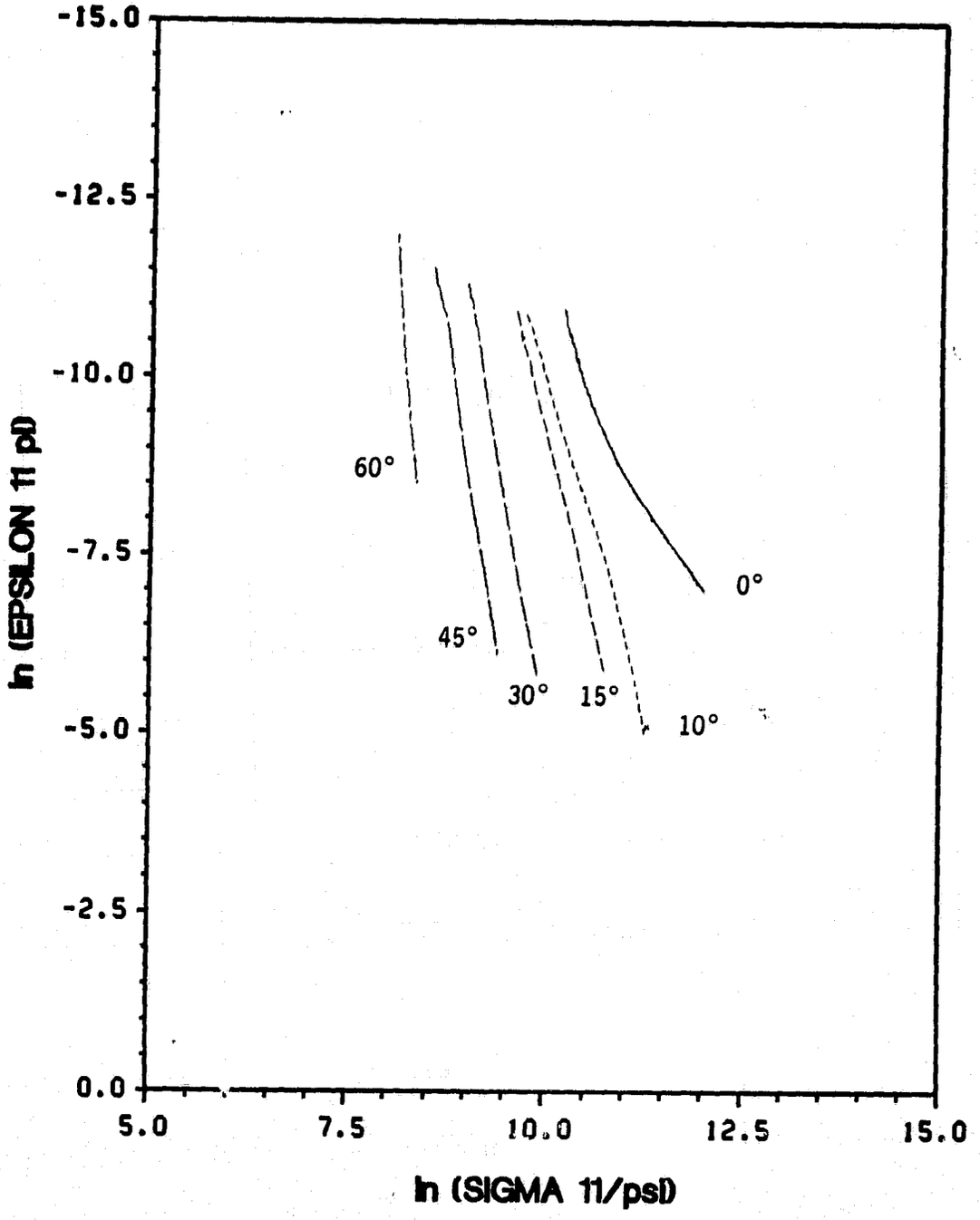

Figure 27. Functional Form of the In-Plane Longitudinal Response

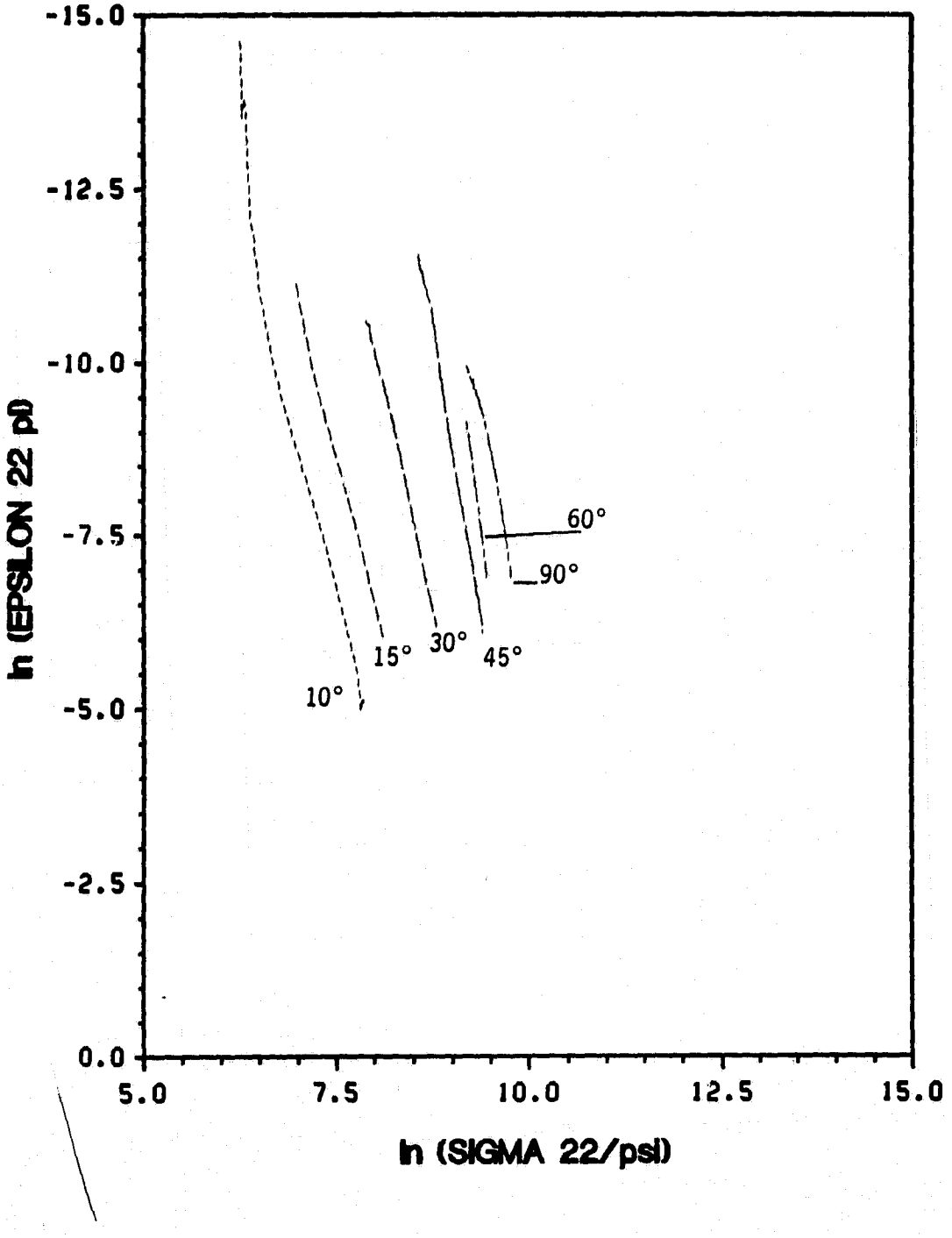

Figure 28. Functional Form of the In-Plane Transverse Response

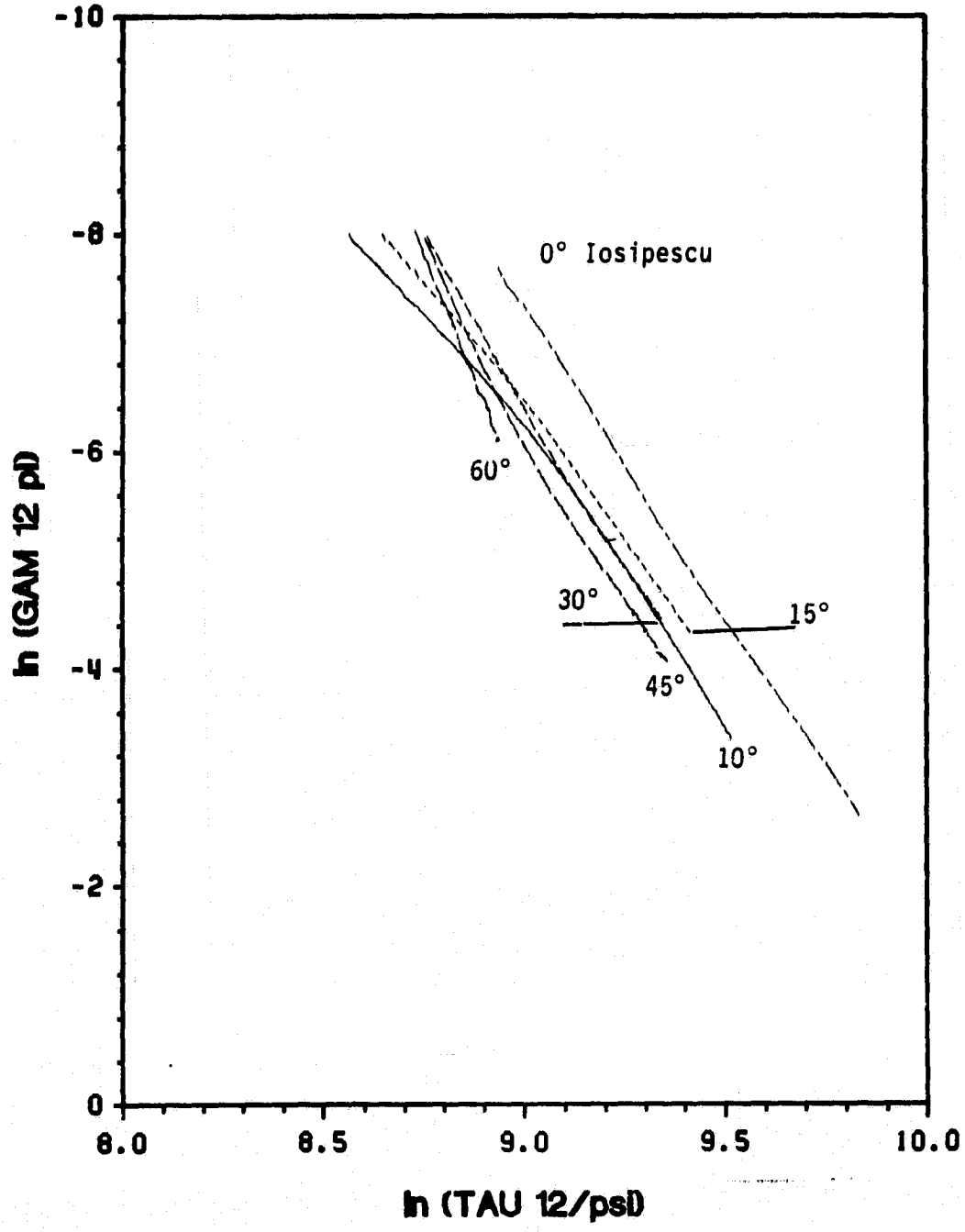

Figure 29. Functional Form of the In-Plane Shear Response

Cyclic Test

In order to obtain a complete characterization of the plastic response of boron/aluminum, cyclic tests were performed. The dissipative nature of the nonlinear response is well documented in the figures shown in Appendix A.2, where a large amount of permanent strain accumulation is observed. Even for the 0° tensile test, permanent strains are evident. This is unlike the results of 0° compression tests as will be shown in Section 3.2.2. Another significant result of the cyclic tests is the fact that the unloading and reloading paths are nearly identical, even though loud cracking noises could be heard, indicating the possibility of interior damage during the last loading cycle. The difference between the unloading and reloading paths increased with the number of cycles during each test, but still remained very small. The slope of each unloading and reloading cycle also remained nearly the same during each cyclic test. The large amount of permanent strain accumulation in the 10°, 15°, and 45° off-axis tests and shear strain accumulation in the 10° and 15° off-axis tests is a result of large plastic strains in the aluminum matrix.

The cyclic loading of the specimens also influenced the ultimate strength values. With the exception of the 45° off-axis test, where early grip failure due a high stress concentration at the interface between grip and gage area occurred, cyclic loading increased the failure stresses and strains. For the other off-axis tests, the failure stress was increased by about 4 % and the failure strain by about 20%. The largest increase was observed in the case of the 90° on-axis test, where the failure stress was increased by about 25 % and the failure strain by almost 40 %.

Failure Stress (Strength)

The failure stress (strength) of a material is always an important factor in material characterization. The strength may be influenced by factors such as temperature, radiation, humidity, loading conditions and history, and the material structure itself. For anisotropic materials such as composites, the material structure plays an important roll. Recent studies by Johnson [11] on fatigue damage and by Shorshorov et al [12] on interface strength showed the dependence of the strength of

boron/aluminum composites on the various effects mentioned above. Lynch et al [18] showed how material strength depends on thermal history during the manufacturing process and subsequent application. For the present study it can be shown that the axial strength of the unidirectional boron/aluminum is a function of the fiber orientation. As illustrated in Figure 30, the strength decreases drastically in the off-axis range 0° - 20°.

Two different failure criteria were used to predict failure for the tested off-axis configurations. The first criterion is the 'Maximum Stress Criterion', where failure is predicted by relating in-plane stresses directly to the various failure modes given in eqn. (3.19) [20].

$$\begin{aligned} \sigma_1 &= X_t \\ \sigma_2 &= Y_t \\ |\tau_{12}| &= S \end{aligned} \tag{3.19}$$

In the above, X_t is the longitudinal and Y_t is the transverse strength in tension and S is the in-plane shear strength. The predicted failure occurs when the first of the three equations is satisfied.

The second criterion used to predict strength is the 'Tsai-Wu Criterion', which uses a tensor polynomial approach. For on orthotropic lamina under plane stress, the three-dimensional tensor polynomial expression

$$F_i F_j \sigma_{ij} = 1 \tag{3.20}$$

reduces to

$$F_1\sigma_1 + F_2\sigma_2 + F_6\tau_{12} + F_{11}\sigma_1^{\,2} + F_{22}\sigma_2^{\,2} + F_{66}\tau_{12}^{\,2} + 2F_{12}\sigma_1\sigma_2 = 1 \tag{3.21}$$

where

$$
\begin{aligned}
F_1 &= \frac{1}{X_t} + \frac{1}{X_c} \\
F_2 &= \frac{1}{Y_t} + \frac{1}{Y_c} \\
F_{11} &= -\frac{1}{X_t X_c} \\
F_{22} &= -\frac{1}{Y_t Y_c} \\
F_{12} &= -\frac{\sqrt{F_{11} F_{22}}}{2}
\end{aligned}
\tag{3.22}
$$

In view of the fact that the shear strength in the principal material directions is independent of the shear stress sign [20], the shear terms in the Tsai-Wu polynomial become :

$$
\begin{aligned}
F_6 &= 0 \\
F_{66} &= \frac{1}{S^2}
\end{aligned}
\tag{3.23}
$$

The influence of the F_{12} term on the Tsai-Wu polynomial was thoroughly studied by Pipes et al [20, 37]. They concluded that the coupling term F_{12} does not influence significantly the Tsai-Wu prediction. In the present study the in-plane coupling term was included for completeness.

In order to incorporate the end-constraint effects caused by the shear coupling phenomenon in the failure criteria, the Maximum Stress and the Tsai-Wu criterion were modified as follows.

Considering the state of stress in the off-axis coupon derived by Pagano and Halpin [25] (eqn. 2.7),

$$
\begin{bmatrix} \sigma_1 \\ \sigma_2 \\ \tau_{12} \end{bmatrix} = \begin{bmatrix} \cos^2\theta & \sin^2\theta & 2\sin\theta\cos\theta \\ \sin^2\theta & \cos^2\theta & -2\sin\theta\cos\theta \\ -\sin\theta\cos\theta & \sin\theta\cos\theta & \cos^2\theta - \sin^2\theta \end{bmatrix} \begin{bmatrix} \sigma_{xx} \\ 0 \\ \tau_{xy} \end{bmatrix} \tag{3.24}
$$

and the relation between the global axial stress and the global shear stress introduced by the end-constraints,

$$\tau_{xy} = \beta\sigma_{xx} \tag{3.25}$$

where β is given by eqn. (2.10), Section 2.2.4, the stresses in the principal material direction can be expressed as follows:

$$\begin{aligned}
\sigma_1 &= \sigma_{xx}[\cos^2\theta + 2\beta \sin\theta\cos\theta] \\
\sigma_2 &= \sigma_{xx}[\sin^2\theta - 2\beta \sin\theta\cos\theta] \\
\tau_{12} &= \sigma_{xx}[-\sin\theta\cos\theta + \beta(\cos^2\theta - \sin^2\theta)]
\end{aligned} \tag{3.26}$$

Based on the new definition of the in-plane stress components (eqn. 3.26), the Maximum Stress criterion becomes:

$$\sigma_{xx} = \frac{X_t}{\cos^2\theta + 2\beta \sin\theta\cos\theta}$$

$$\sigma_{xx} = \frac{Y_t}{\sin^2\theta - 2\beta \sin\theta\cos\theta} \tag{3.27}$$

$$\sigma_{xx} = \frac{S}{\sin\theta\cos\theta - \beta(\cos^2\theta - \sin^2\theta)}$$

While the modified Tsai-Wu criterion (eqn. 3.21) takes the form:

$$A\sigma_{xx}^{\ 2} + B\sigma_{xx} - 1 = 0 \tag{3.28}$$

where

and the relation between the global axial stress and the global shear stress [illegible] is:

$$\tau_{xy} = \beta\sigma_{xx} \tag{3.27}$$

where β is given by eqn. 3.11. Section 2.2.4, the stresses in the principal material direction can be expressed as follows:

$$\begin{aligned} \sigma_1 &= \sigma_{xx}[\cos^2\theta - 2\beta\sin\theta\cos\theta] \\ \sigma_2 &= \sigma_{xx}[\sin^2\theta - 2\beta\sin\theta\cos\theta] \\ \tau_{12} &= \sigma_{xx}[-\sin\theta\cos\theta + \beta(\cos^2\theta - \sin^2\theta)] \end{aligned} \tag{3.26}$$

Based on the new definition of the in-plane stress components (eqn. 3.26), the Maximum Stress criterion becomes:

$$\sigma_{xx} = \frac{X_t}{\cos^2\theta + 2\beta\sin\theta\cos\theta}$$

$$\sigma_{xx} = \frac{Y_t}{\sin^2\theta - 2\beta\sin\theta\cos\theta} \tag{3.27}$$

$$\sigma_{xx} = \frac{S}{\sin\theta\cos\theta - \beta(\cos^2\theta - \sin^2\theta)}$$

While the modified Tsai-Wu criterion (eqn. 3.21) takes the form:

$$A\sigma_{xx}^2 + B\sigma_{xx} - 1 = 0 \tag{3.28}$$

where

$$A = F_{11}(\cos^4\theta + 4\beta \sin\theta \cos^3\theta + 4\beta^2 \sin^2\theta \cos^2\theta)$$
$$+ F_{22}(\sin^4\theta - 4\beta \sin^3\theta \cos\theta + 4\beta^2 \sin\theta \cos\theta)$$
$$+ F_{66}[\sin^2\theta \cos^2\theta - 2\beta \sin\theta \cos\theta(\cos^2\theta - \sin^2\theta) + \beta^2(\cos^2\theta - \sin^2\theta)^2]$$
$$+ 2F_{12}[\sin^2\theta \cos^2\theta - 2\beta \sin\theta \cos\theta(\cos^2\theta - \sin^2\theta) - 4\beta^2 \sin^2\theta \cos^2\theta]$$

$$B = F_1(\cos^2\theta + 2\beta \sin\theta \cos\theta) + F_2(\sin^2\theta - 2\beta \sin\theta \cos\theta)$$

After solving the quadratic equation (3.28), the axial strength as a function of the fiber orientation θ finally can be written in the following manner,

$$\sigma_{xx} = -\frac{B}{2A} + \sqrt{\frac{B^2 + 4A}{4A^2}} \tag{3.29}$$

where the negative root is neglected for physical reasons.

Table 9. Material Strengths

X_t	=	187.5	ksi
Y_t	=	17.1	ksi
X_c	=	-194.4	ksi
Y_c	=	-45.3	ksi
S_{los}	=	19.5	ksi
S_{ten}	=	15.7	ksi

S_{los} 0° Iosipescu test results
S_{ten} 10° tension test results

The input data for the two failure criteria are given in Table 9. In the above table, the subscripts t and c denote tensile and compressive properties, respectively. The axial strength in tension (X_t) is somewhat questionable due to the fact that all 0° tension test specimens failed in the grip area and not in the gage section. The location of the failure may also explain the large scatter in the experimental data. Therefore, the value given in Table 9 may be interpreted as a lower bound of

the axial strength. Pipes et al [3] obtained a value of X_t = 223.9 ksi for monotonic loading conditions, which is close to the value obtained from the 0° cyclic test. The transverse strength in tension (Y_t) obtained from the 90° test is larger than the strength values from the 60° off-axis test, as also observed by Pipes [3].

Two values are given in Table 9 for the in-plane shear strength 'S'. One was obtained from the 10° off-axis test (S_{ten} = 15.5 ksi) and the other from the 0° Iosipescu shear test (S_{Ios} = 19.9 ksi). The shear strength from the 0° Iosipescu shear test was defined as the stress level where the first drop in the recorded load occurred. This drop corresponds to the initiation of axial splitting at the V-notch of the Iosipescu specimen. It is believed that after the first crack occurred, the measured data is more representative of structural rather than material response. Recent studies at Virginia Tech [21, 36] indicate that this particular value from the 0° Iosipescu shear test yields a good upper lower bound on the in-plane shear strength 'S'.

The two different theoretical predictions, Maximum Stress and Tsai-Wu criteria, are compared in Figure 30. For both criteria, the shear strength estimate from the 0° Iosipescu test was used. It can be seen in Figure 30 that the Maximum Stress criterion overestimates the off-axis strengths in comparison to the tensor polynomial criterion. For a more sophisticated approximation of the material strength, the Tsai-Wu criterion was used, taking into account the linear and quadratic terms. Comparison between the theoretical predictions, using the two different definitions of the in-plane shear strength, and the experimental results from monotonic and cyclic tests is given in Figure 31. The influence of the different definition of shear strength on the Tsai-Wu tensor polynomial is also illustrated in Figure 31. For the 30° and 60° off-axis tests, S_{ten} provided an excellent correlation between theoretical prediction and experimental results, whereas for the other off-axis configurations the prediction based on the 0° Iosipescu shear test value S_{Ios} gave a better correlation.

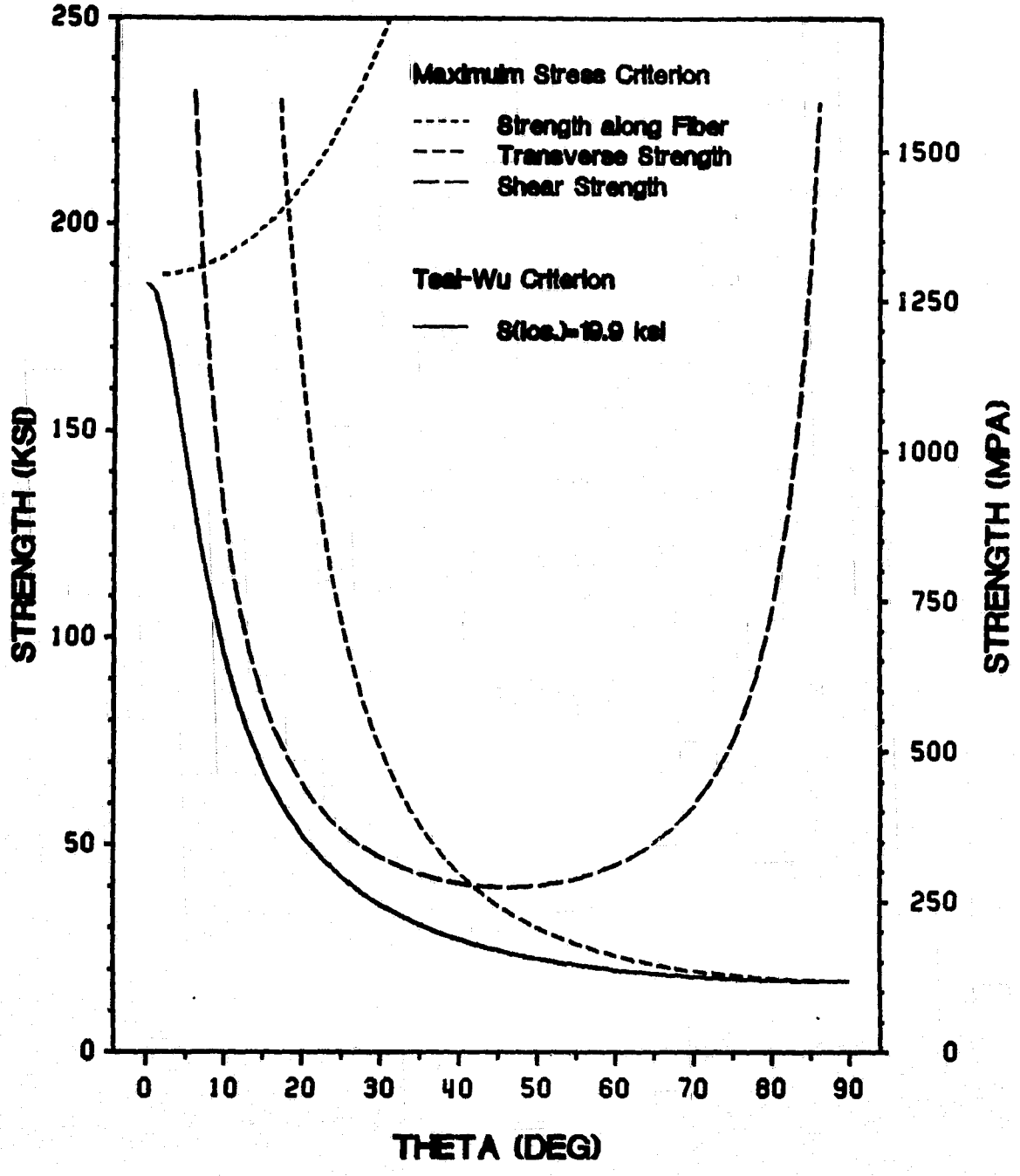

Figure 30. Maximum Stress & Tsai-Wu Failure Criterion

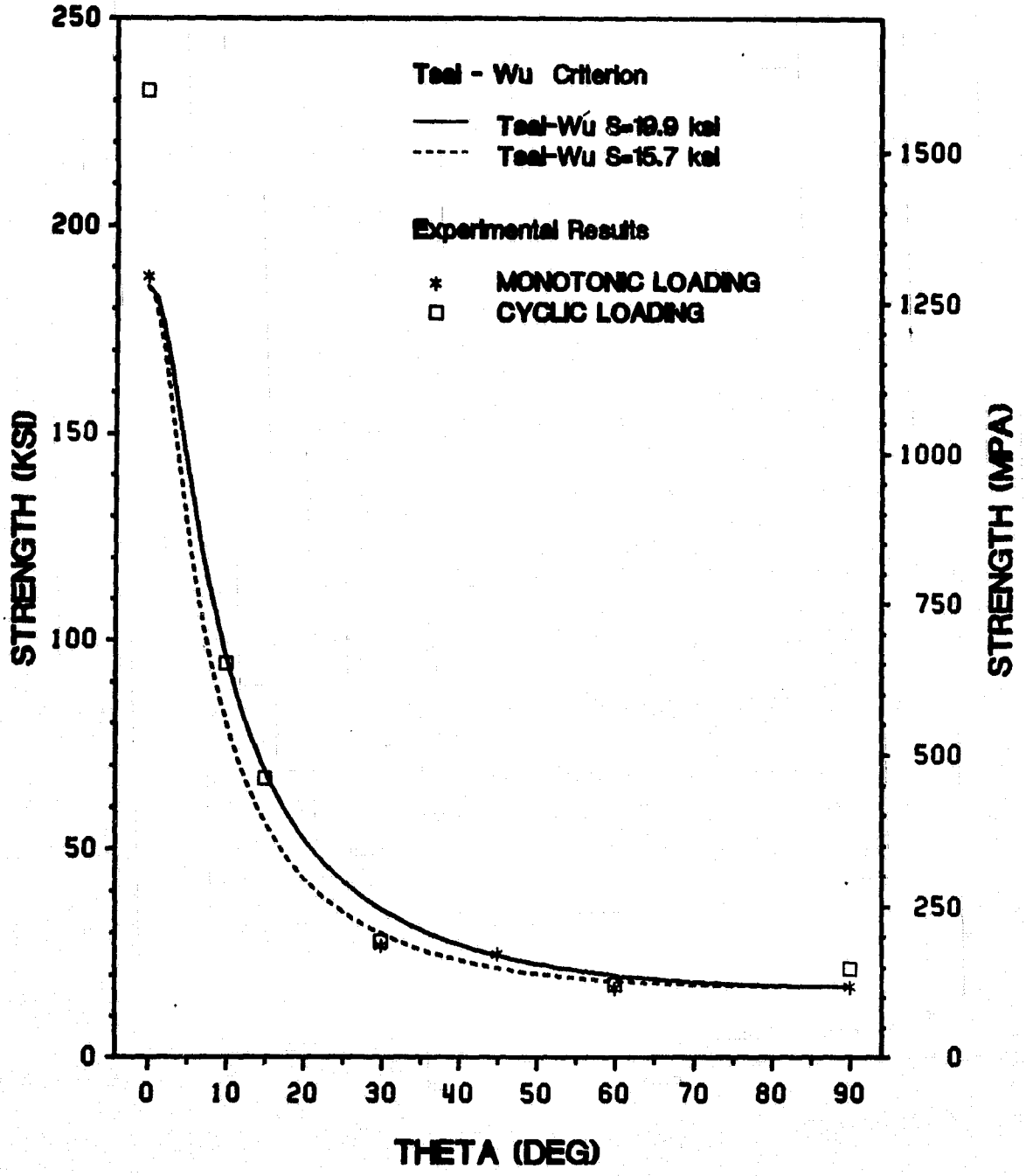

Figure 31. Tsai-Wu Predictions & Experimental Results

Failure Modes

Different failure modes were observed for different configurations. Catastrophic failure was observed for the 0° test, resulting in a rough failure surface. Up to 40 % of the fibers were broken in the 10° off-axis test; one test failed in shear along the fibers. The amount of fiber breakage was smaller for all other off-axis tests. Whereas for the 30° off-axis test only shear failure along the fibers occurred, up to 10 % of the fibers were broken in a 15° and 45° test. For the 60° off-axis test fibers were broken throughout the failure surface in an irregular pattern. In the case of the 90° test fiber breakage was observed at both edges of the failure surface.

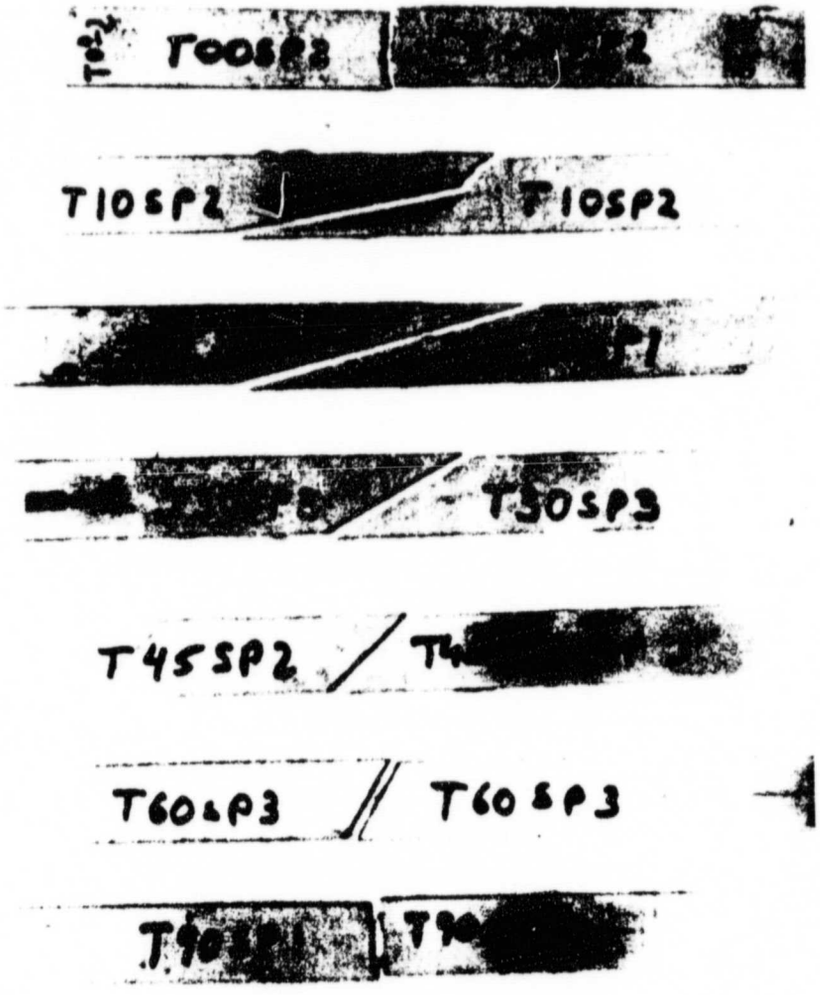

Figure 32. Failed Off-Axis Tension Test Specimens

3.2 *Compression Test Results*

Typical results for global stress-strain, Poisson and principal shear response from monotonic off-axis compression tests are given in Figures 33 and 35. The presented results are all apparent values corrected only for bending. As in the case of the off-axis tension tests, only one representative plot for each fiber orientation is given in the above figures. The observed scatter in the experimental data was larger than for the off-axis tension tests, but still small enough to justify the choice of a representative plot for each fiber orientation.

3.2.1 Elastic Response

The average compressive material properties are given in Tables 10 and 11, whereas the individual monotonic test results are given in Appendix B.1.

Table 10. Average Compressive Properties

Fiber Orientation θ	Elastic Modulus E_{xx}(msi)	Poisson's Ratio ν_{xy}	Ultimate Stress σ^{*}_{xx}(ksi)	Ultimate Strain ε_{xx}(%)
0°	33.27	0.421	194.4	0.610
10°	32.10	0.333	183.9	0.771
15°	31.21	0.465	128.9	0.740
30°	27.00	0.373	79.4	2.106
45°	23.44	0.396	55.7*	7.184*
90°	20.44	0.140	45.3	2.592

* no failure

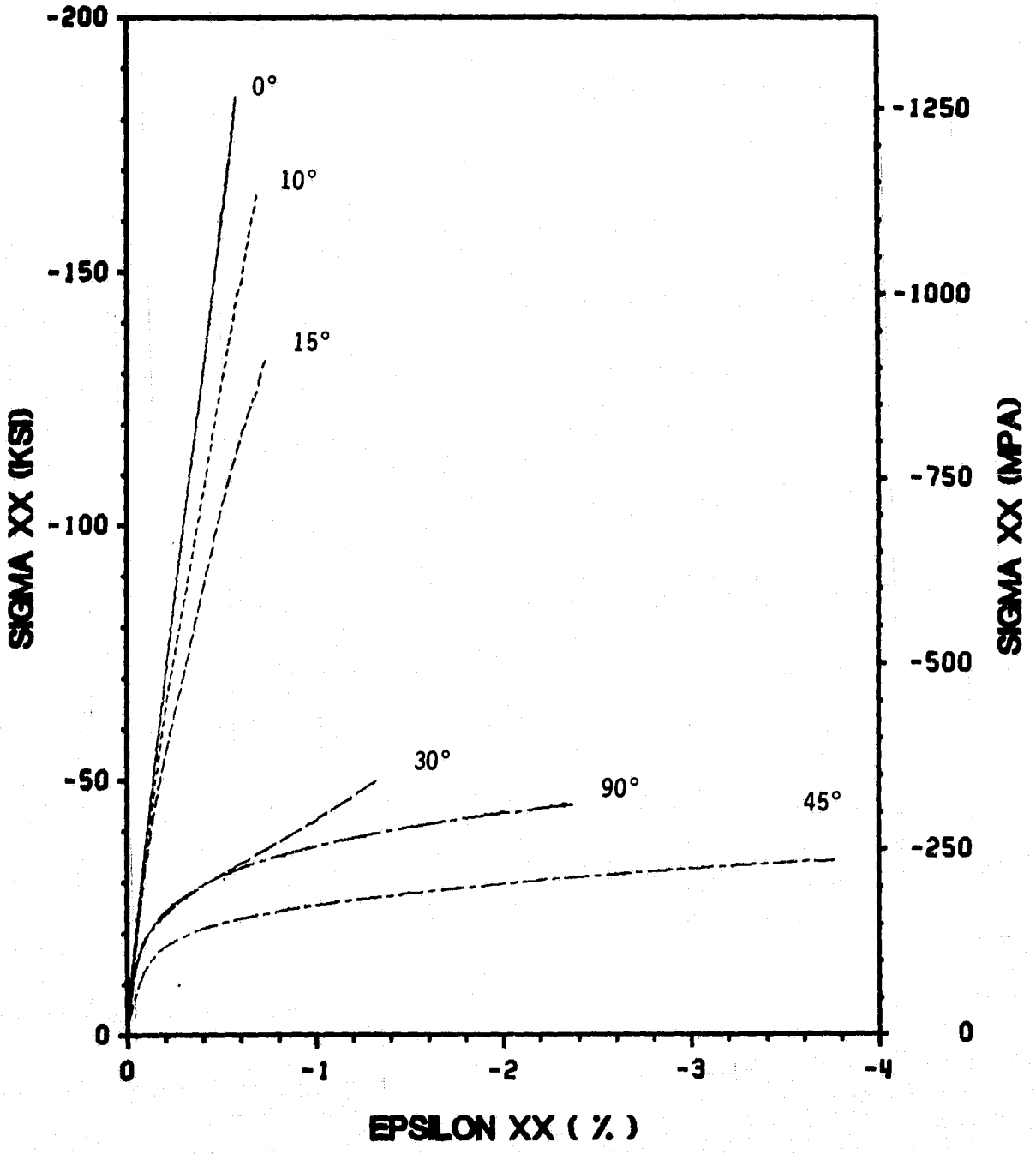

Figure 33. Global Compressive Stress-Strain Response

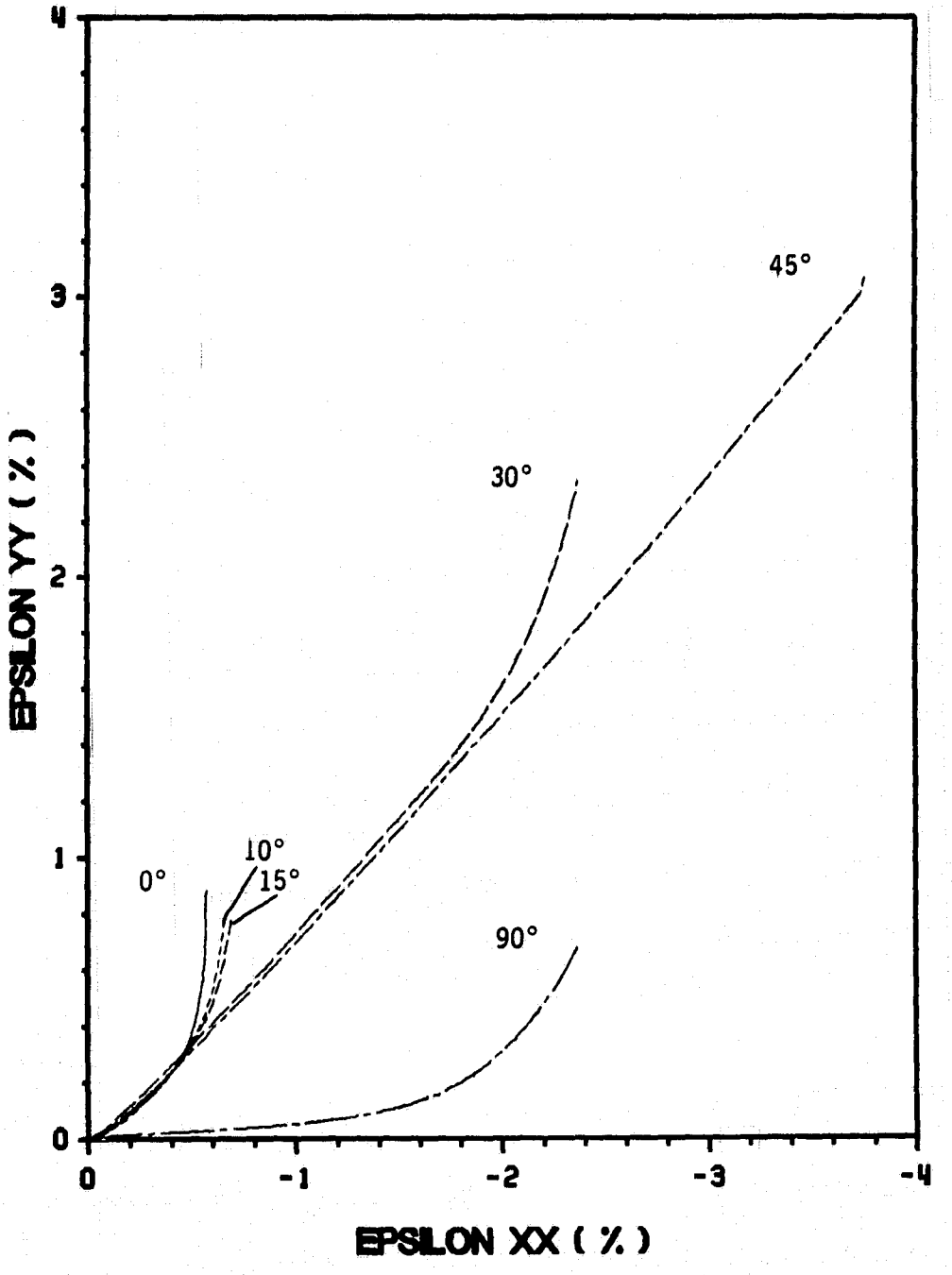

Figure 34. Global Compressive Poisson's response

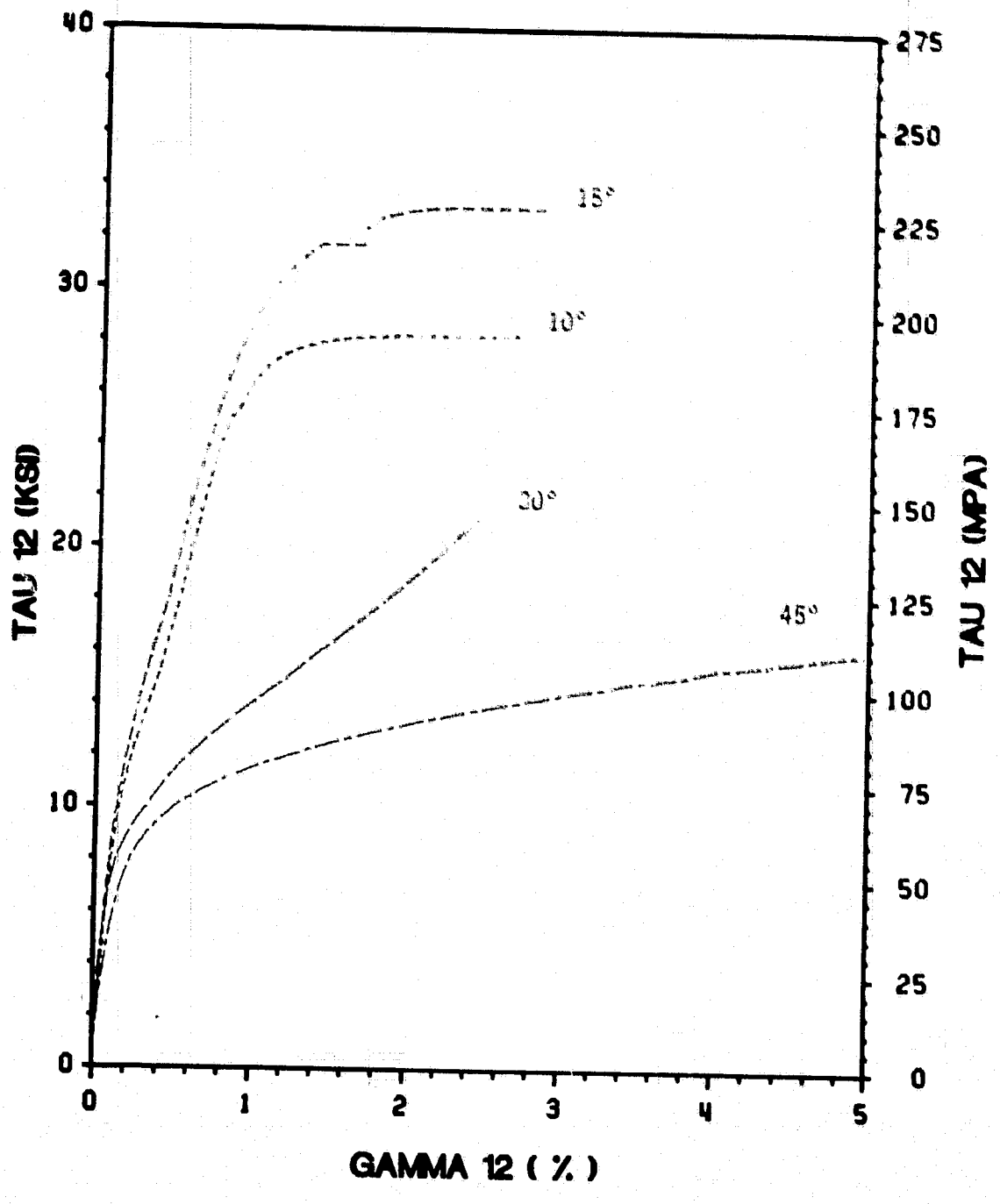

Figure 35. Compressive In-Plane Shear Response

Table 11. Average Shear Properties from Off-Axis Compression Test

Fiber Orientation 0	Shear Modulus G_{12}^{c}(msi)	Ultimate Stress τ_{12}^{c}(ksi)	Ultimate Strain γ_{12}(%)
10°	10.38	32.01	1.658
15°	9.71	33.10	2.850
30°	9.82	34.46	4.311
45°	7.94	27.83*	7.301*

* no failure

The individual test results are compared with the theoretical predictions of the transformation theory based on the far field stress only, the Pagano-Halpin model, and finite element analysis (Figures 36 - 38). For the global Young's Modulus in compression (Figure 36), the influence of the small aspect ratio is negligibly small, as shown in the small difference between the theoretical predictions based on the far field stress ($\bar{\sigma}_{xx}$) only and the Pagano-Halpin model. The correlation between theory and experiment is excellent. The finite element predictions also correlate well with the experimental results. Small differences between the results of finite element analyses based on two different boundary conditions are observed. The finite element results based on boundary condition #2 (only one side node fixed in the y-direction at the top and at the bottom grip) yielded the best correlation with experimental data.

The remaining elastic constants were influenced by the end-constraint effects. For the global Poisson's ratio (Figure 37), distinct differences between the predictions based on the far field stress ($\bar{\sigma}_{xx}$) and Pagano-Halpin model were observed. The predictions of the finite element analysis exhibit the same general trend as the Pagano-Halpin model, with the fully clamped boundary conditions predicting higher, and the simply supported in the y-direction boundary conditions smaller, Poisson's ratios. The experimental results did not follow any pattern, resulting in poor correlation between theory and experiment. Whereas the transverse Poisson's ratio in compression (ν_{21}^{com} =

0.140) was close to the one in tension (ν_{21}^{tm} = 0.150), the longitudinal Poisson's ratio in compression (ν_{12}^{cm} = 0.421) was nearly twice as large as that in tension (ν_{12}^{tm} = 0.237). The small amount of scatter in the data of ν_{12}^{cm} confirms the consistency of the experimentally obtained value. The reason for the discrepancies observed in the compressive Poisson's response is not clear.

The influence of the end-constraint effects on the in-plane shear modulus G_{12} is documented in Figure 38. Large differences between the actual and apparent values can be seen, especially for small off-axis angles. This is due to the small aspect ratio of the employed compressive specimens, in contrast to the tensile coupons. The difference in the finite element results based on the the two different set of boundary conditions increases with decreasing off-axis angle. The correlation between the theoretical predictions and the experimental results is not as good as for the off-axis tension test. The difference in the extent of scatter in the experimental results in tension and compression can be explained by the far more complicated test procedure in compression than in tension.

3.2.2 Plastic Response

Yielding

The same methods were used to determine the yield point in compression as in tension. The yield point was defined as the proportional limit of the compressive stress-strain response ($\bar{\sigma}_{xx}$ vs. ε_{xx}), the compressive Poisson's response ($-\varepsilon_{yy}$ vs. ε_{xx}), and the compressive in-plane shear response (τ_{12}' vs. γ_{12}). Figures 39 - 42 show the various yield loci of the average axial stress $\bar{\sigma}_{xx}$, the actual axial strain ε_{xx} , the apparent in-plane shear stress τ_{12}', and the actual in-plane shear strain γ_{12}. Average values for each on- and off-axis configuration were plotted. The difference between the results of the three different methods is small, except for the 0° on-axis test. The in-plane shear response

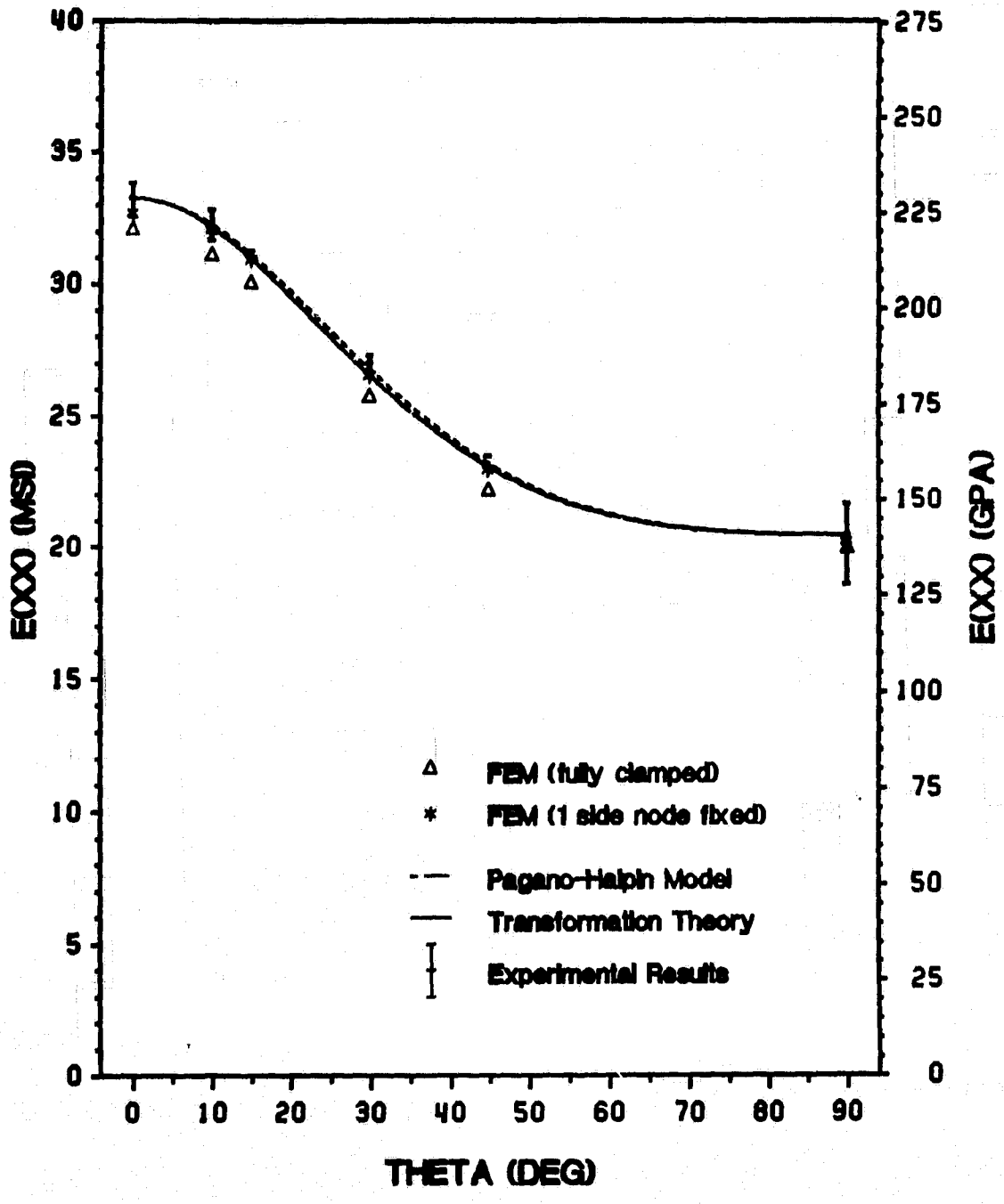

Figure 36. Global Compressive Young's Modulus E_{xx} (θ)

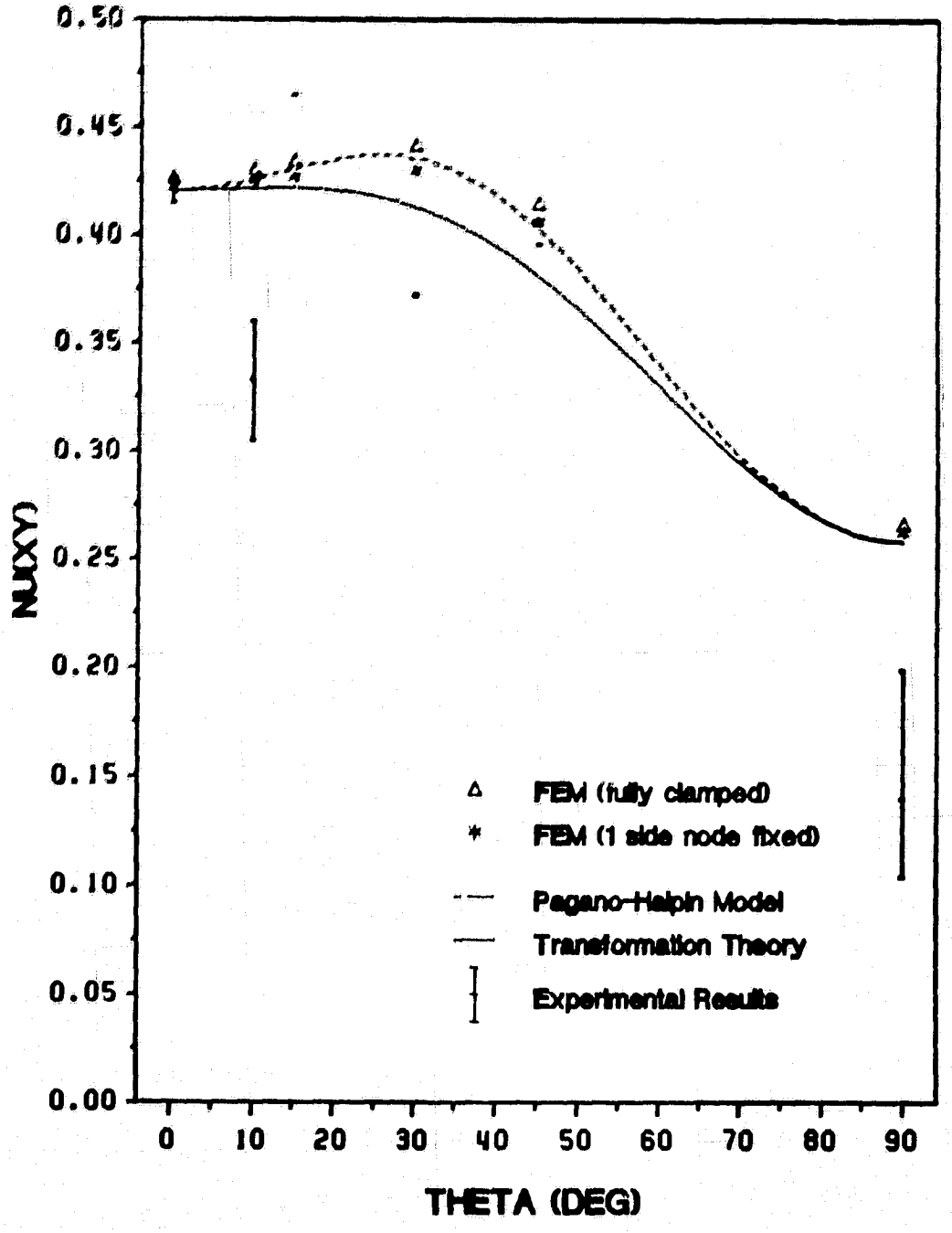

Figure 37. Global Compressive Poisson's ratio ν_{xy} (0)

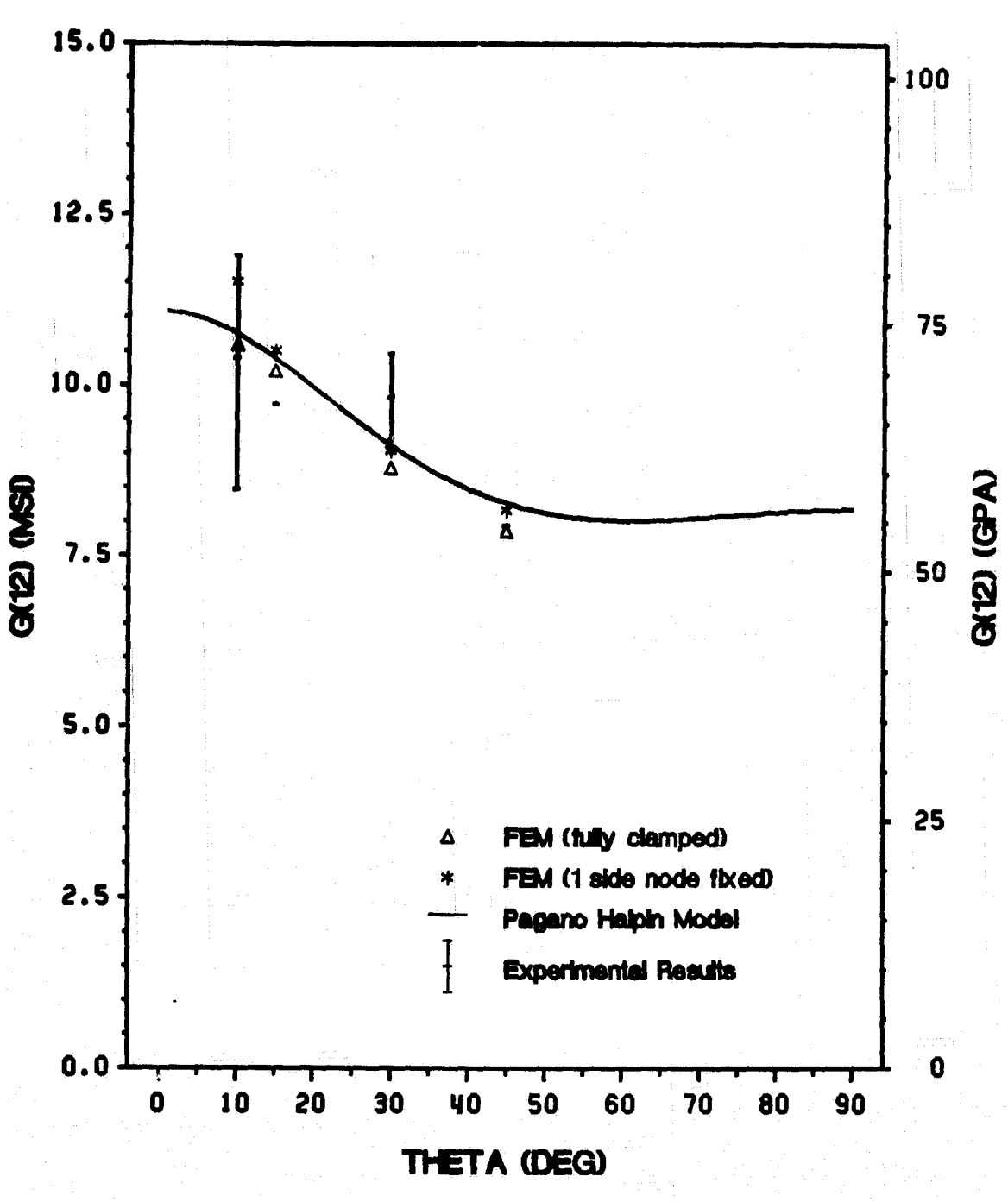

Figure 38. Apparent In-Plane Compressive Shear Modulus G_{12}^{*} (0)

predicted the smallest values. The highest values were obtained from the Poisson's response, which were nearly identical to the values obtained from the stress-strain response.

The high yield stress of the 0° specimen is most likely due to tensile residual stresses in the matrix. Due to the high-pressure bonding at approximately 1000°F, thermal residual stresses are introduced into the composite during cooling to room temperature. A quantitative analysis of the thermal residual stresses is given in Appendix F. Based on a closed form elasticity solution for an isotropic cylindrical fiber surrounded by isotropic matrix, the magnitudes of axial, radial, and circumferential residual stresses, due to a temperature change of $\Delta T = -100°F$ are given. The particular choice of the inner and outer radius of fiber and matrix corresponds to the fiber volume fraction of 46 %. An extensive study is necessary in order to determine the effective temperature change ΔT^{eff} corresponding to the actual residual stresses present in the boron/aluminum composite after curing. This is beyond the scope of the present investigation. However, it can be qualitatively stated that high tensile residual stresses must be present in the matrix of the boron/aluminum composite due to the large temperature drop during manufacturing process, resulting in the differences in tensile and compressive yield stresses.

The high yield points obtained from the 10° and 15° off-axis tests can be explained by the specimen geometry and the resulting boundary conditions, since for the 10° and for the 15° off-axis compression test 74 % and 60 % of the fibers in the specimen are simultaneously held by the top and bottom grips. This imposes an additional constraint on the deformation of the specimen. Although in the 30° off-axis compression specimen 15 % of the fibers were running directly from the top to the bottom grip, the yield point was not noticeably different from the yield point of the corresponding tensile coupon. Complete comparison between the yield loci in tension, compression, and shear is given in Chapter 4.

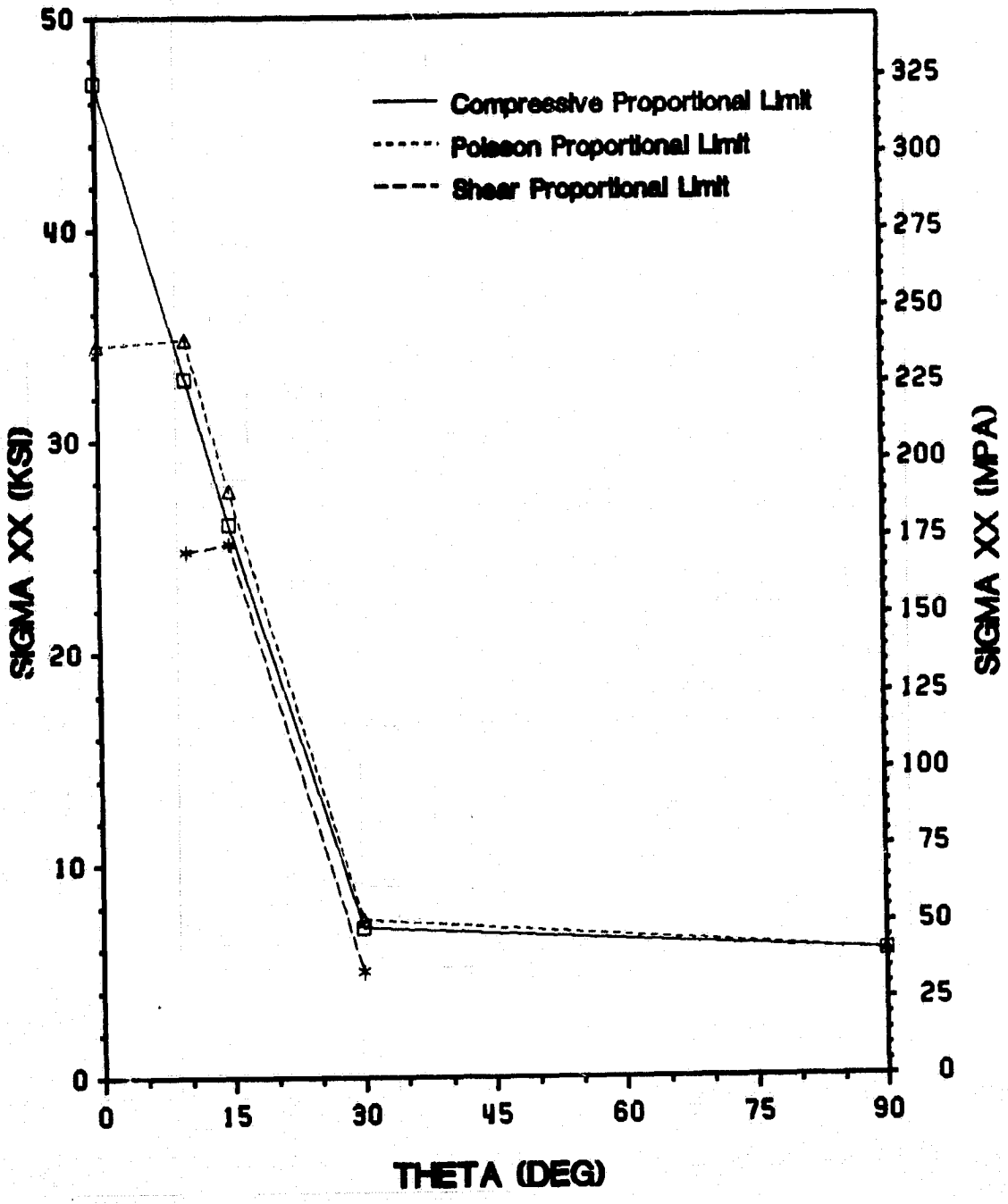

Figure 39. Apparent Axial Yield Stress in Compression $\bar{\sigma}^{y}_{xx}(\theta)$

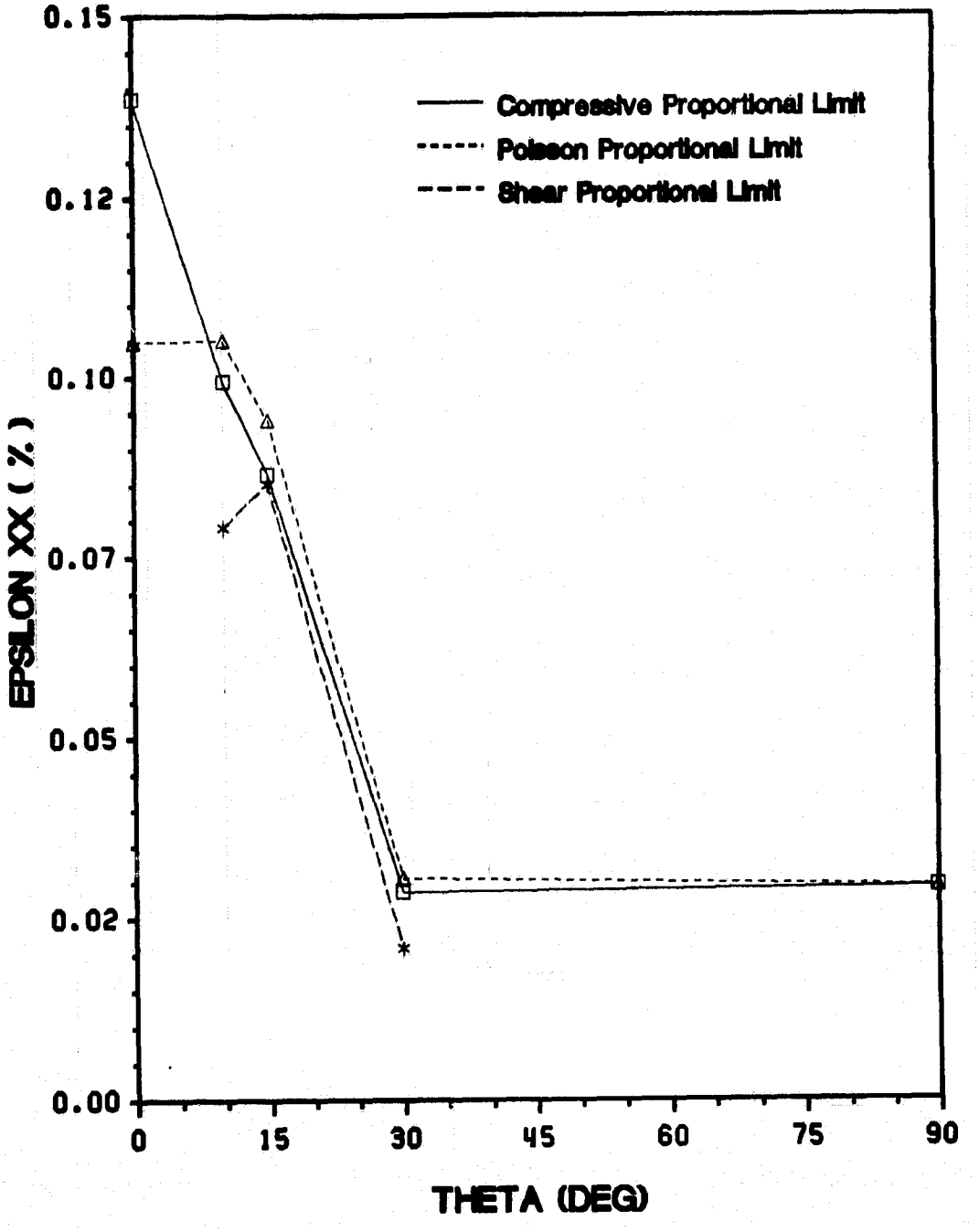

Figure 40. Axial Yield Strain in Compression ε^{y}_{xx} (θ)

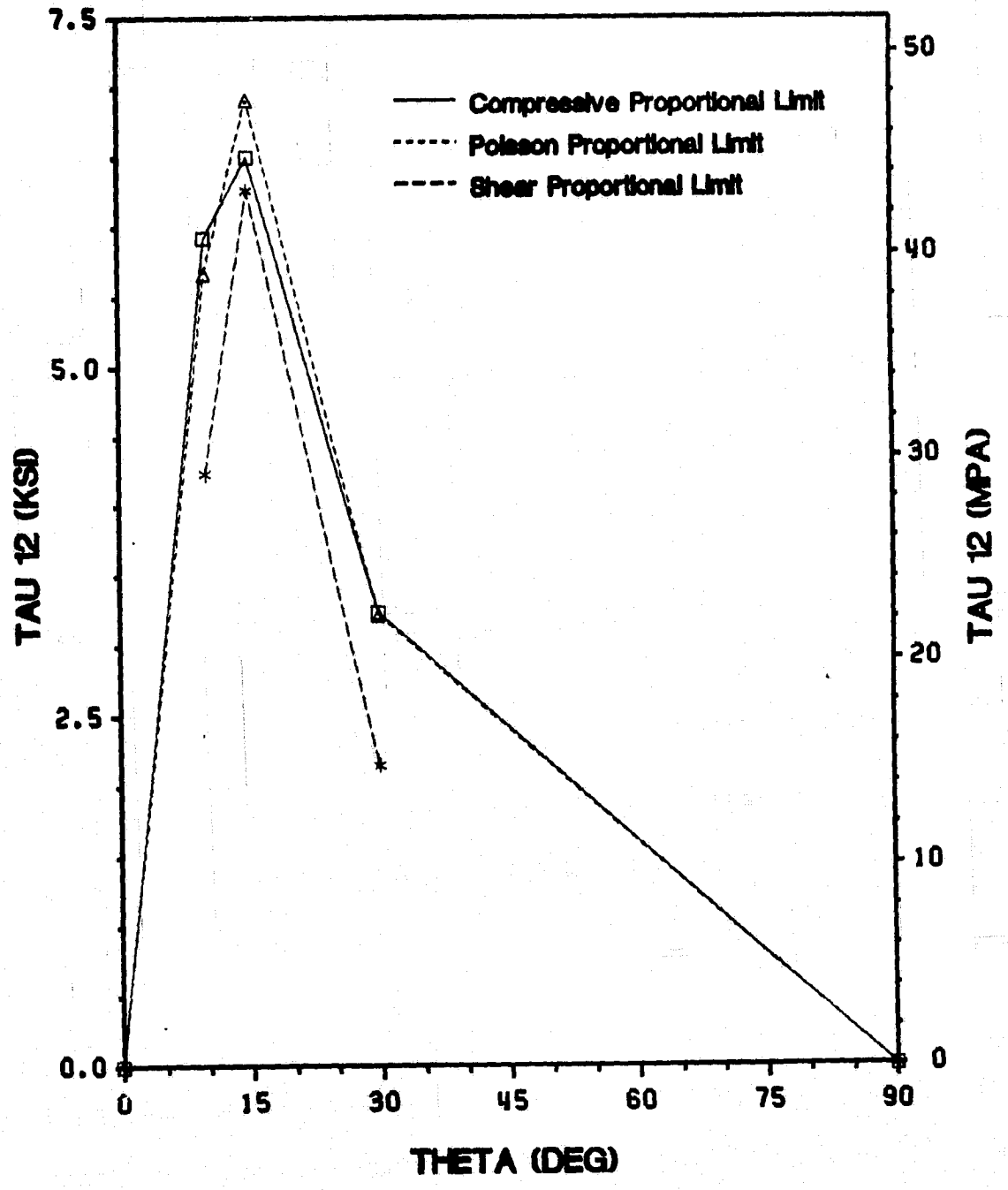

Figure 41. Apparent In-Plane Shear Yield Stress in Compression $\tau'_{12}(\theta)$

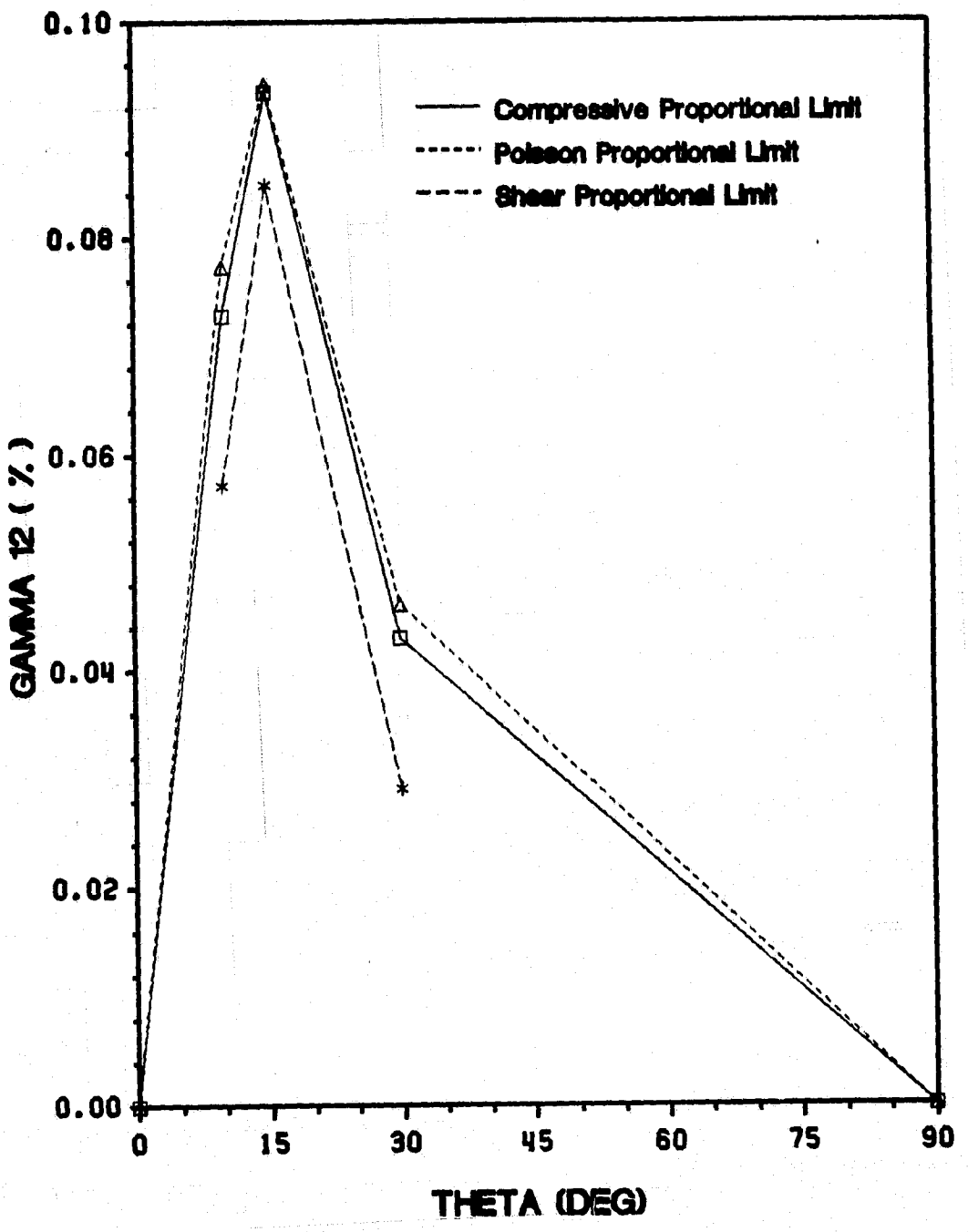

Figure 42. In-Plane Shear Yield Strain in Compression γ_{12} (θ)

Subsequent Hardening

Monotonic Test

The nonlinear response in compression is a function of the fiber orientation. For the off-axis compression test,the specimen geometry and the resulting end constraints are also an influencing factor. Material softening was observed for all on- and off-axis configurations. The extent of softening observed in the response of 0°, 10° and 15° specimens is limited. In the case of the 0° specimen the majority of the load is carried by the fibers, while in the case of the 10° and 15° specimens the constraint of the fibers might have influenced the plastic deformation. In the remaining orientations, significant amount of plastic deformation is evident.

Material stiffening was also observed in the plastic region after an initial softening due to yielding in 10°, 15° and 30° specimens. This phenomenon is questionable and may be the result of the end constraints mentioned above. By loading fibers directly and preventing them from rotating, global and local buckling effects influence the experimental test results in compression, especially in the plastic range. A distinction between pure material and structural response must be made in such circumstances. In view of the high amount of bending observed in the individual compression tests, the recorded experimental data become meaningless after a certain point. For the 45° off-axis and for the 90° specimens, on the other hand, no stiffening of the material was observed in the plastic range. This was expected, since the fibers were able to rotate, being constrained only by the matrix (material response) and not by the fixture (structural response). It can be stated in general that for all on- and off-axis compression tests of the same fiber orientation, differences in the nonlinear (plastic) response were observed in contrast to the initial elastic response.

The Poisson's response exhibited even larger differences for the same on- and off-axis configurations in the plastic range, especially in the case of the 30° off-axis test. In the case of the 0°, 10°, and 15° specimens, the Poisson's ratio approaches infinity at large strains (Appendix B), which has to be interpreted as a structural and not a material response. The 45° off-axis test exhibits a nearly con-

stant Poisson's ratio, as expected, since it is unaffected by the end constraints. For the 90° tests the Poisson's response produced two different trends. In one test, the Poisson's ratio approached infinity, as observed in the 0°, 10°, and 15° tests, whereas a change in sign in the plastic range was observed in two other tests. This phenomenon was also observed by Herakovich and Shuart [9], who argued that it was caused by "a failure mechanism in the matrix material."

The in-plane shear response in compression exhibited material stiffening in the nonlinear region for the 10°, 15°, and 30° off-axis tests, after an initial material softening. Again, this can be seen as a result of the end constraints, and therefore as a structural response. Similar to the off-axis tension tests, pronounced nonlinear behavior in the in-plane shear response in compression was observed. This leads to the conclusion that the overall nonlinear response in compression also is influenced significantly by the intralaminar shear stress.

Cyclic Test

The significant effect of the end constraints on the nonlinear stress-strain response was clearly demonstrated in cyclic compression tests. Unlike the cyclic off-axis tension tests, the 0° and 10° off-axis test exhibited no permanent strain accumulation. Also, enormous differences between unloading and reloading paths, especially for the 10° off-axis test, were observed, resulting in questionable Poisson's and in-plane shear responses. Comparison of front and back gage readings showed that bending was present in the specimen during loading and reloading. However, no permanent out-of-plane deformation occurred since during the unloading the specimen lost its curvature and was perfectly flat at the zero load level. The results of the 45° cyclic test are somehow more meaningful and useful for the characterization of the material response. Like the cyclic off-axis tension tests, a high extent of nonlinearity and dissipation was observed, resulting in a large amount of permanent strain accumulation. Also, the unloading and reloading paths were nearly identical.

Failure Stress (Strength)

Based on the equations given in Section 3.1.2, the failure strength curves shown in Figures 43 and 46 were obtained. In these figures theoretical predictions and experimental results are compared. The influence of the different aspect ratios in tension and compression is additionally shown in Figure 44. A change in aspect ratio in the modified Tsai-Wu failure criterion had significant influence on the predicted strength. The influence of the different Poisson's ratio in tension (ν_{12} = 0.237) and in compression (ν_{12} = 0.421) on the other hand, was negligibly small. In Figure 43, the two different failure criteria are compared with each other, using compressive input data (L/H = 1.5) and the shear strength from the 0° Iosipescu test. A large difference between the two criteria for high off-axis angles was observed. The correlation between the theoretical predictions based on the Tsai-Wu failure criterion and the experimental results is rather poor (Figure 44). The poor correlation can be explained to a certain extent by the presence of end-constraint effects which result in a structural rather than material response at failure. Also, the tensile residual stresses in the supporting matrix, by delaying matrix yielding, may increase the failure stress. This may explain the difference in the transverse strength in tension $|Y_t|$ = 15.7 ksi and compression $|Y_c|$ = 19.9 ksi, where the matrix is directly loaded.

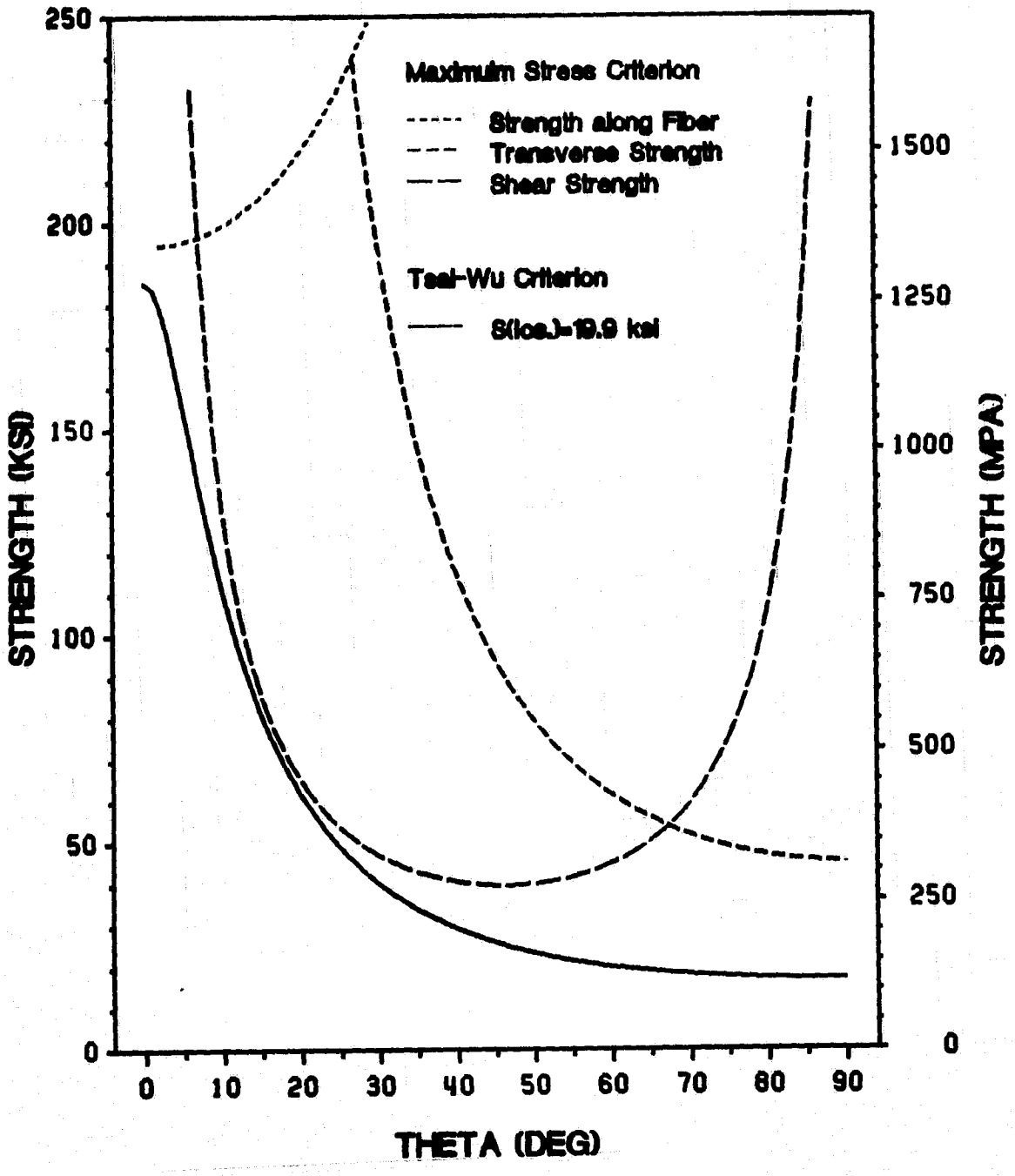

Figure 43. Tsai-Wu & Maximum Stress Failure Criterion in Compression

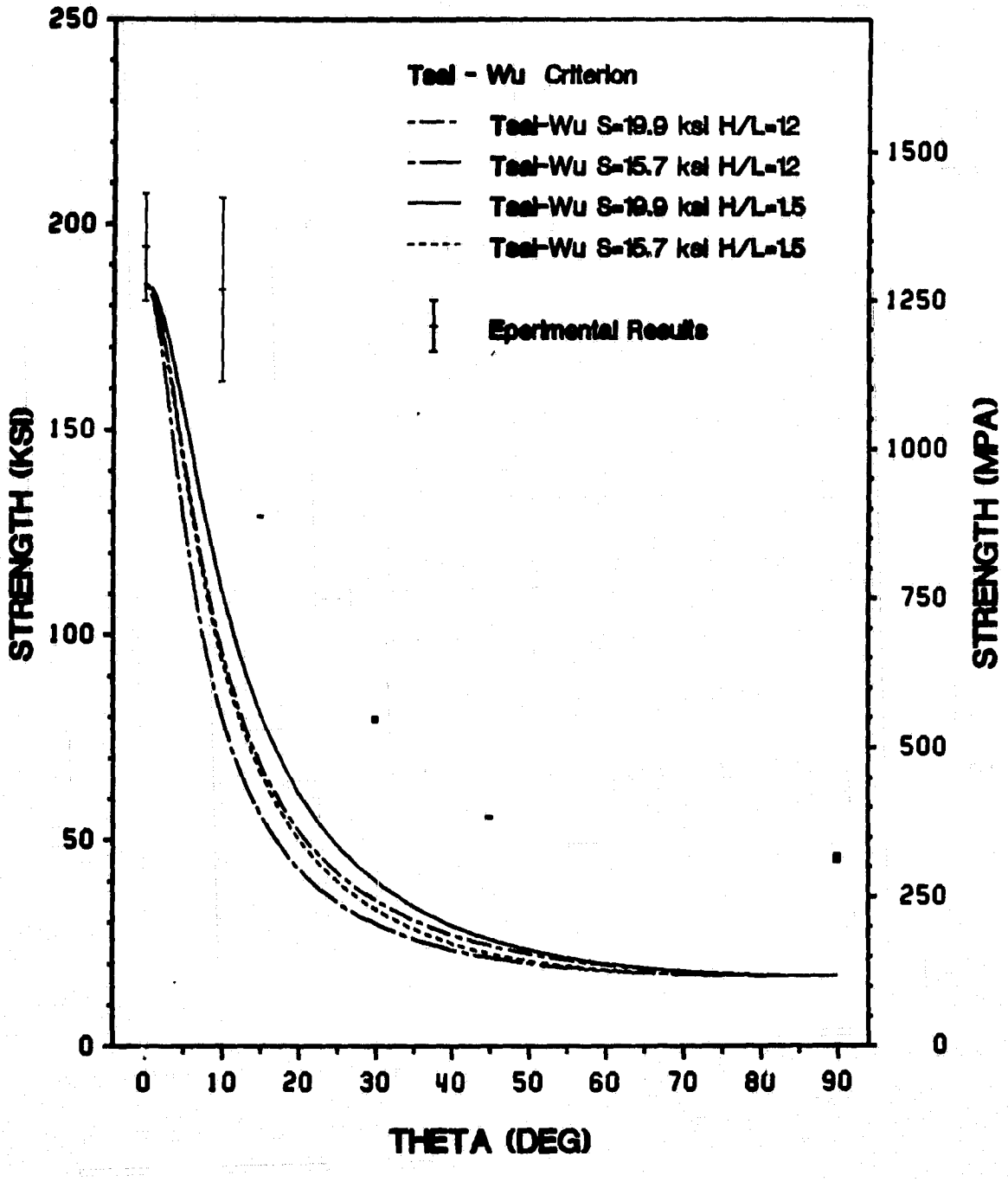

Figure 44. Tsai-Wu Failure Criterion & Experimental Results in Compression

Failure Modes

The failure modes in compression were influenced by the specimen geometry and end-constraint effects. The failure of the 0° specimen was catastrophic and characteristic of compression tests. The failure was accompanied by an extremely load noise. Parts of the failed specimen were scattered in all directions and other parts were attached to the grips of the test fixture and had to be removed with screw-driver and sand paper. The 10°, 15°, and 30° off-test coupons failed differently than the 0° coupons. Only the directly supported fibers were broken, always at the same location for each individual test. Failure occurred always close to, but never in the grip area. All failures for each individual on- and off-axis compression test occurred in the test section. In the 45° off-axis test a shear failure was observed, resulting in no fracture of the specimen, but in an asymmetric barrel-like permanent deformation. The deformation in this case reached the limit of the fixture, so that the loading of the specimen up to failure was not possible. No fiber breakage was observed. The 90° coupon showed the characteristic 45° shear failure before buckling occurred, which was ultimately responsible for failure. Failure in this case occurred close to the location where failure took place in the 10°, 15°, and 30° off-axis specimens. Representative failed off-axis compression specimens are shown in Figure 45.

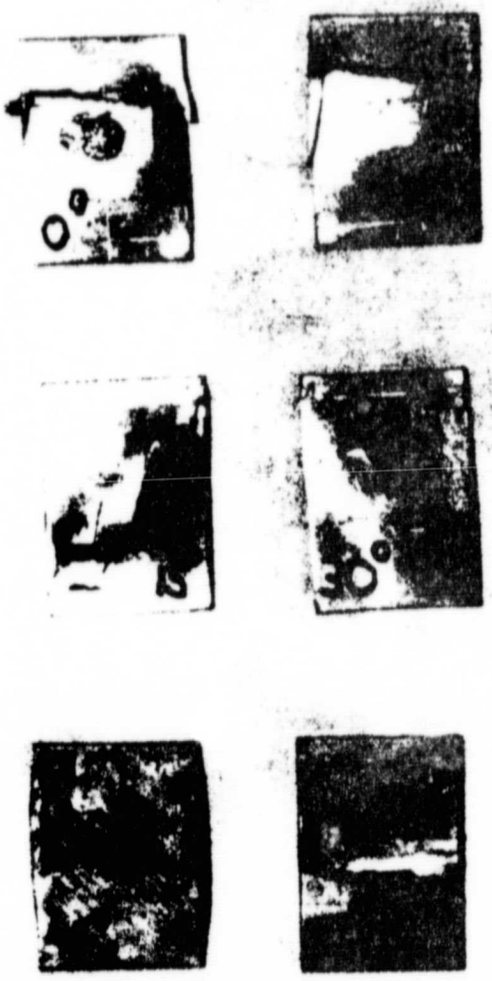

Figure 45. Failed Off-axis Compression Test Specimens

3.3 *Iosipescu Shear Test Results*

The Iosipescu shear test was performed in order to provide additional data on the in-plane properties, such as the shear modulus G_{12} , the shear strength S (τ_{12}^{u}), and the ultimate shear strain γ_{12}^{u}. Typical monotonic in-plane shear responses for various on- and off-axis Iosipescu shear tests are given in Figure 46. As mentioned earlier, two different data acquisition systems were used for the Iosipescu shear tests. The results presented in Figures 46 and 47 are based on results obtained with the aid of the IBM-XT computer system, which was believed to give more accurate values. For completeness, the data obtained with the MINC system are also listed together with the individual test results in Appendix C. Only one representative plot for each on- and off-axis orientation is presented in Figure 46.

3.3.1 Elastic Response

Based on the individual test results (Appendix C), the average shear properties are listed in Table 12. The average values for the yield point and the in-plane shear modulus are based on individual tests obtained using both data acquisition systems. For the determination of the ultimate stresses and strains only the results obtained with the aid of the IBM-XT computer system were considered.

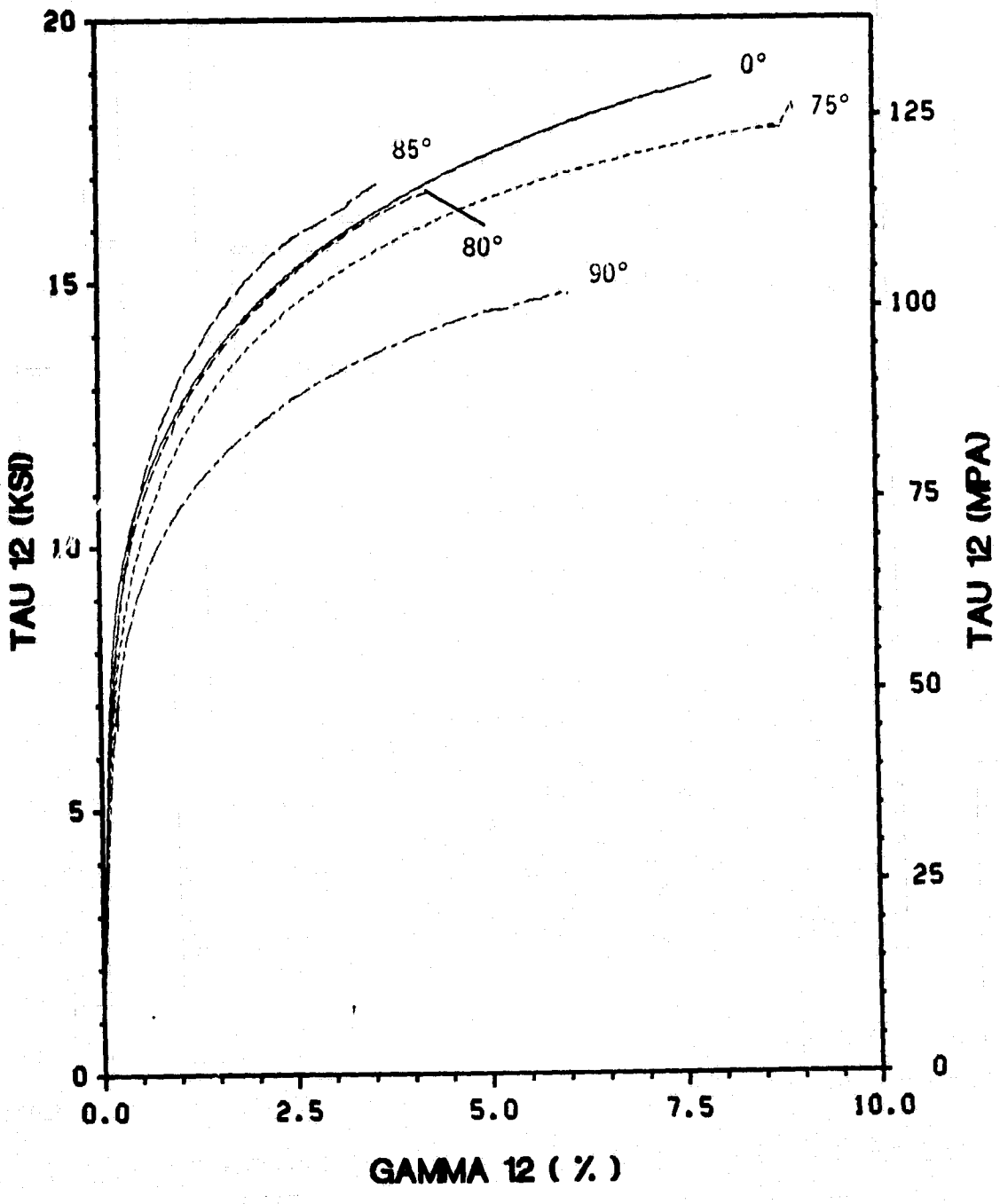

Figure 46. Apparent In-Plane Shear Response of the Iosipescu Shear Tests

Table 12. Average Shear Properties from Iosipescu Shear Test

Fiber Orientation θ	Shear Modulus G_{12}^{*}(msi)	Ultimate Stress τ_{12}^{*}(ksi)	Ultimate Strain γ_{12}(%)
0°	6.67	19.87	6.540
75°	6.42	14.44	8.965
80°	6.65	17.39	4.047
85°	6.72	17.47	3.796
90°	5.67	15.23	6.915

The apparent in-plane shear modulus G_{12}^{*}, obtained from the various on- and off-axis Iosipescu shear tests is shown in Figure 47, together with the theoretical predictions by the finite element analysis, based on an input value of G_{12} = 8.35 ksi from the 45° off-axis tension test. The correlation between theory and experiment and between the off-axis tension test and the Iosipescu shear test results was unexpectedly poor. The results were unexpected because recent studies at Virginia Tech [21, 36] have illustrated the ability of the Iosipescu shear test to provide an accurate value of the in-plane shear modulus for resin matrix composites. A more complete discussion of this issue is given in Chapter 4.

3.3.2 Plastic Response

Yielding

The yield point was defined as the proportional limit of the in-plane shear response (τ_{12}^{*} vs. γ_{12}). The corresponding yield loci for the apparent shear stress τ_{12}^{*} and the actual shear strain γ_{12} are given

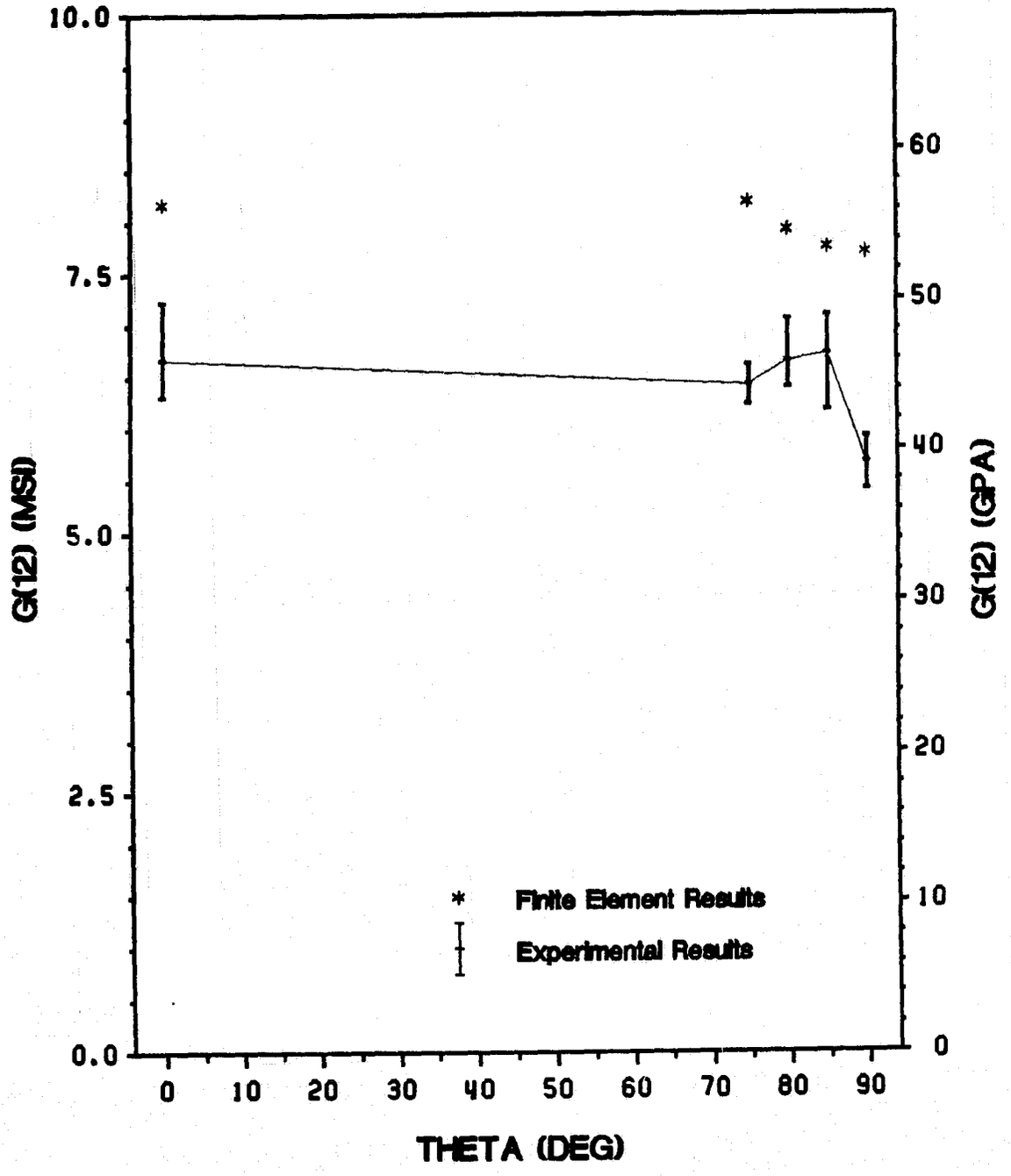

Figure 47. Apparent In-Plane Shear Modulus form Iosipescu Shear Test $G_{12}^{*}(\theta)$

in Figures 48 and 49. It is interesting to note the large differences in the yield stress obtained from the 0° and 90° Iosipescu specimens. Theoretically, these should be the same if the applied shear stress is the same. While some differences exist in the test section shear stress distributions in the 0° and 90° Iosipescu specimens, these diffeences are not sufficient to explain the large differences in the yield stress observed in the two specimens.

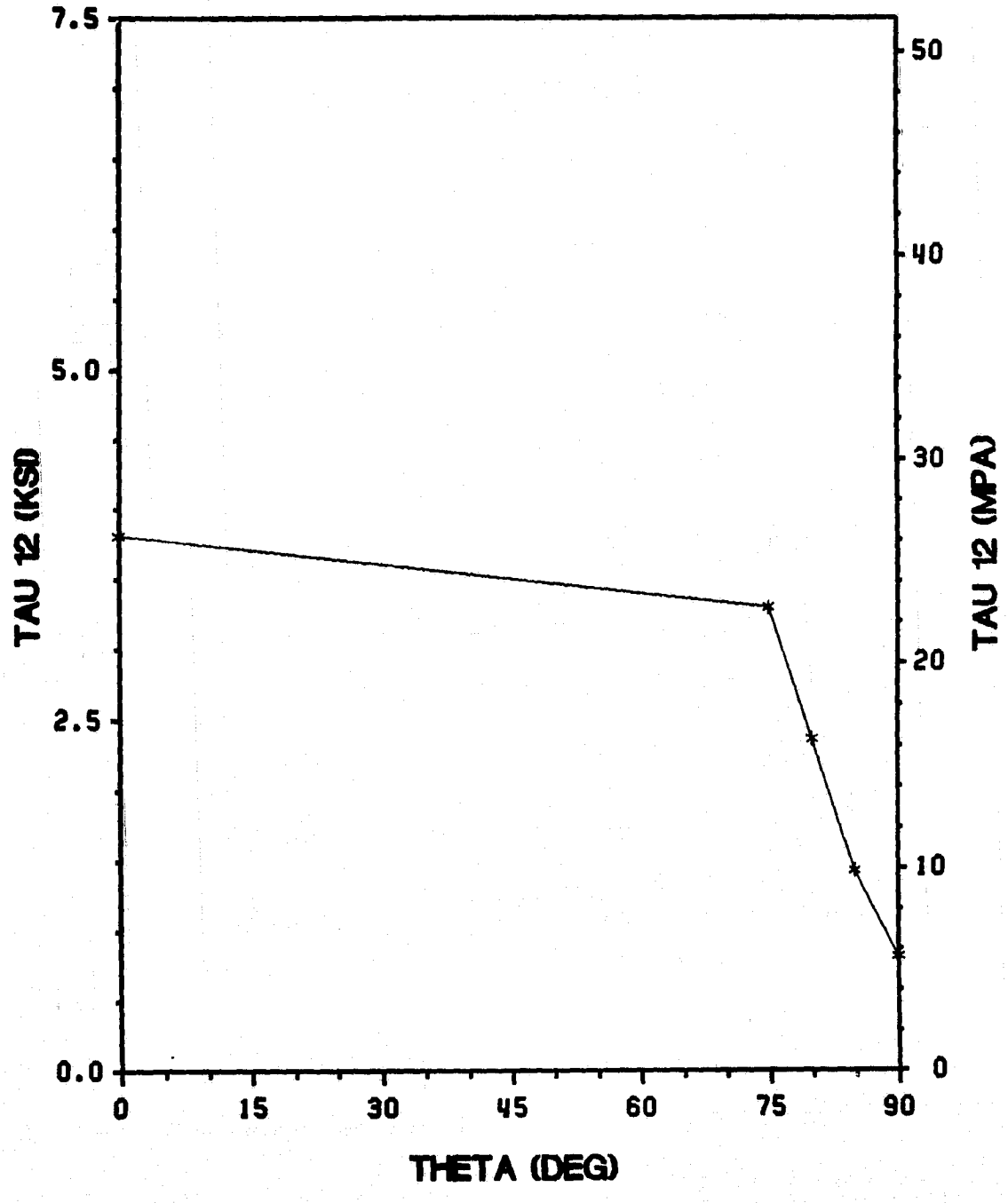

Figure 48. Apparent In-Plane Shear Yield Stress in Simple Shear τ_{12}^{γ} (0)

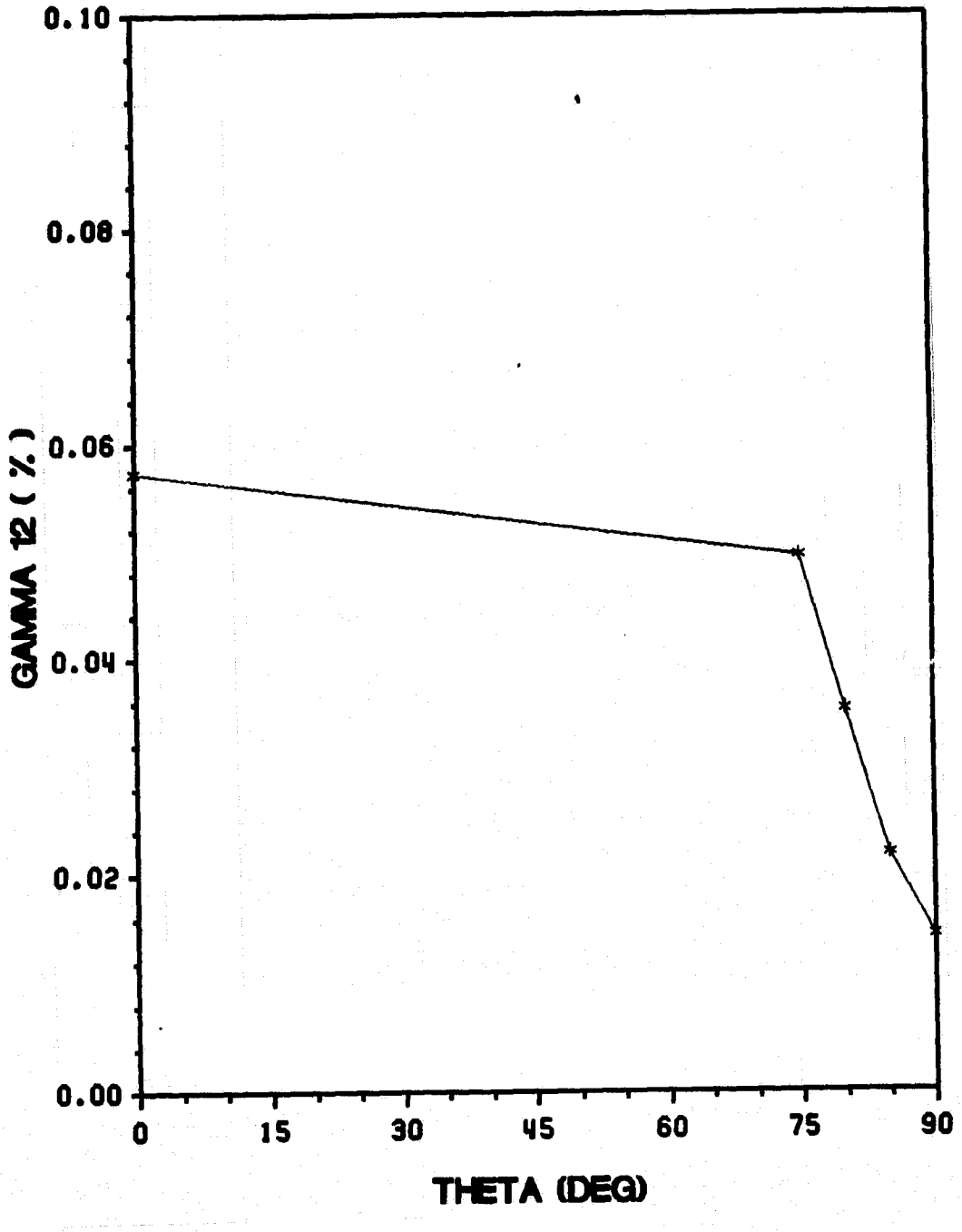

Figure 49. In-Plane Shear Yield Strain in Simple Shear γ_{12}^{y} (θ)

Subsequent Hardening

Monotonic Test

As observed in the off-axis tension and off-axis compression tests, the nonlinear response is a function of the fiber orientation. However, no discernible trend could be observed in the hardening response obtained from the Iosipescu shear tests which could be related to the off-axis angle. The amount of hardening in the plastic region followed an irregular pattern. As in the case of the yield stress, significant differences in the nonlinear response of the 0° and 90° specimens are observed. This may be due to the way the load is introduced into the test section of the Iosipescu specimen in the presence of relatively large boron fibers. Nevertheless, the extent of nonlinearity and corresponding dissipation is well documented in Figure 46 and in the individual test results in Appendix C, leading to the conclusion that the nonlinear response of the unidirectional boron/aluminum composite is highly influenced by the intralaminar shear stress.

Cyclic Test

Cyclic Iosipescu shear tests provided additional information on the nonlinear response of boron/aluminum (see Appendix C). The cyclic tests exhibited a high extent of permanent strain accumulation. Similar to the previous test results, the unloading and reloading paths were nearly identical throughout the entire test. A very small increase in the difference between the two paths was observed during the last unloading-reloading cycle of the 0° Iosipescu specimen. By fixing the bottom plate of the Iosipescu shear test fixture, reverse cyclic tests also were performed. The reverse cyclic test results were characterized by large permanent strain accumulation in the positive and negative plastic range, linearly elastic unloading and reloading during different states of the loading history, and kinematic hardening. The above results indicate that plasticity is the major dissipative mechanism in this material system.

The cyclic loading also influenced the ultimate values. For the off-axis specimens, a decrease in failure strength and strain was observed, whereas for the 0° specimens the cyclic loading resulted in an increase in the ultimate stresses and strains. This increase, however, was rather small.

Failure Stress (Strength)

The fiber orientation also influenced the failure stress in an Iosipescu shear test. The influence of the fiber orientation on the shear strength was not as drastic as on the tensile or compressive strength. Individual results are presented in Appendix C.

Failure Modes

The failure modes of the Iosipescu shear specimens were also a function of the fiber orientation. For the 0° specimen, failure occurred at the notch tip running along the fibers. After the first crack initiated, a drop in load (stress) was observed, but the specimen could be reloaded to higher load levels. The loading of the damaged specimen resulted in no further propagation of the crack in the test section, but in damage to the specimen in the grips, until finally a grip failure occurred. This can be interpreted as structural and not material response.

The off-axis Iosipescu specimens also failed in the test section. Two cracks initiated nearly simultaneously at the opposite notch tips. The cracks propagated initially along the fibers. After failure, about 10 % fiber breakage was observed in the off-axis Iosipescu shear specimens. For the 90° test, failure also initiated at the notch tip, running along the fibers. Whether a crack initiated at one or both notch tips can not be said, due to the fast crack propagation.

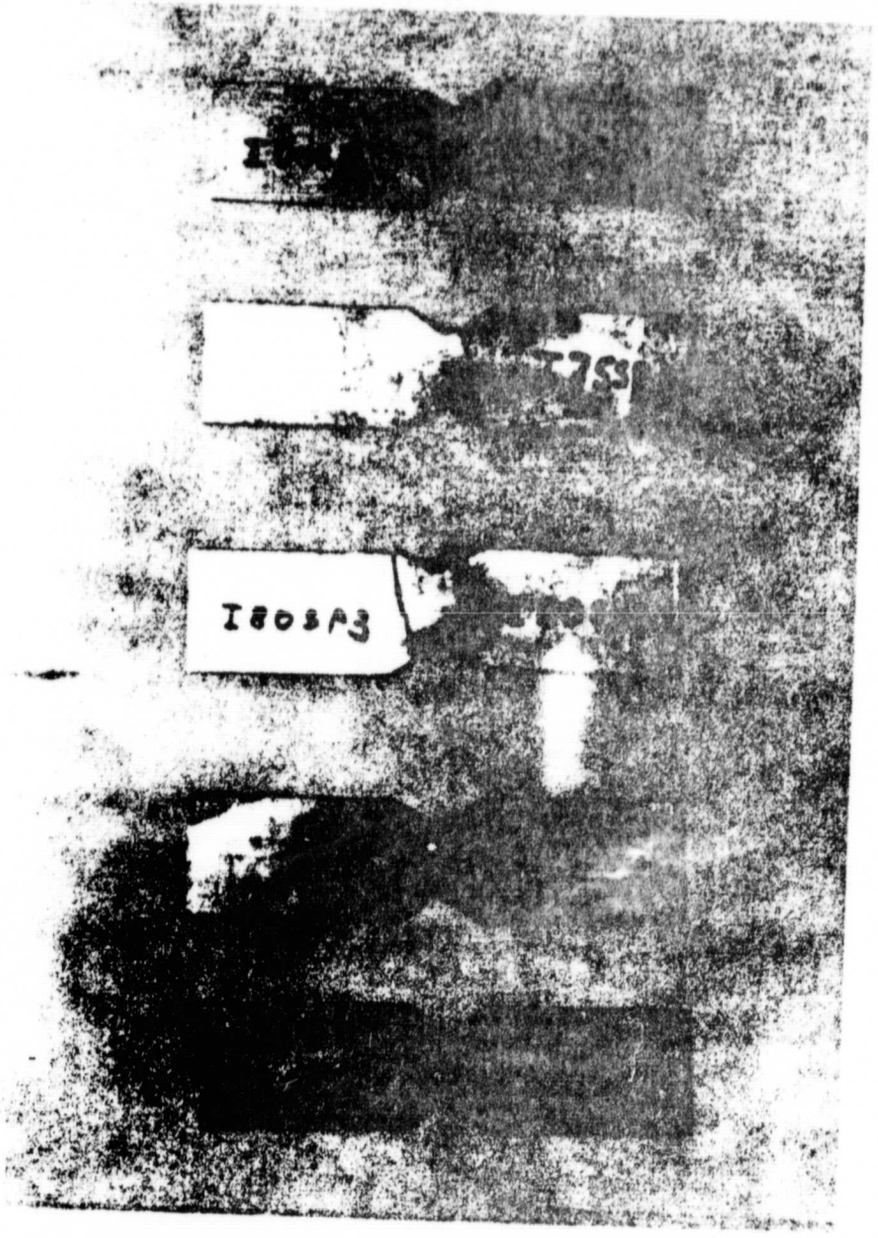

Figure 50. Failed Iosipescu Shear Test Specimens

4.0 COMPARISON AND DISCUSSION

In this chapter, the results obtained from the three different test methods, namely: off-axis tension, off-axis compression, and Iosipescu shear, are compared. The apparent material properties presented in Chapter 3 are corrected for end-constraint effects and stress nonuniformity in the test section, and listed for the various on- and off-axis configurations. A discussion of the correlation between the experimental data and the corrected results is given for the three different test methods.

4.1 Young's Modulus

Typical stress-strain responses in tension and compression are shown in Figure 51 for the 0° and 90° tests, and in Figure 52 for the off-axis tests. These figures show that the global Young's Moduli in tension and in compression are essentially the same for any given fiber orientation. Comparison of the results presented in Tables 7 and 10 indicates that the off-axis compression moduli are slightly higher than the tensile moduli (by about 1 to 6 %). All results correlate quite well with the theoretical predictions. The good correlation between theoretical predictions and experimental re-

sults, and the very small influence of the shear coupling effect indicated by the very small difference between the prediction based on the far field stress ($\bar{\sigma}_{xx}$) and the Pagano-Halpin model, made the correction of the apparent values of the global Young's Modulus unnecessary.

4.2 *Poisson's Ratio*

Typical results for the Poisson's response in tension and compression are compared in Figure 53 for the on-axis tests and in Figure 54 for the off-axis tests. The on-axis tests in Figure 53 exhibit a different slope for the 0° tests in tension and in compression, resulting in different longitudinal Poisson's ratios ($\nu_{12}^{ten} = 0.237$, $\nu_{12}^{com} = 0.421$). For the 90° tests no significant change in the initial slope between tension and compression is evident. Nearly the same value for the transverse Poisson's ratio in tension and compression was obtained ($\nu_{21}^{ten} = 0.150$, $\nu_{21}^{com} = 0.140$). Since the on-axis loading does not result in shear deformation of the specimen, no correction of the test data is necessary.

The off-axis results (Figure 54) follow no regular pattern. Because of the inconsistency and the high amount of scatter in the experimental data, correction based on the Pagano-Halpin model was deemed meaningless. Due to the limited amount of test material, the present study could not provide meaningful values of the off-axis Poisson's ratio in compression.

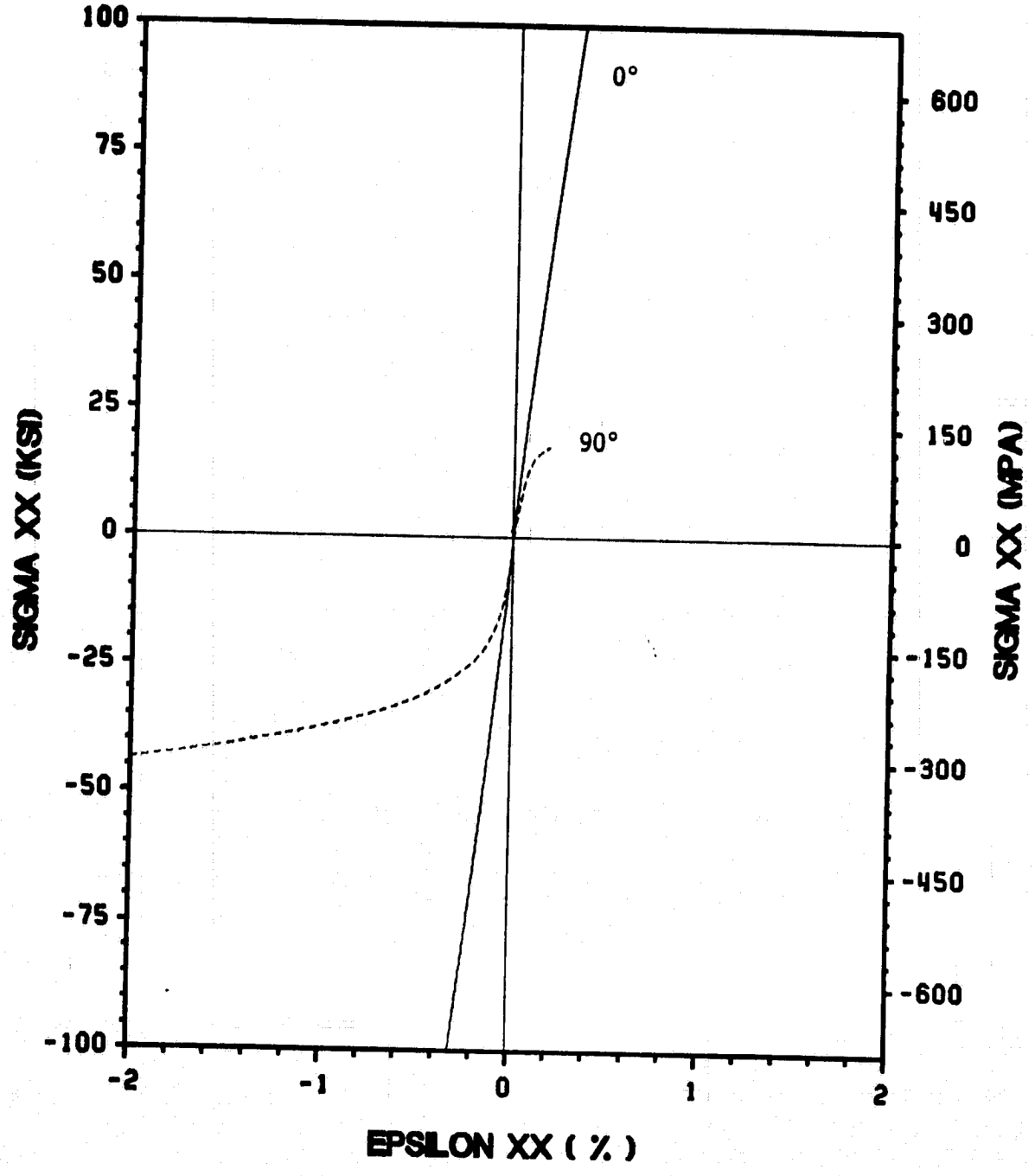

Figure 51. Tensile & Compressive On-Axis Stress-Strain Response

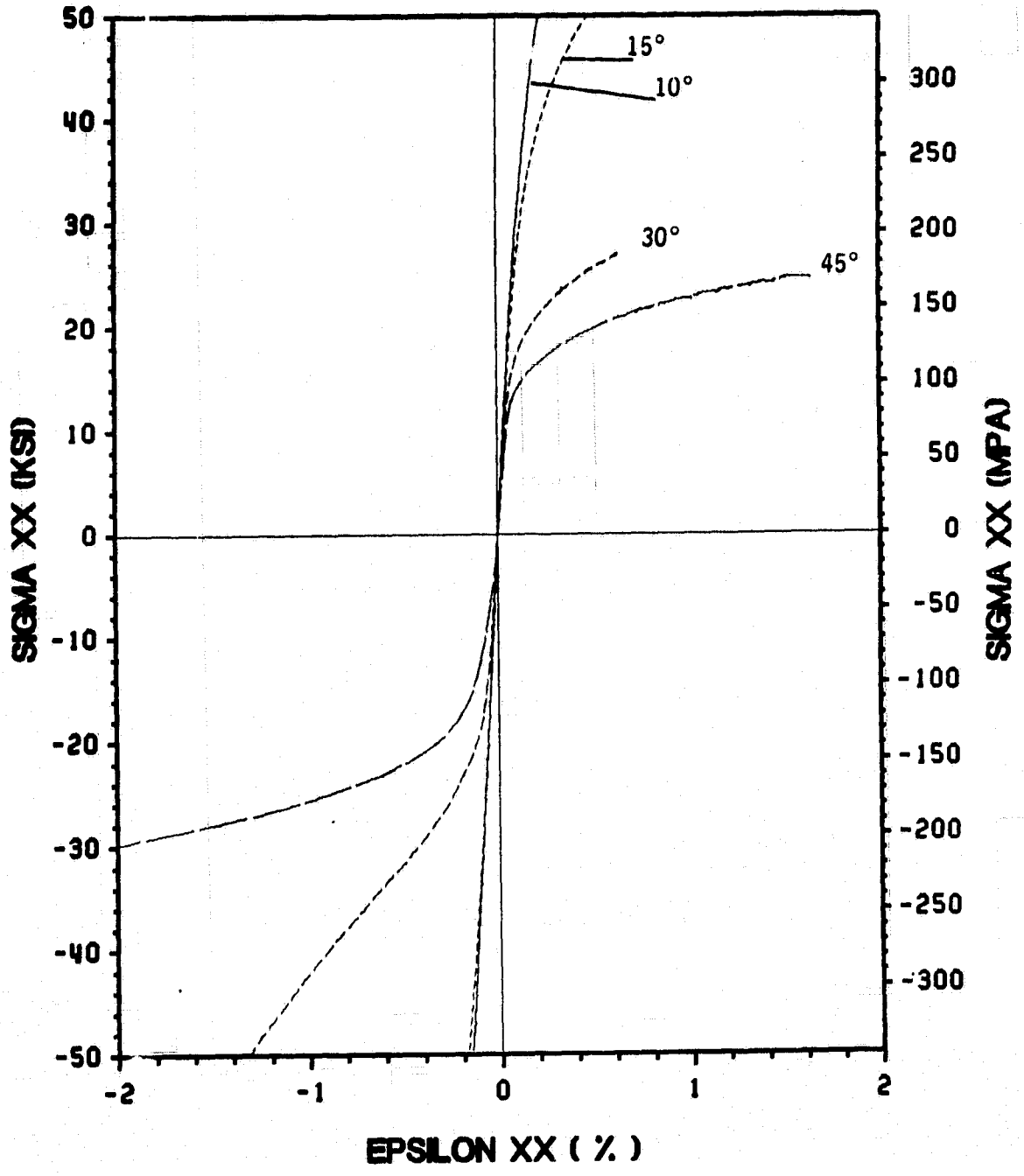

Figure 52. Tensile & Compressive Off-Axis Stress-Strain Response

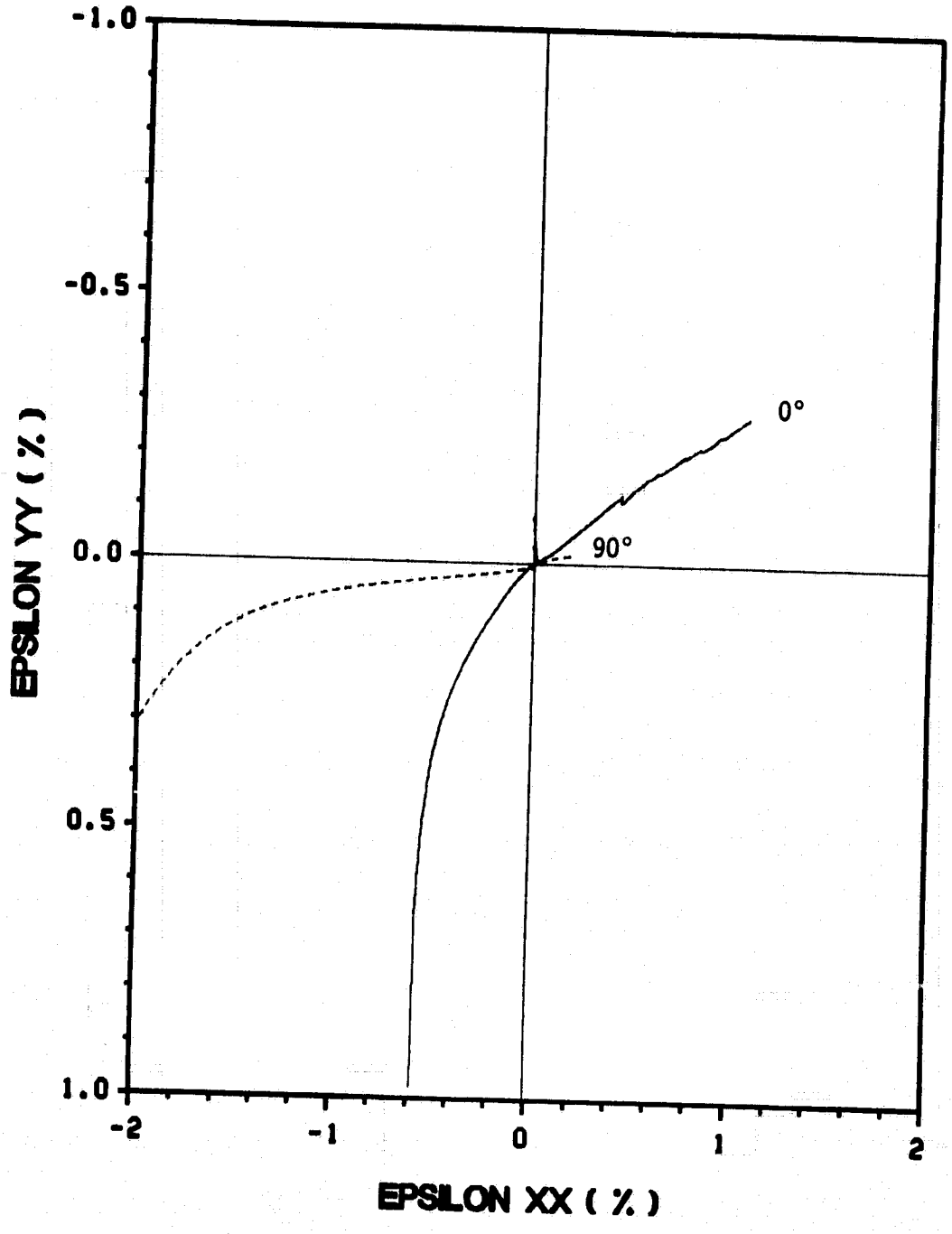

Figure 53. Tensile & Compressive On-Axis Poisson's response

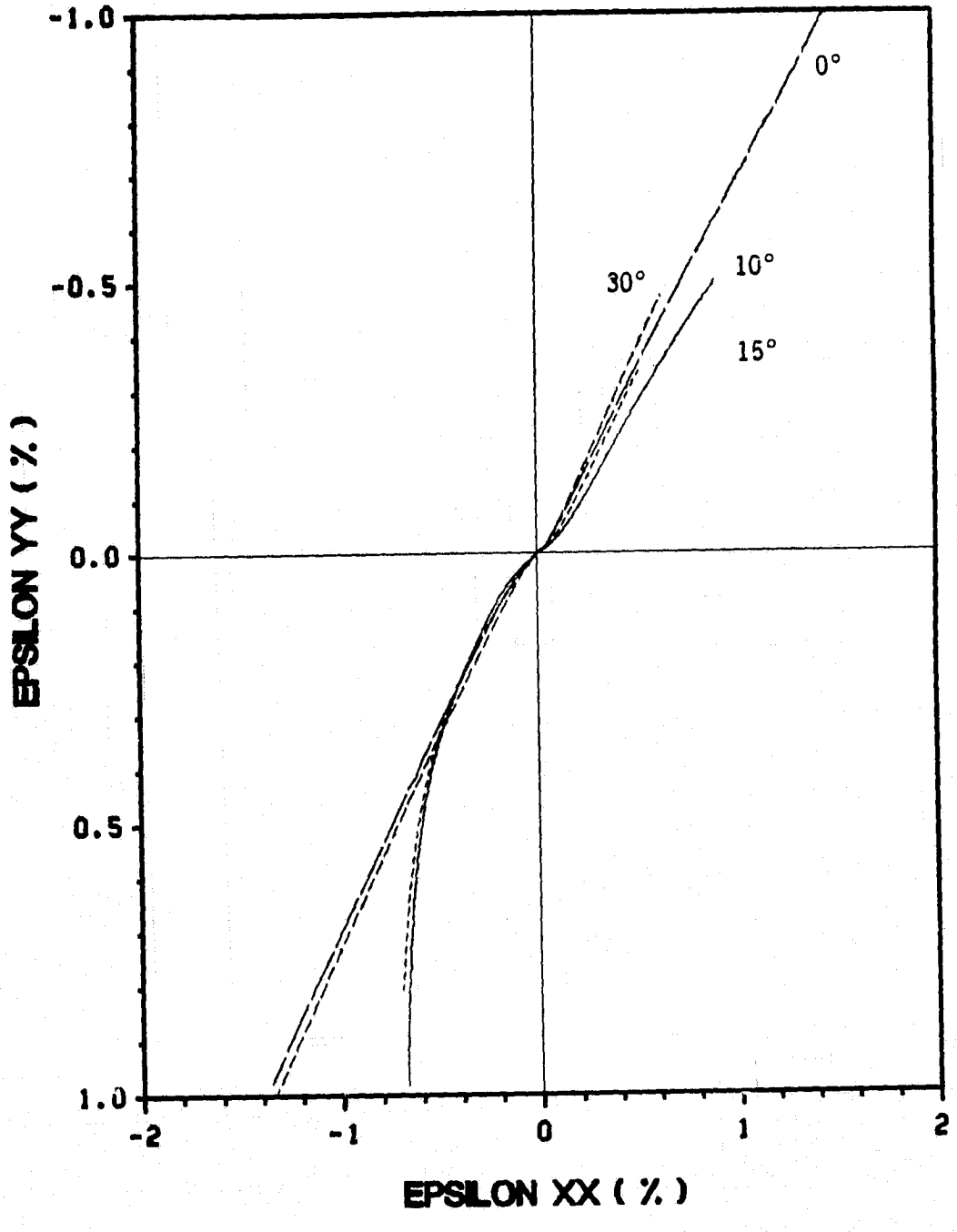

Figure 54. Tensile & Compressive Off-Axis Poisson's response

4.3 *In-Plane Shear Modulus*

The apparent and actual values of the in-plane shear modulus G_{12} are given in Tables 13, 14 and 15 for all three different test methods and fiber orientations. Likewise, the correction factors based on the Pagano-Halpin model and finite element analysis are given. The apparent shear moduli listed in the tables below are average values for each different fiber orientation and each different test method.

Table 13. In-Plane Shear Modulus for Off-Axis Compression Test

Fiber Orientation	Apparent Modulus G_{12}^{*}(msi)	Correction Factor $\frac{G_{12}}{G_{12}^{*}}$	Actual Modulus G_{12}(msi)
Pagano-Halpin Correction			
10°	10.38	0.7779	8.07
15°	9.71	0.8059	7.83
30°	9.82	0.9160	8.99
45°	7.94	1.0192	8.09
Finite Element Correction			
10°	10.38	0.7979	8.28
15°	9.71	0.8148	7.91
30°	9.82	0.9240	9.01
45°	7.94	1.0449	8.30

Table 14. In-Plane Shear Modulus for Off-Axis Tension Test

Fiber Orientation	Apparent Modulus G_{12}^{*}(msi)	Correction Factor $\frac{G_{12}}{G_{12}^{*}}$	Actual Modulus G_{12}(msi)
Pagano-Halpin Correction			
10°	8.50	0.9875	8.39
15°	8.41	0.9898	8.32
30°	8.59	0.9967	8.56
45°	8.35	1.0000	8.35
60°	8.24	1.0010	8.25

Table 15. In-Plane Shear Modulus for Iosipescu Shear Test

Fiber Orientation	Apparent Modulus G_{12}^{*}(msi)	Correction Factor $\frac{G_{12}}{G_{12}^{*}}$	Actual Modulus G_{12}(msi)
Finite Element Correction			
0°	6.67	1.0231	6.82
75°	6.42	1.0589	6.80
80°	6.65	1.0680	7.10
85°	6.72	1.0810	7.26
90°	5.67	1.0899	6.18

From Table 14 it can be seen that the shear modulus from the 45° off-axis tension test gives the most accurate value of G_{12}. The amount of scatter in the off-axis tension test results was fairly

small. The corrected off-axis compression test results, on the other hand (Table 13), exhibit a larger amount of scatter than the off-axis tension test results.

The poor correlation between the shear modulus obtained from the Iosipescu shear and the off-axis tension test is not understood. The fact that the Iosipescu shear test provided excellent results for other highly anisotropic composites [21, 36] leads to the conclusion that the observed discrepancy is not caused by the testing procedure. The large boron fibers and the complicated displacement field in the test section (Figure 55), may be responsible for the low apparent moduli. The finite element code "ANFRAC" developed for modeling homogeneous, anisotropic materials, predicted the nonuniform stress distribution quite well for composites with small fibers, such as aramid/epoxy [21]. For large fiber composites such as boron/aluminum however, the predicted stress-distribution might not be accurate. Consequently, the calculated correction factor might be inaccurate. Additional correction procedures have to be developed, in order to incorporate effects such as the large fiber diameter and/or the fiber rotation in the test section of the Iosipescu specimen. The difference between a state of simple shear and pure shear also has to be considered for the correct interpretation of the stress field in the Iosipescu specimen.

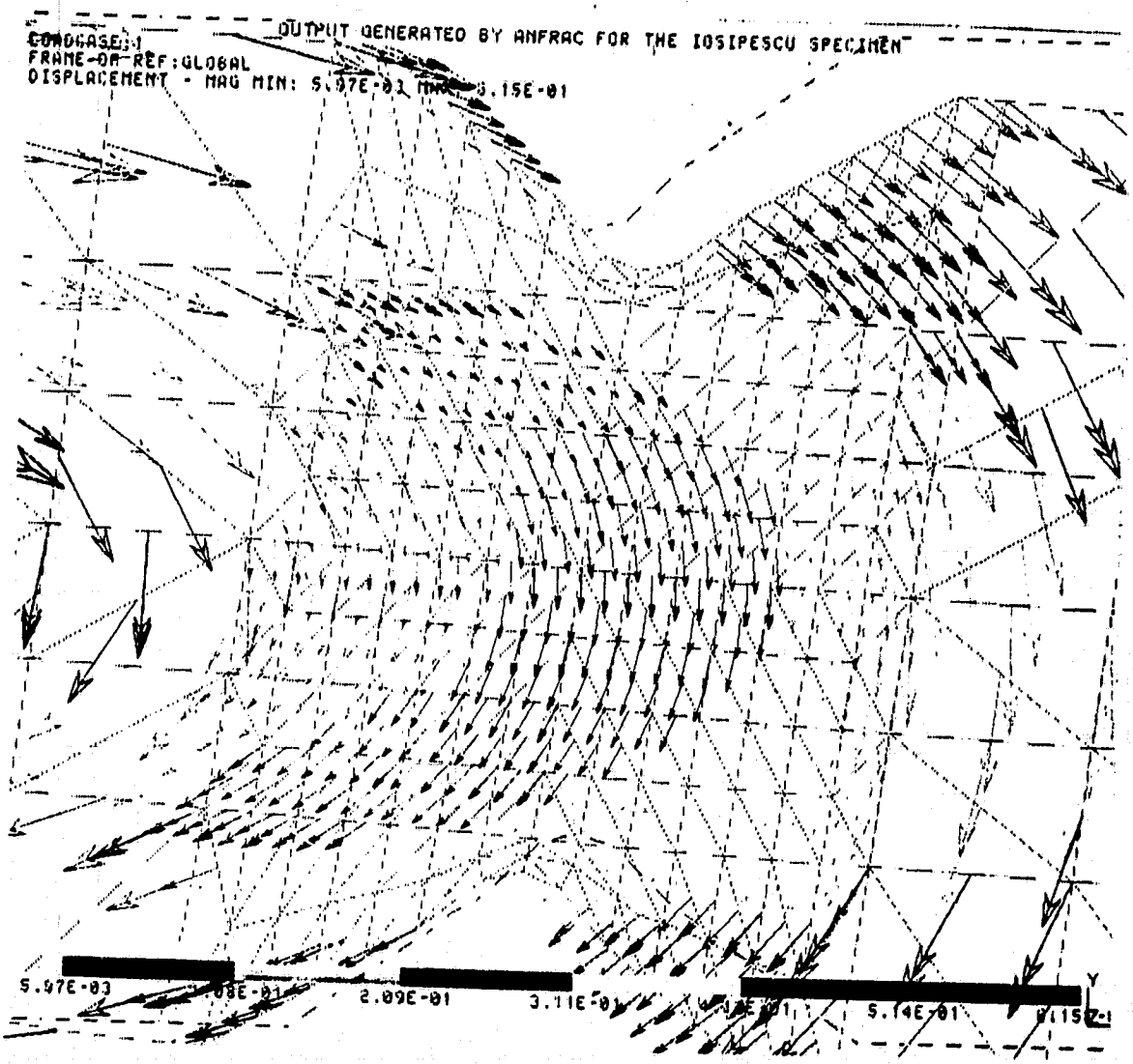

Figure 55. Displacement Field in an Iosipescu Shear Test Coupon

4.4 *Yield Loci*

The different yield loci obtained by the three different test methods are shown in Figures 56 - 59. Only one representative curve for each test method is presented. The presented curves are not averaged for each test method. Due to the different test methods and the correspondingly different end-constraint effects, different in-plane states of stress were present. In order to obtain meaningful comparison of the yield loci in tension, compression and shear, all parameters have to be considered.

The difference in the axial yield stresses observed in tension and compression (Figure 56) can be explained by the presence of the tensile residual stresses in the matrix in the case of the 0° tests, and the end-constraint effect in the case of the off-axis tests. Good correlation between the two different yield loci in tension and compression was obtained for higher off-axis angles, where the end-constraint effect was negligibly small.

The end-constraint effects also influenced the in-plane shear yield loci in compression. Since the fibers were rigidly constrained and directly loaded in low off-axis configurations, early yielding was prevented. This resulted in high yield shear stresses in the low off-axis range. The differences in the yield stresses between the results of Iosipescu tests and off-axis tension tests are due to the presence of different stress ratios in the test sections of the respective specimens.

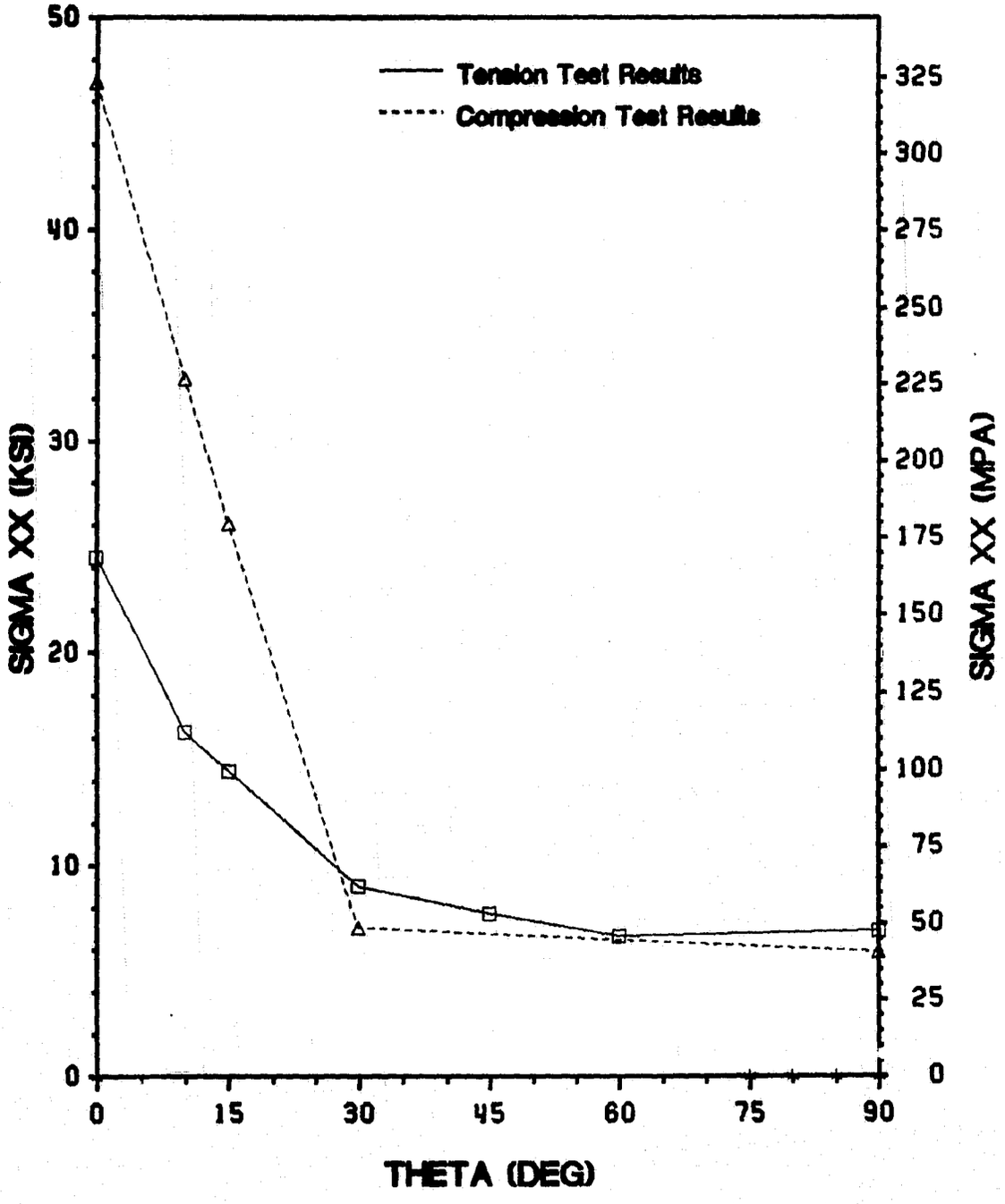

Figure 56. Axial Yield Stress for Different Test Methods

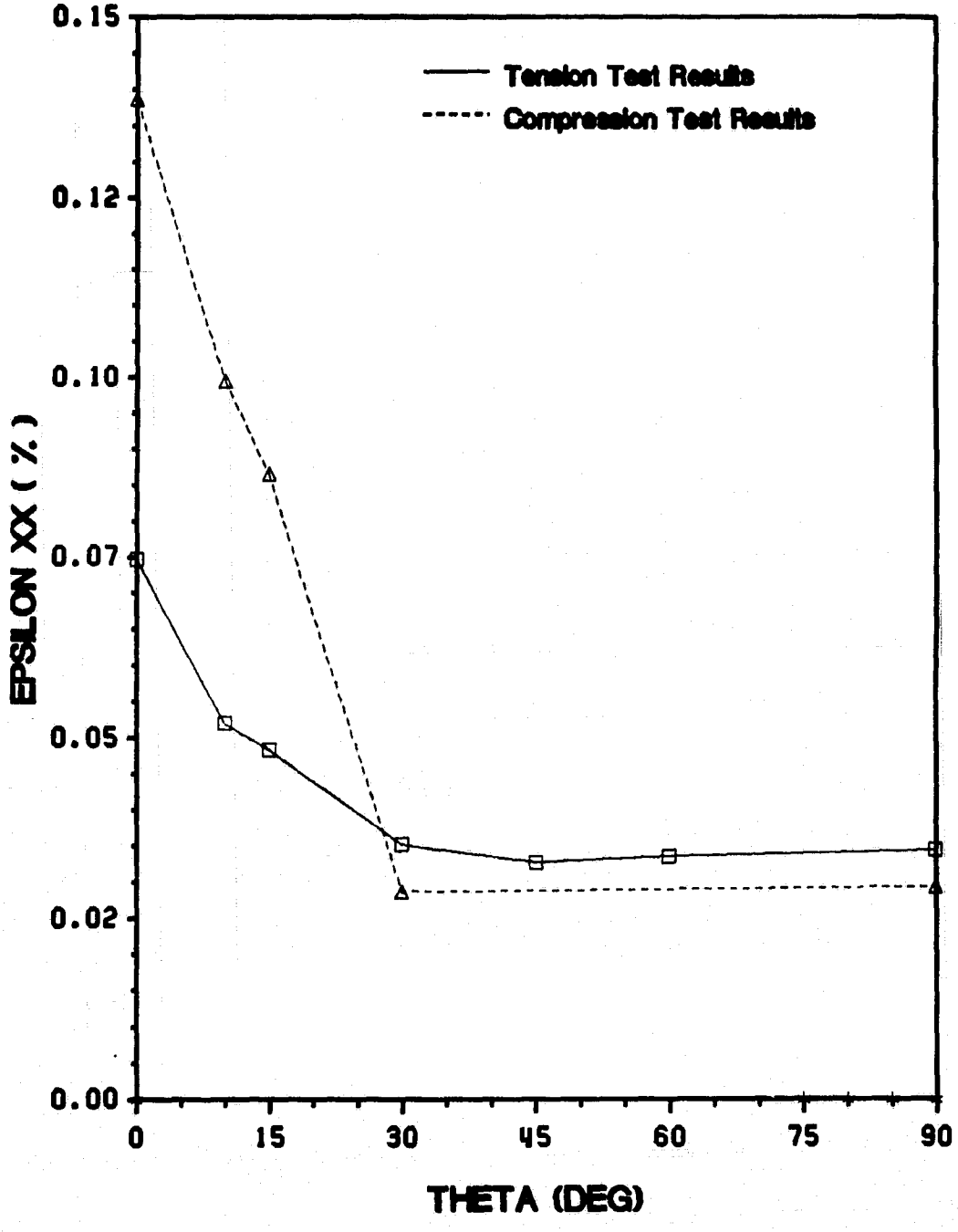

Figure 57. Axial Yield Strain for Different Test Methods

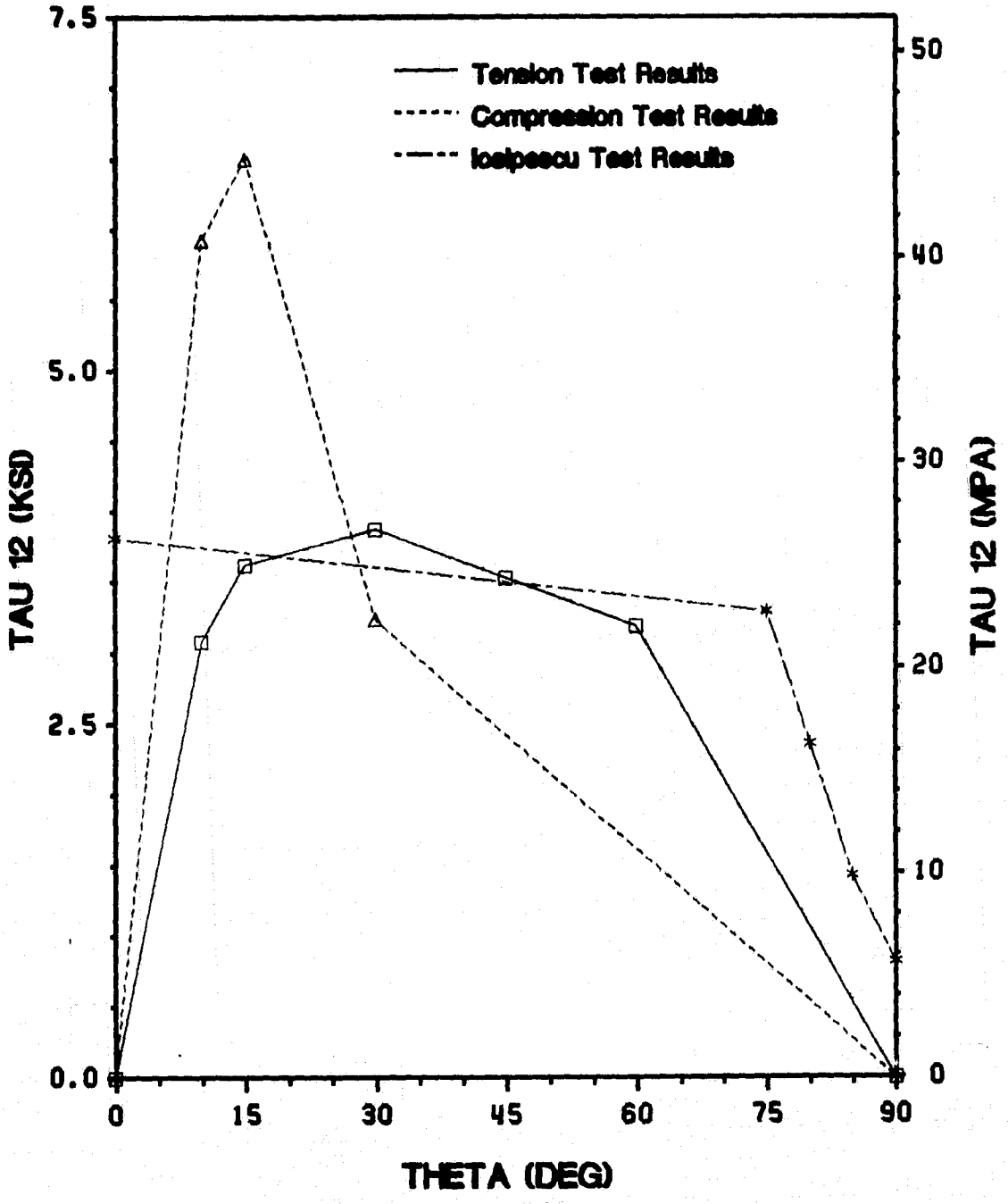

Figure 58. In-Plane Shear Yield Stress for Different Test Methods

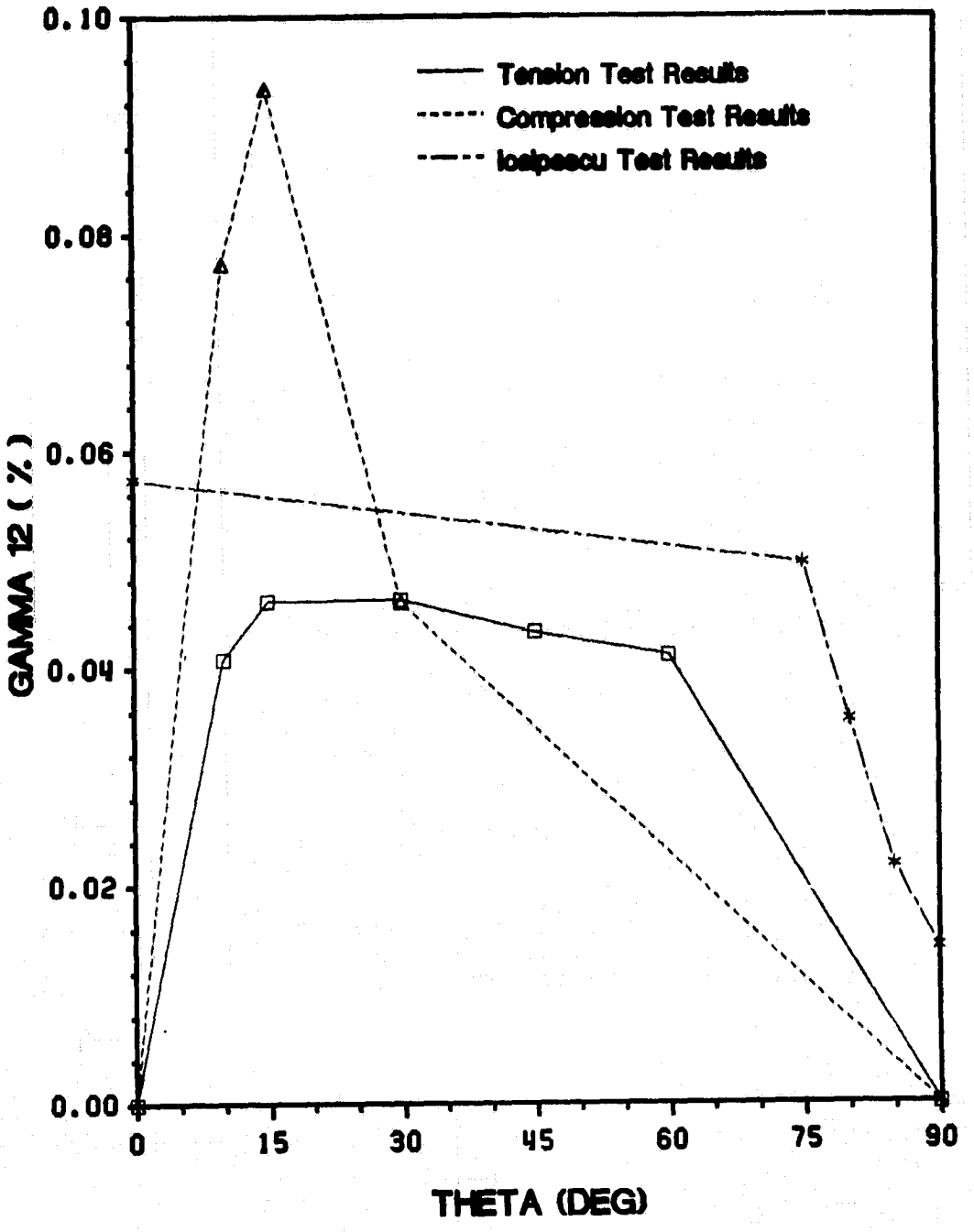

Figure 59. In-Plane Shear Yield Strain for Different Test Methods

5.0 MICROMECHANICAL MODEL

In order to predict the yield surface of the boron/aluminum composite, an analytical micromechanical model was used [38]. Elastic properties of the fiber, matrix and composite are employed in the model in conjunction with a yield criterion for the matrix phase in the course of generating the composite yield surface. In the present study, only the in-plane shear yield stress was investigated. For future work the model can be easily extended to predict the in-plane longitudinal and transverse yield loci in a similar fashion. The dependence of the model on the experimentally obtained input parameters, which takes into account the influence of scatter in the experimental data, is also discussed.

5.1 Mathematical Model

For an accurate mathematical description of the material behavior at yield, the interaction between fiber and matrix has to be modeled accurately. The nonlinear response of the composite is a result of the nonlinear behavior of its softest component; the aluminum matrix in this case. Yielding of

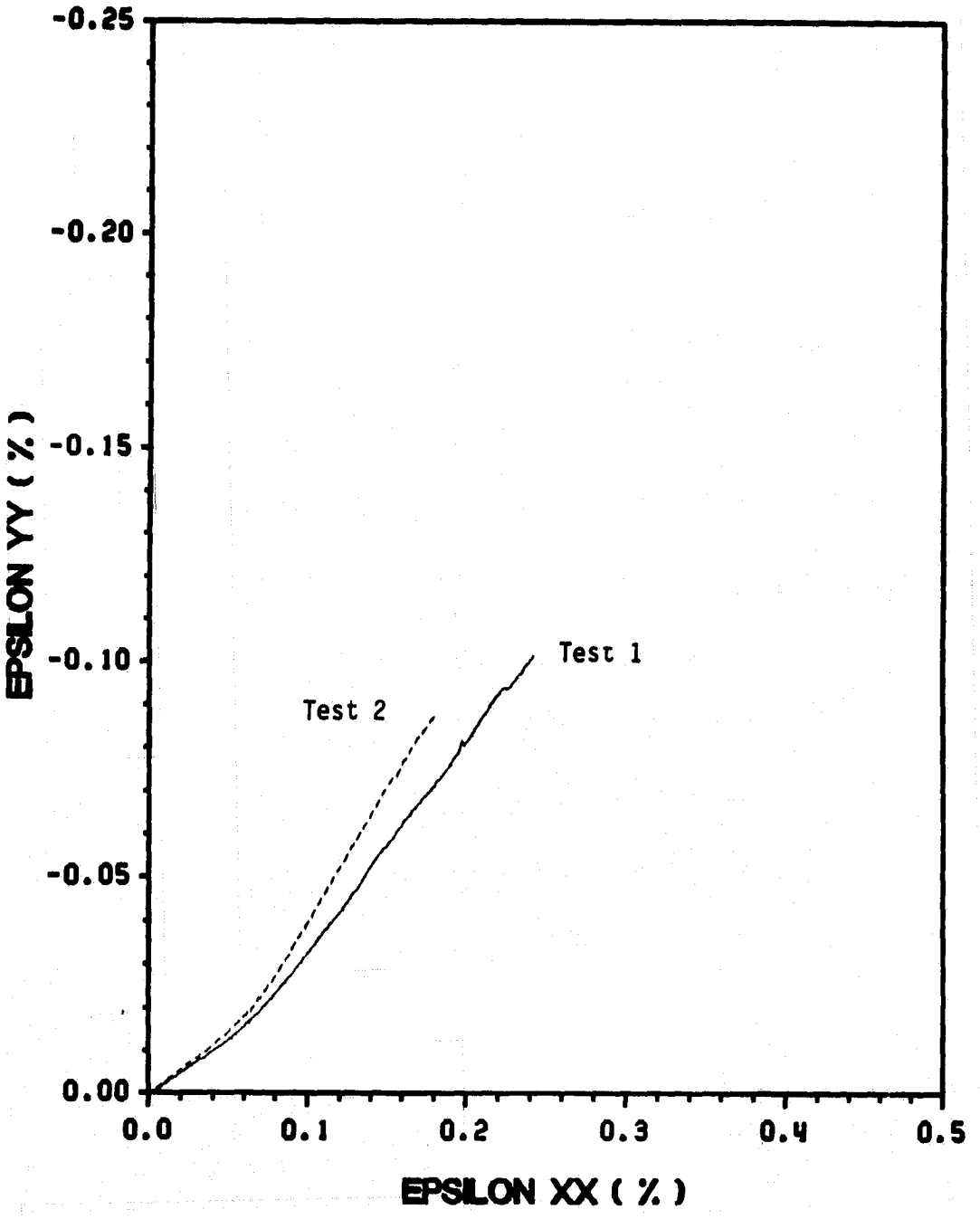

Figure 76. 60° Off-Axis Tests: Poisson's Response

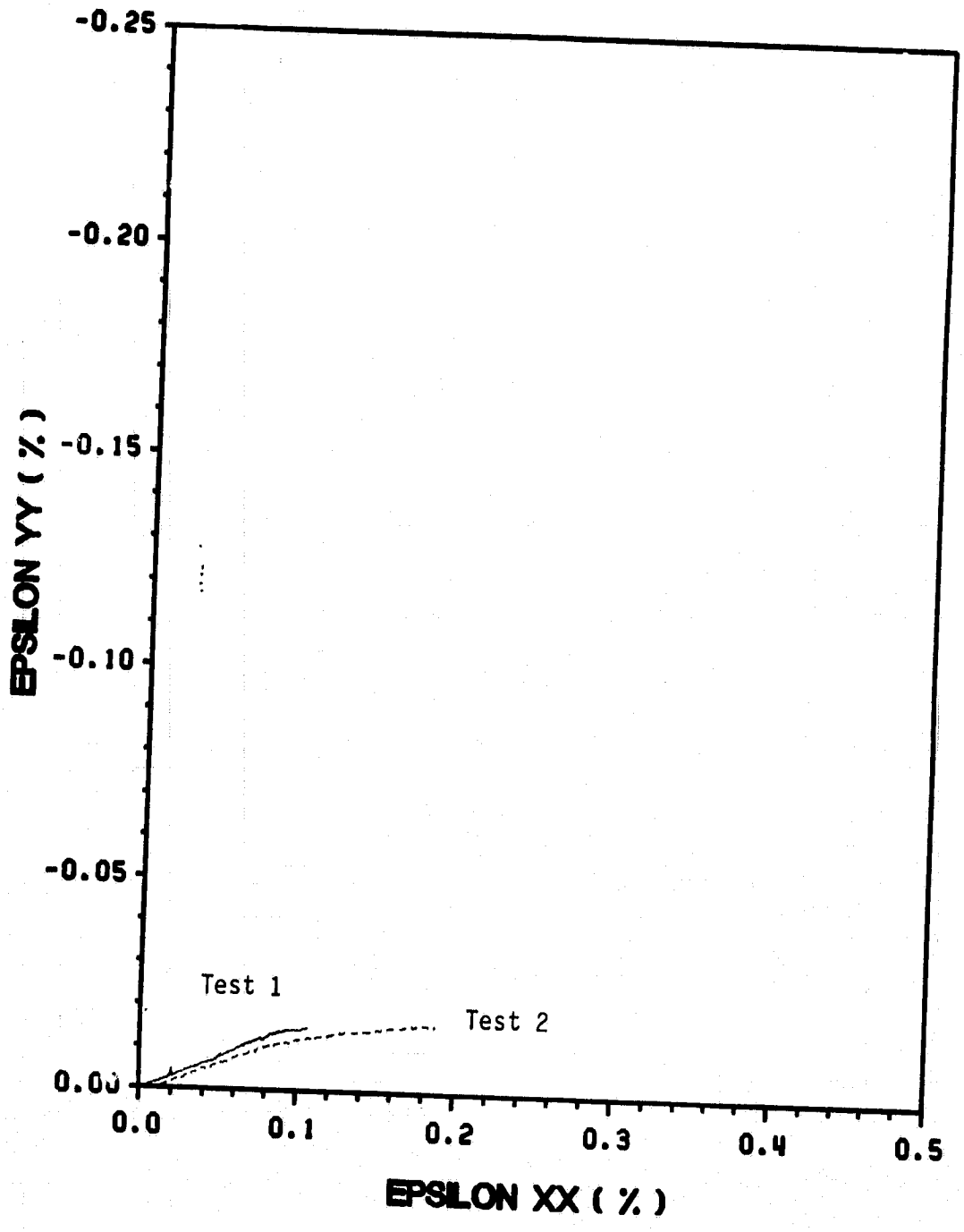

Figure 77. 90° On-Axis Tests: Poisson's Response

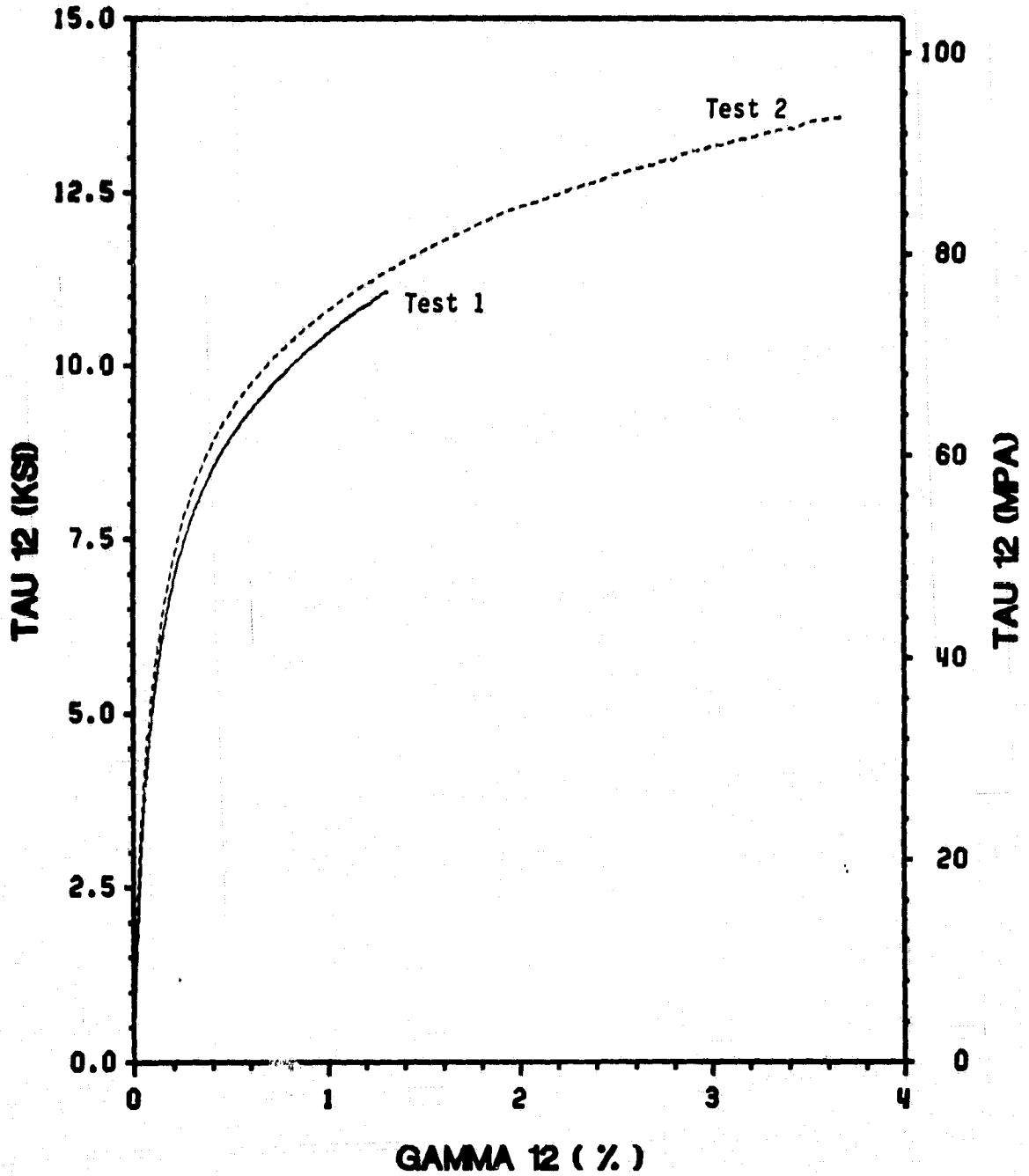

Figure 78. 10° Off-Axis Tests: In-Plane Shear Response

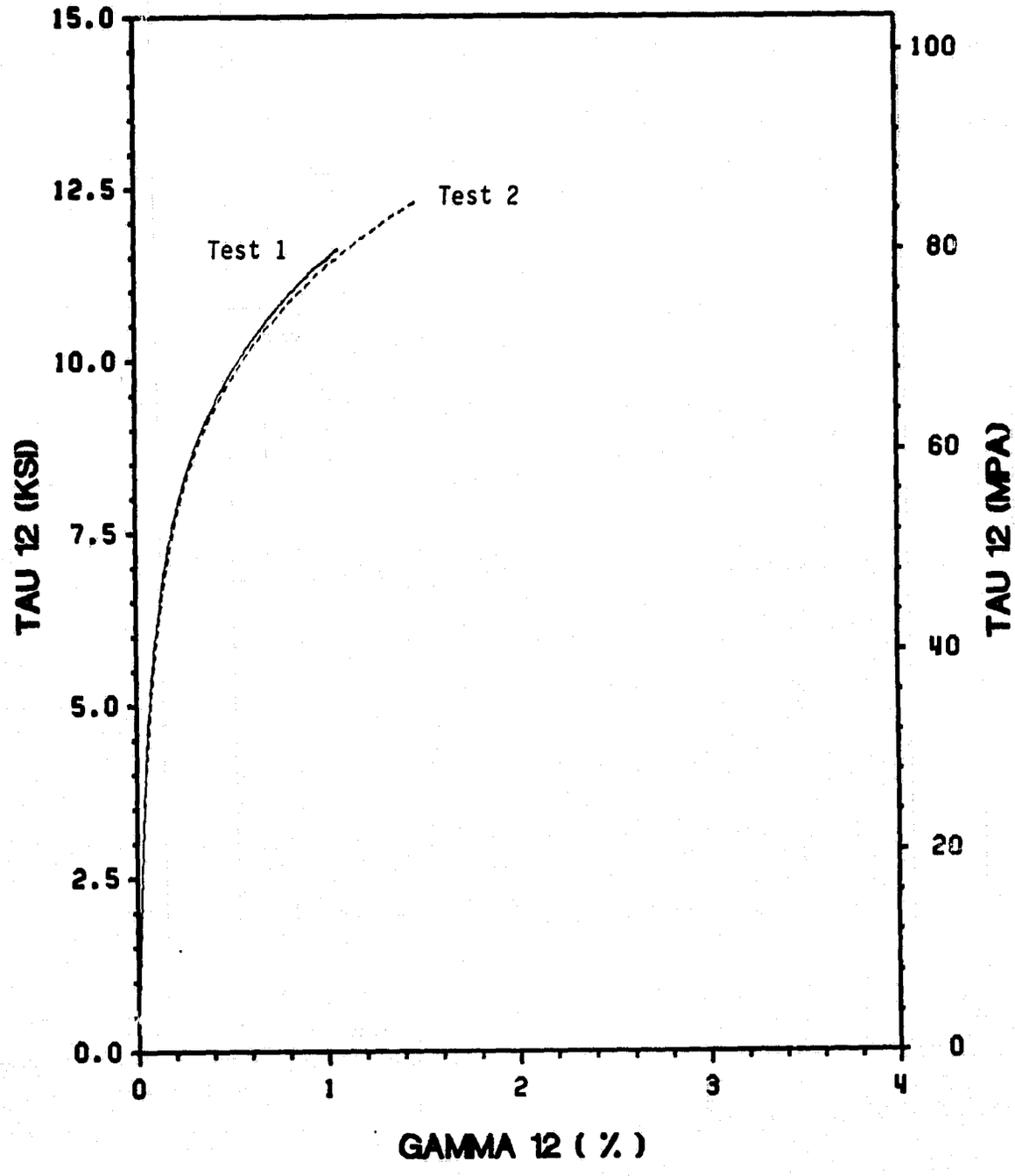

Figure 79. 15° Off-Axis Tests: In-Plane Shear Response

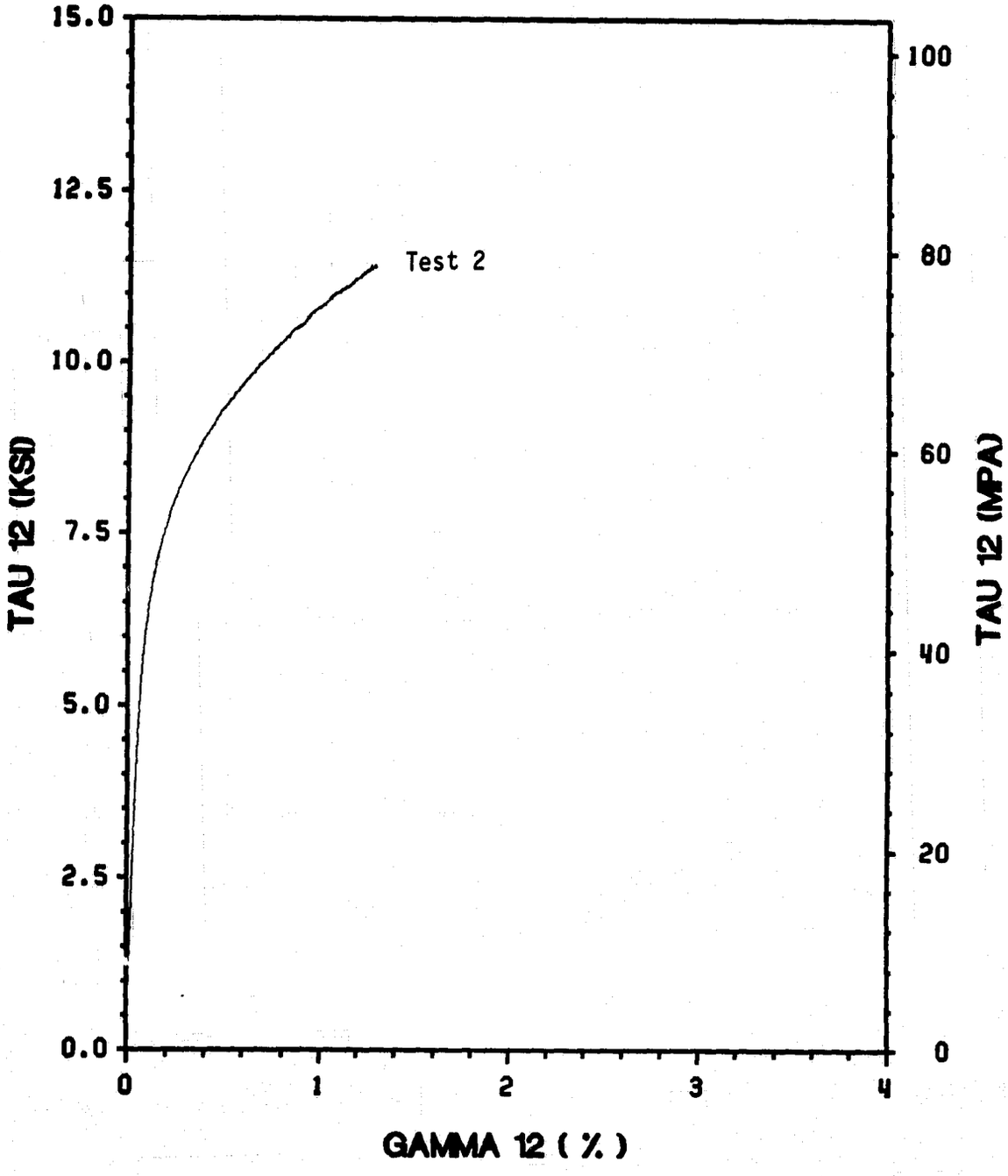

Figure 80. 30° Off-Axis Tests: In-Plane Shear Response

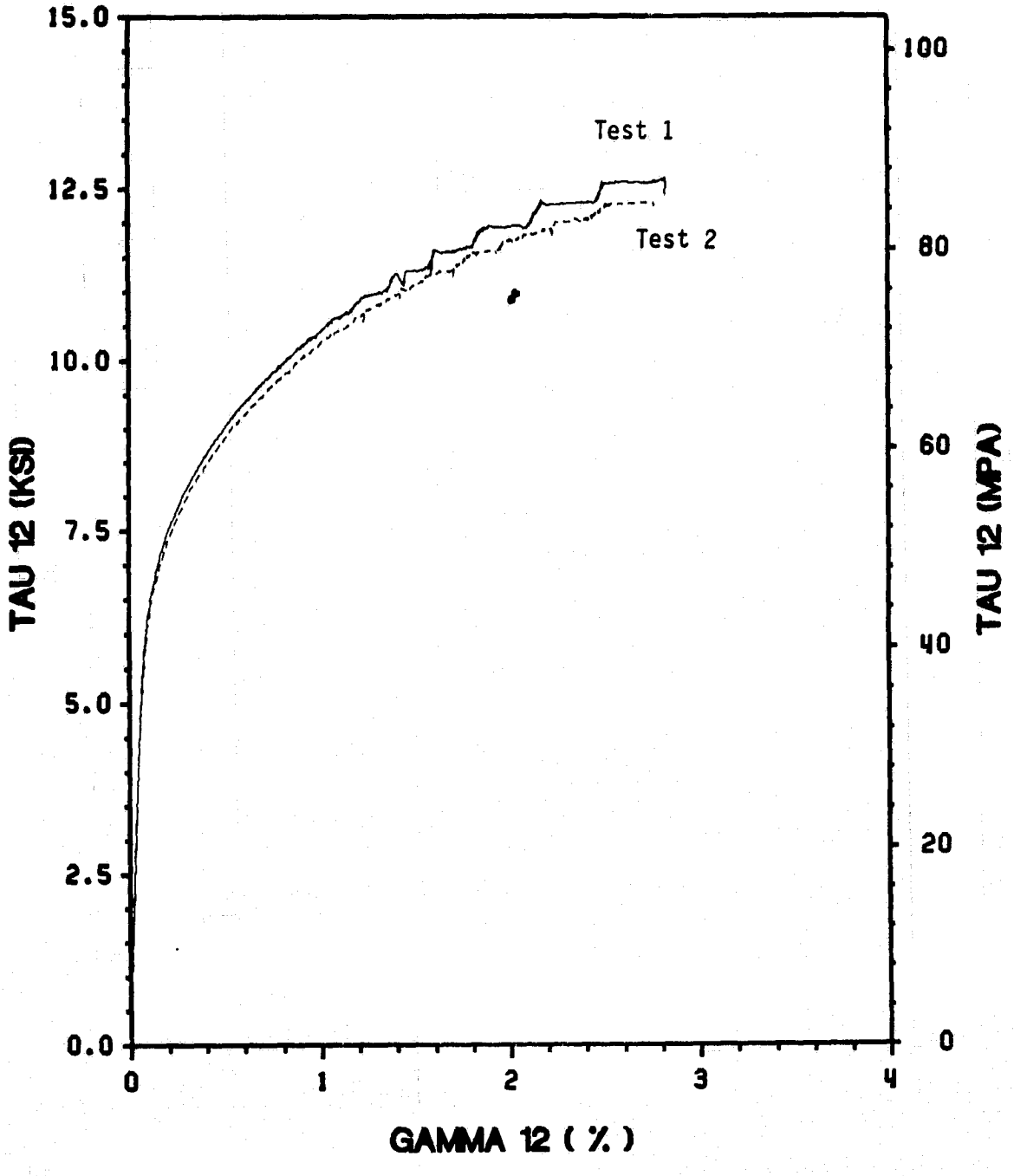

Figure 81. 45° Off-Axis Tests: In-Plane Shear Response

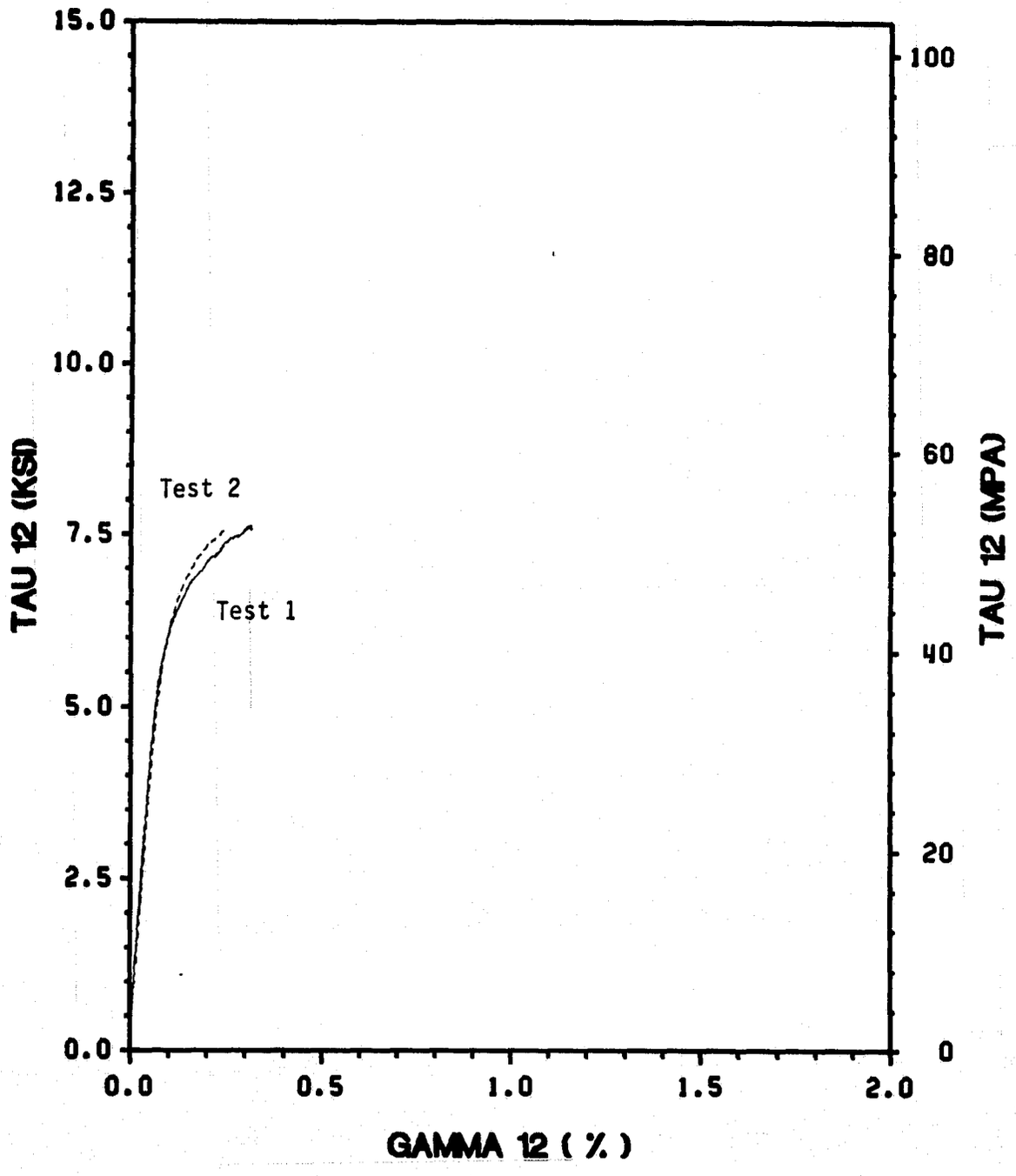

Figure 82. 60° Off-Axis Tests: In-Plane Shear Response

A.2 Cyclic Test Results

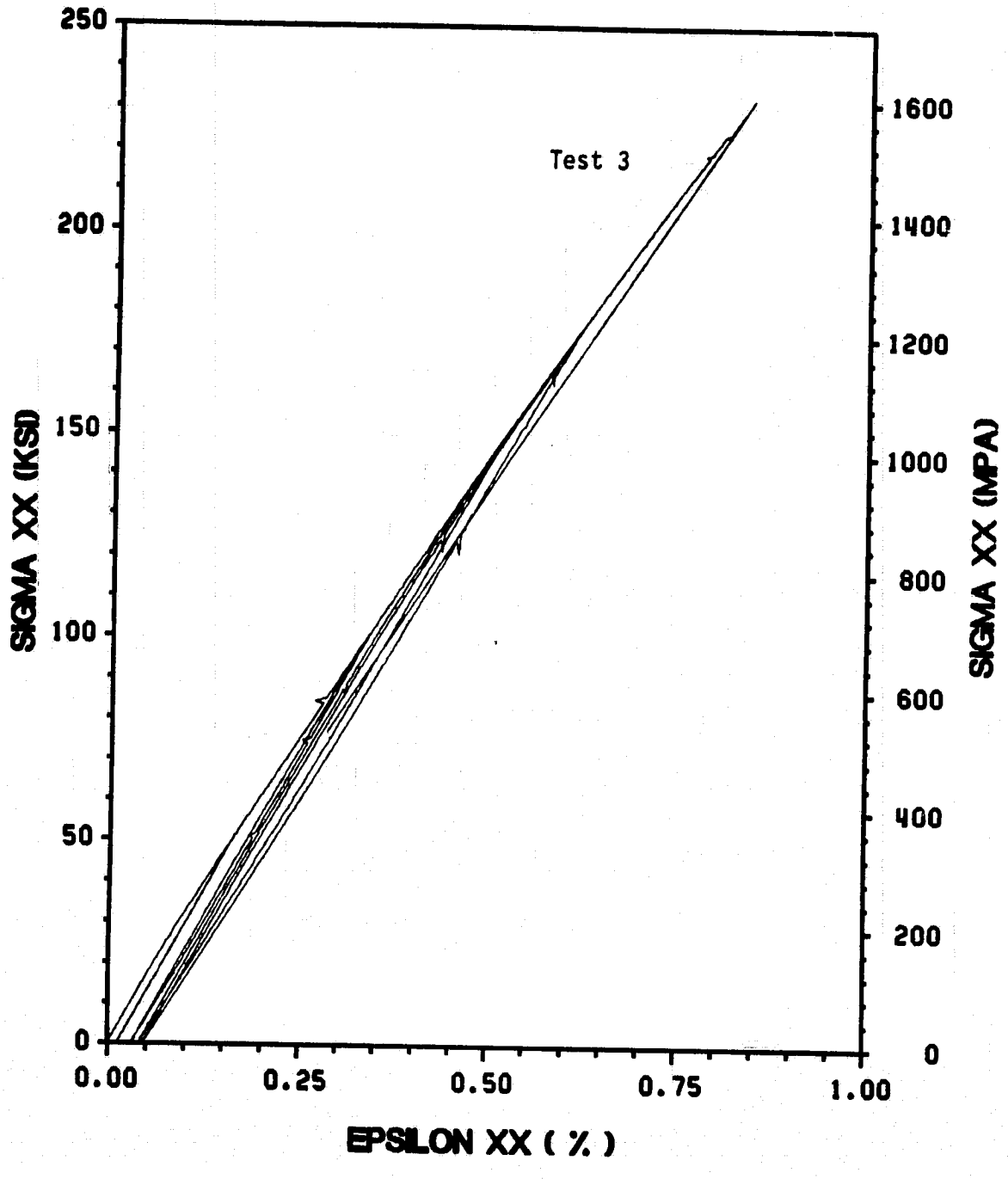

Figure 83. 0° On-Axis Tests: Tensile Stress-Strain Response

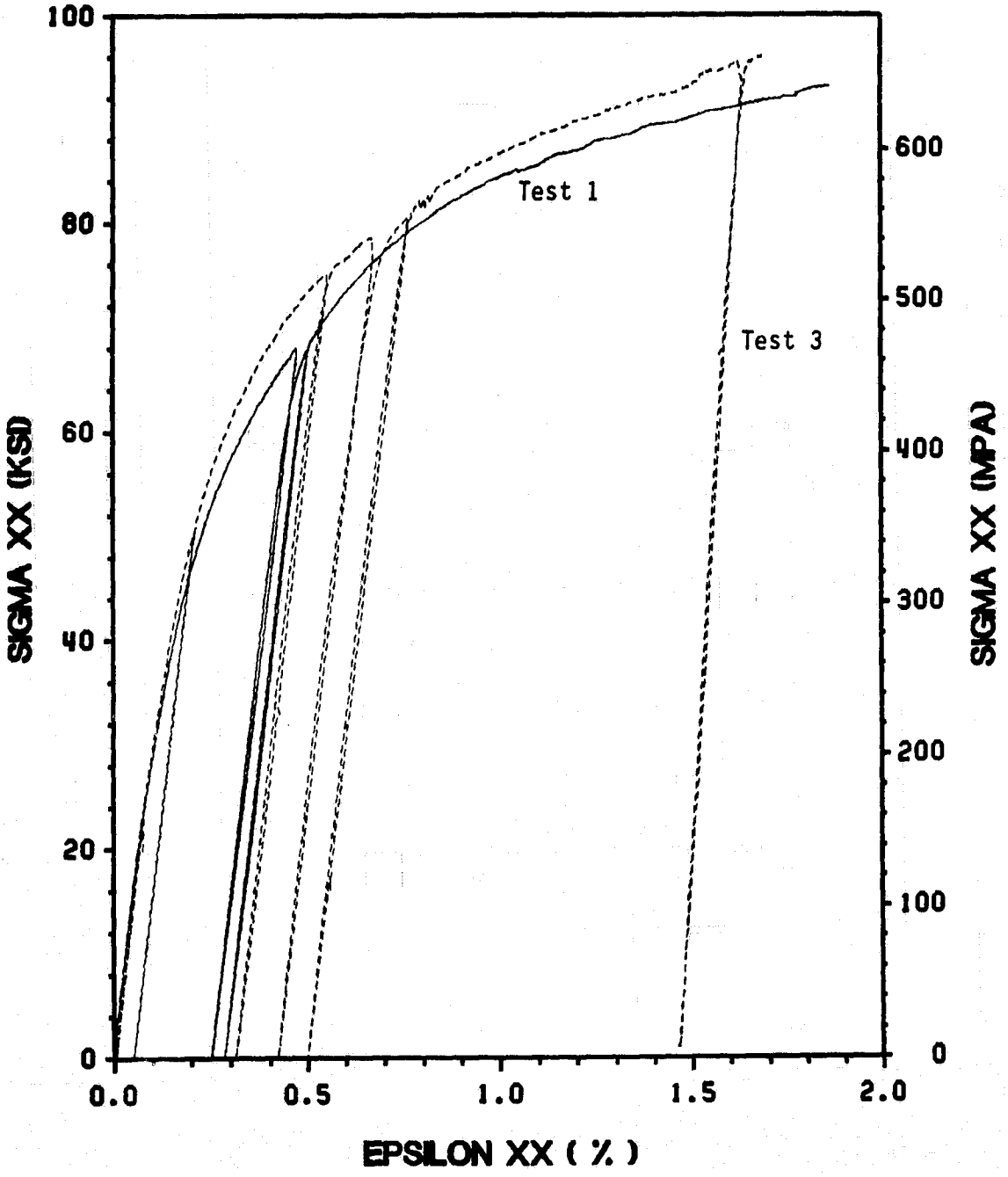

Figure 84. 10° Off-Axis Tests: Tensile Stress-Strain Response

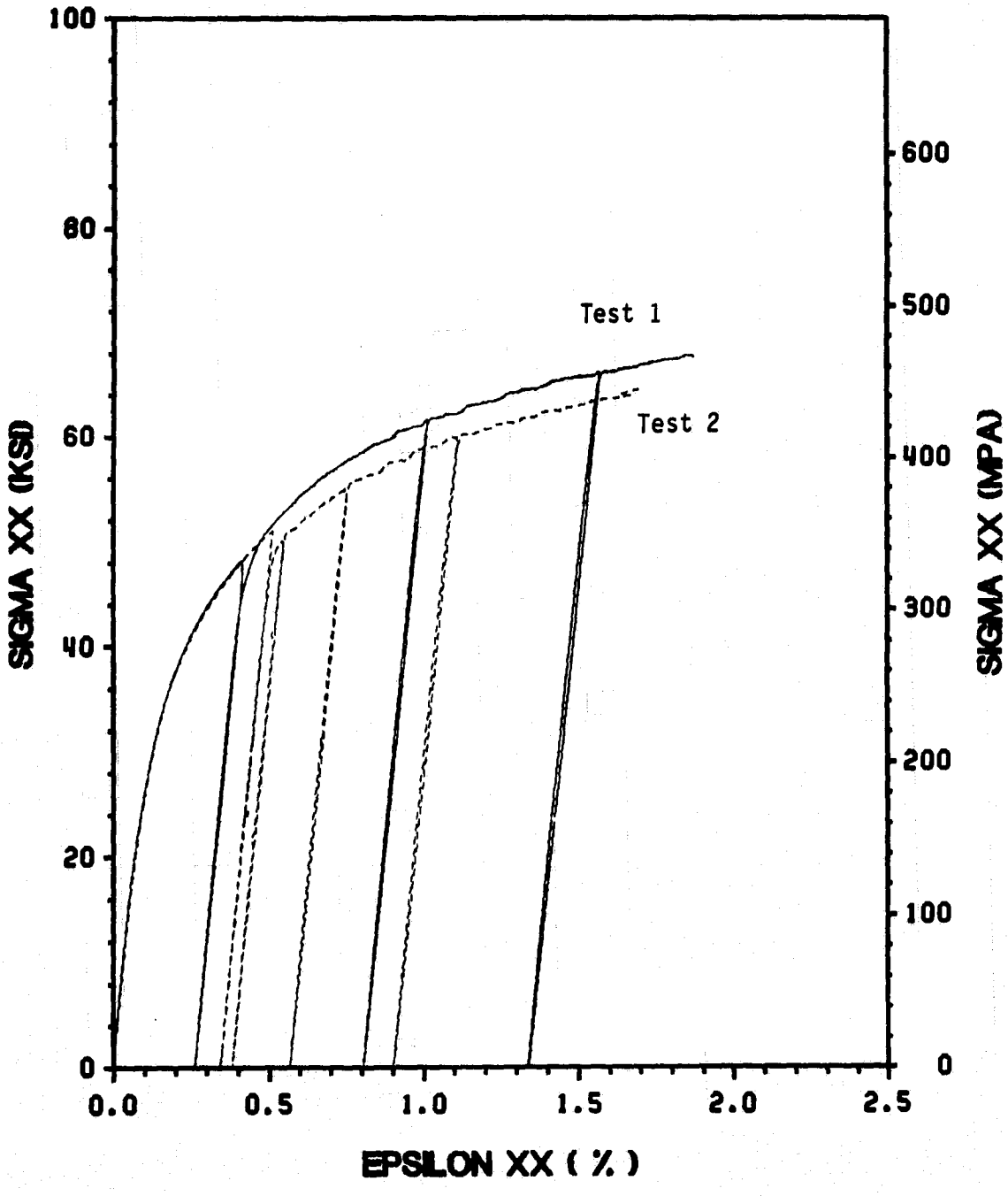

Figure 85. 15° Off-Axis Tests: Tensile Stress-Strain Response

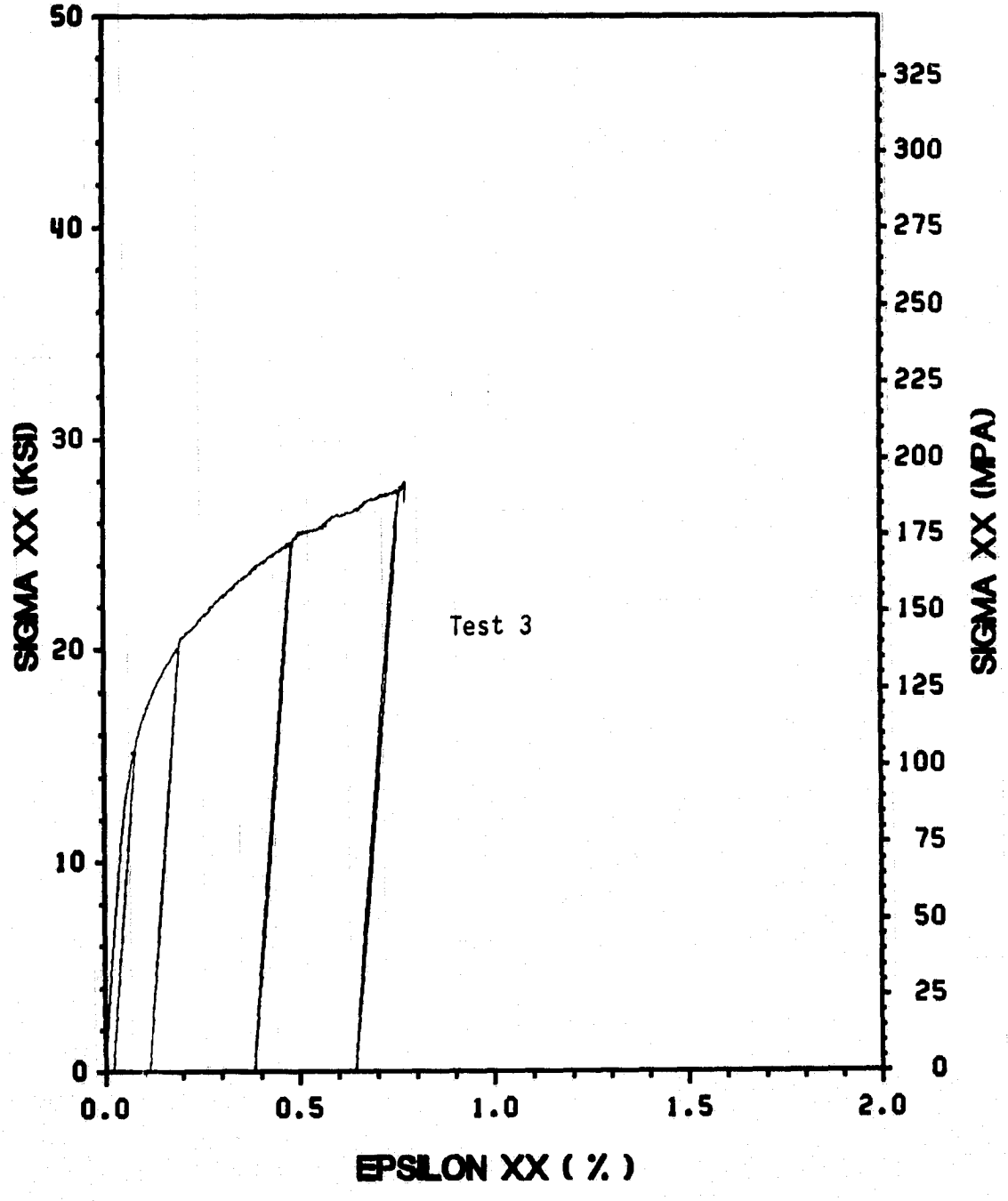

Figure 86. 30° Off-Axis Tests: Tensile Stress-Strain Response

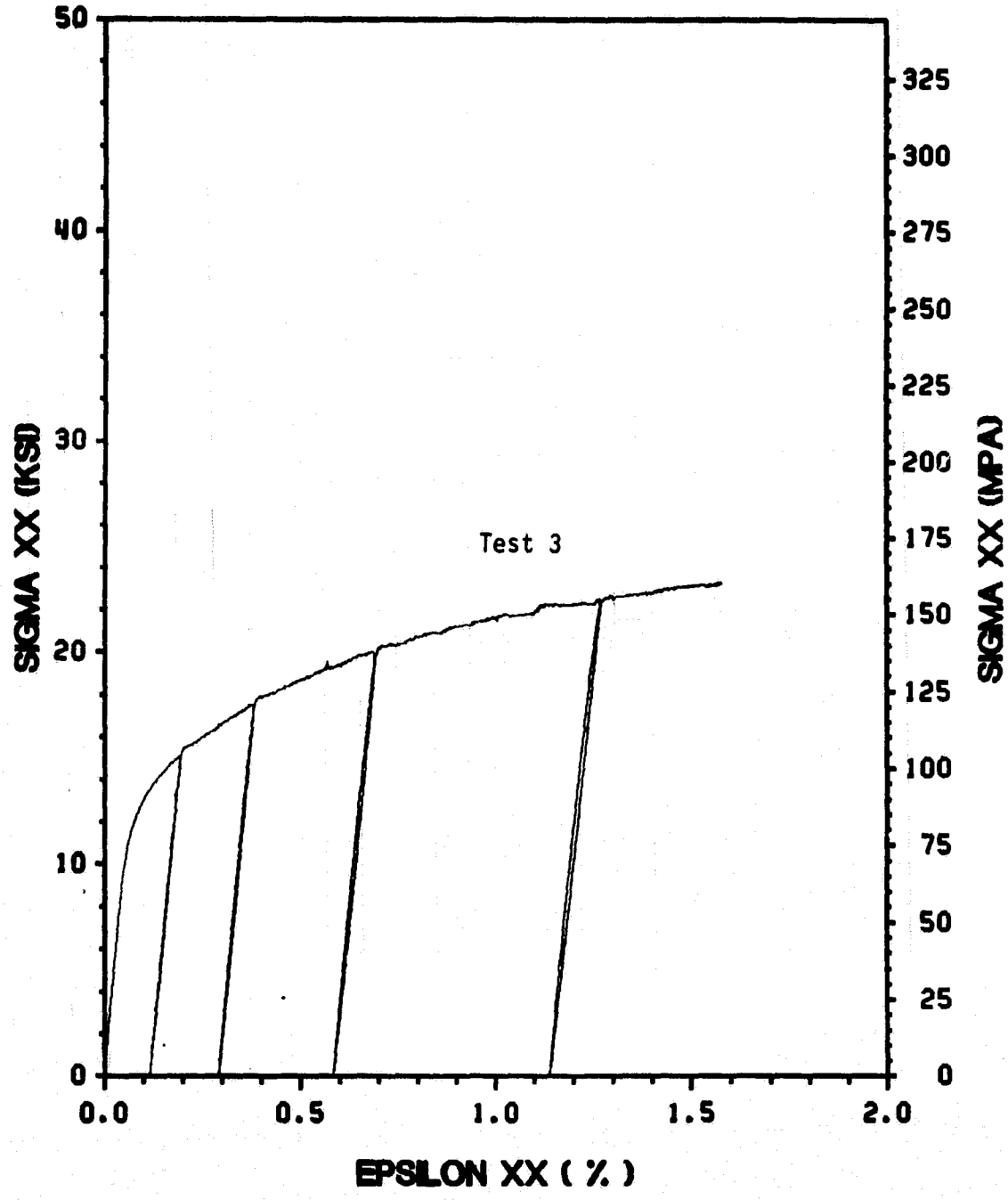

Figure 87. 45° Off-Axis Tests: Tensile Stress-Strain Response

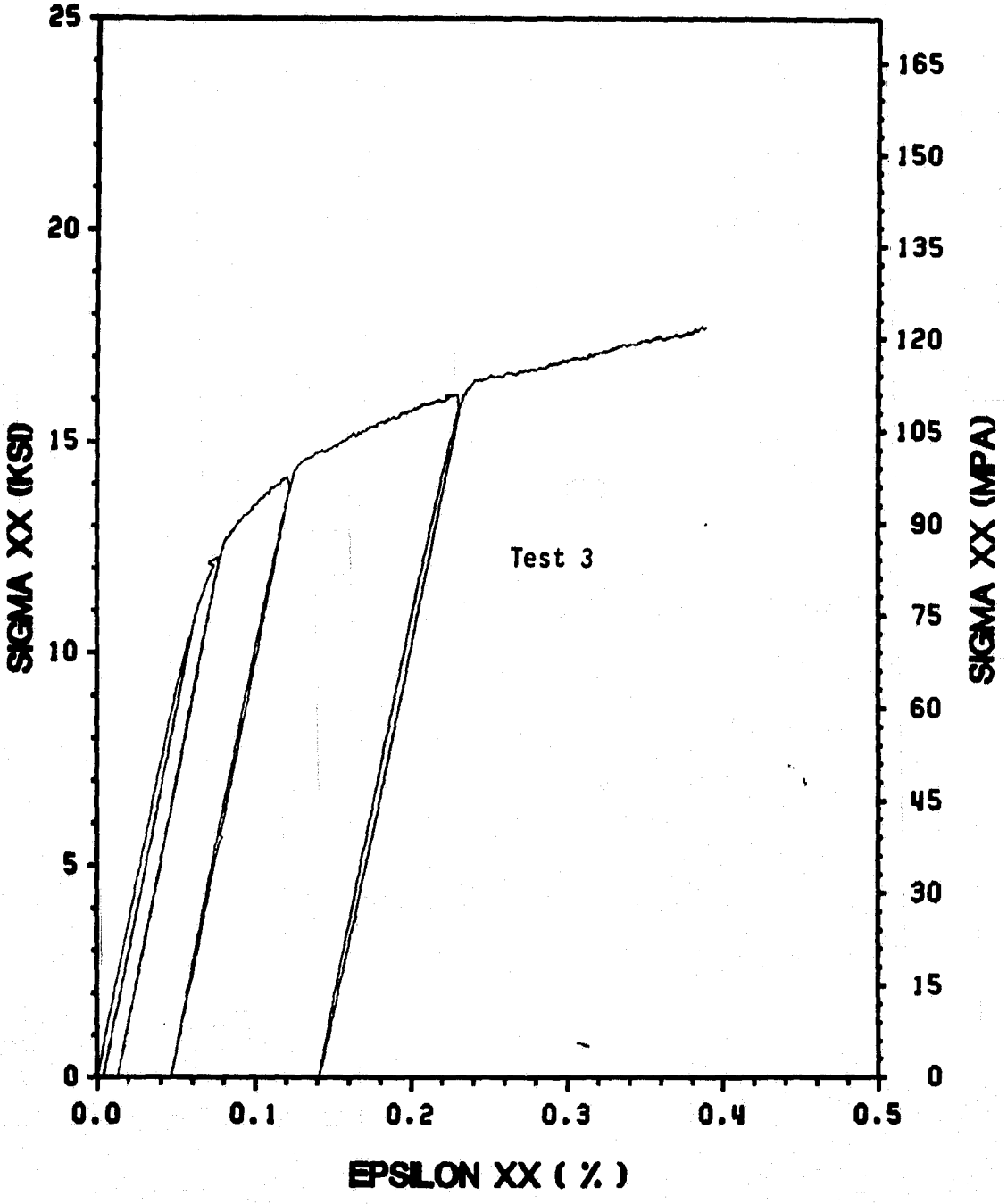

Figure 88. 60° Off-Axis Tests: Tensile Stress-Strain Response

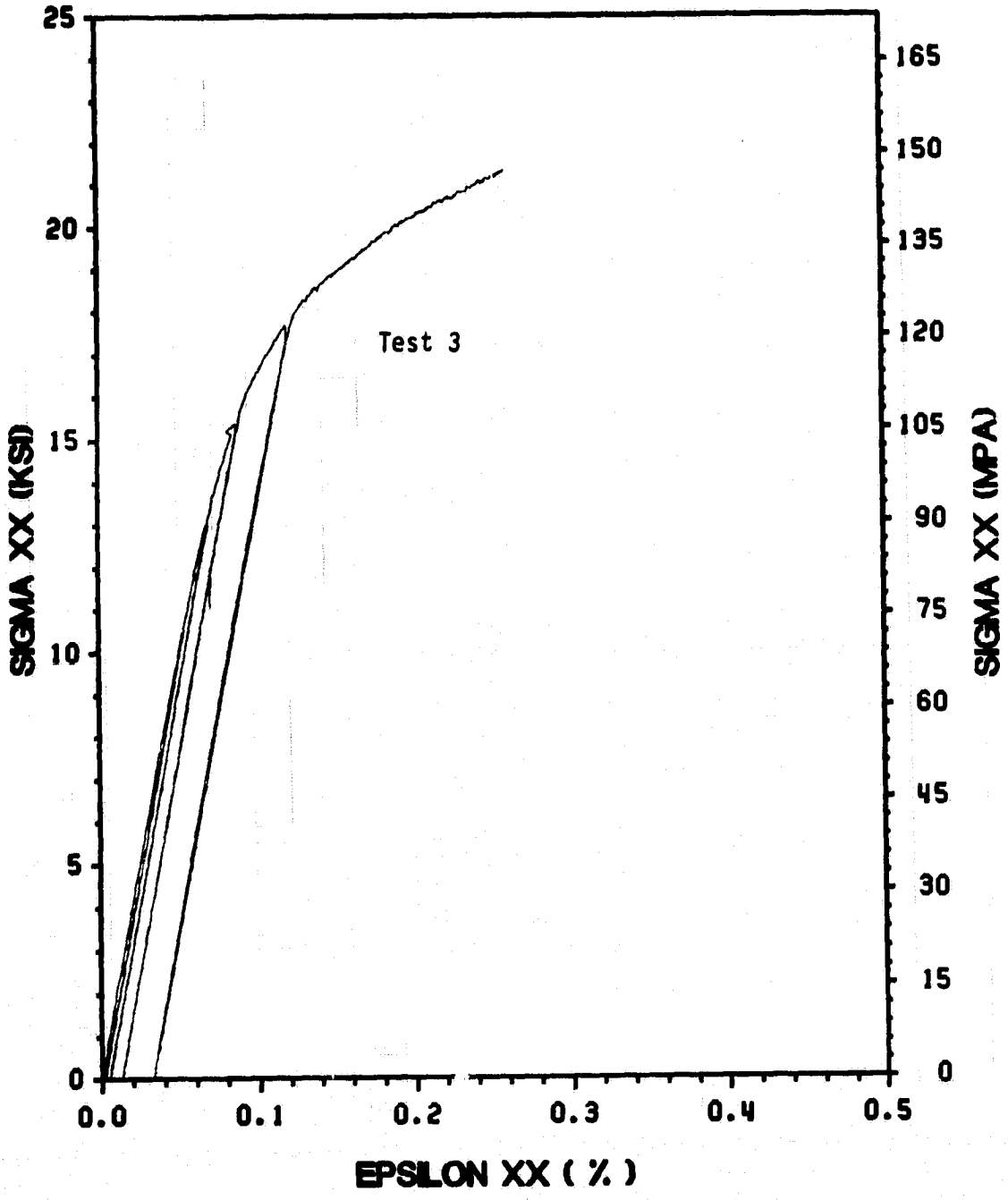

Figure 89. 90° On-Axis Tests: Tensile Stress-Strain Response

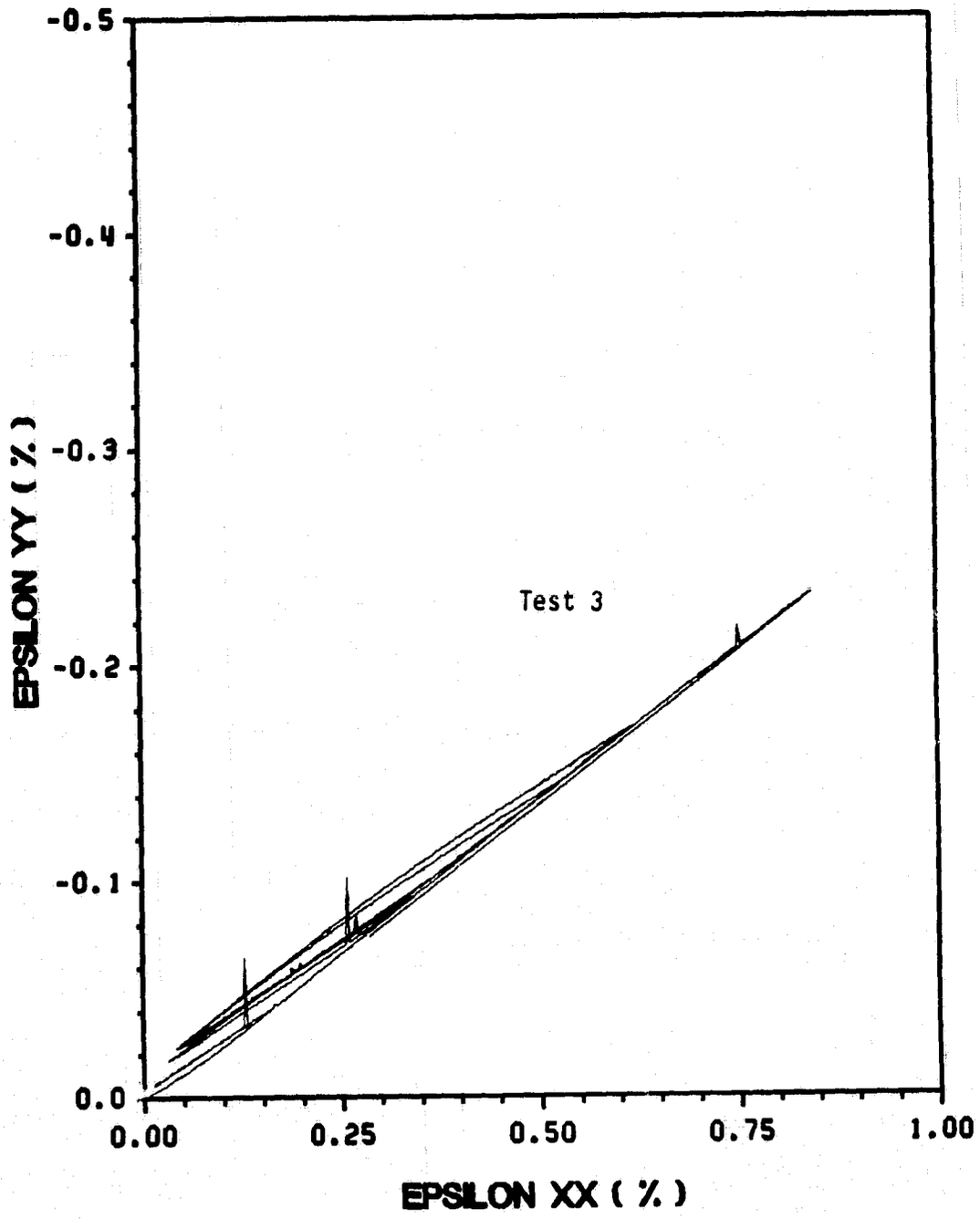

Figure 90. 0° On-Axis Tests: Poisson's Response

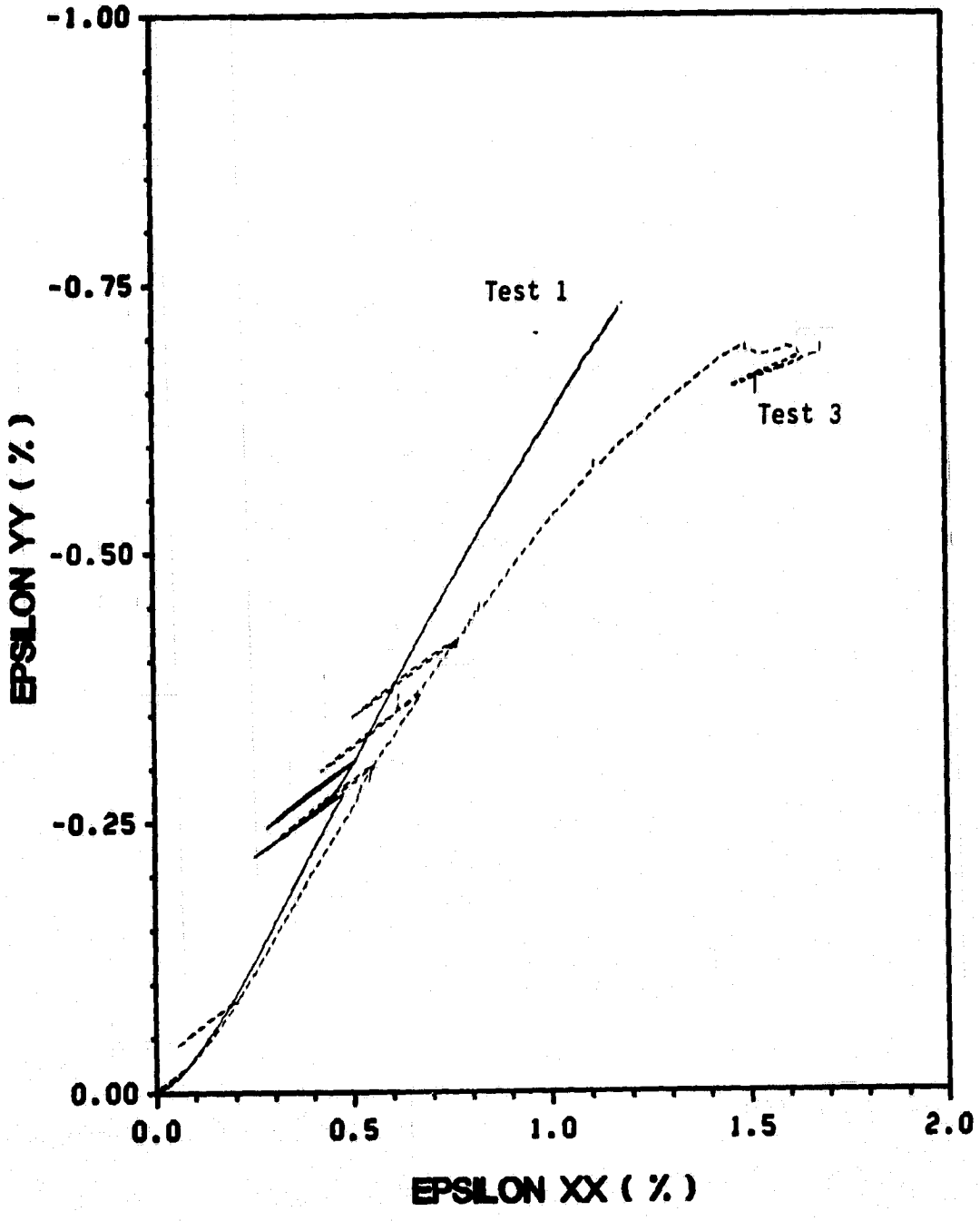

Figure 91. 10° Off-Axis Tests: Poisson's Response

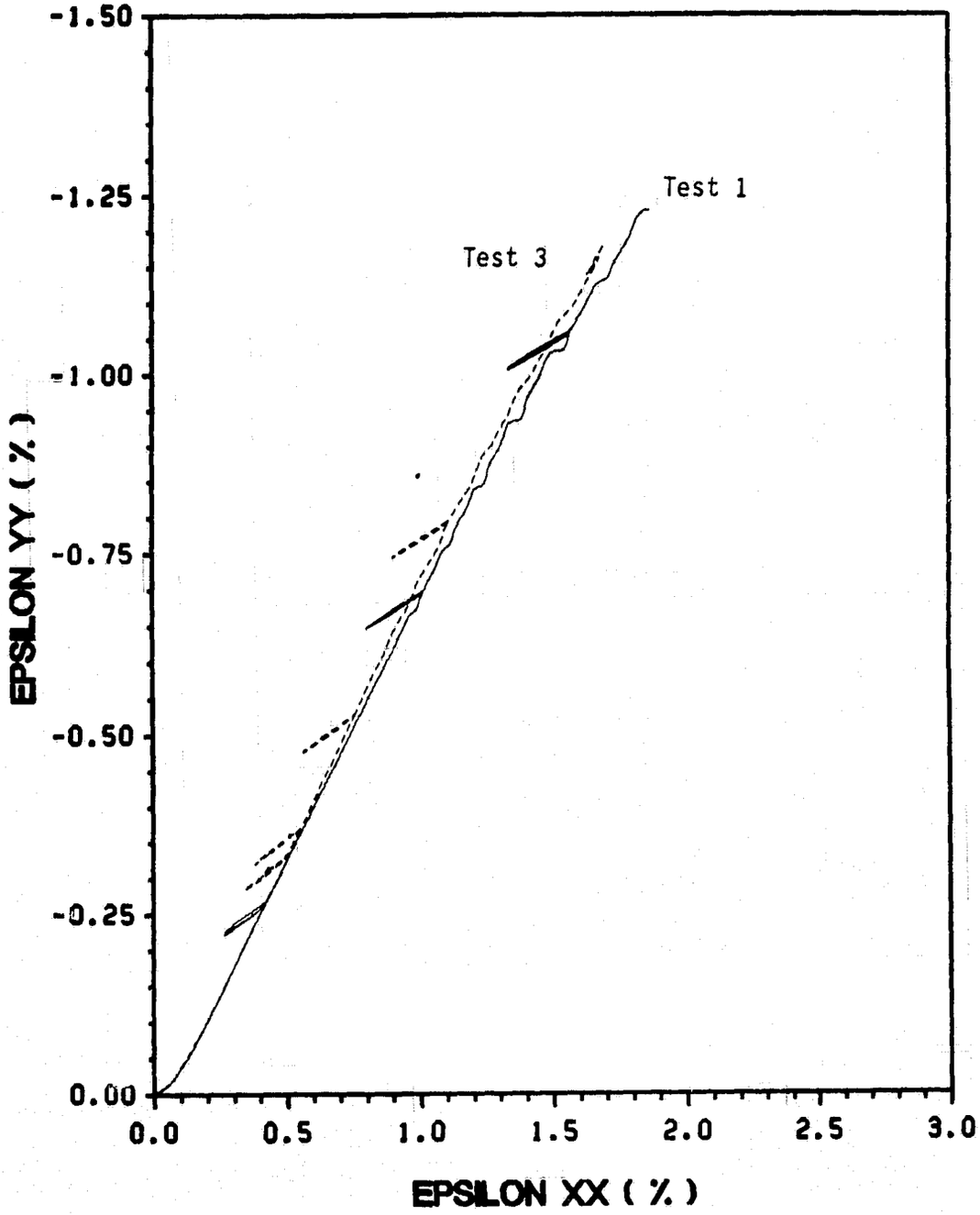

Figure 92. 15° Off-Axis Tests: Poisson's Response

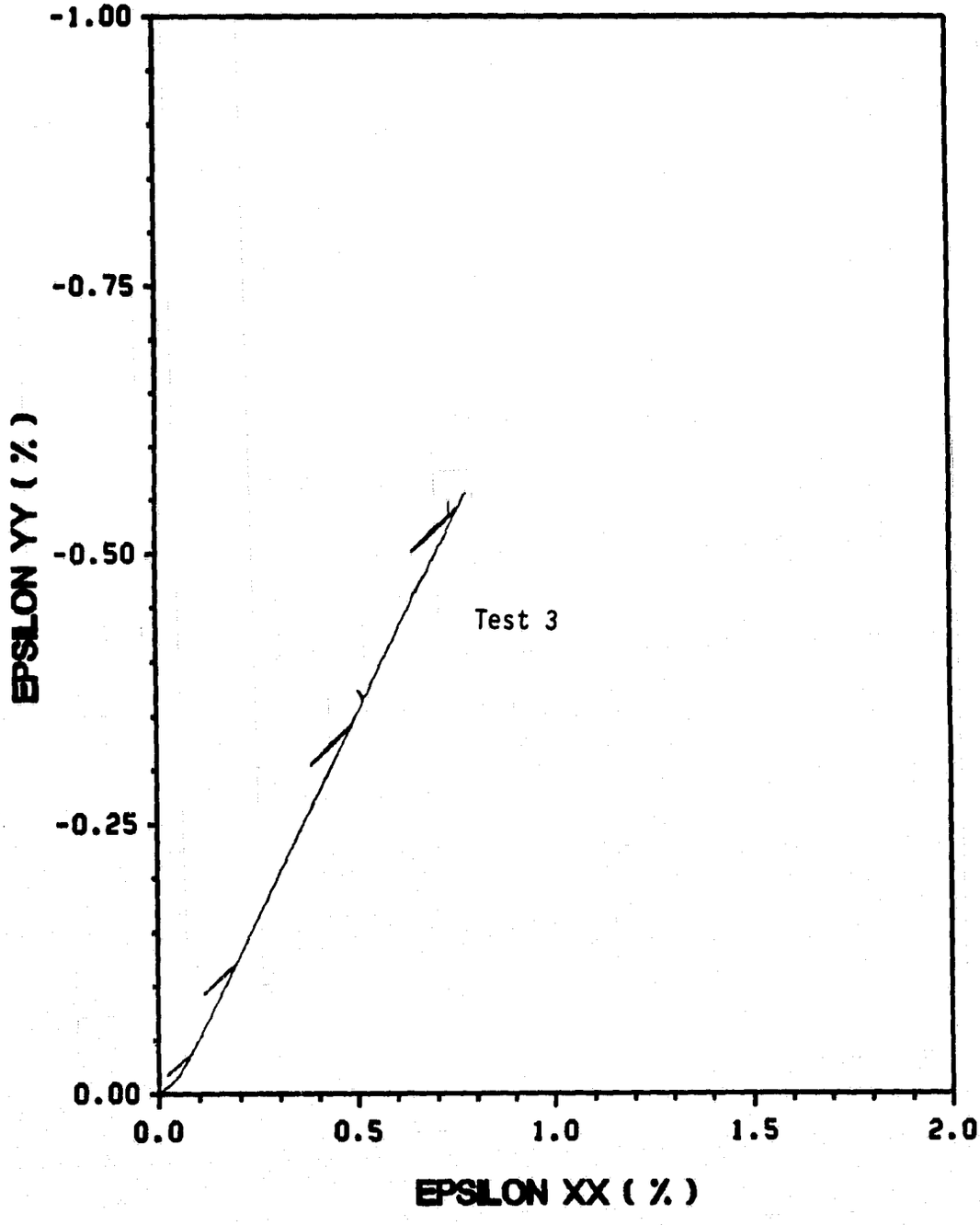

Figure 93. 30° Off-Axis Tests: Poisson's Response

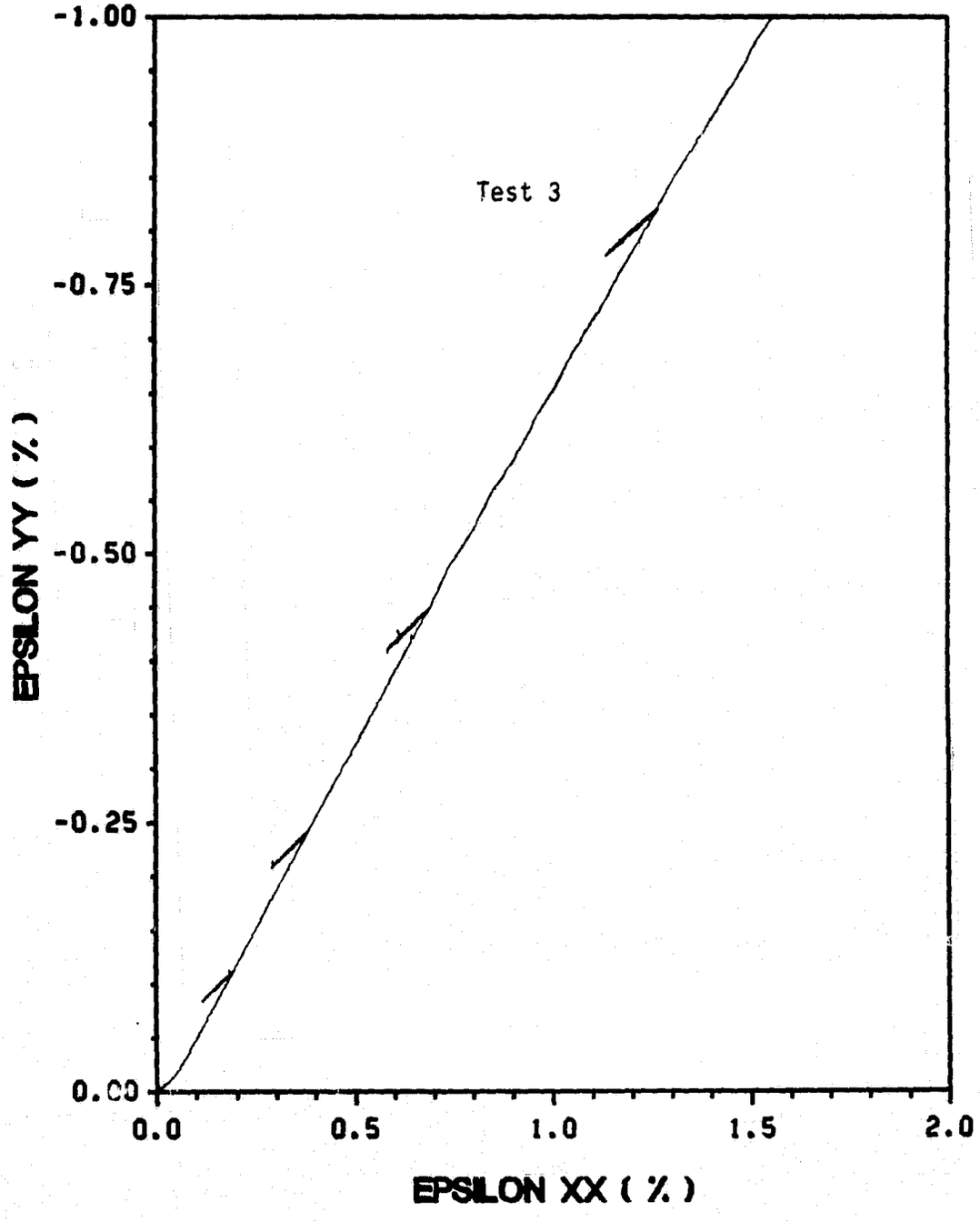

Figure 94. 45° Off-Axis Tests: Poisson's Response

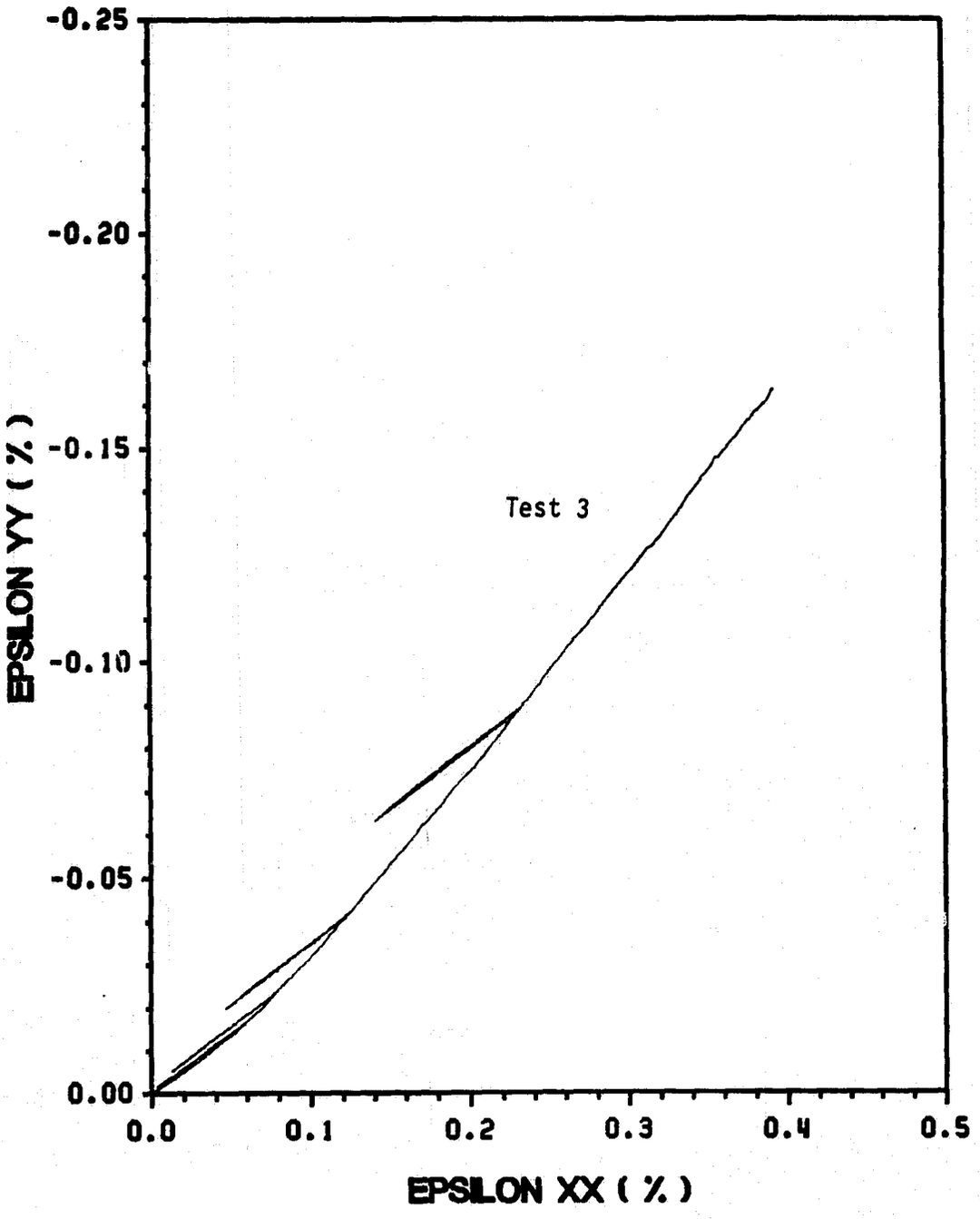

Figure 95. 60° Off-Axis Tests: Poisson's Response

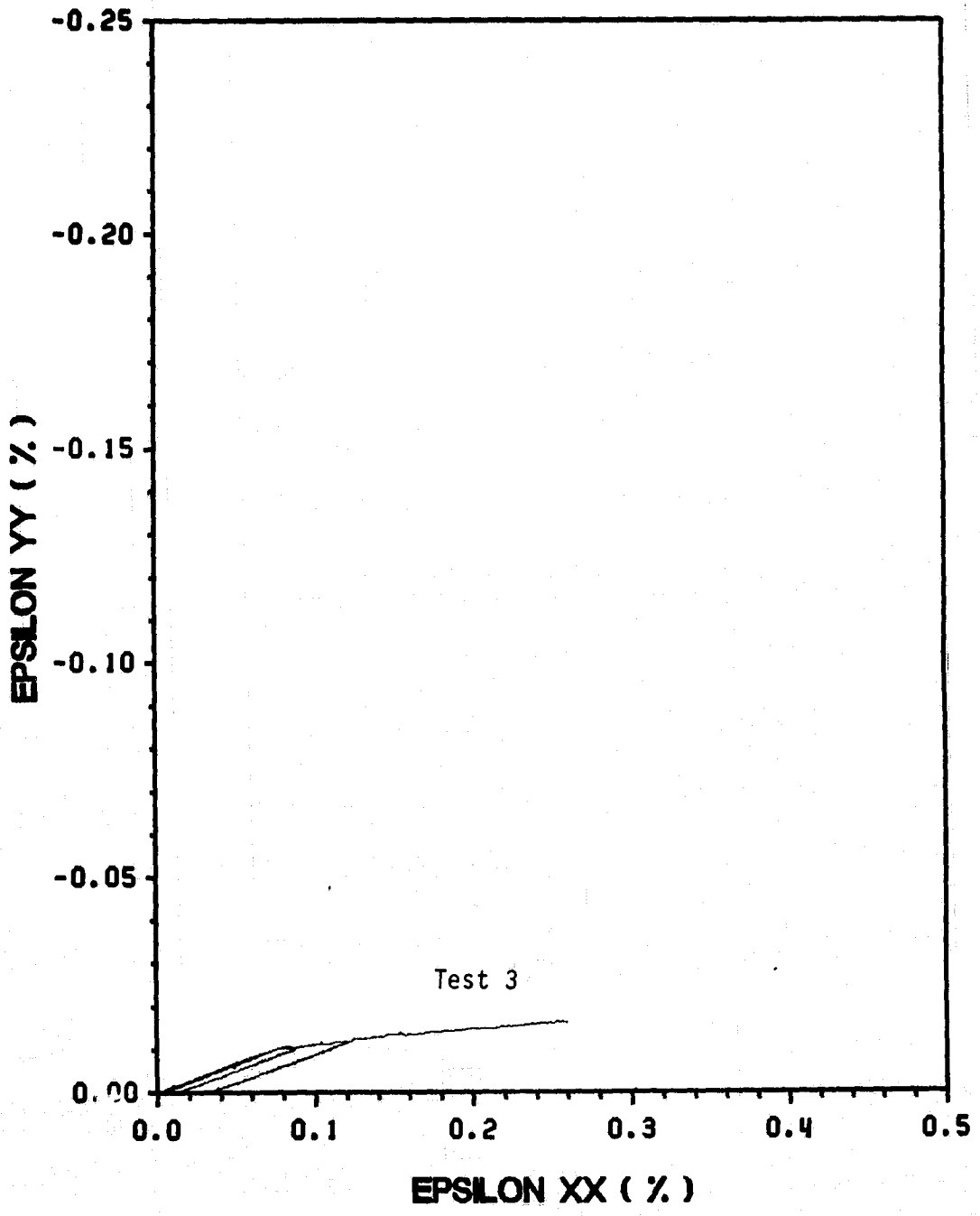

Figure 96. 90° On-Axis Tests: Poisson's Response

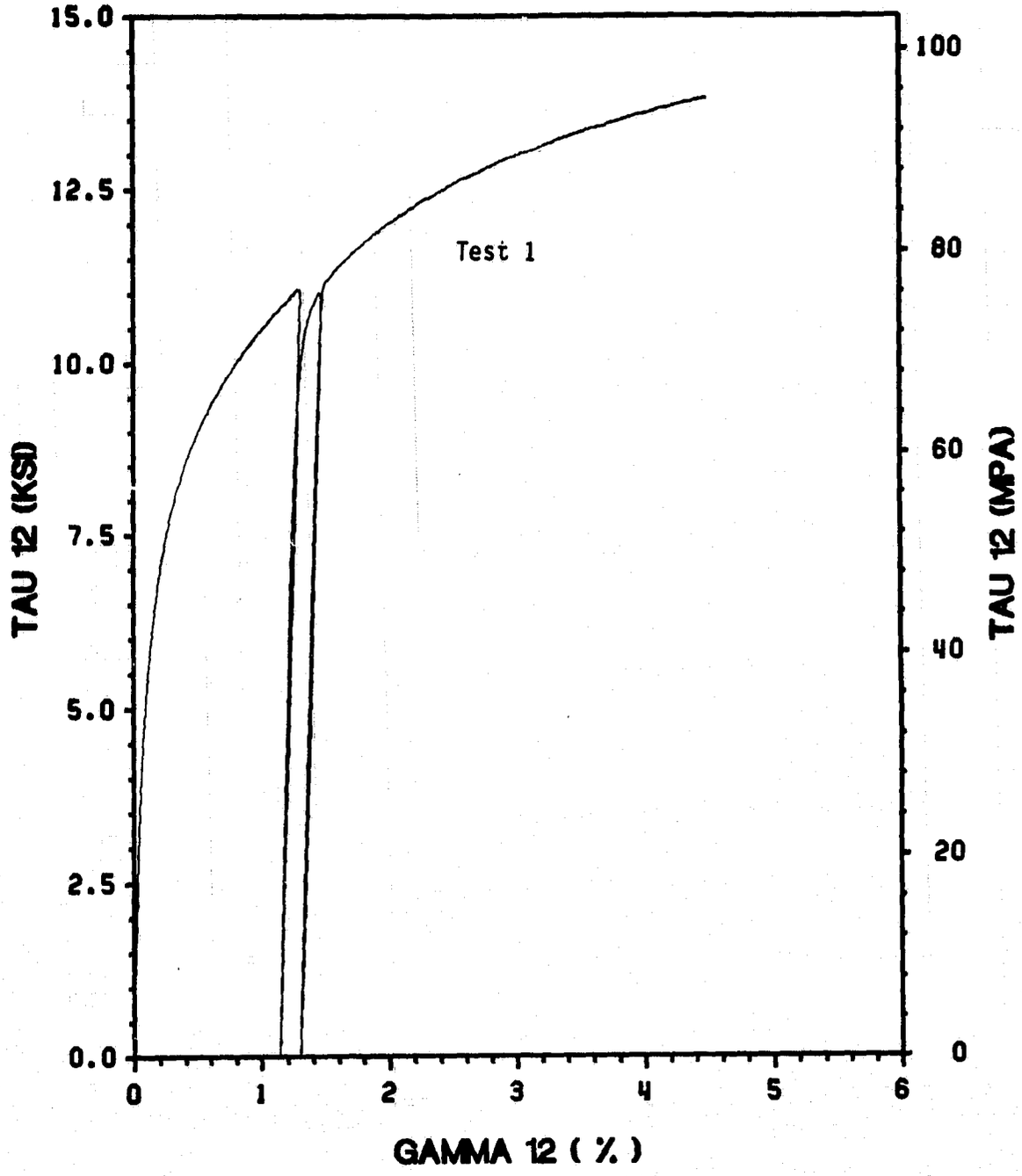

Figure 97. 10° Off-Axis Tests: In-Plane Shear Response

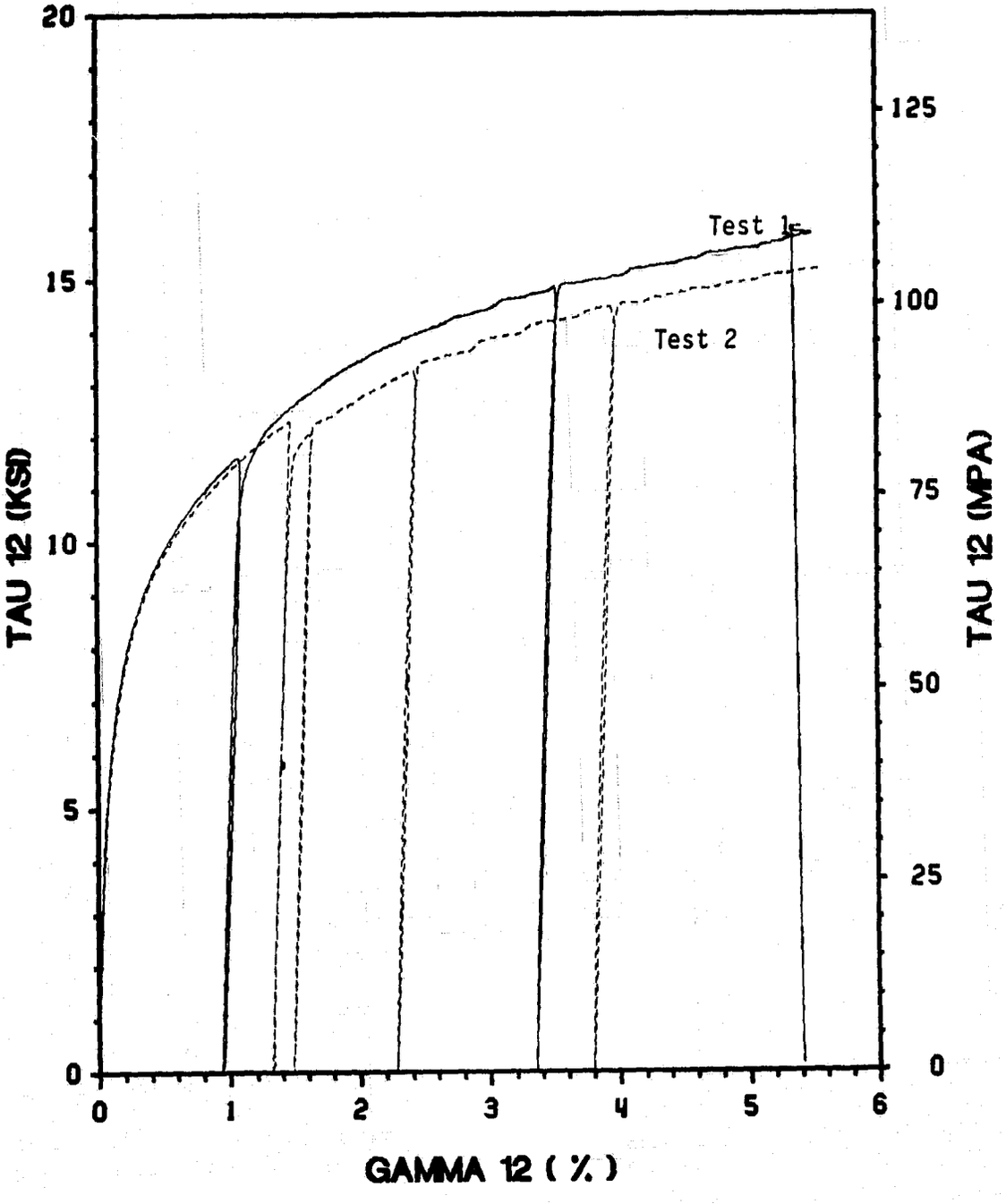

Figure 98. 15° Off-Axis Tests: In-Plane Shear Response

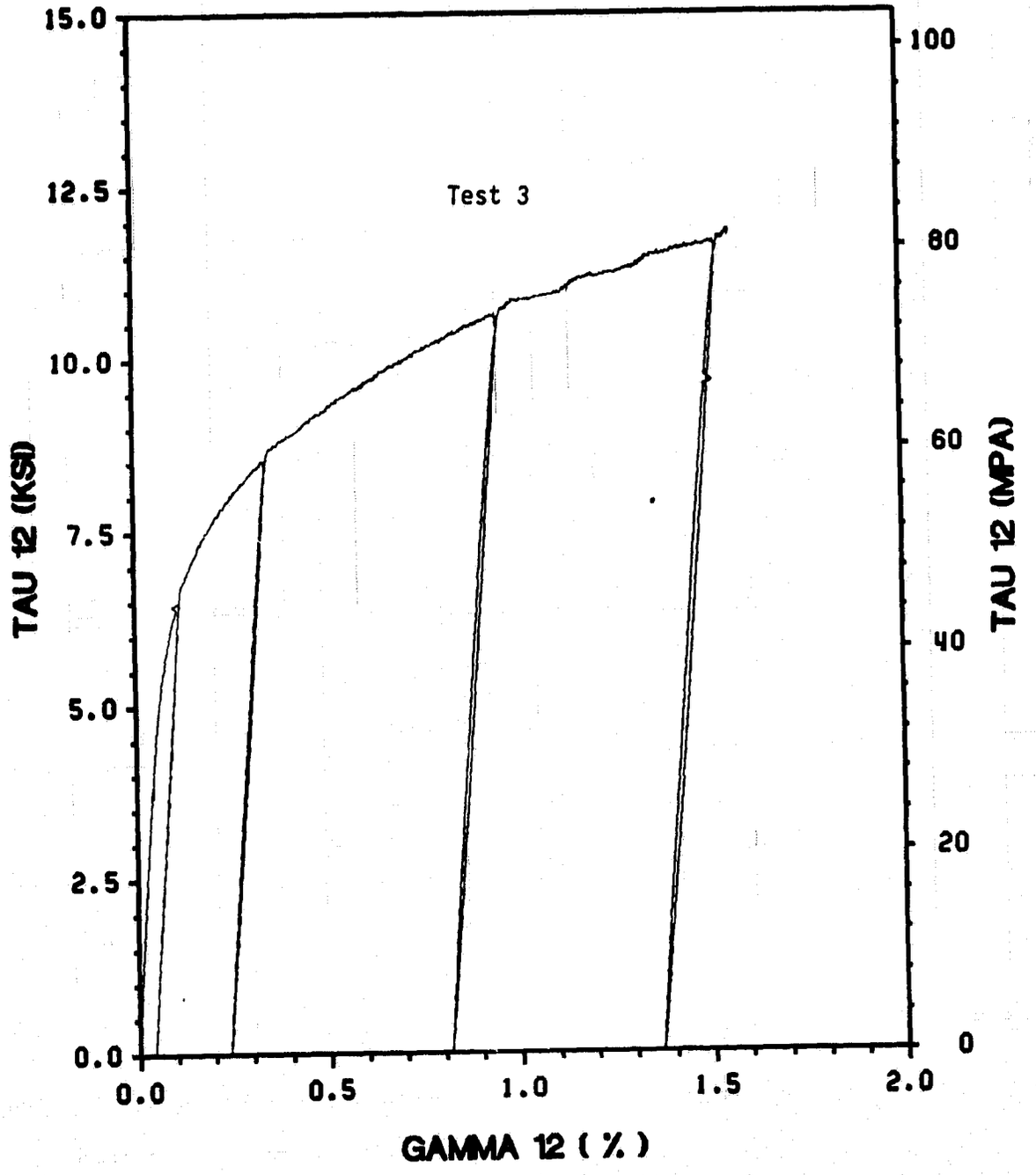

Figure 99. 30° Off-Axis Tests: In-Plane Shear Response

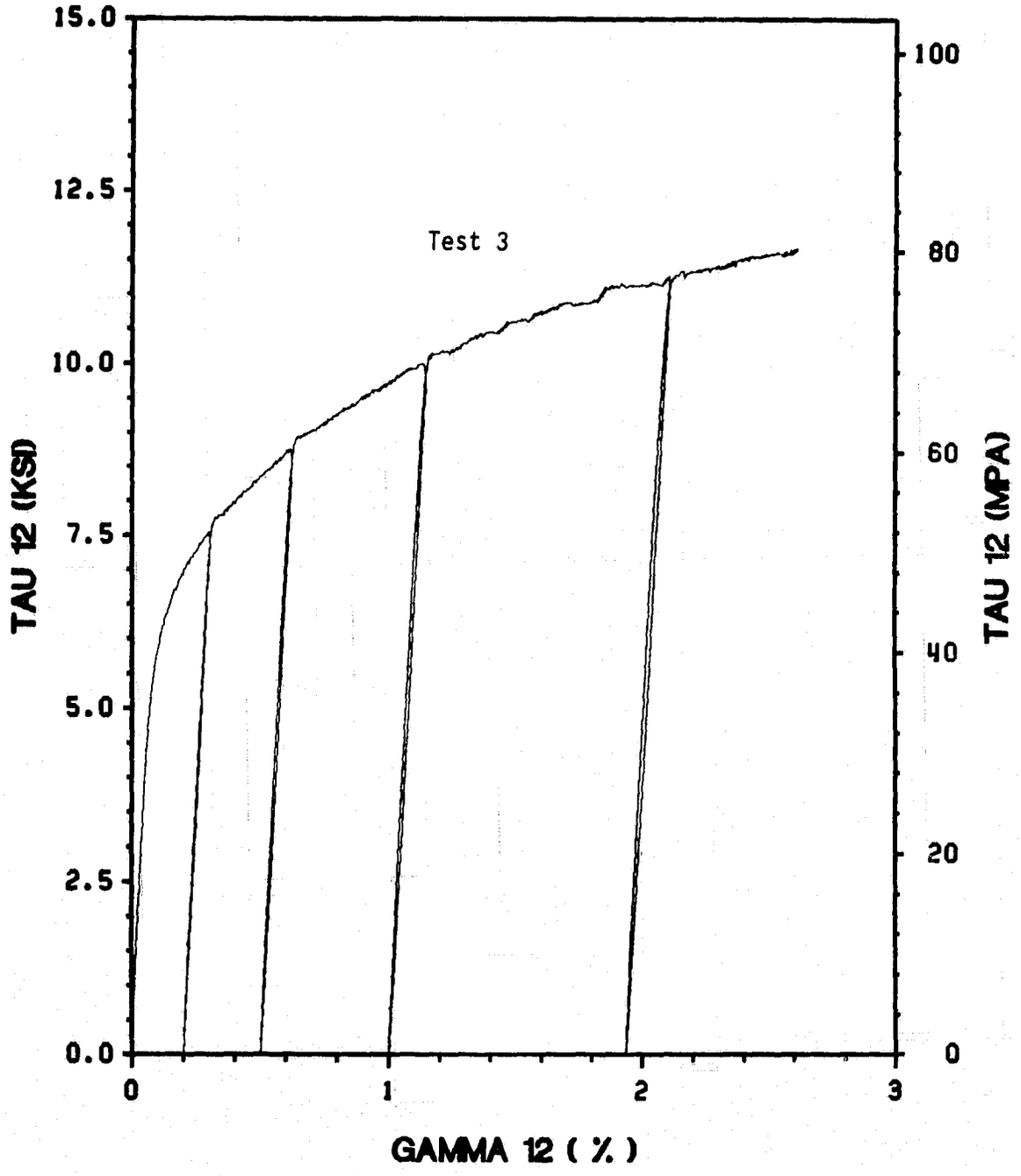

Figure 100. 45° Off-Axis Tests: In-Plane Shear Response

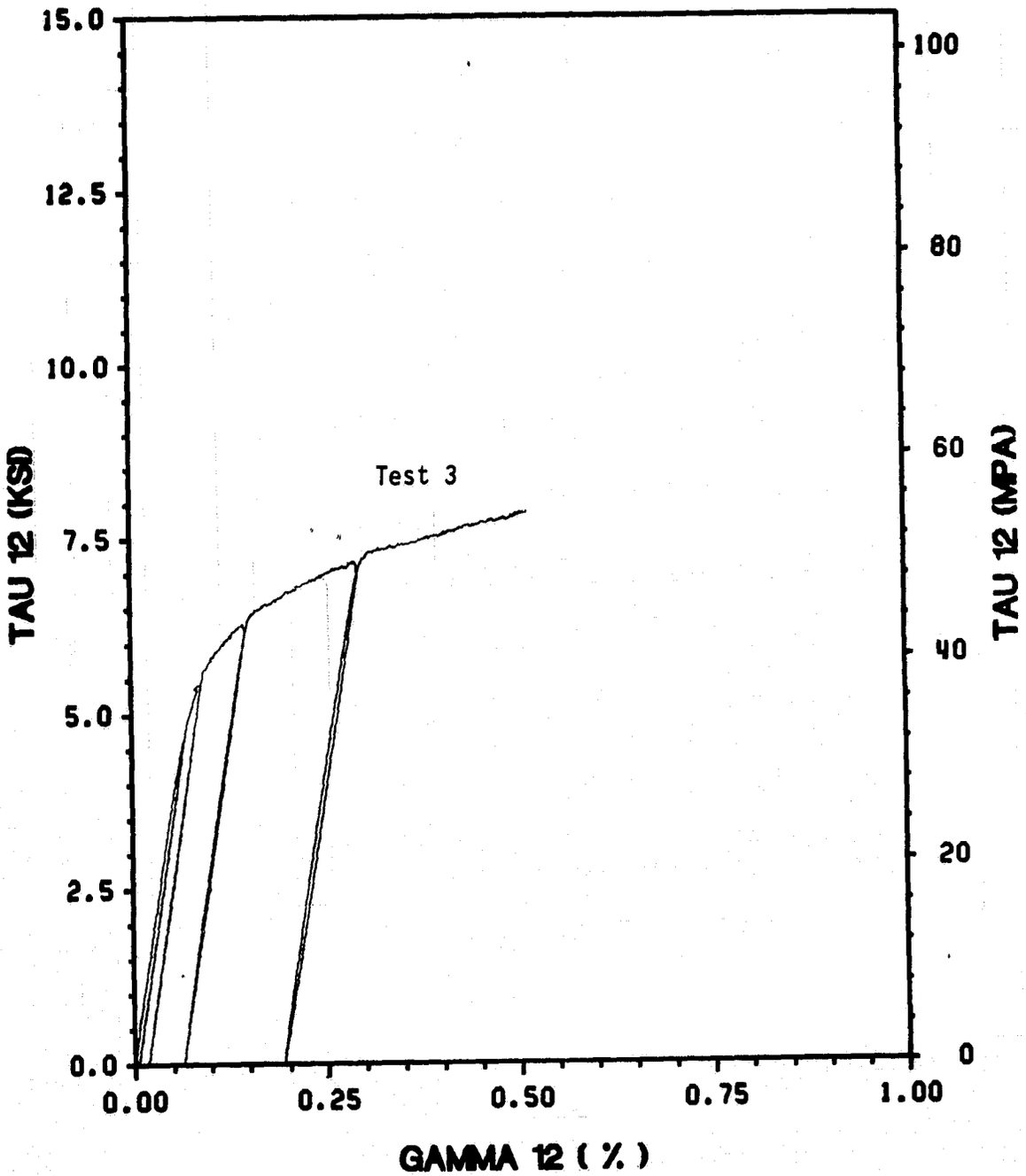

Figure 101. 60° Off-Axis Tests: In-Plane Shear Response

Appendix B. Individual Off-Axis Compression Test Results

Table B.1 Individual Off-Axis Compression Test Results: Material Properties

Specimen Group	Specimen Number	Elastic Modulus, E_{xx}(msi)	Poisson's Ratio, ν_{xy}	Shear Modulus, G_{12}(msi)	Ultimate Stress, σ^U_{xx}(ksi)	Ultimate Strain, ε^U_{xx}(%)
0° monotonic						
	2	33.82	0.426	*	181.3	0.581
	3	32.55	0.415	*	207.4	0.658
cyclic						
	1	33.43	****	*	207.8	0.670
	mean	33.27	0.421	*	194.4***	0.610***
10° monotonic						
	2	32.81	0.305	10.81	206.3	0.845
	3	31.67	0.360	8.47	161.5	0.696
cyclic						
	1	31.82	****	11.87	171.6	0.652
	mean	32.10	0.333	10.38	183.9***	0.771***
15° cyclic						
	1	31.21	0.465	9.71	128.8	0.740
	mean	31.21	0.465	9.71	128.8	0.740
30° monotonic						
	1	26.70	0.373	10.45	79.0	1.872
	2	27.30	0.372	9.19	79.8	2.339
	mean	27.00	0.373	9.82	79.4***	2.106***
45° monotonic						
	1	23.44	0.396	7.94	55.7#	7.814#
	mean	23.44	0.396	7.94	55.7#	7.814#

Table B.1 Individual Off-axis Compression Test Results: Material Properties (continued)

Specimen Group	Specimen Number	Elastic Modulus, E_{xx}(msi)	Poisson's Ratio, ν_{xy}	Shear Modulus, G_{12}(msi)	Ultimate Stress, σ^{U}_{xx}(ksi)	Ultimate Strain, ε^{U}_{xx}(%)
90° monotonic						
	1	21.59	0.116	*	44.8	2.685
	2	18.57	0.104	*	44.7	2.748
	3	21.60	0.199	*	46.4	2.344
	mean	20.44	0.140	*	45.3***	2.592***

* Not applicable
** Grip Failure
*** Only monotonic data included in average
**** Data not available
\# No Failure

Table B.2 Individual Off-axis Compression Test Results: Yield Point obtained from the Stress-Strain Response

Specimen Group	Specimen Number	Yield Stress $\bar{\sigma}^{y}_{xx}$(ksi)	Yield Strain ε^{y}_{xx}(%)	Yield Stress τ_{12}(ksi)	Yield Strain γ_{12}(%)
0° monotonic					
	1	48.20	0.148	*	*
	2	39.75	0.118	*	*
	3	52.88	0.151	*	*
	mean	46.94	0.139	*	*
10° monotonic					
	1	****	****	****	****
	2	31.29	0.087	5.35	0.061
	3	34.59	0.112	6.49	0.085
	mean	32.94	0.099	5.92	0.073
15° monotonic					
	1	26.06	0.087	6.50	0.094
	mean	26.06	0.087	6.50	0.094
30° monotonic					
	1	6.97	0.026	3.02	0.045
	2	7.18	0.031	3.46	0.041
	mean	7.08	0.029	3.24	0.043
45° monotonic					
	1	****	****	****	****
	mean	****	****	****	****
90° monotonic					
	1	6.18	0.030	*	*
	2	5.37	0.030	*	*
	3	6.20	0.029	*	*
	mean	5.92	0.030	*	*

* Not applicable
** Grip Failure
*** Only monotonic data included in average
**** Data not available

Table B.3 Individual Off-axis Compression Test Results: Yield Point obtained from the Poisson's Response

Specimen Group	Specimen Number	Yield Stress $\bar{\sigma}^{y}_{xx}$(ksi)	Yield Strain ε^{y}_{xx}(%)	Yield Stress τ^{y}_{12}(ksi)	Yield Strain γ^{y}_{12}(%)
0° monotonic					
	1	34.96	0.107	*	*
	2	34.66	0.103	*	*
	3	33.93	0.105	*	*
	mean	34.52	0.105	*	*
10° monotonic					
	1	****	****	****	****
	2	36.05	0.112	6.17	0.081
	3	33.58	0.098	5.17	0.074
	mean	34.81	0.105	5.67	0.077
15° monotonic					
	1	27.66	0.094	6.91	0.094
	mean	27.66	0.094	6.91	0.094
30° monotonic					
	1	8.05	0.031	3.48	0.053
	2	6.89	0.030	2.96	0.039
	mean	7.47	0.031	3.22	0.046
45° monotonic					
	1	****	****	****	****
	mean	****	****	****	****
90° monotonic					
	1	6.18	0.030	*	*
	2	5.37	0.030	*	*
	3	6.20	0.029	*	*
	mean	5.92	0.030	*	*

* Not applicable
** Grip Failure
*** Only monotonic data included in average
**** Data not available

Table B.4 Individual Off-axis Compression Test Results: Yield Point obtained from the Shear Response

Specimen Group	Specimen Number	Yield Stress $\bar{\sigma}^{y}_{xx}$(ksi)	Yield Strain ε^{y}_{xx}(%)	Yield Stress τ^{y}_{12}(ksi)	Yield Strain γ^{y}_{12}(%)
0° monotonic					
	1	*	*	*	*
	2	*	*	*	*
	3	*	*	*	*
	mean	*	*	*	*
10° monotonic					
	1	****	****	****	****
	2	23.79	0.074	4.07	0.051
	3	25.81	0.084	4.41	0.063
	mean	24.80	0.079	4.24	0.057
15° monotonic					
	1	25.16	0.085	6.29	0.085
	mean	25.16	0.085	6.29	0.085
30° monotonic					
	1	4.63	0.017	1.97	0.026
	2	5.39	0.025	2.33	0.032
	mean	5.01	0.021	2.15	0.029
45° monotonic					
	1	****	****	****	****
	mean	****	****	****	****
90° monotonic					
	1	*	*	*	*
	2	*	*	*	*
	3	*	*	*	*
	mean	*	*	*	*

* Not applicable
** Grip Failure
*** Only monotonic data included in average
**** Data not available

B.1 Monotonic Test Results

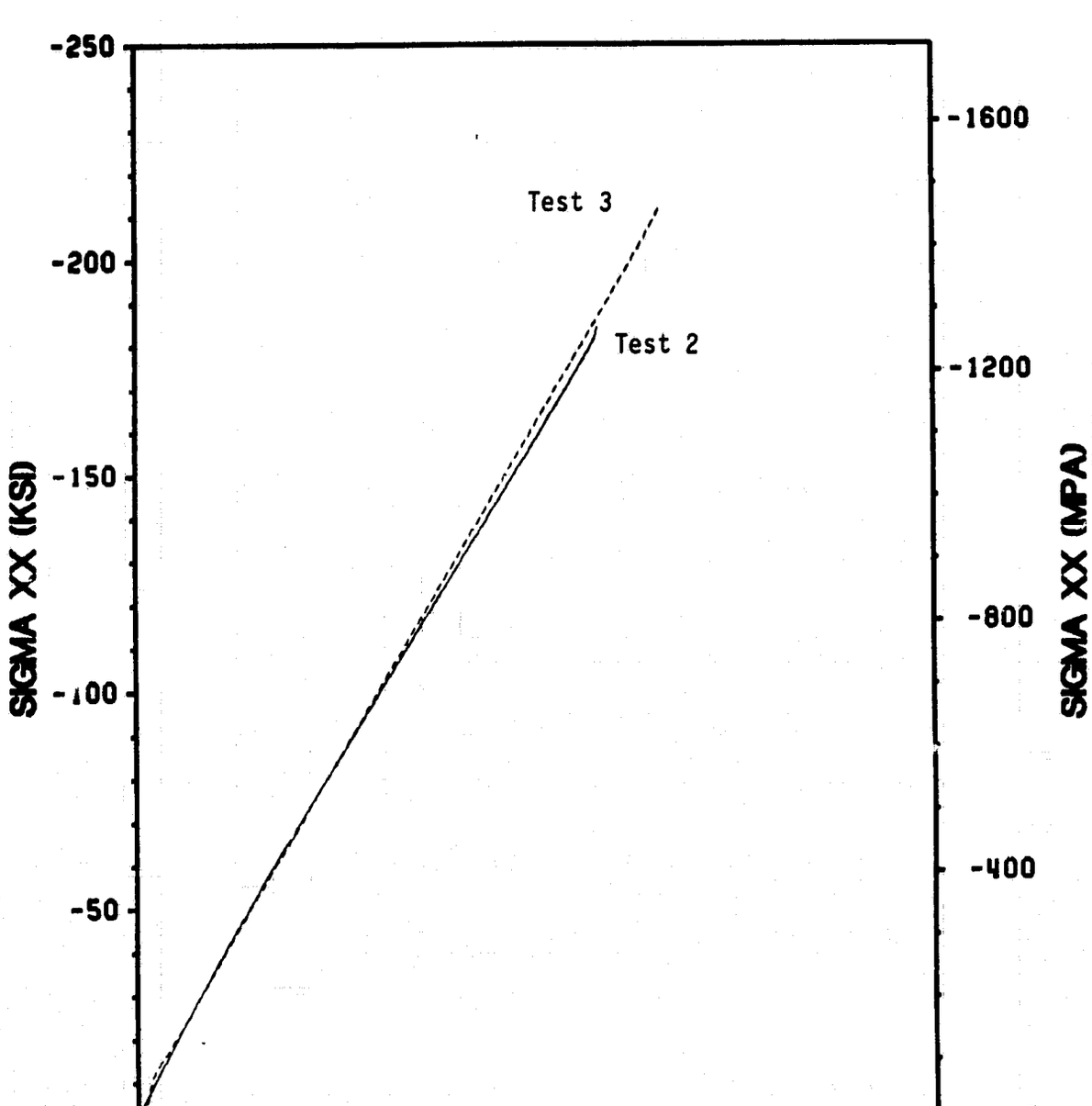

Figure 102. 0° On-Axis Tests: Compressive Stress-Strain Response

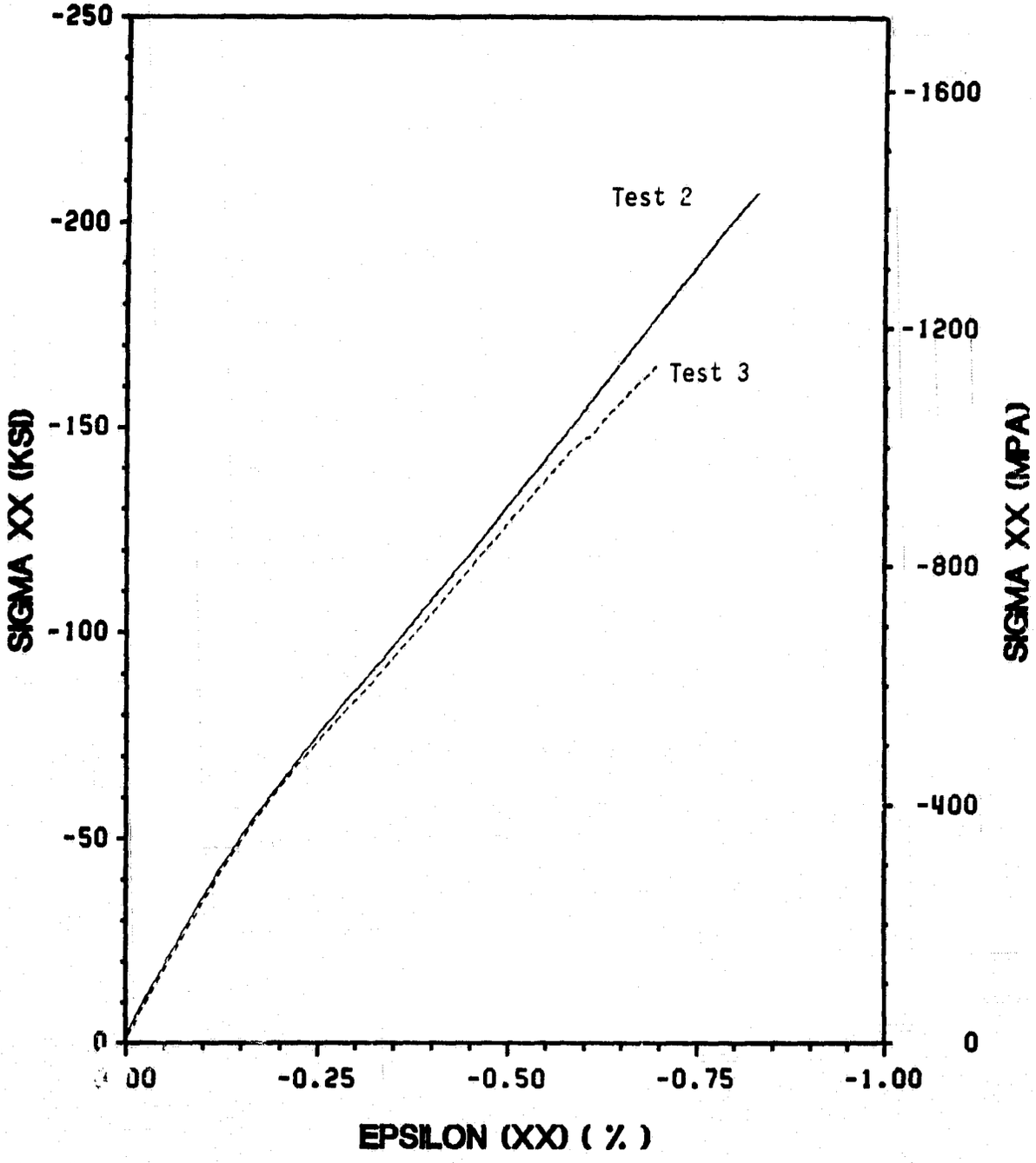

Figure 103. 10° Off-Axis Tests: Compressive Stress-Strain Response

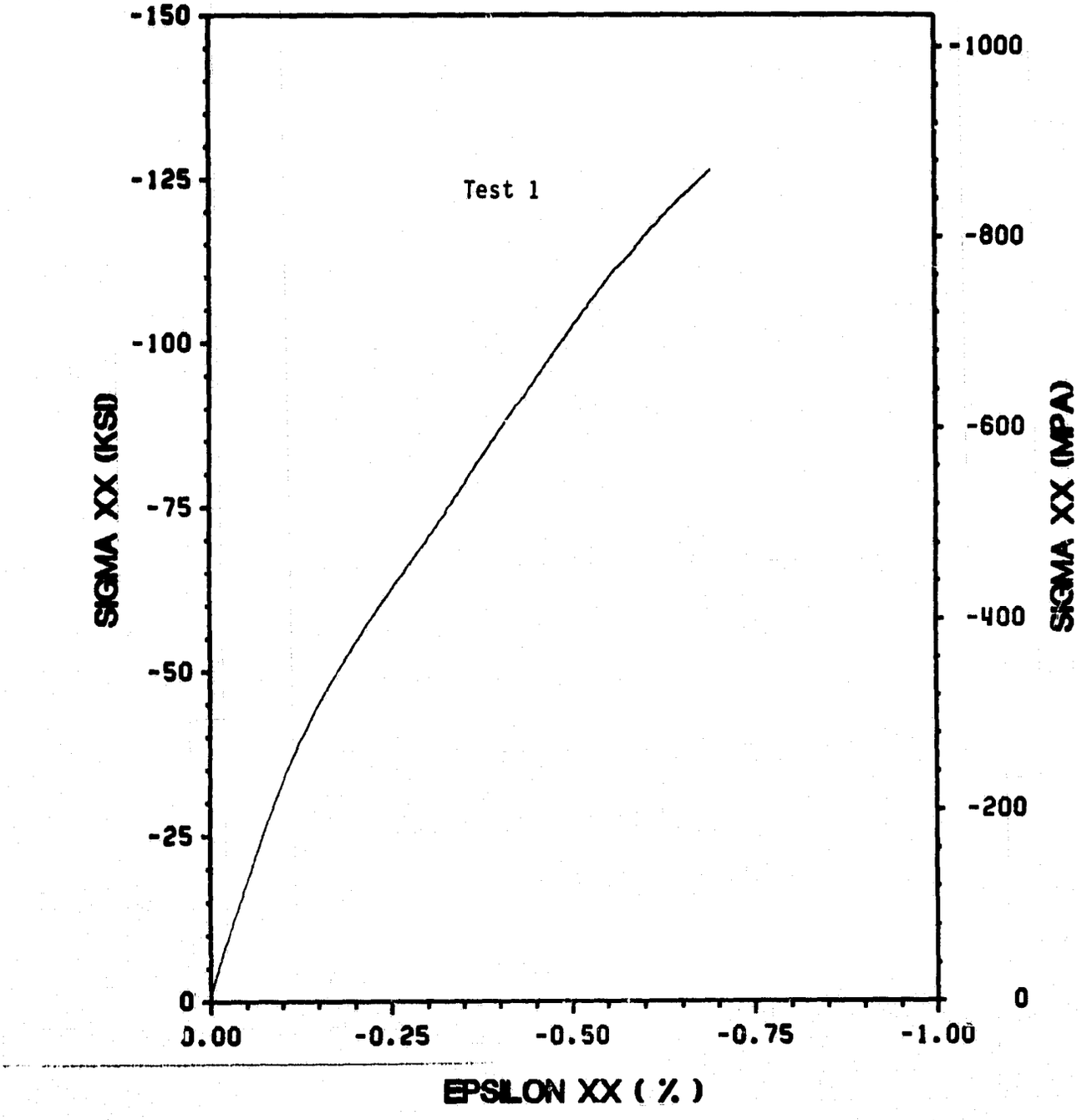

Figure 104. 15° Off-Axis Tests: Compressive Stress-Strain Response

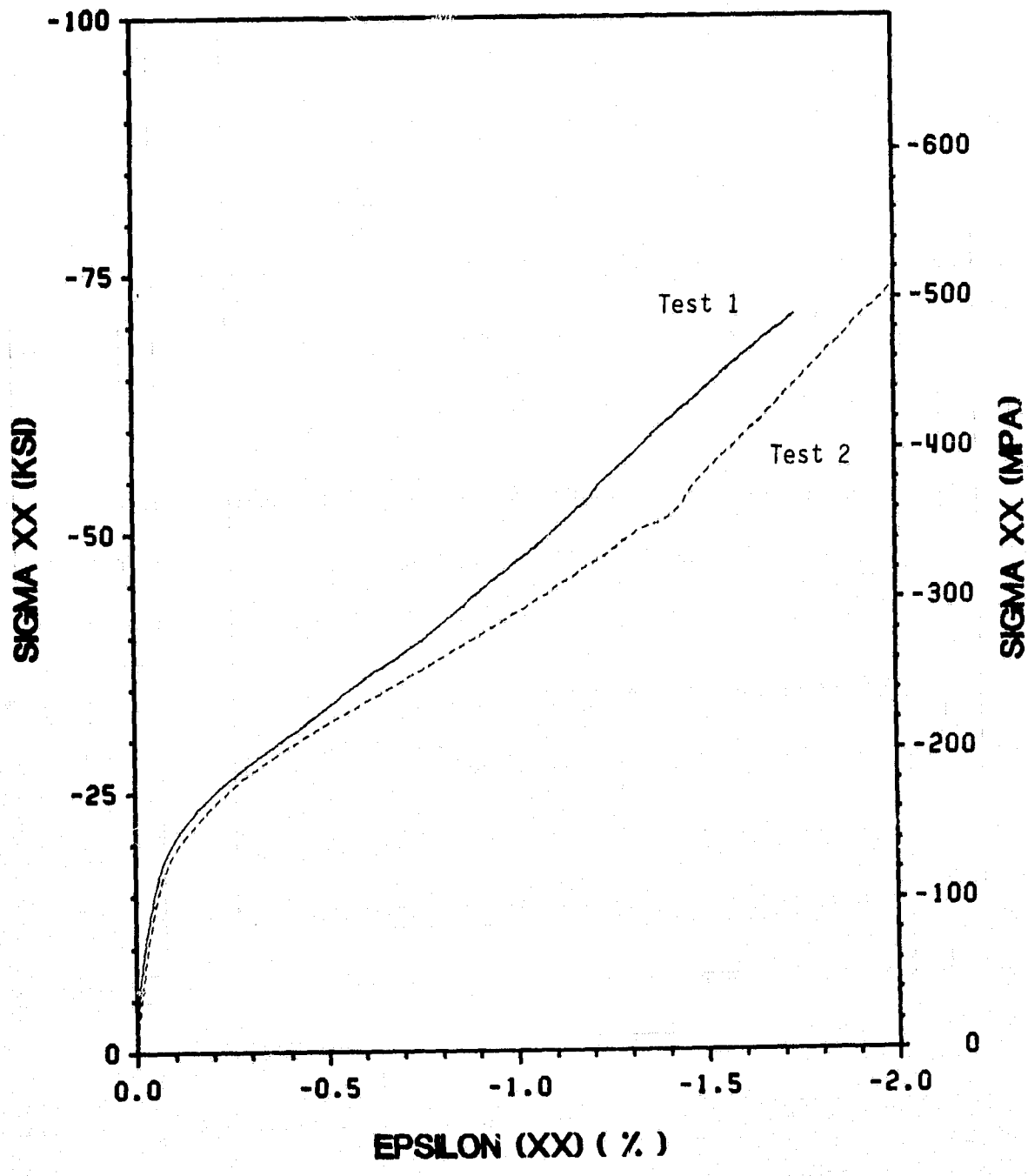

Figure 105. 30° Off-Axis Tests: Compressive Stress-Strain Response

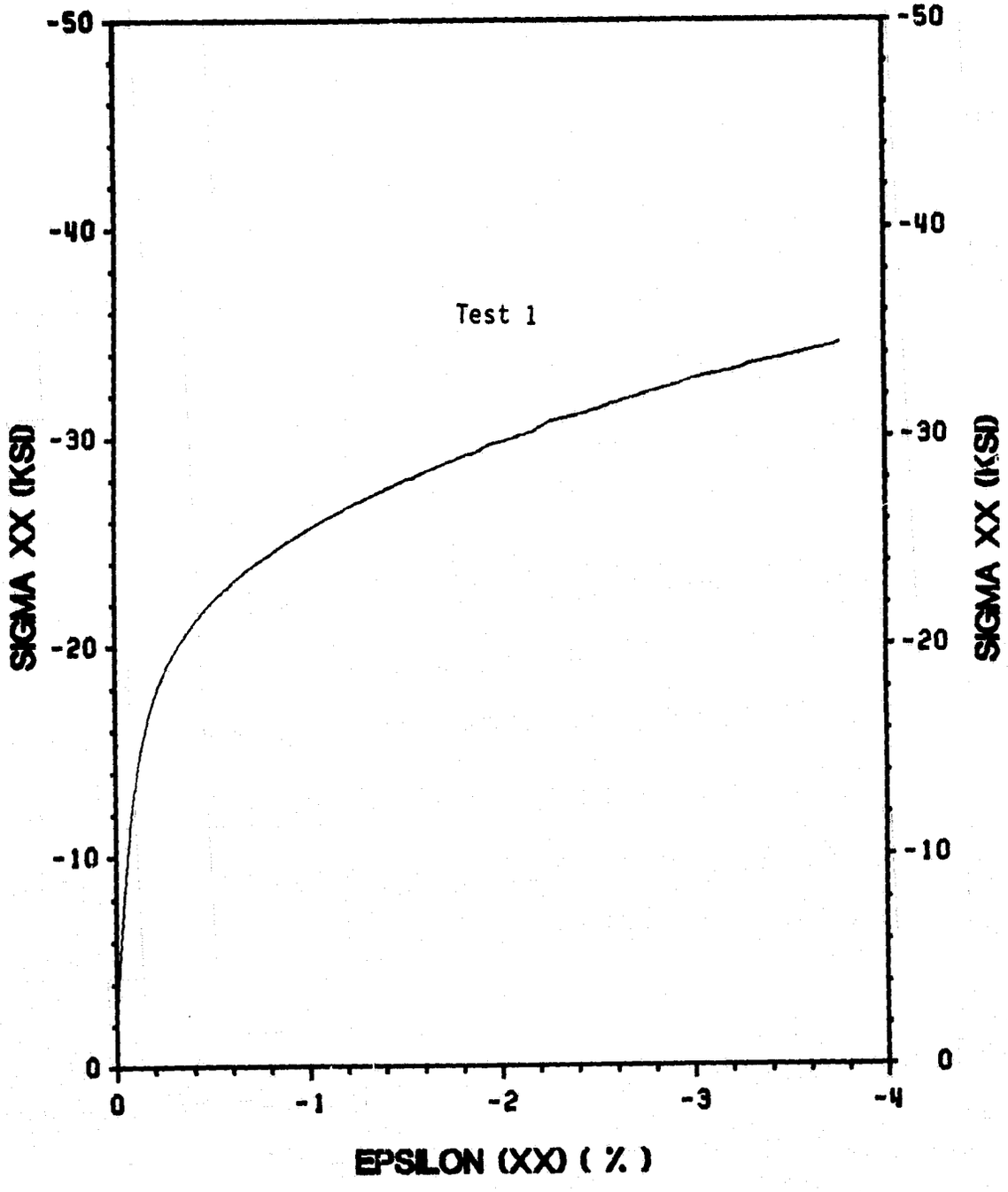

Figure 106. 45° Off-Axis Tests: Compressive Stress-Strain Response

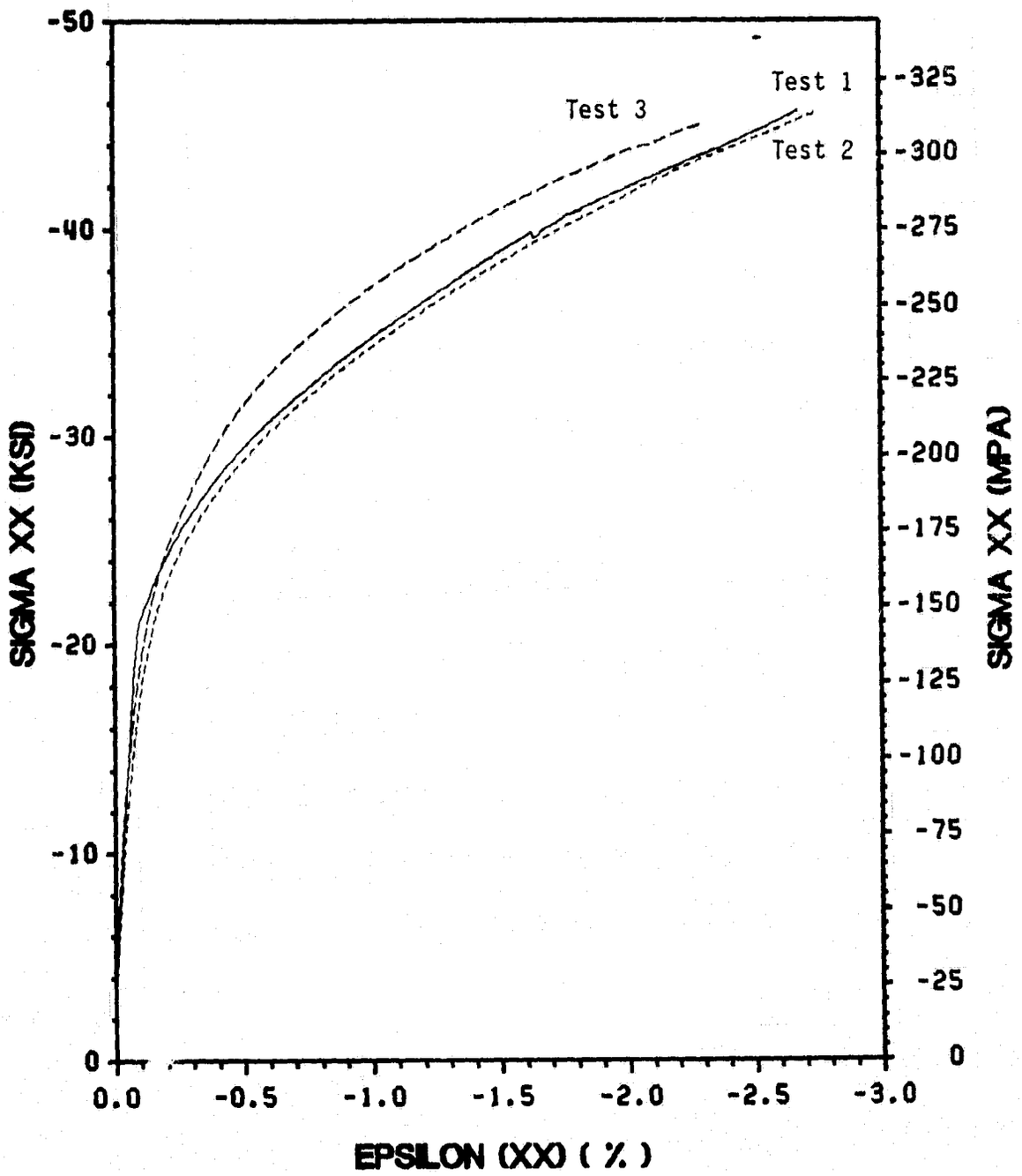

Figure 107. 90° On-Axis Tests: Compressive Stress-Strain Response

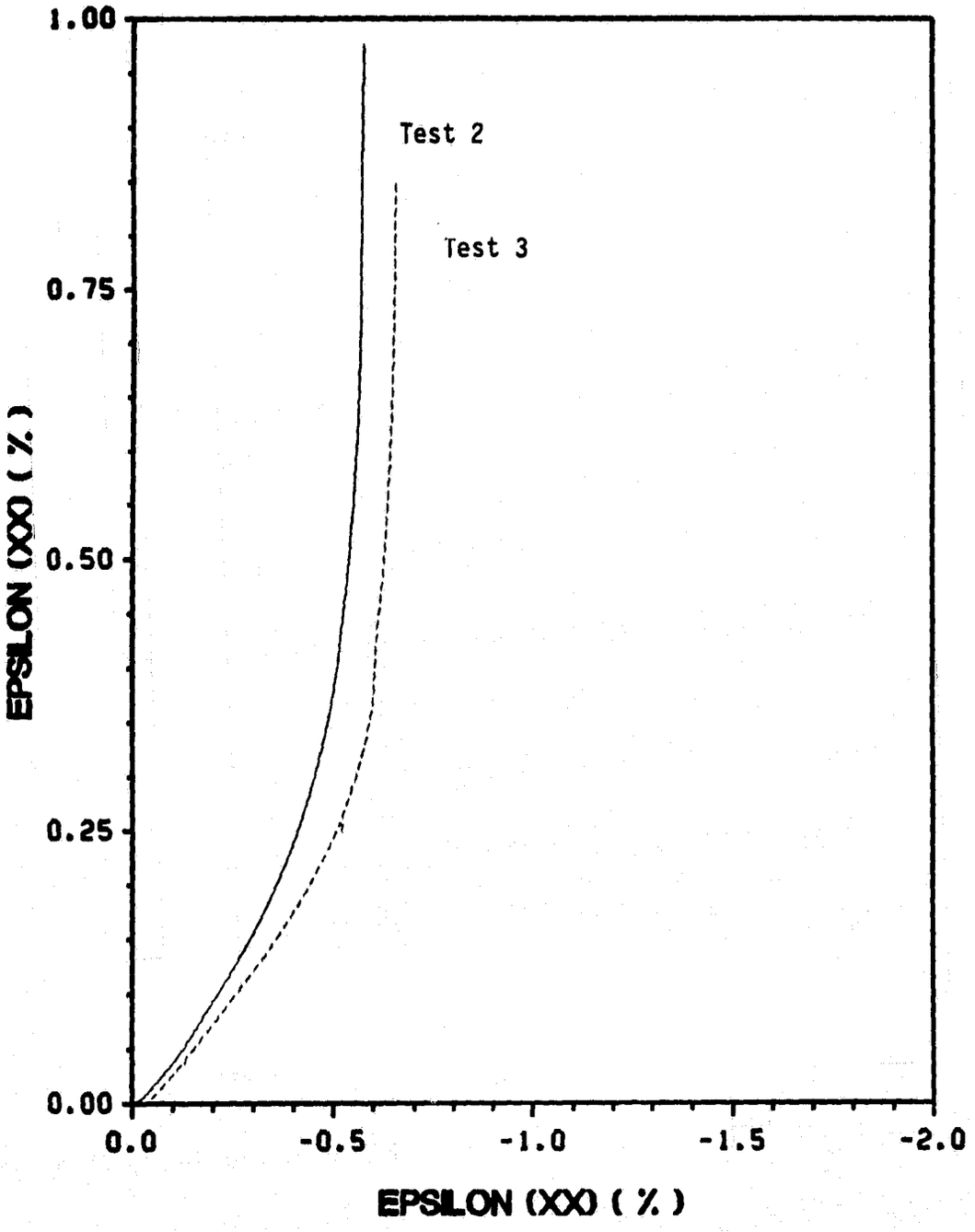

Figure 108. 0° On-Axis Tests: Poisson's Response

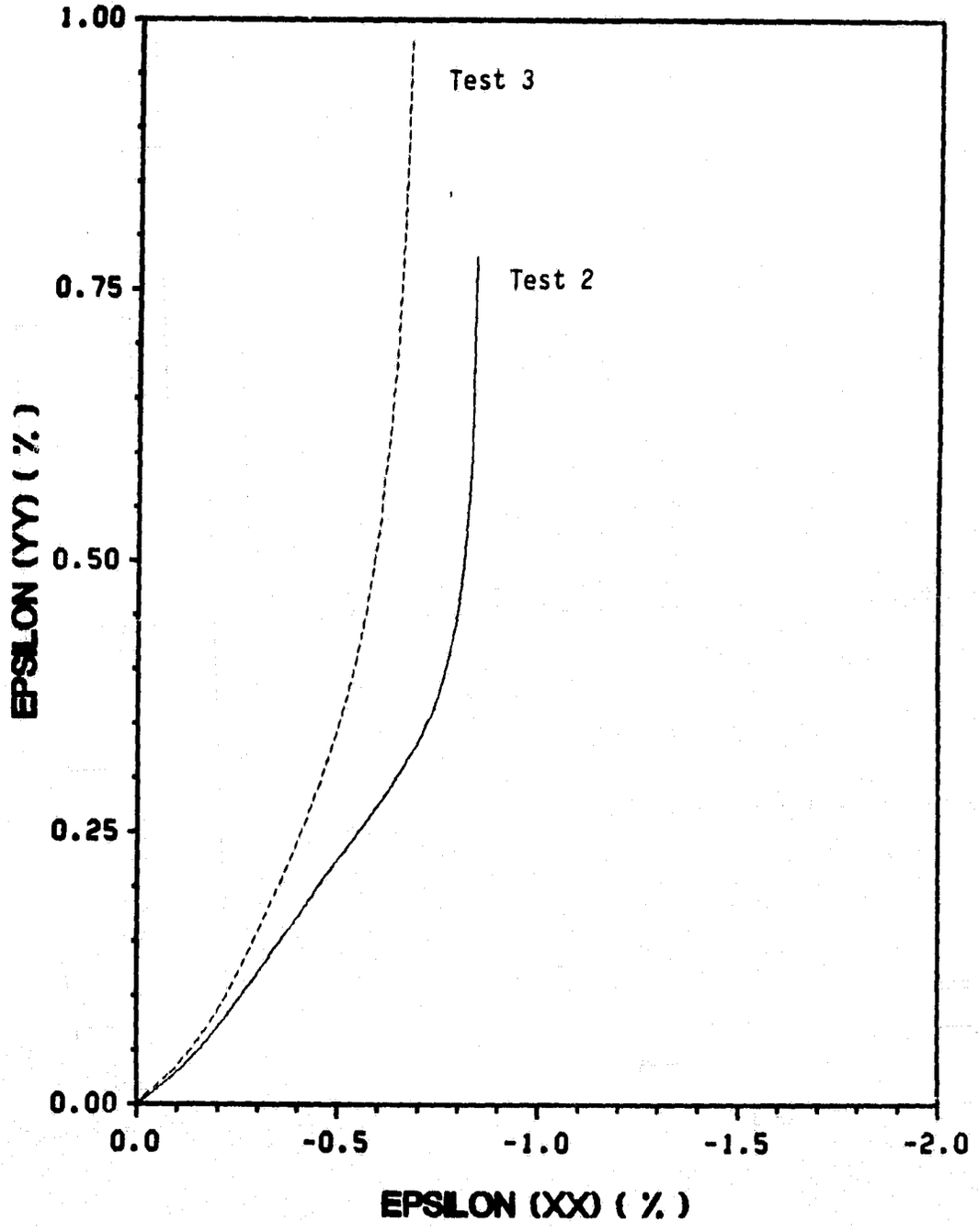

Figure 109. 10° Off-Axis Tests: Poisson's Response

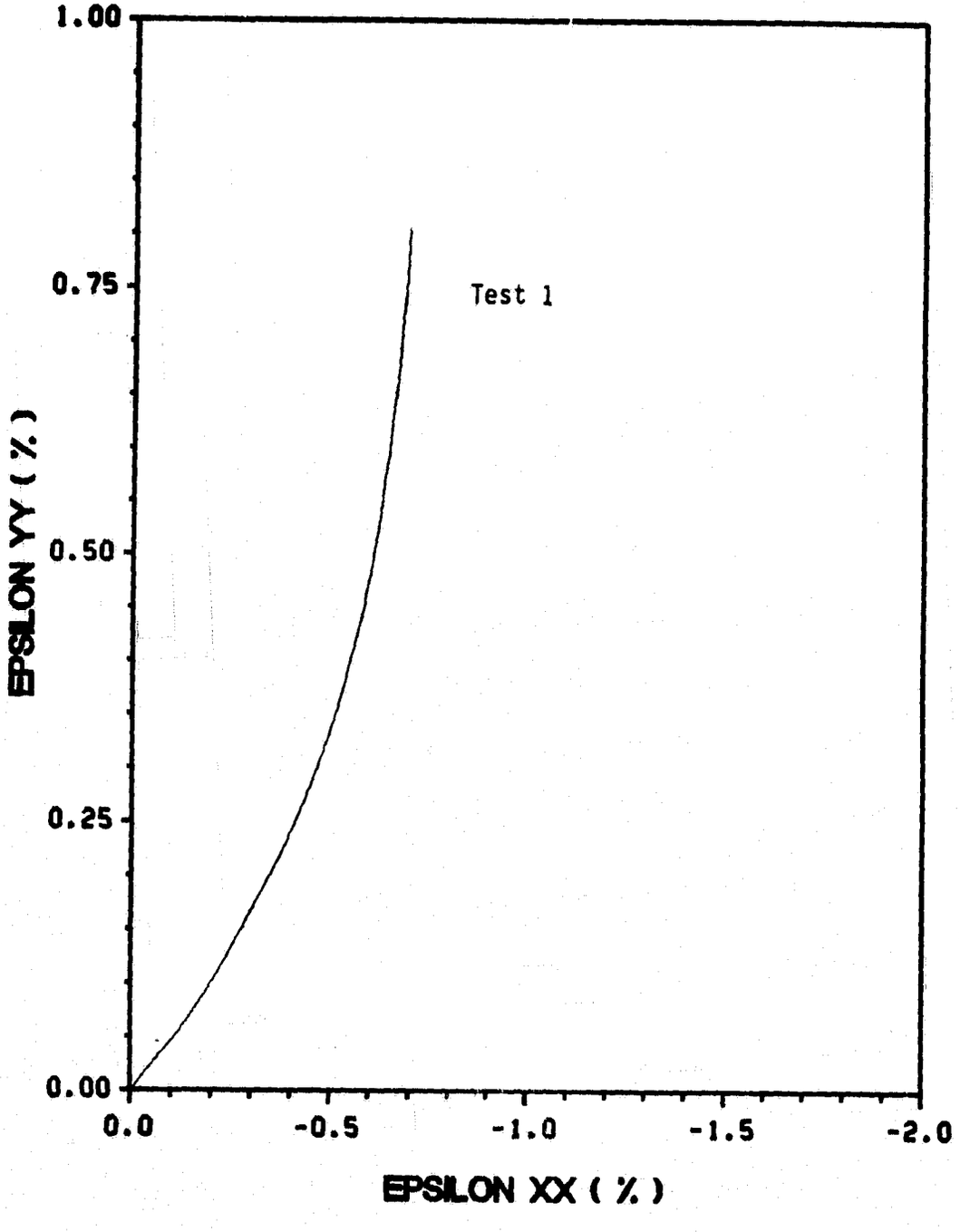

Figure 110. 15° Off-Axis Tests: Poisson's Response

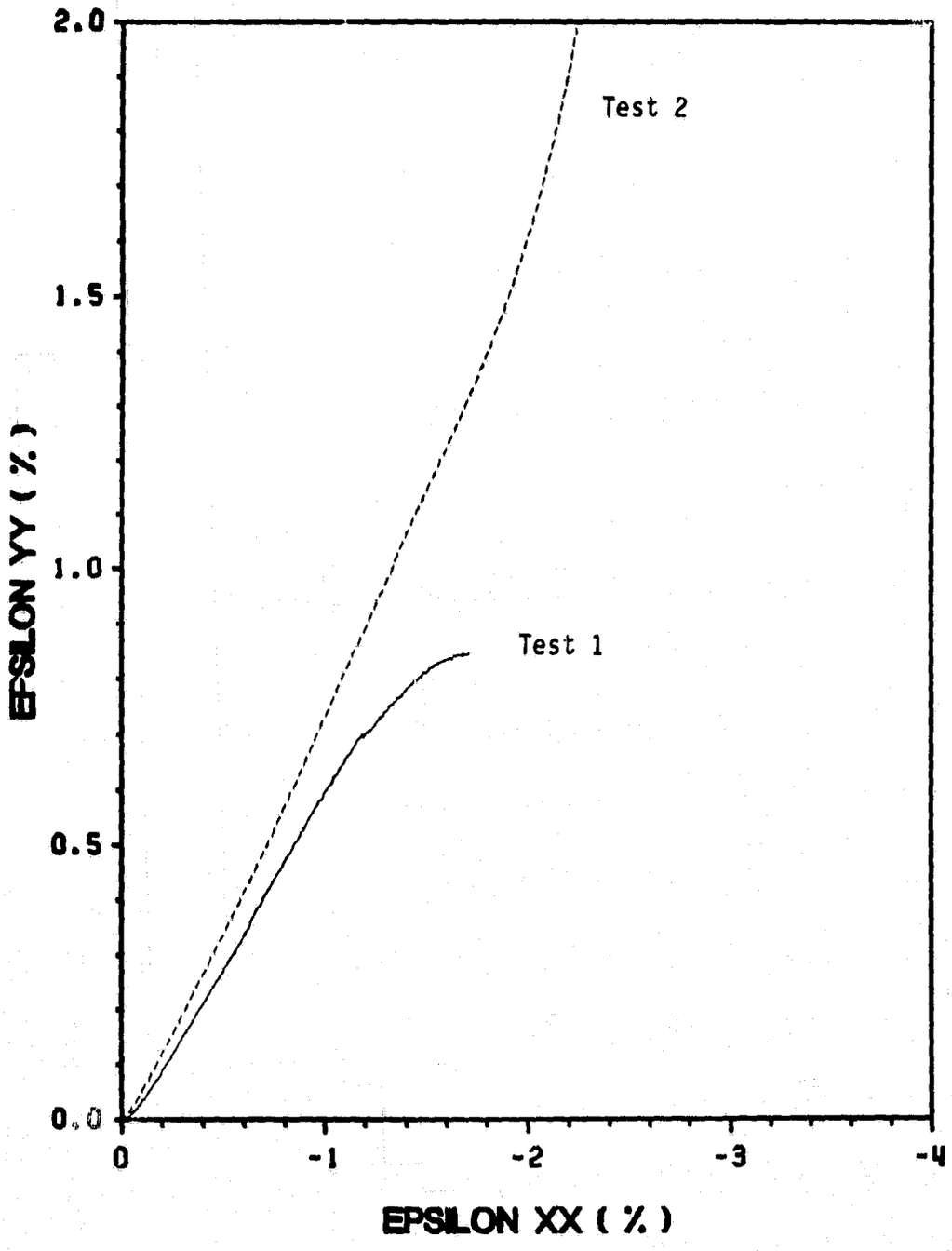

Figure 111. 30° Off-Axis Tests: Poisson's Response

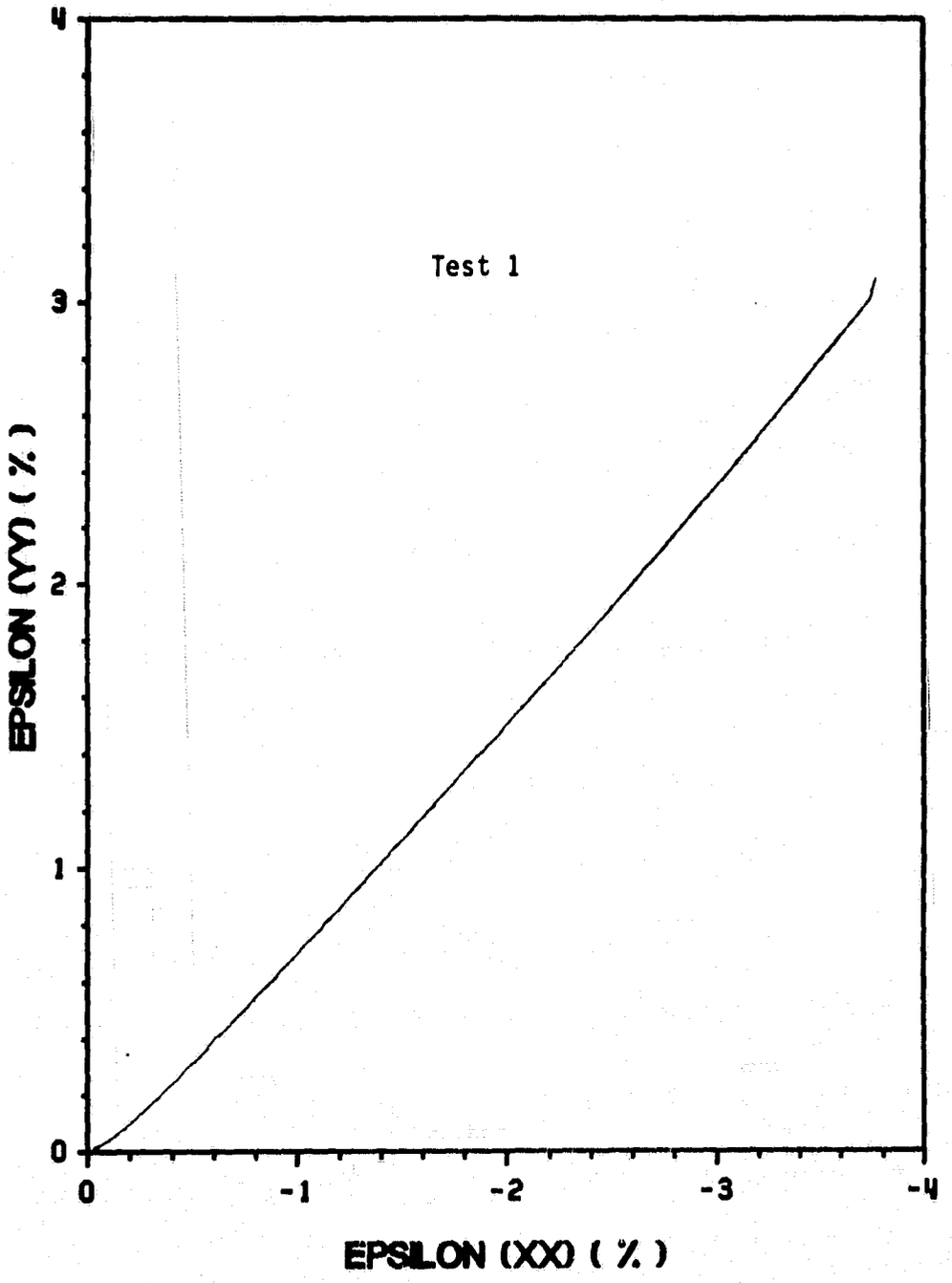

Figure 112. 45° Off-Axis Tests: Poisson's Response

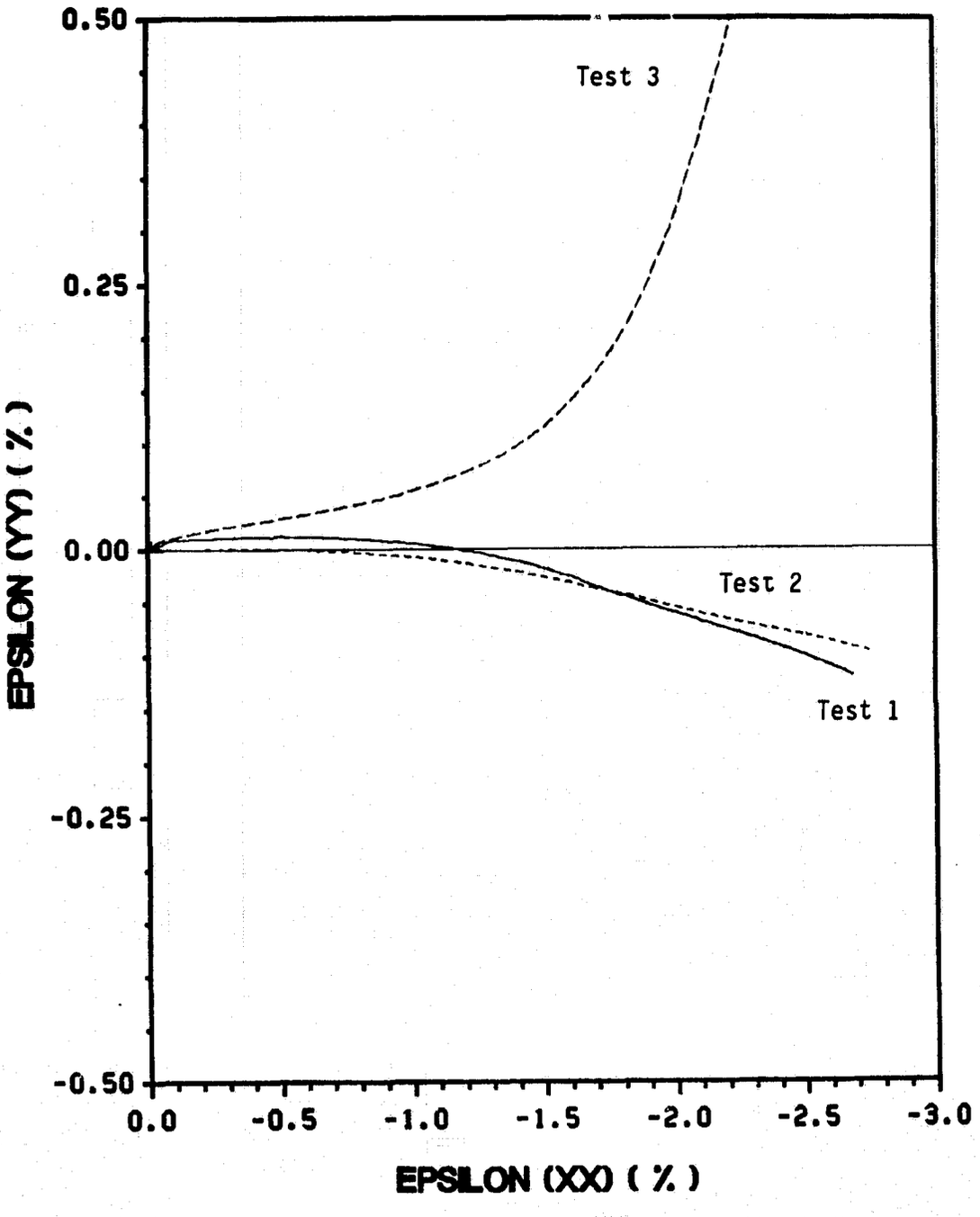

Figure 113. 90° On-Axis Tests: Poisson's Response

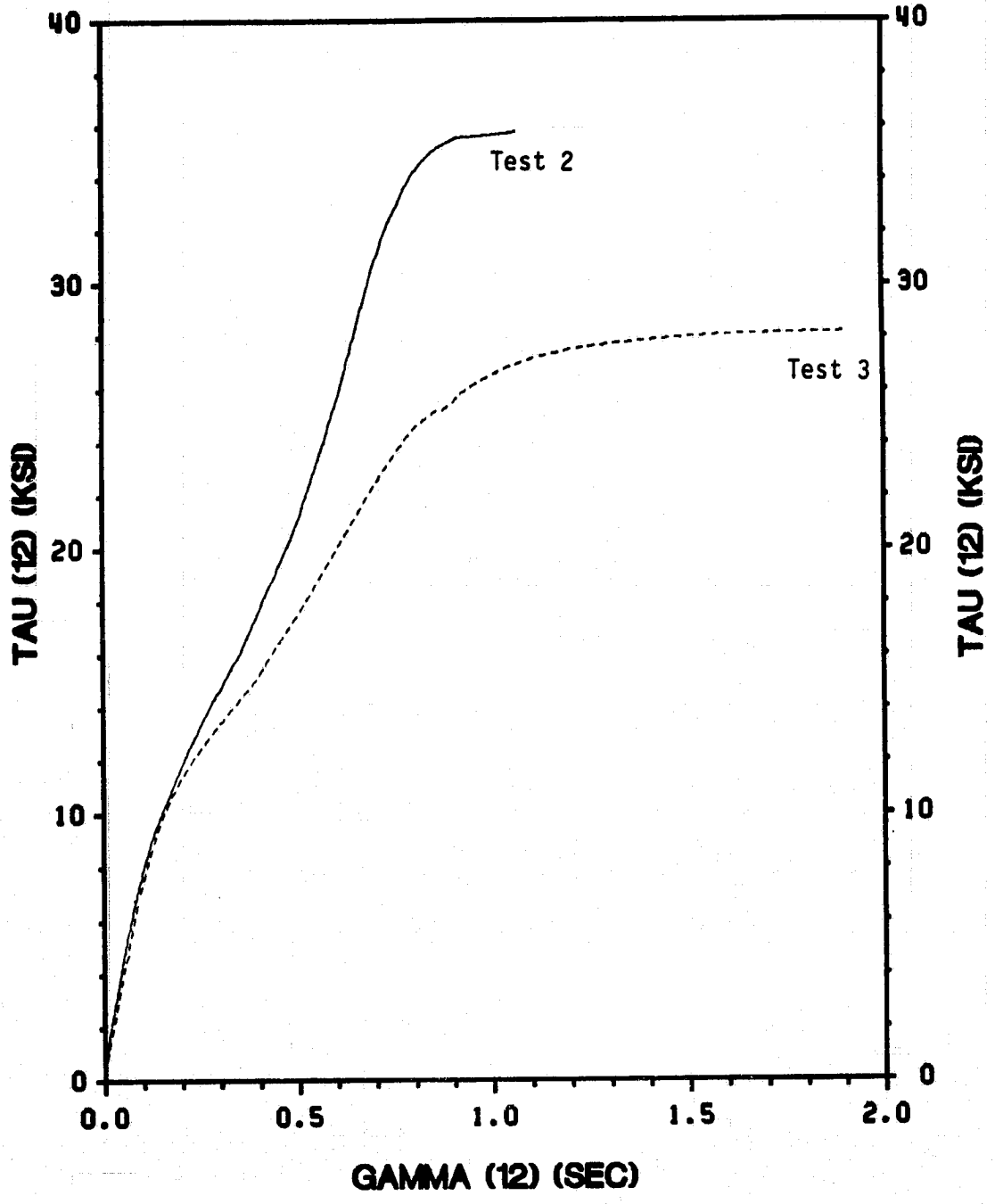

Figure 114. 10° Off-Axis Tests: In-Plane Shear Response

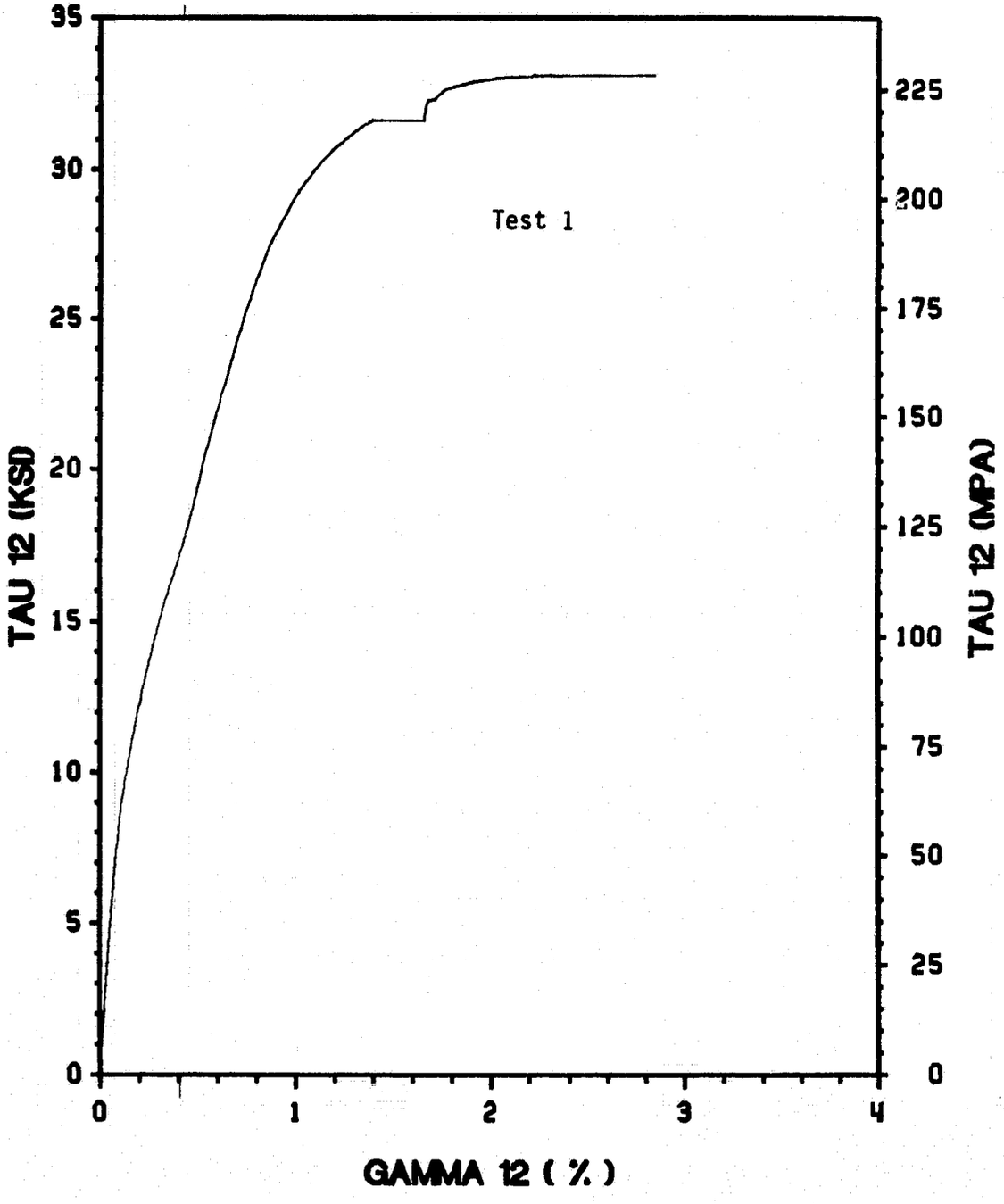

Figure 115. 15° Off-Axis Tests: In-Plane Shear Response

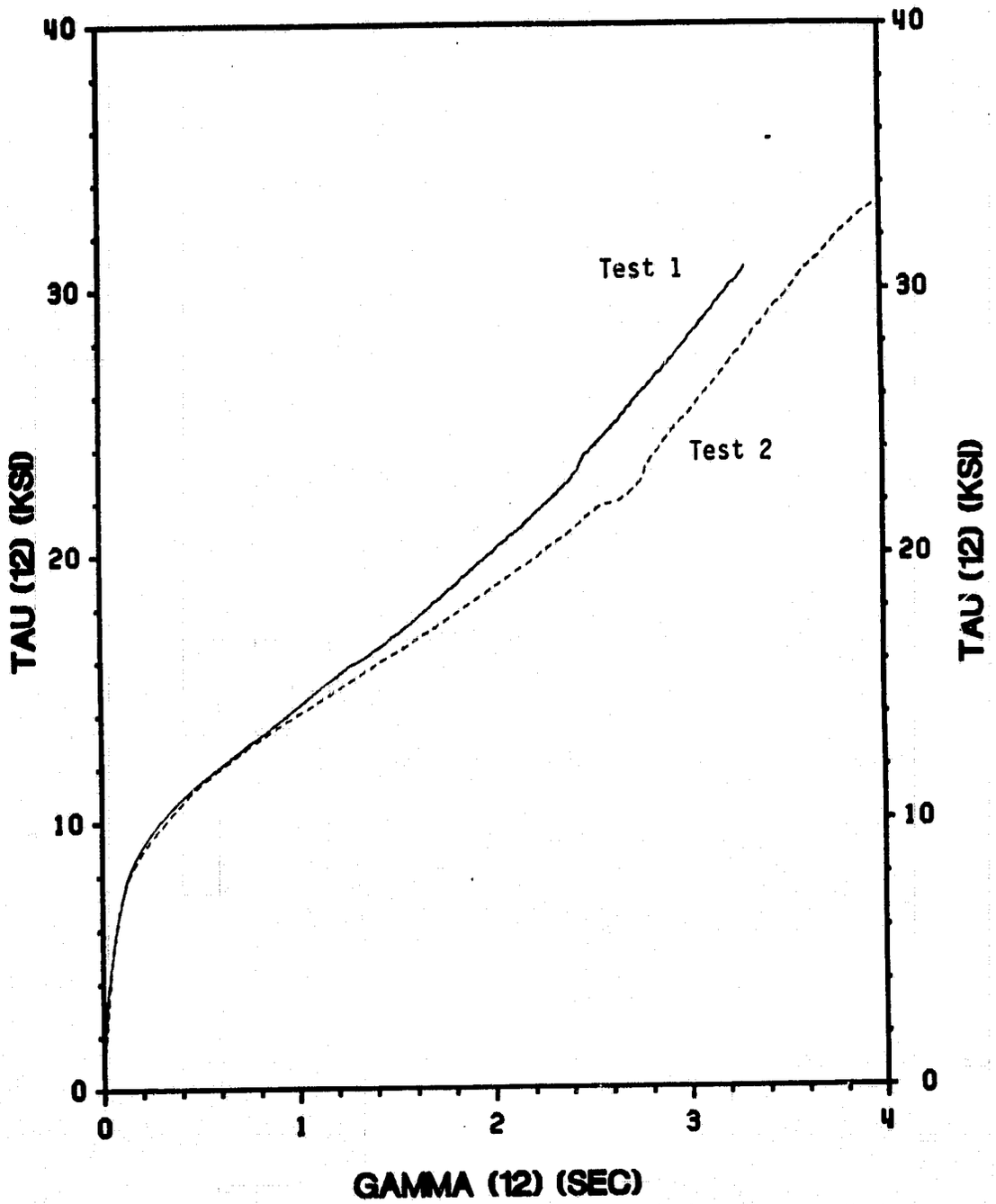

Figure 116. 30° Off-Axis Tests: In-Plane Shear Response

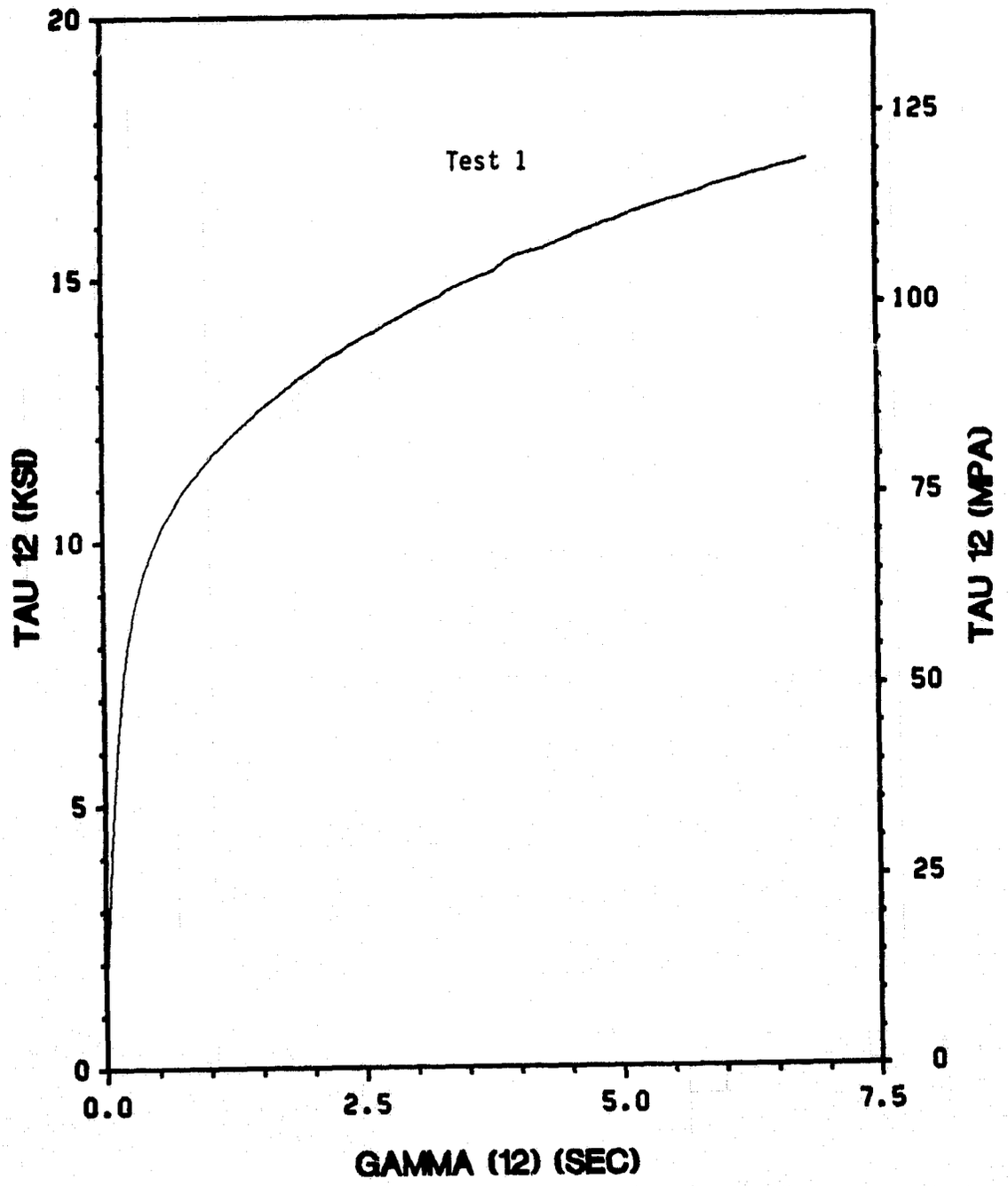

Figure 117. 45° Off-Axis Tests: In-Plane Shear Response

B.2 Cyclic Test Results

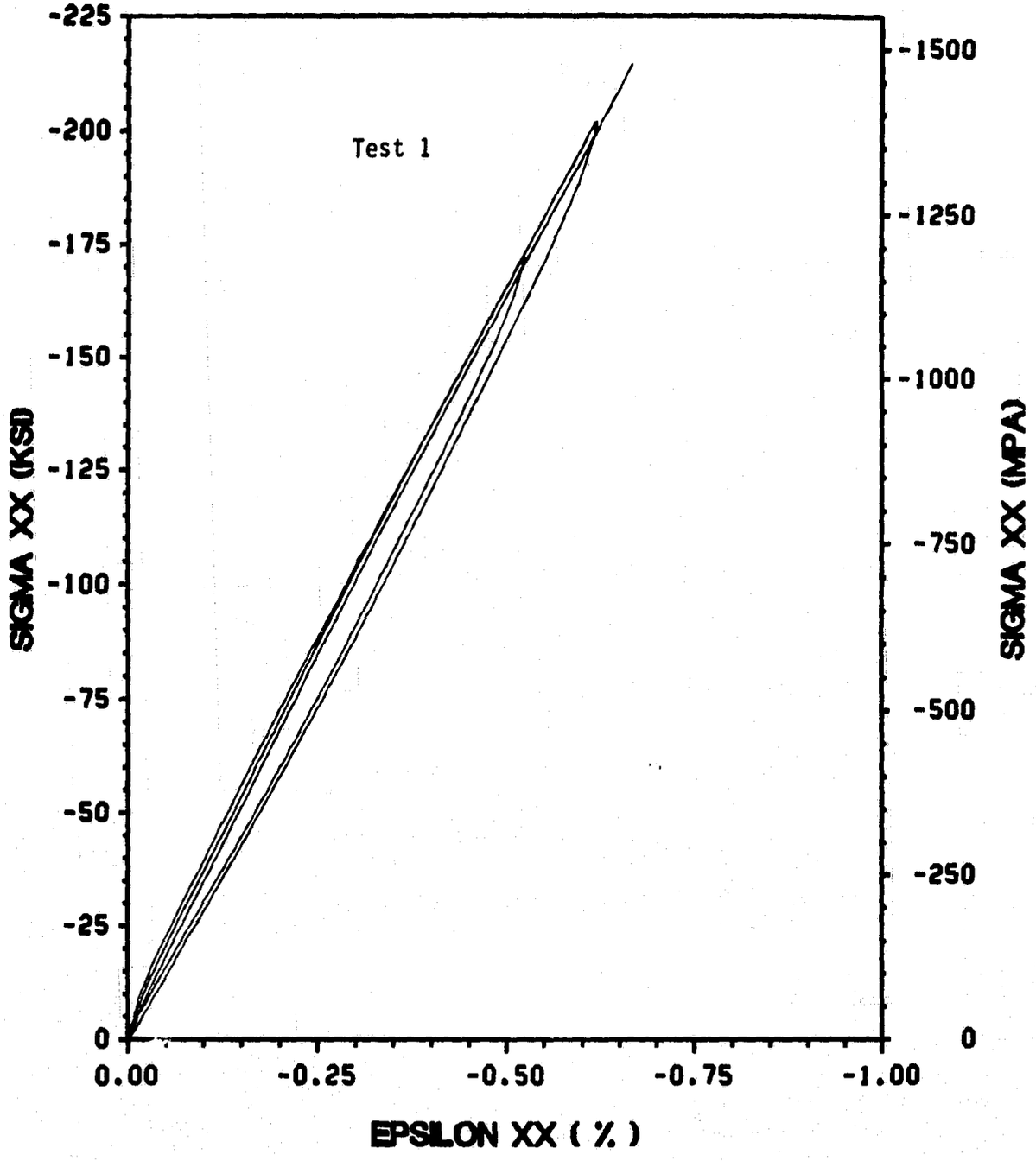

Figure 118. 0° On-Axis Tests: Compressive Stress-Strain Response

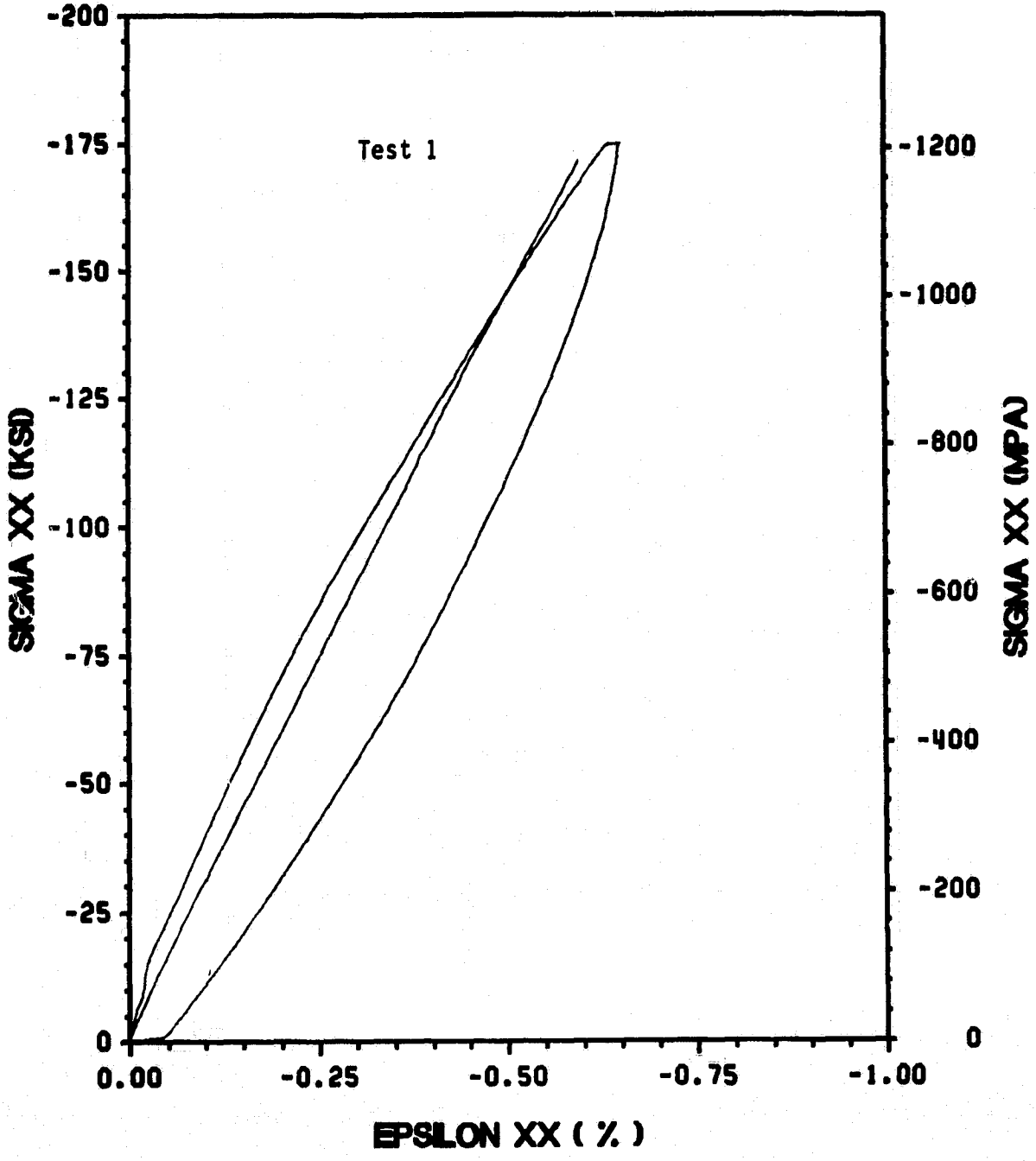

Figure 119. 10° Off-Axis Tests: Compressive Stress-Strain Response

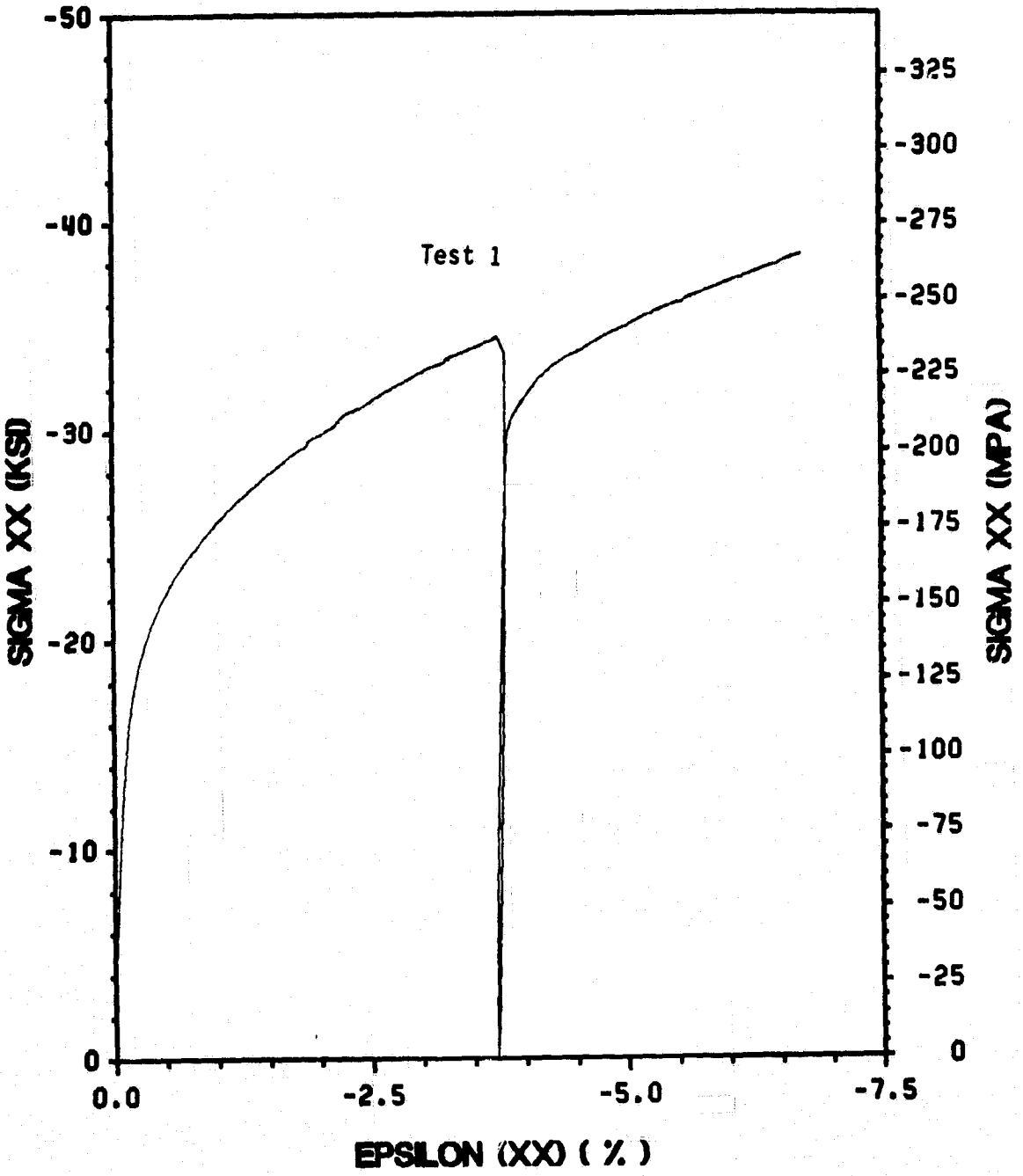

Figure 120. 45° Off-Axis Tests: Compressive Stress-Strain Response

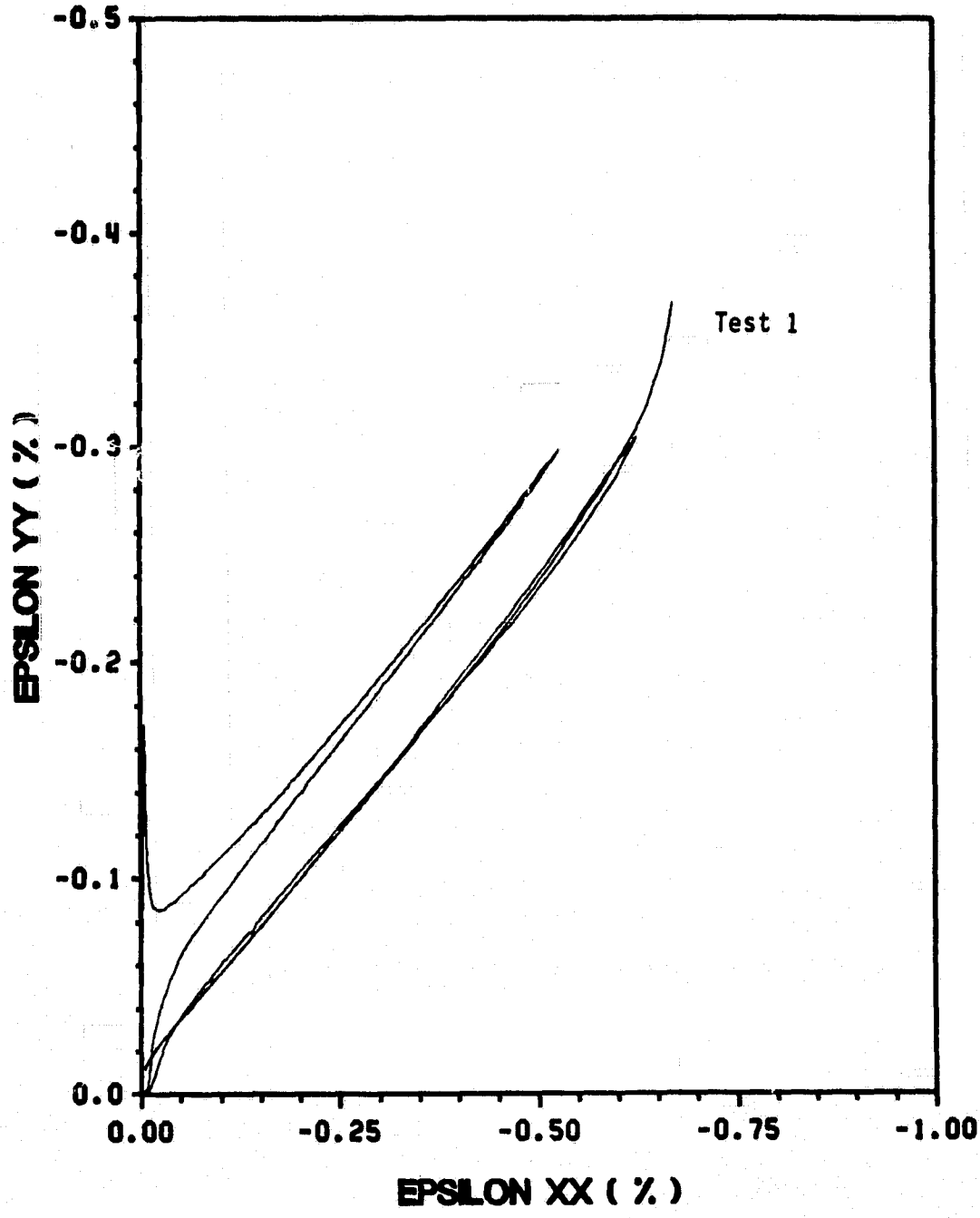

Figure 121. 0° On-Axis Tests: Poisson's Response

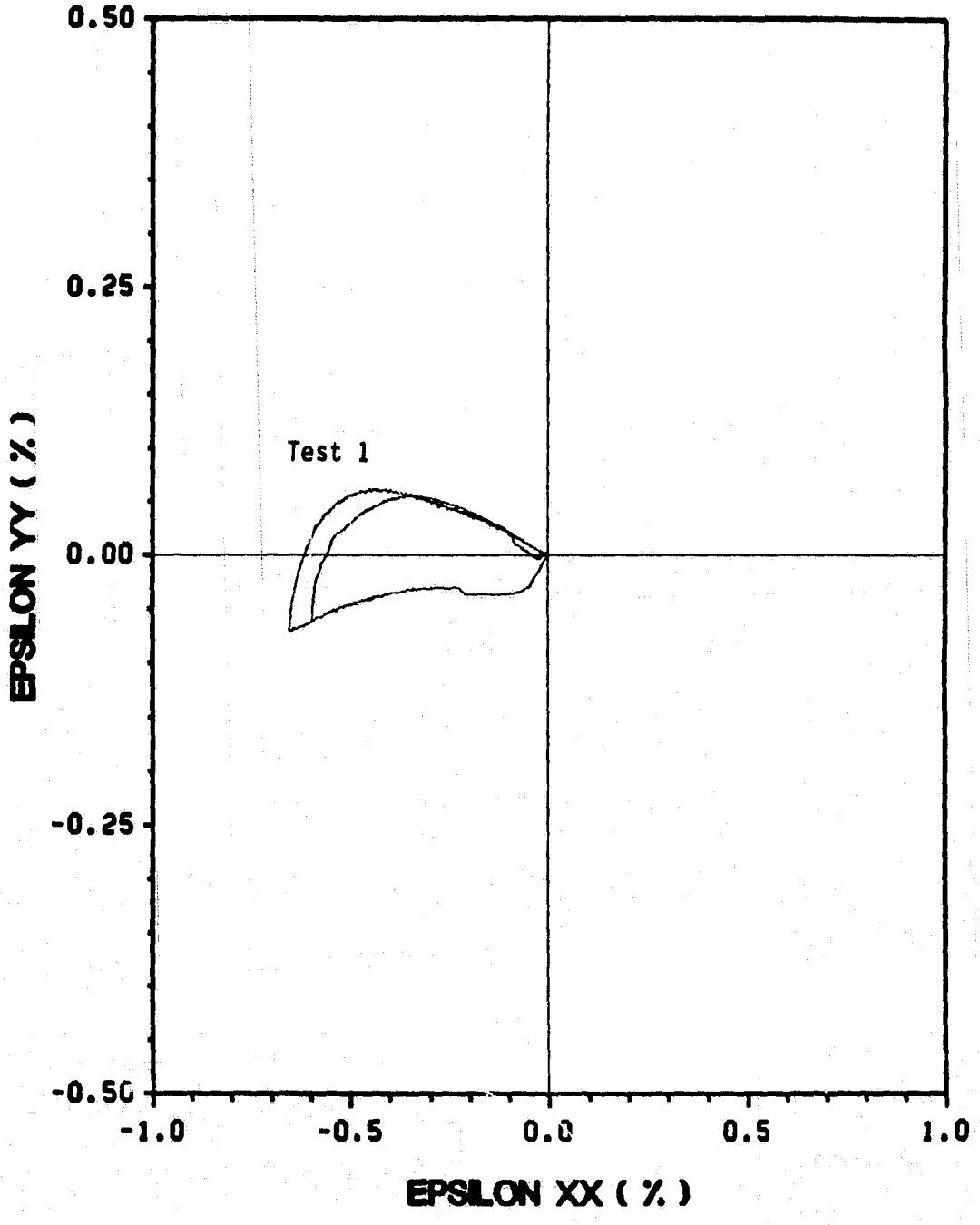

Figure 122. 10° Off-Axis Tests: Poisson's Response

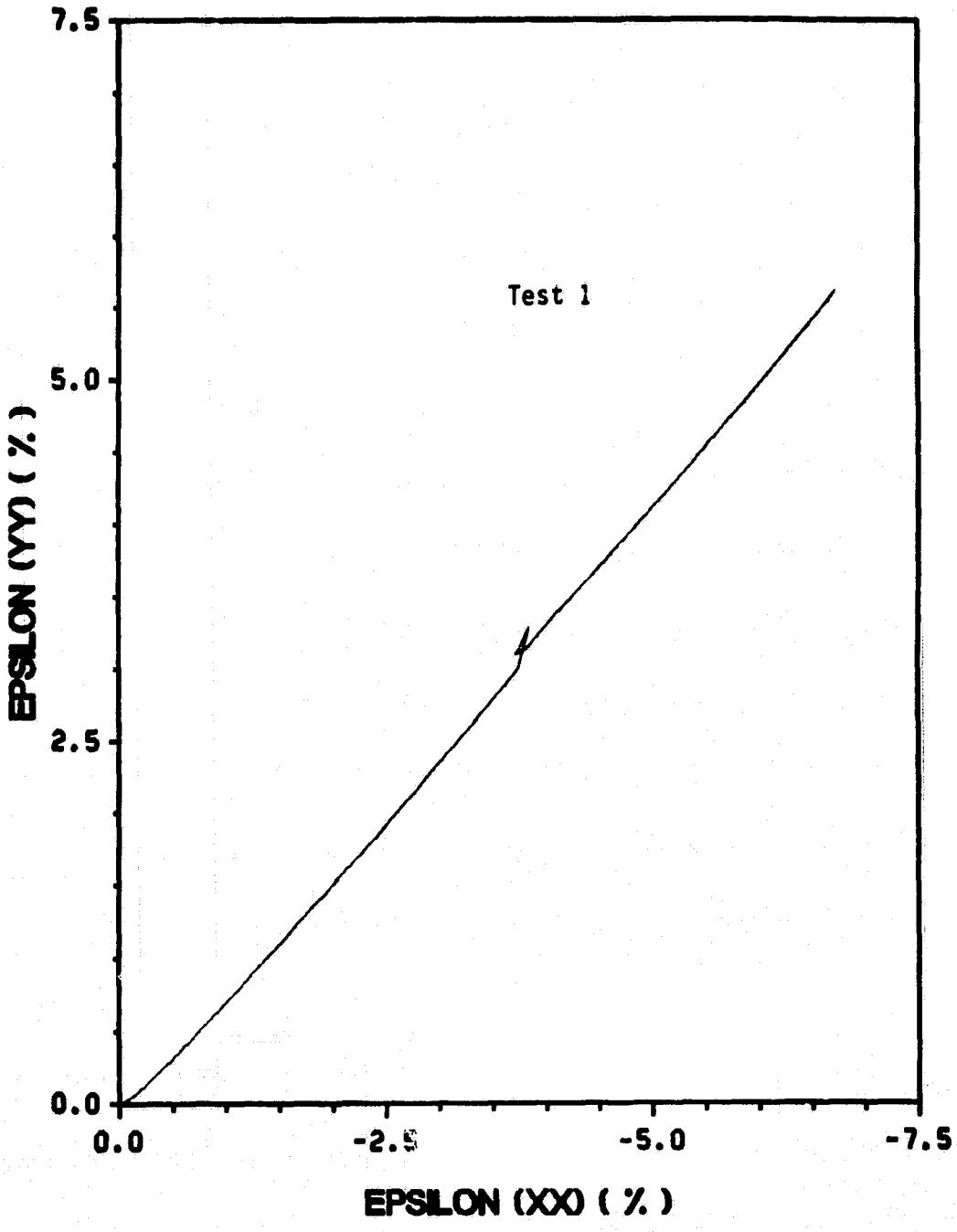

Figure 123. 45° Off-Axis Tests: Poisson's Response

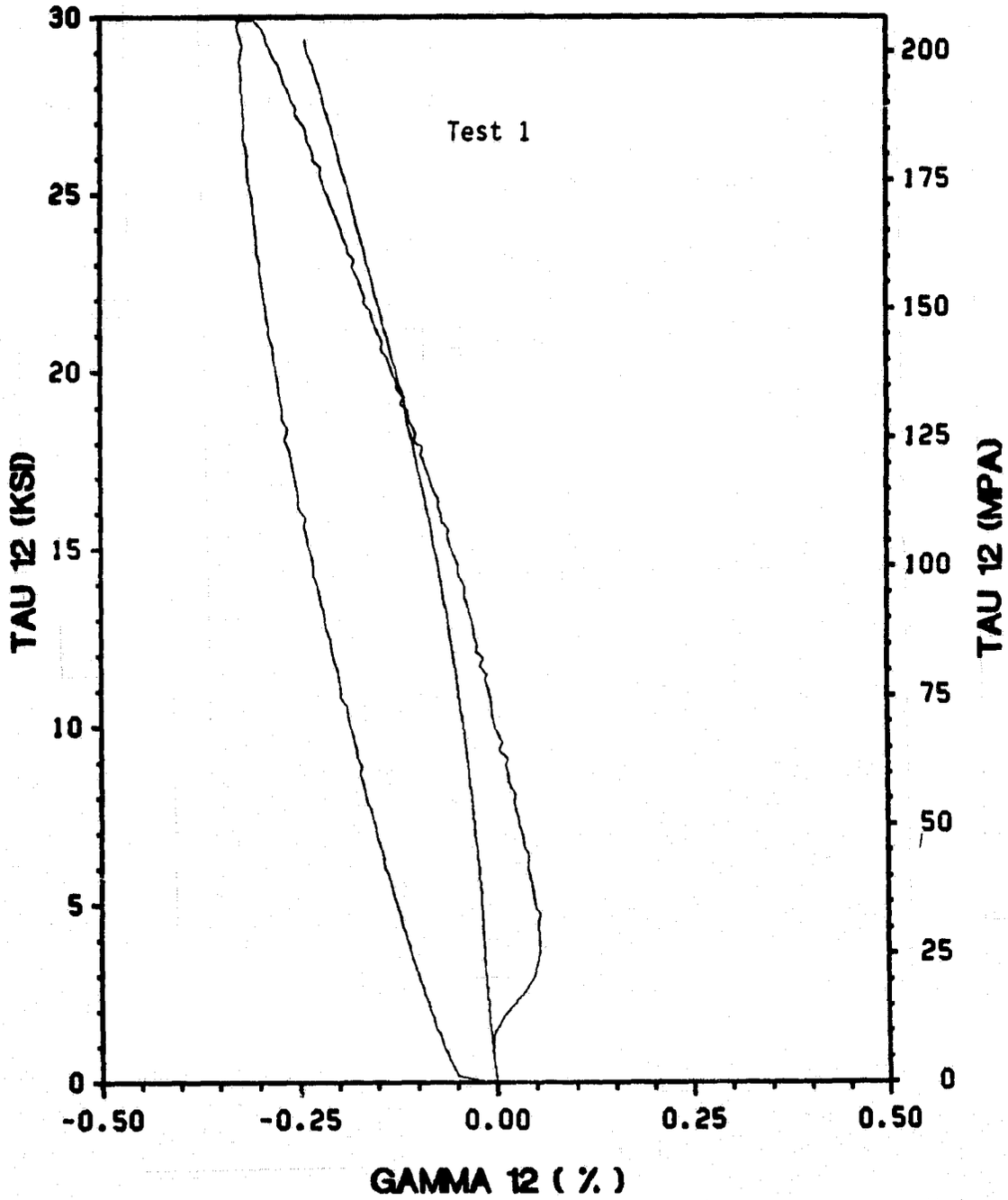

Figure 124. 10° Off-Axis Tests: In-Plane Shear Response

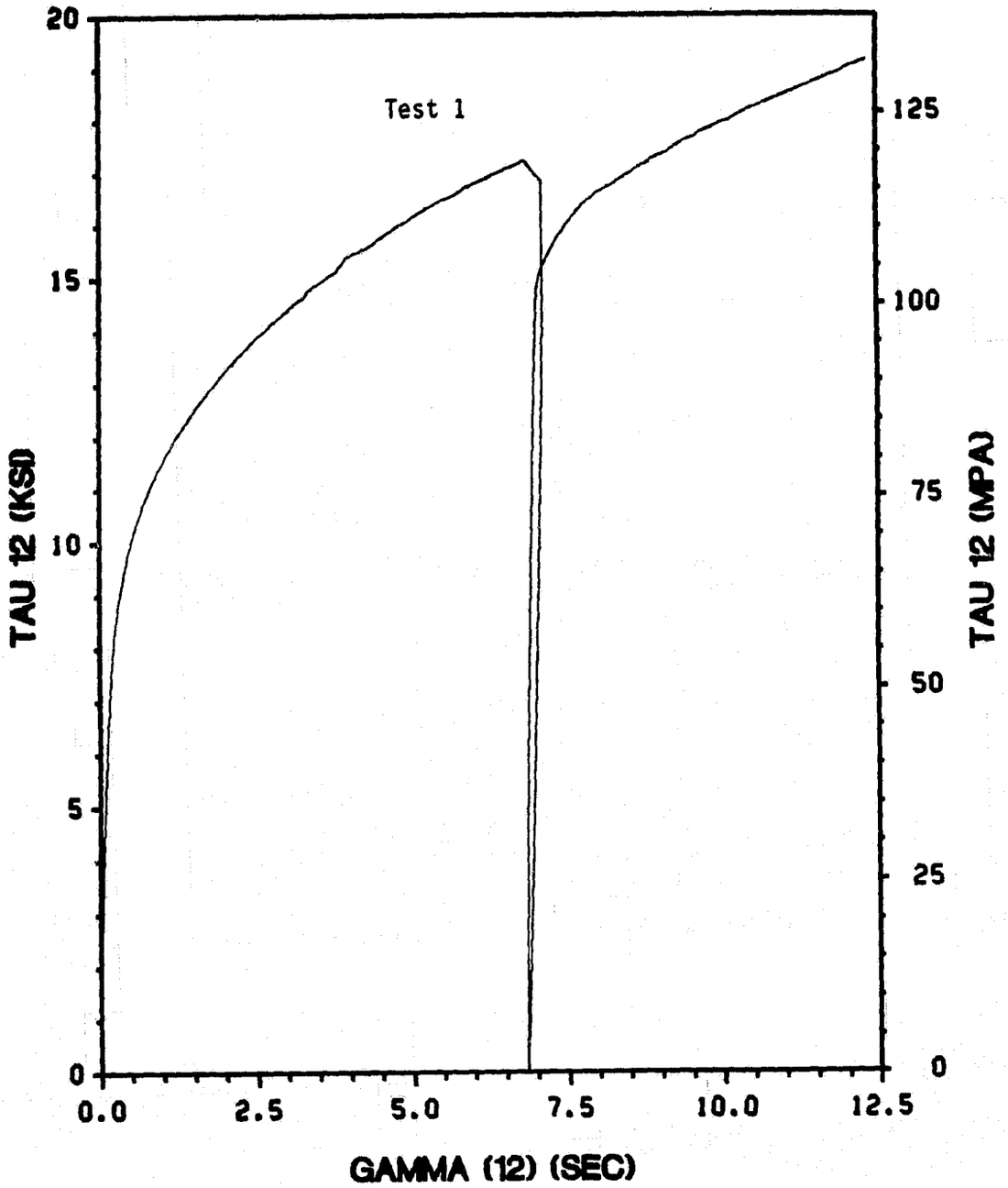

Figure 125. 45° Off-Axis Tests: In-Plane Shear Response

Appendix C. Individual Iosipescu Shear Test Results

Table C.1 Individual Iosipescu Shear Test Results: Material Properties

Specimen Group	Specimen Number	Shear Modulus, G_{12}^{*}(msi)	Ultimate Stress, τ_{12}^{*}(ksi)	Ultimate Strain, γ_{12}^{*}(%)	Yield Stress, τ_{12}^{*}(ksi)	Yield Strain, γ_{12}
0° monotonic						
	1(1)	6.69	28.82	4.101(3)	3.98	0.059
	2(1)	6.83	25.99	4.112(3)	3.63	0.054
	3(1)	6.31	35.23	4.101(3)	3.91	0.054
	4(2)	7.23	22.09(3)	9.521(3)	3.95	0.063
	5(2)	****	19.95(3)	****	****	****
	6(2)	6.31	17.77(3)	3.561(3)	3.81	0.057
	mean	6.67	19.87(4)	6.541(4)	3.81	0.055
75° monotonic						
	1(1)	6.23	18.68	4.659	3.38	0.050
	2(2)	6.61	14.44	8.965	3.21	0.050
	mean	6.42	14.44(4)	8.976(4)	3.29	0.050
80° cyclic						
	1(1)	6.43	19.36	3.649	2.44	0.036
	2(1)	6.57	18.91	3.624	2.39	0.037
	3(2)	6.39	17.04	3.261(3)	2.13	0.034
	4(2)	6.79	17.73	4.832(3)	2.52	0.037
	5(2)	****	****	****	****	****
cyclic						
	6(2)	7.05	15.01	1.986	2.34	0.0331
	mean	6.65	17.39(4)	4.047(4)	2.37	1.846

Table C.1 Individual Iosipescu Shear Test Results: Material Properties (continued)

Specimen Group	Specimen Number	Shear Modulus, G_{12}^{*}(msi)	Ultimate Stress, τ_{12}^{*}(ksi)	Ultimate Strain, γ_{12}^{*}(%)	Yield Stress, τ_{12}^{*}(ksi)	Yield Strain, γ_{12}
85° monotonic						
	1(1)	7.09	20.25	3.995(3)	****	****
	2(1)	6.63	19.45	4.008(3)	****	****
	3(2)	6.68	17.04(3)	3.648(3)	1.18	0.017
	4(2)	7.01	17.90(3)	3.943(3)	1.28	0.019
cyclic						
	5(2)	6.17	15.02	2.170	1.84	0.030
	mean	6.72	17.47(4)	3.802(4)	1.43	0.021
90° monotonic						
	1(1)	5.67	15.64	4.035(3)	1.02	0.019
	2(2)	5.92	14.93	6.079(3)	0.96	0.015
	3(2)	5.41	15.52	7.750(3)	0.48	0.009
	mean	5.67	15.23(4)	6.914(4)	0.82	0.014

* Not applicable
** Grip Failure
*** Only monotonic data included in average
**** Data not available
(1) MINC Data Acquisition System
(2) IBM-XT Data Acquisition System
(3) Gage Failure
(4) Only monotonic IBM-XT data included in average

C.1 Monotonic Test Results

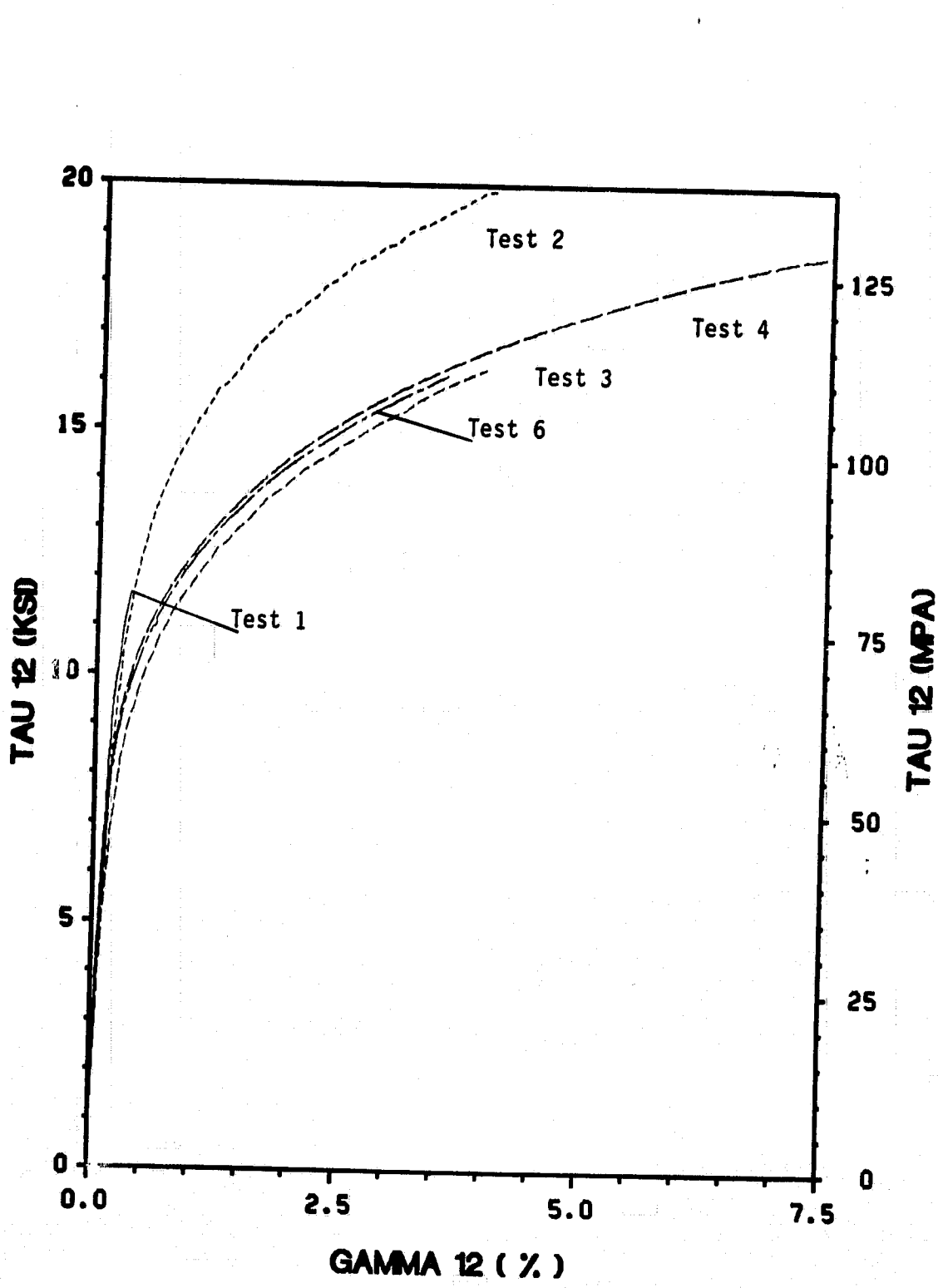

Figure 126. 0° On-Axis Tests: In-Plane Shear Response

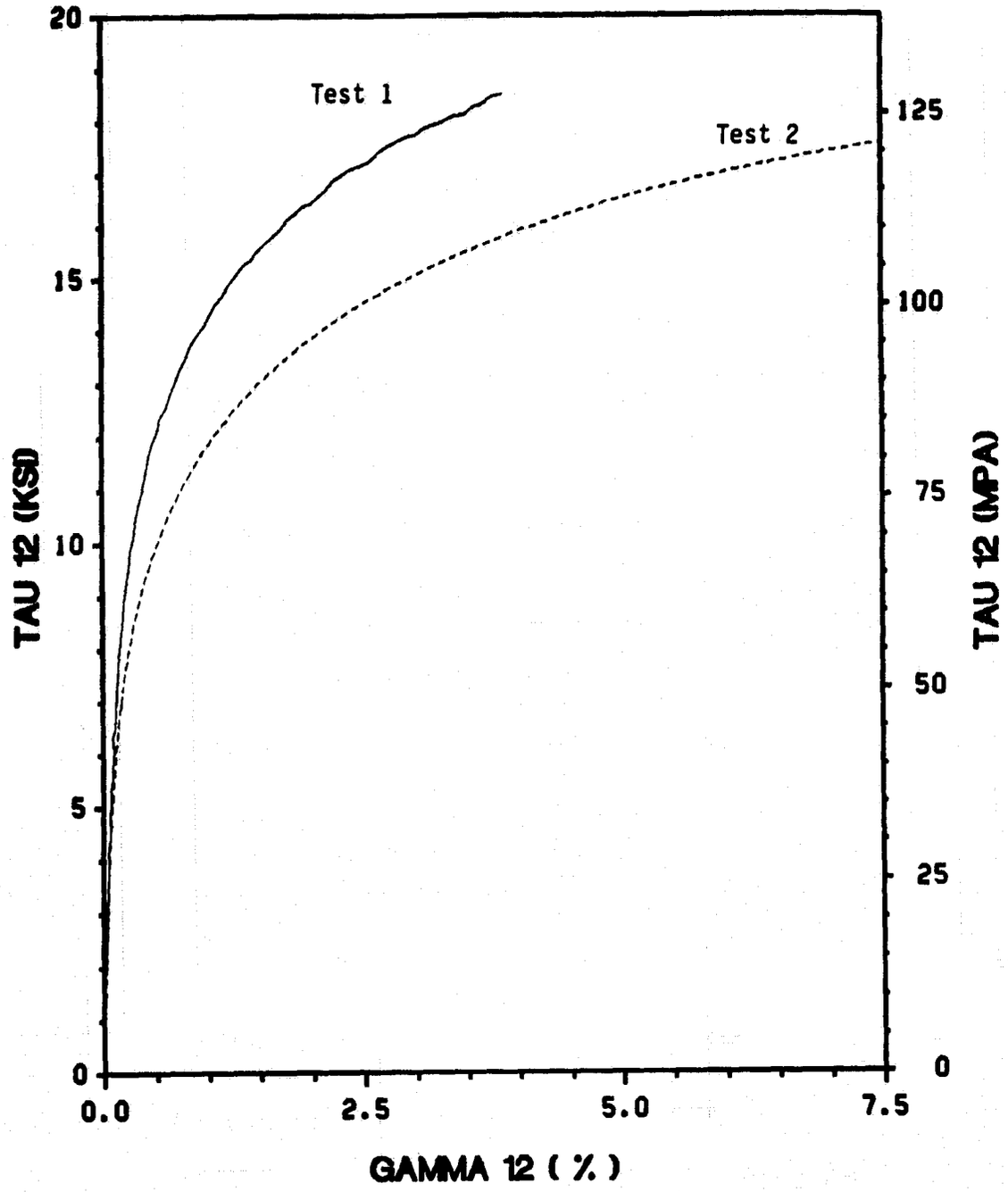

Figure 127. 75° Off-Axis Tests: In-Plane Shear Response

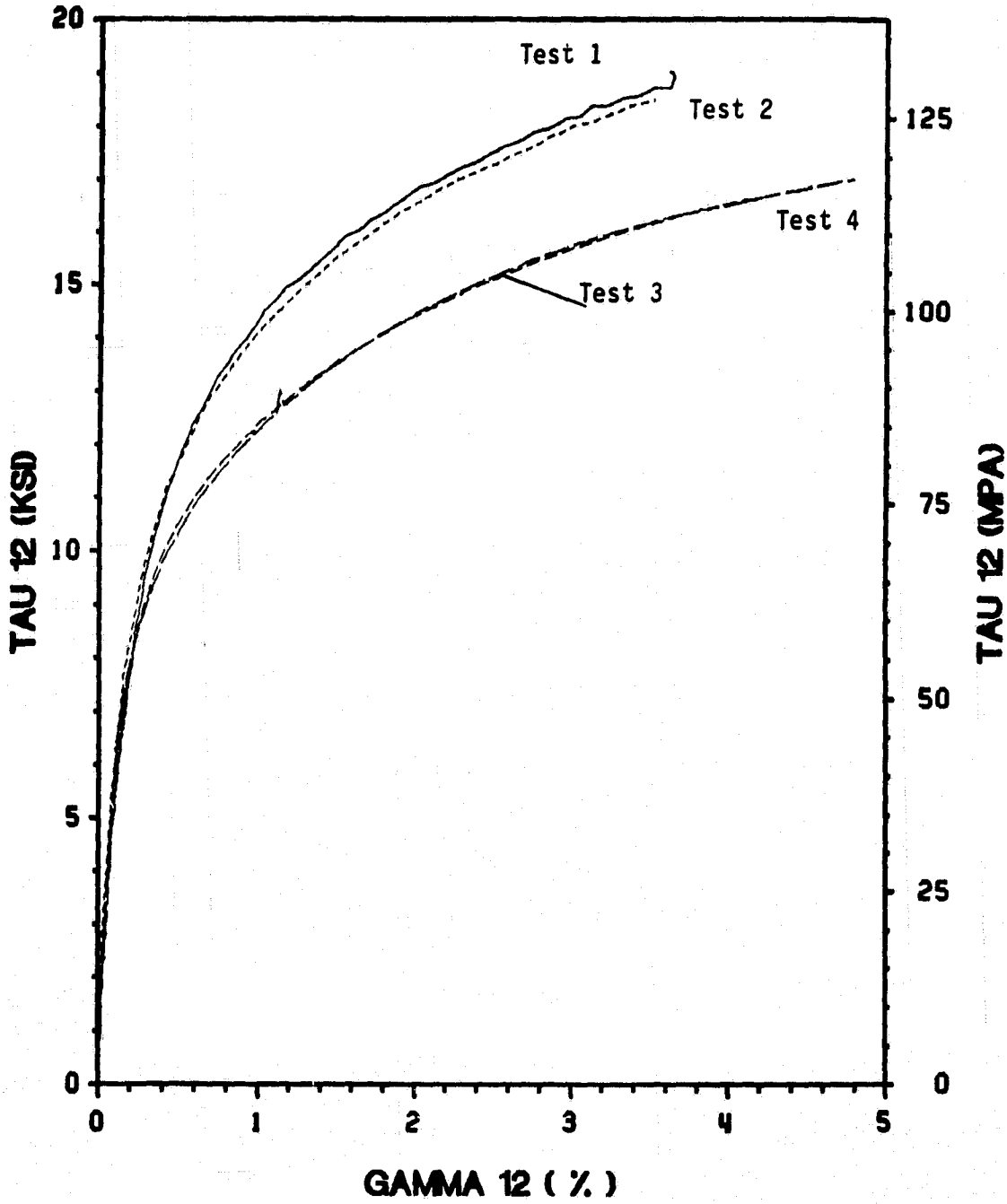

Figure 128. 80° Off-Axis Tests: In-Plane Shear Response

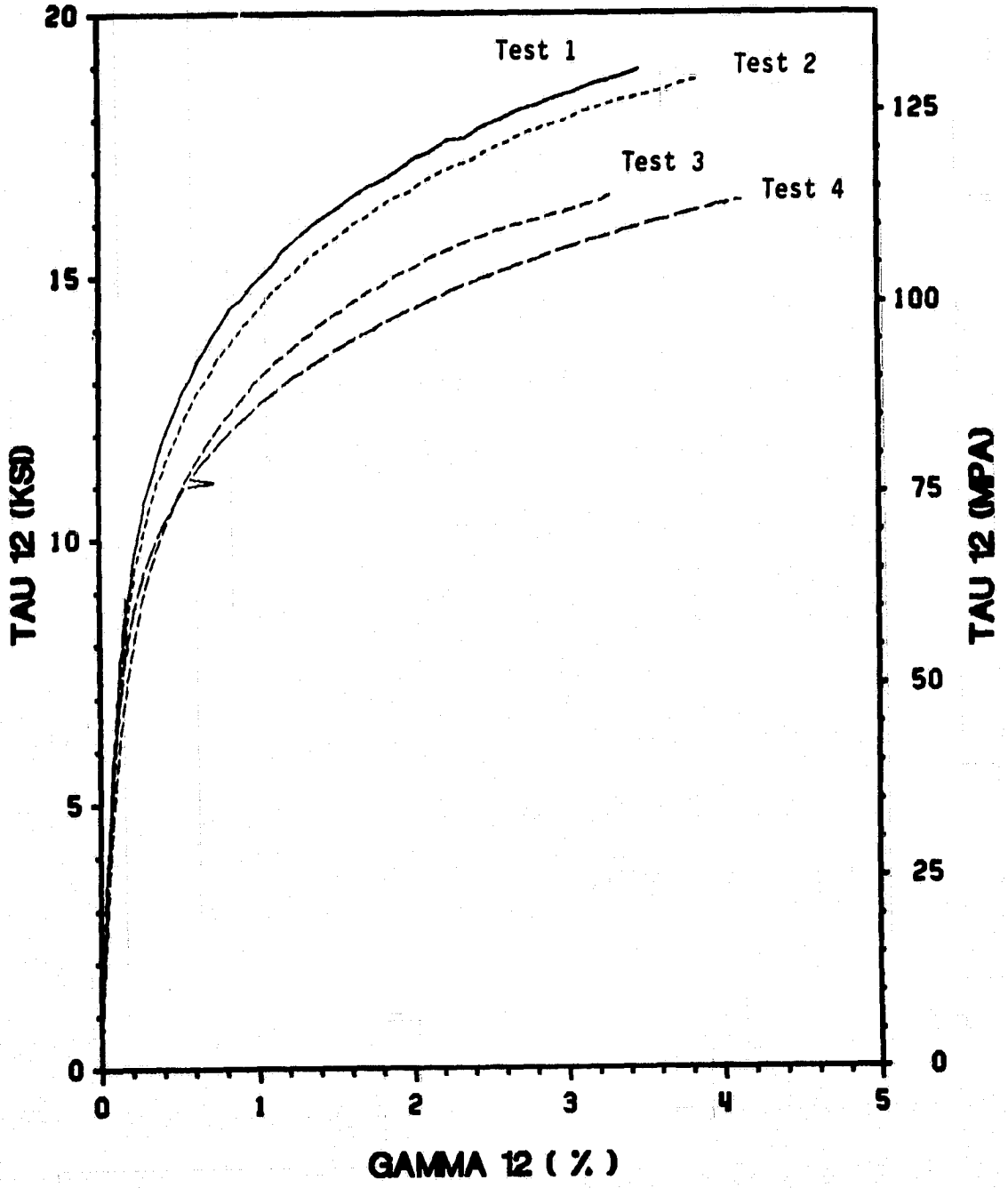

Figure 129. 85° Off-Axis Tests: In-Plane Shear Response

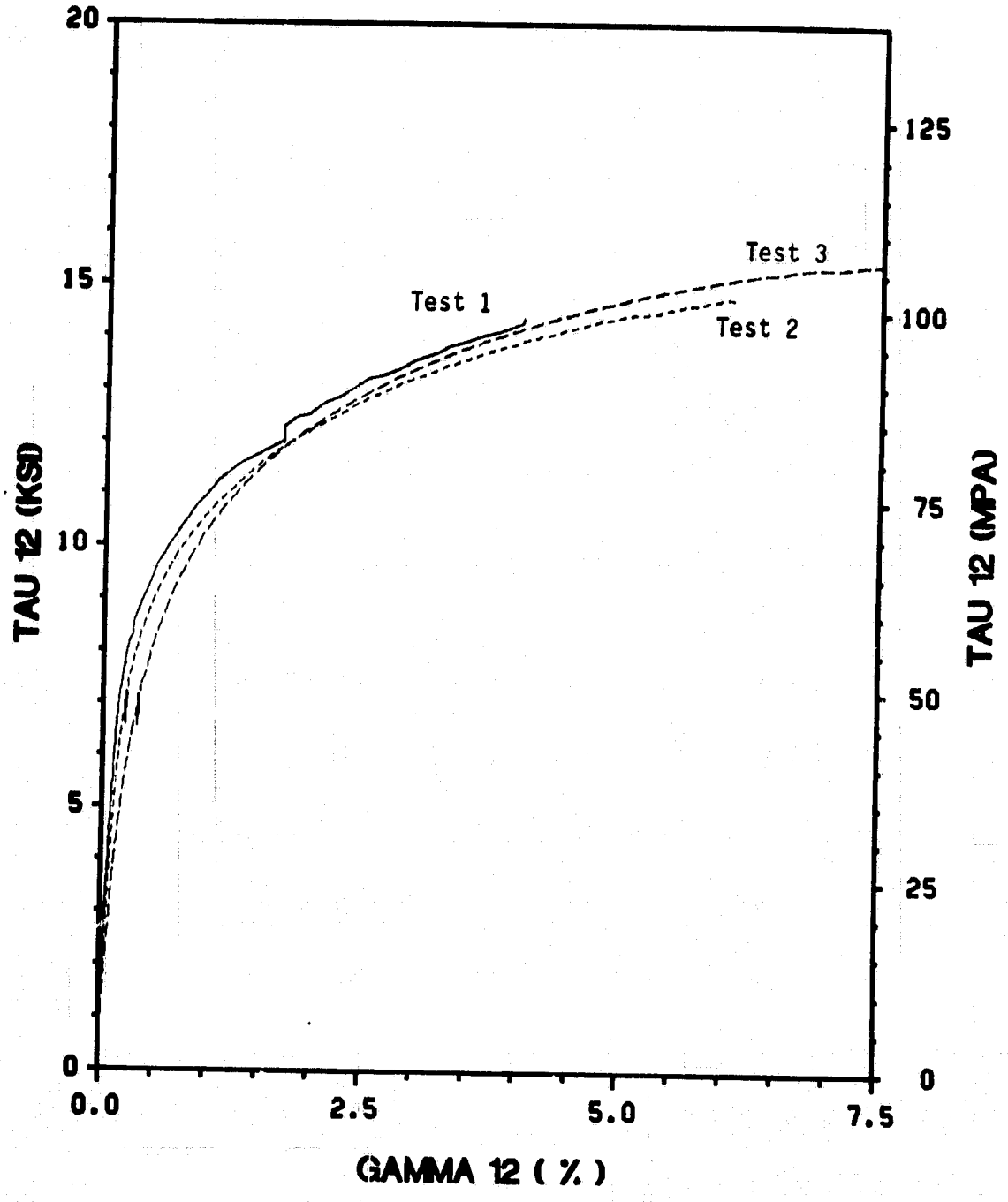

Figure 130. 90° On-Axis Tests: In-Plane Shear Response

C.2 Cyclic Test Results

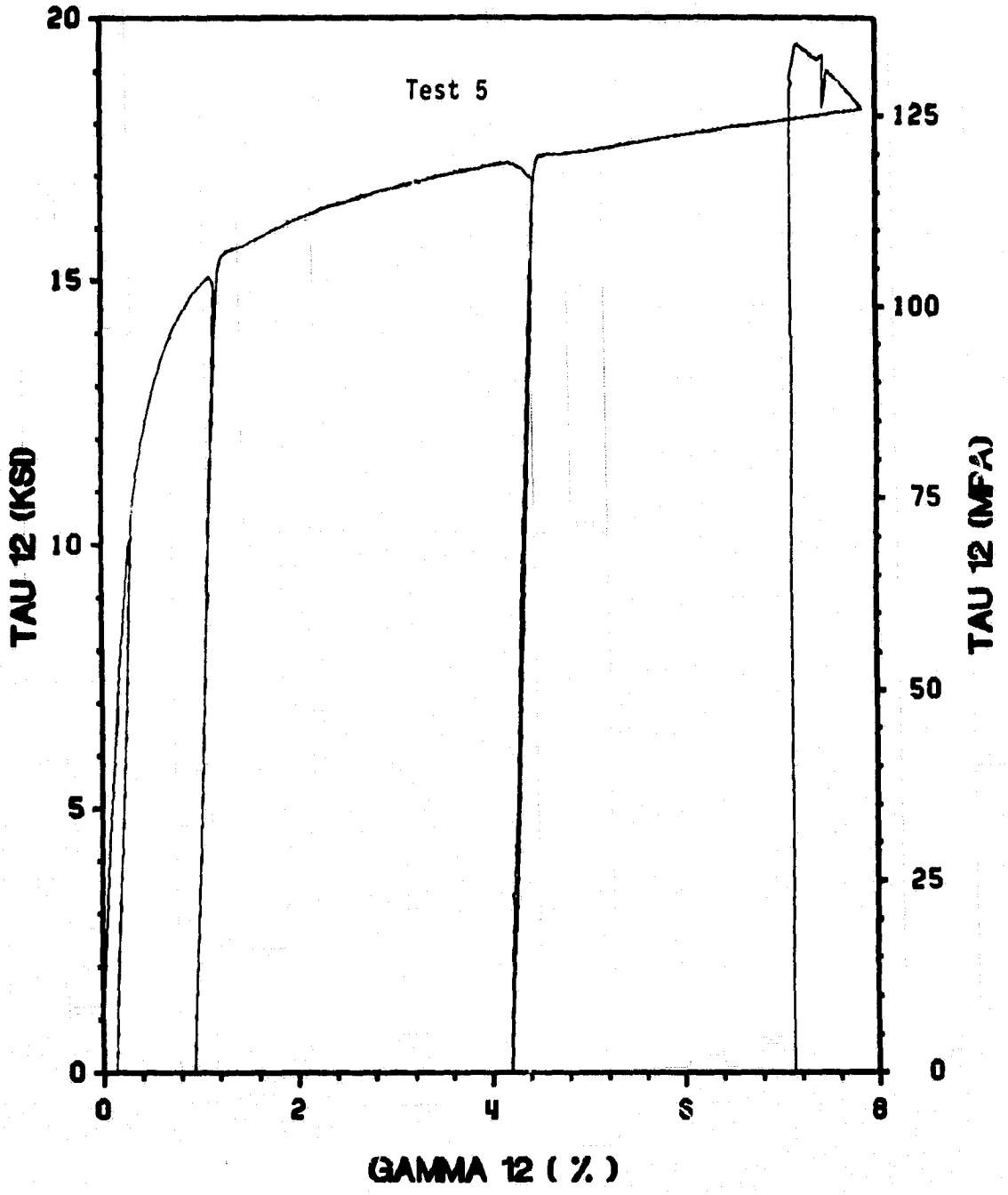

Figure 131. 0° On-Axis Tests: In-Plane Shear Response

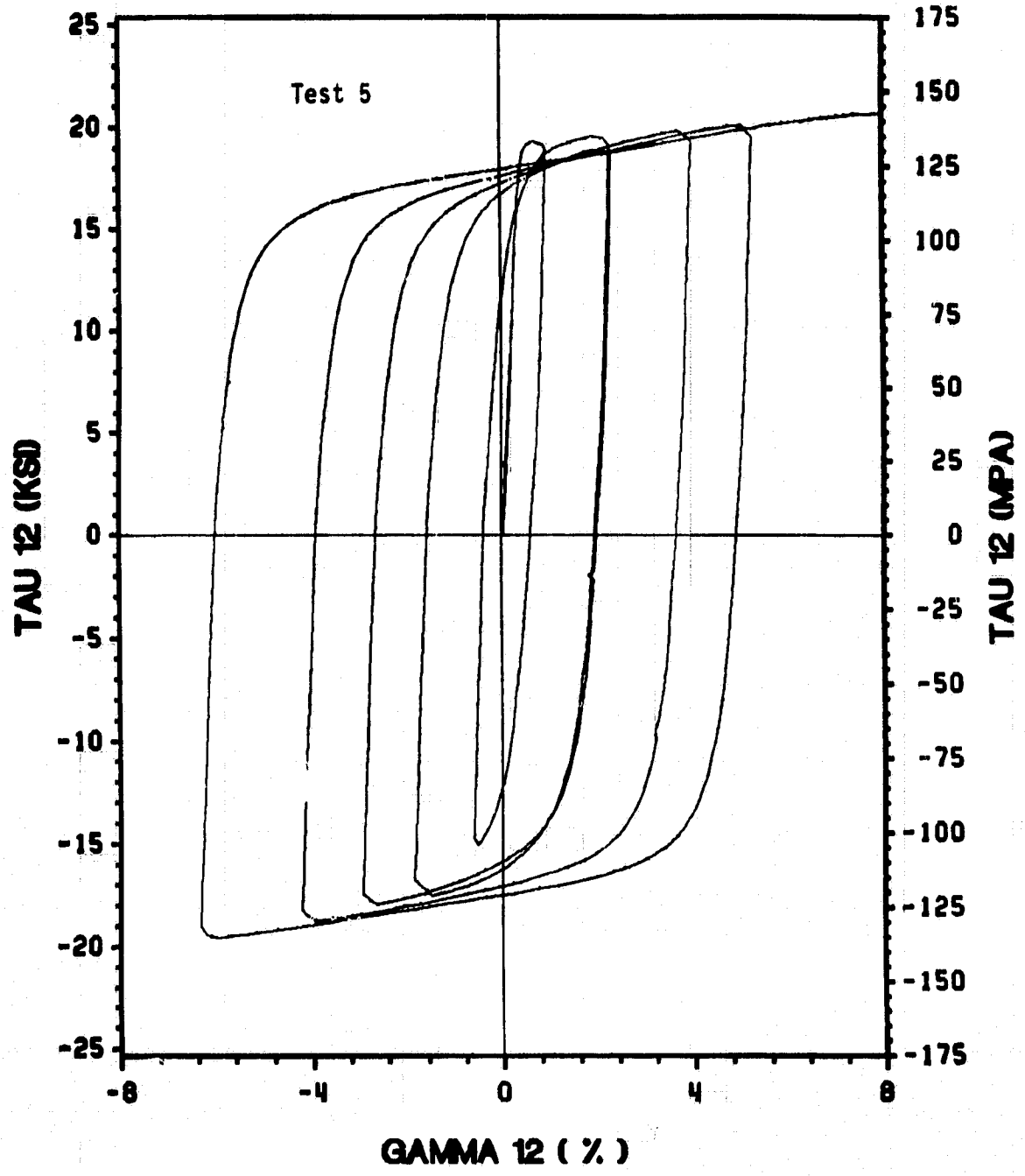

Figure 132. 0° On-Axis Tests: In-Plane Shear Response

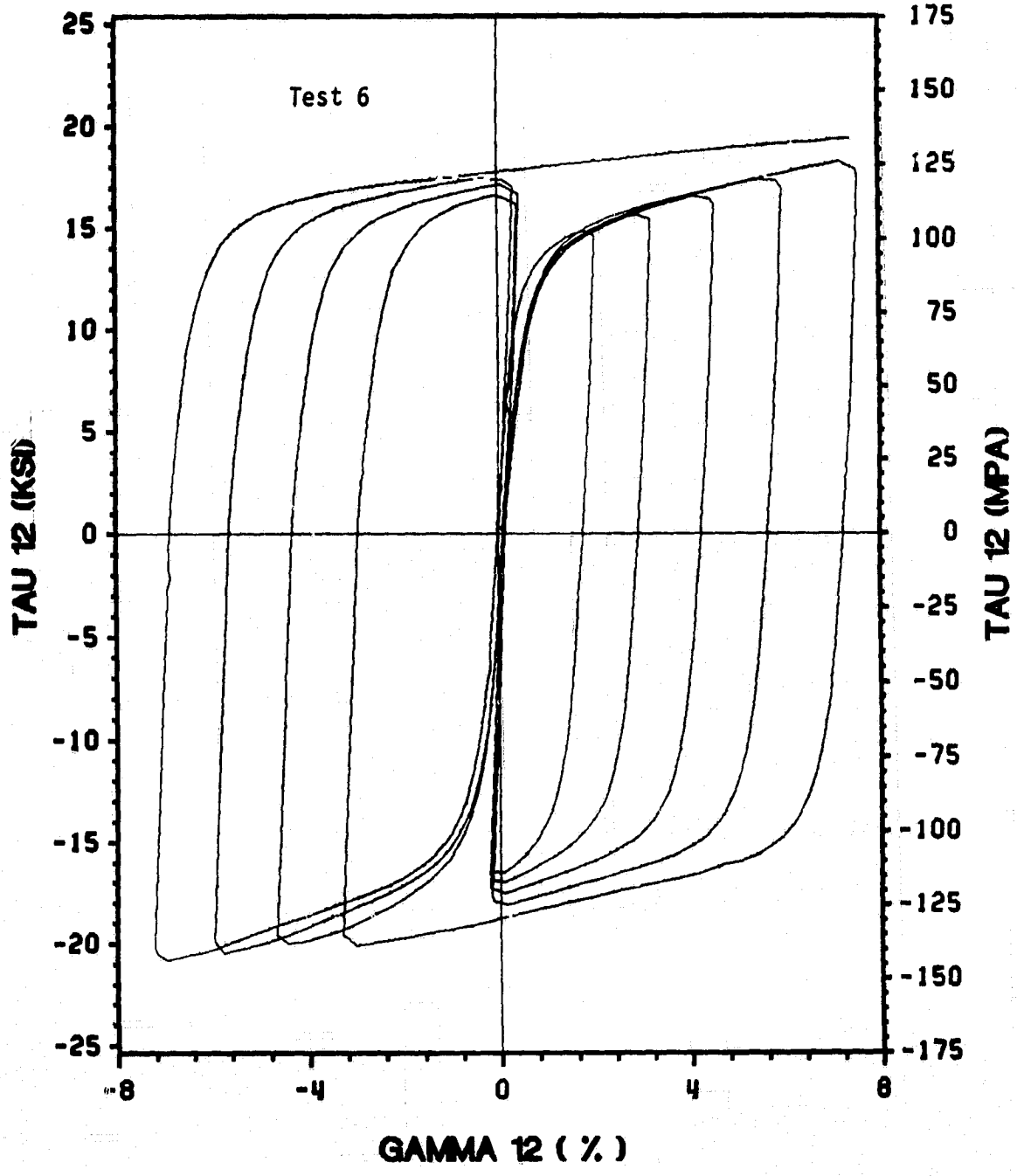

Figure 133. 0° On-Axis Tests: In-Plane Shear Response

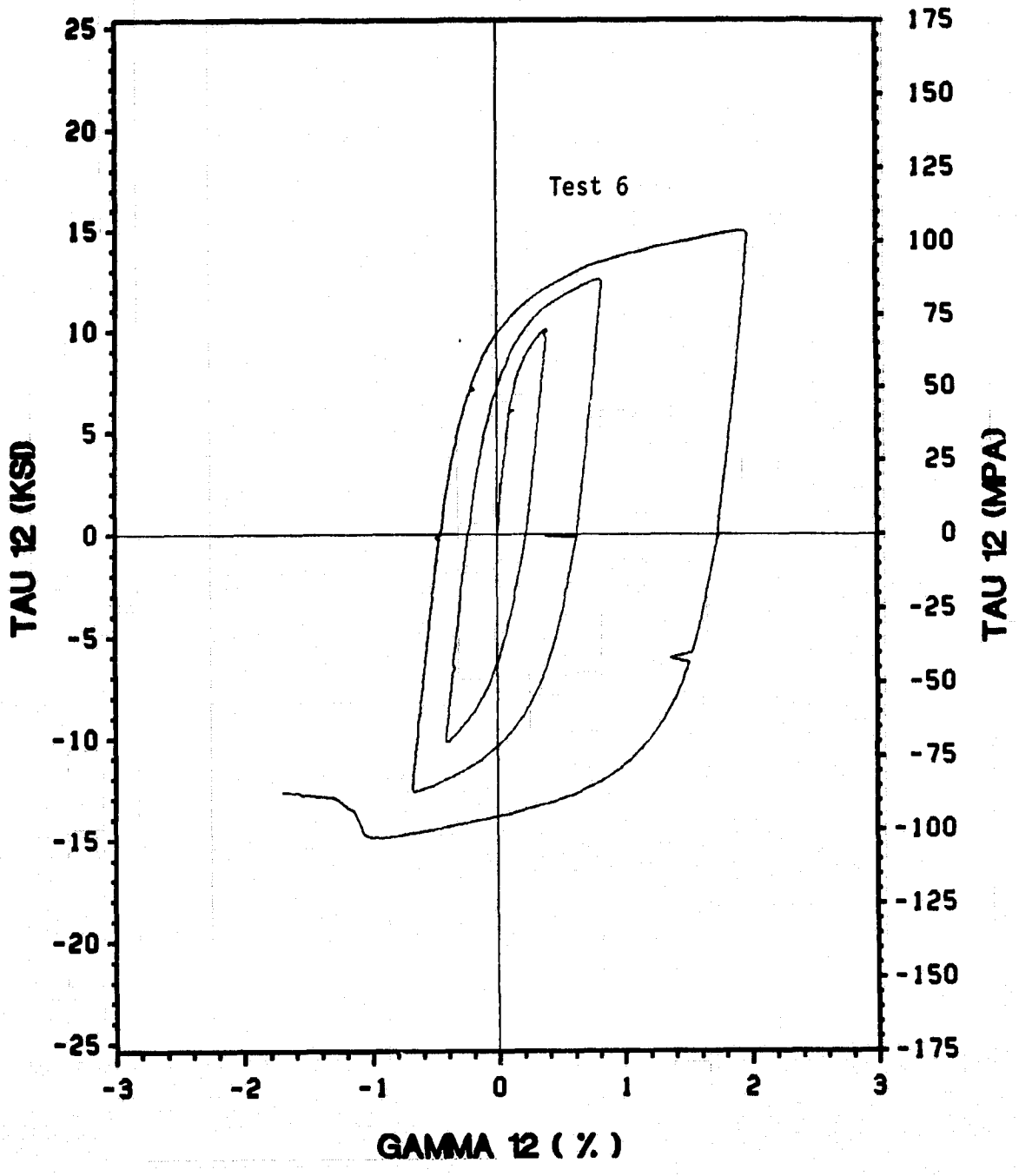

Figure 134. 80° Off-Axis Tests: In-Plane Shear Response

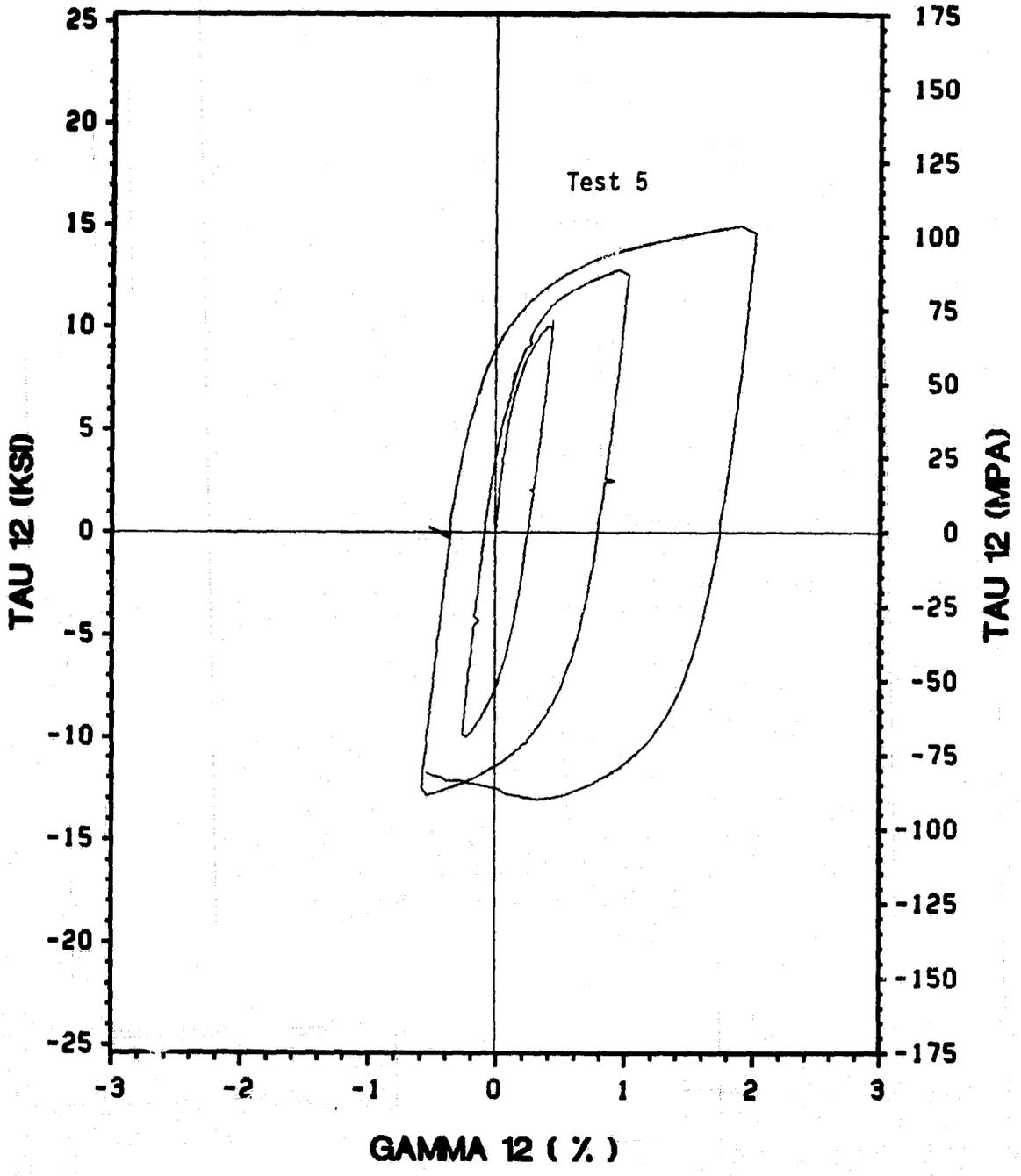

Figure 135. 85° Off-Axis Tests: In-Plane Shear Response

Appendix D. Finite Element Results of a Compression Test Coupon

D.1 Boundary Condition #1 (fully clamped)

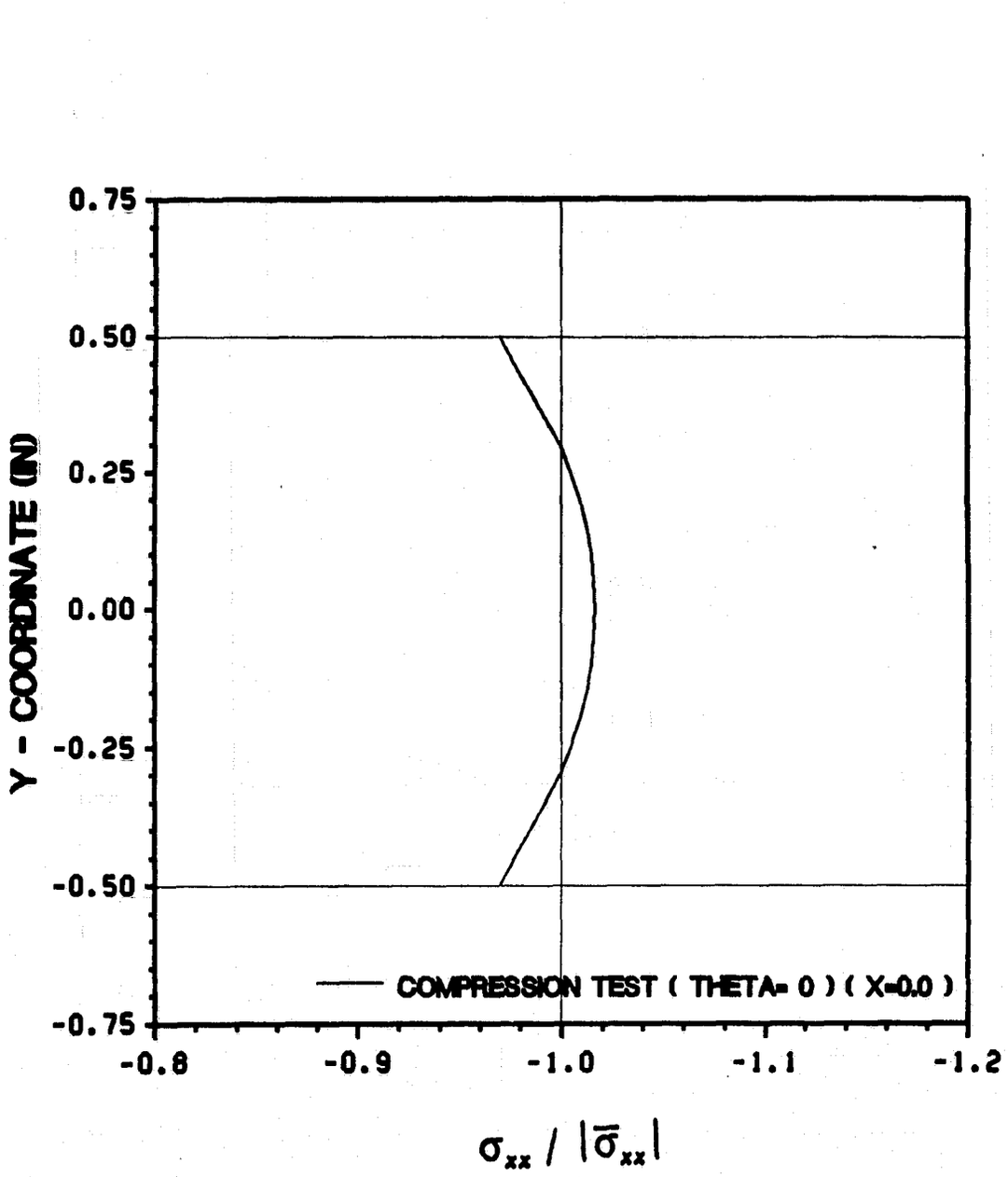

Figure 136. 0° On-Axis Tests: (σ_{xx} / $|\bar{\sigma}_{xx}|$)

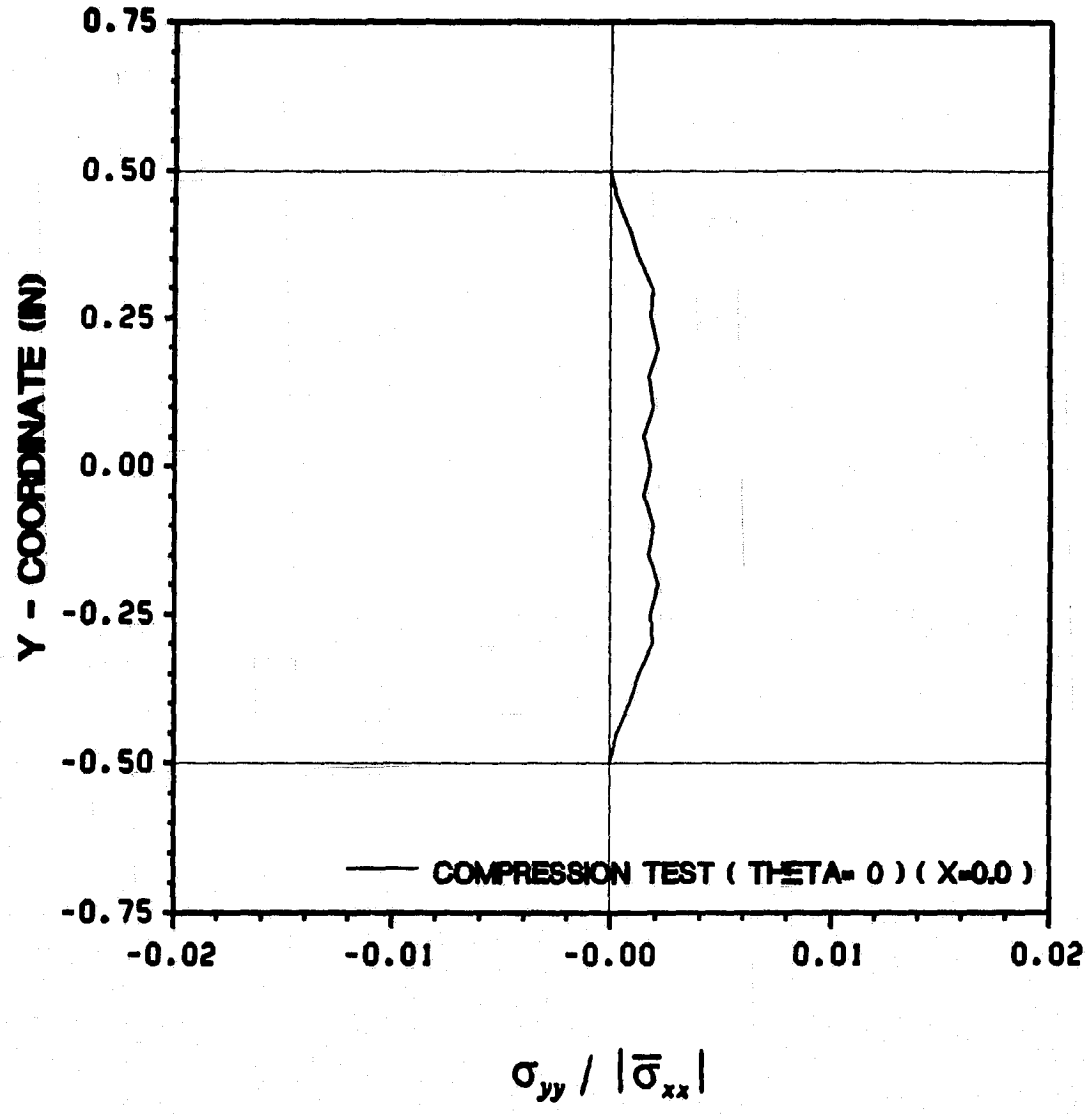

Figure 137. 0° On-Axis Tests: (σ_{yy} / $|\bar{\sigma}_{xx}|$)

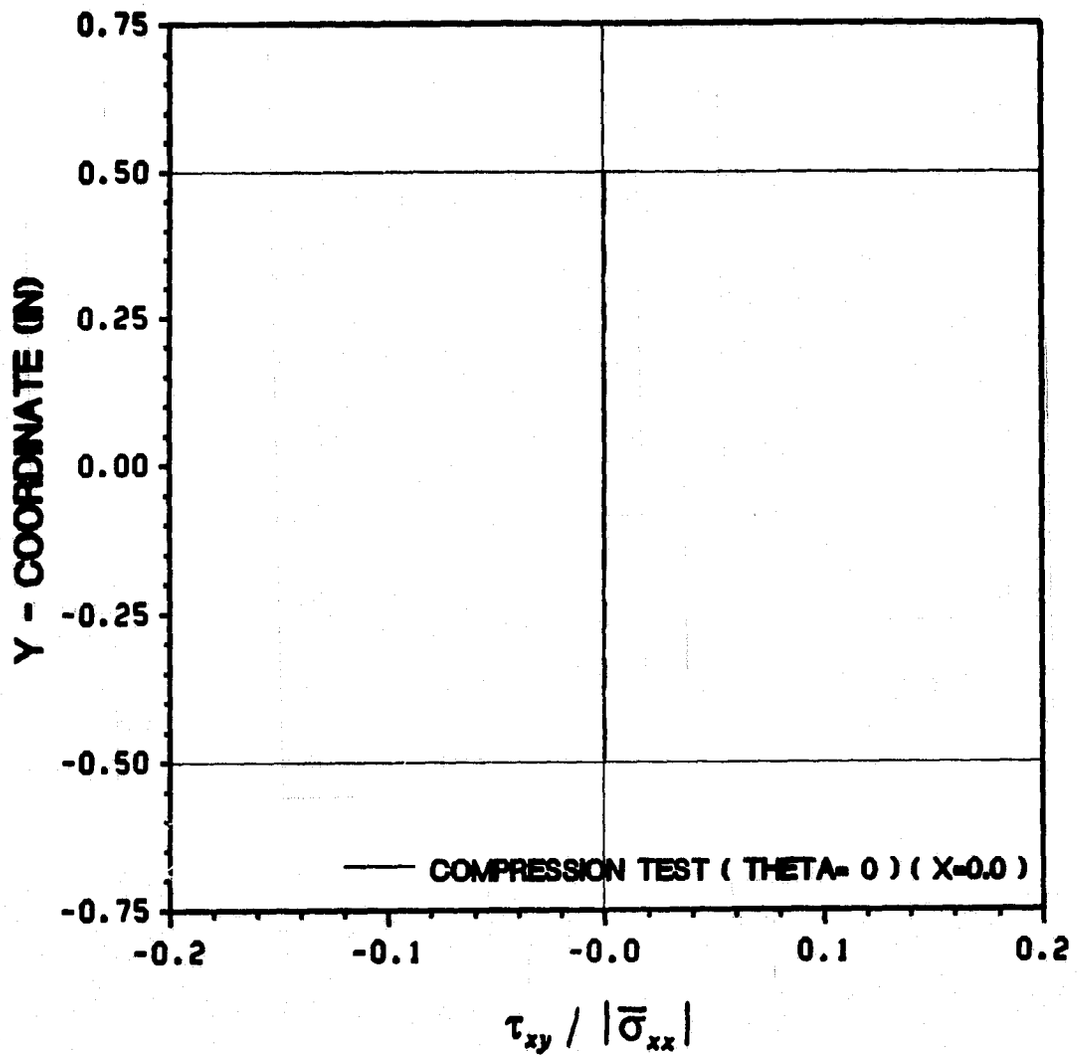

Figure 138. 0° On-Axis Tests: ($\tau_{xy} / |\bar{\sigma}_{xx}|$)

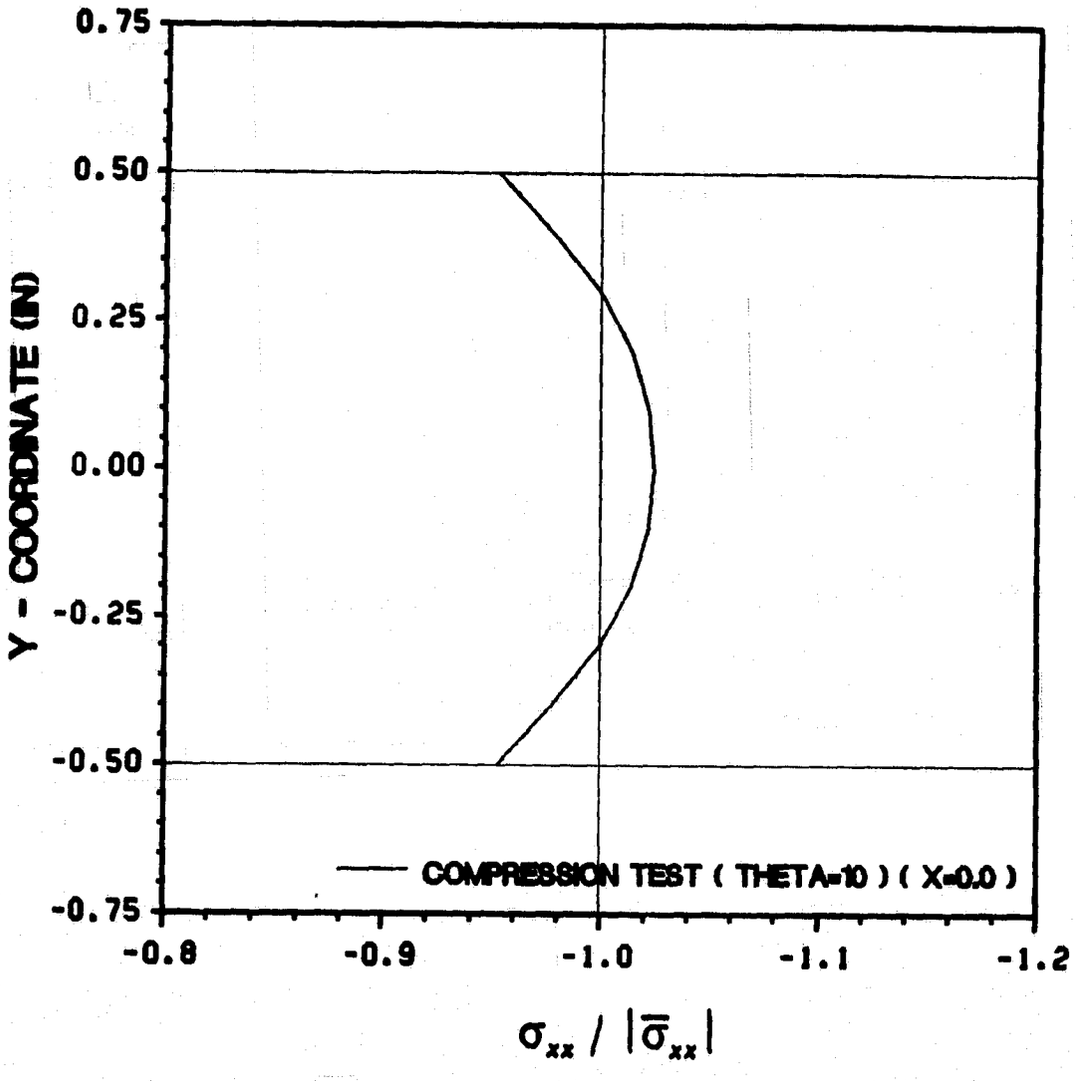

Figure 139. 10° Off-Axis Tests: (σ_{xx} / $|\bar{\sigma}_{xx}|$)

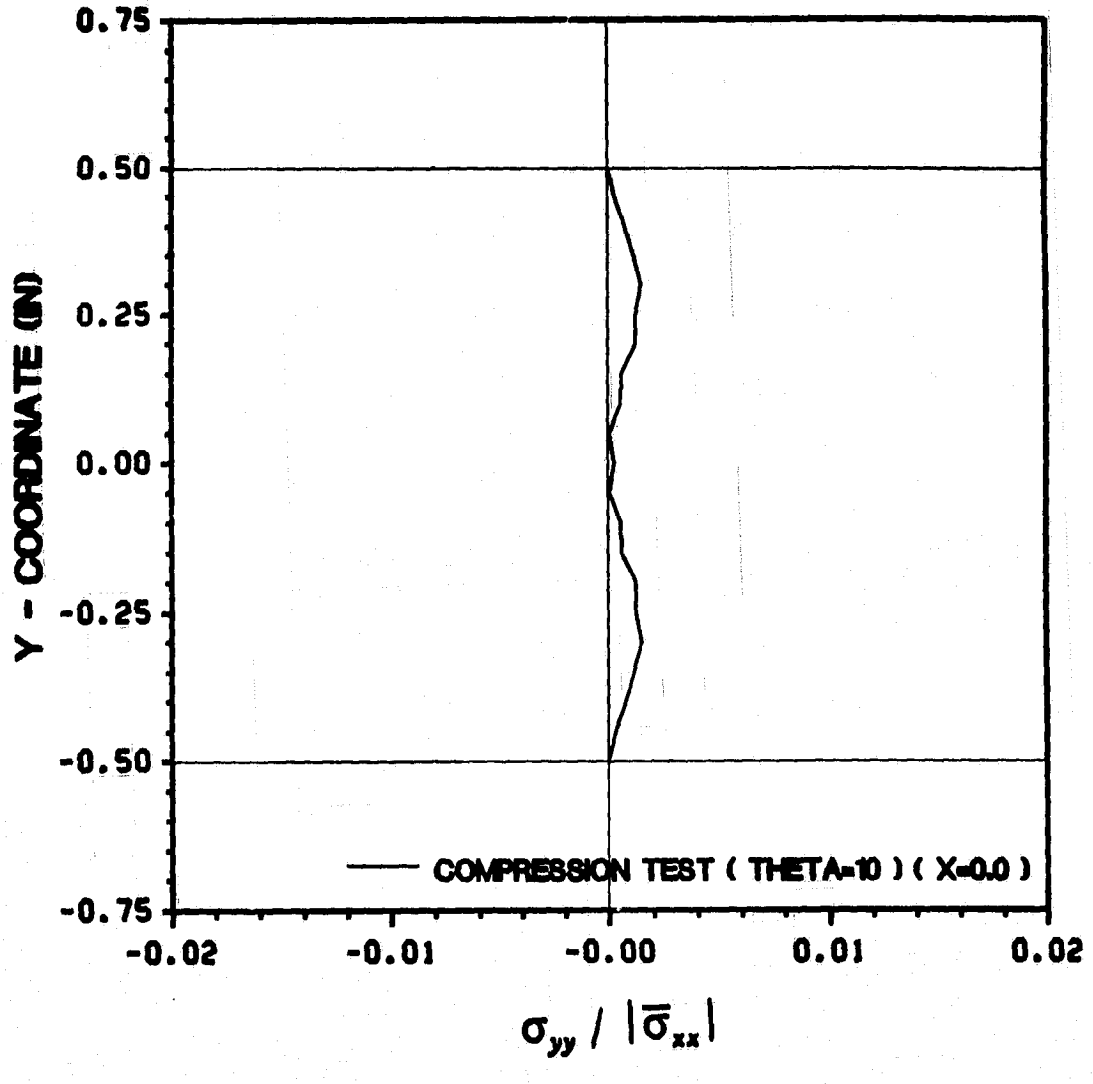

Figure 140. 10° Off-Axis Tests: (σ_{yy} / $|\bar{\sigma}_{xx}|$)

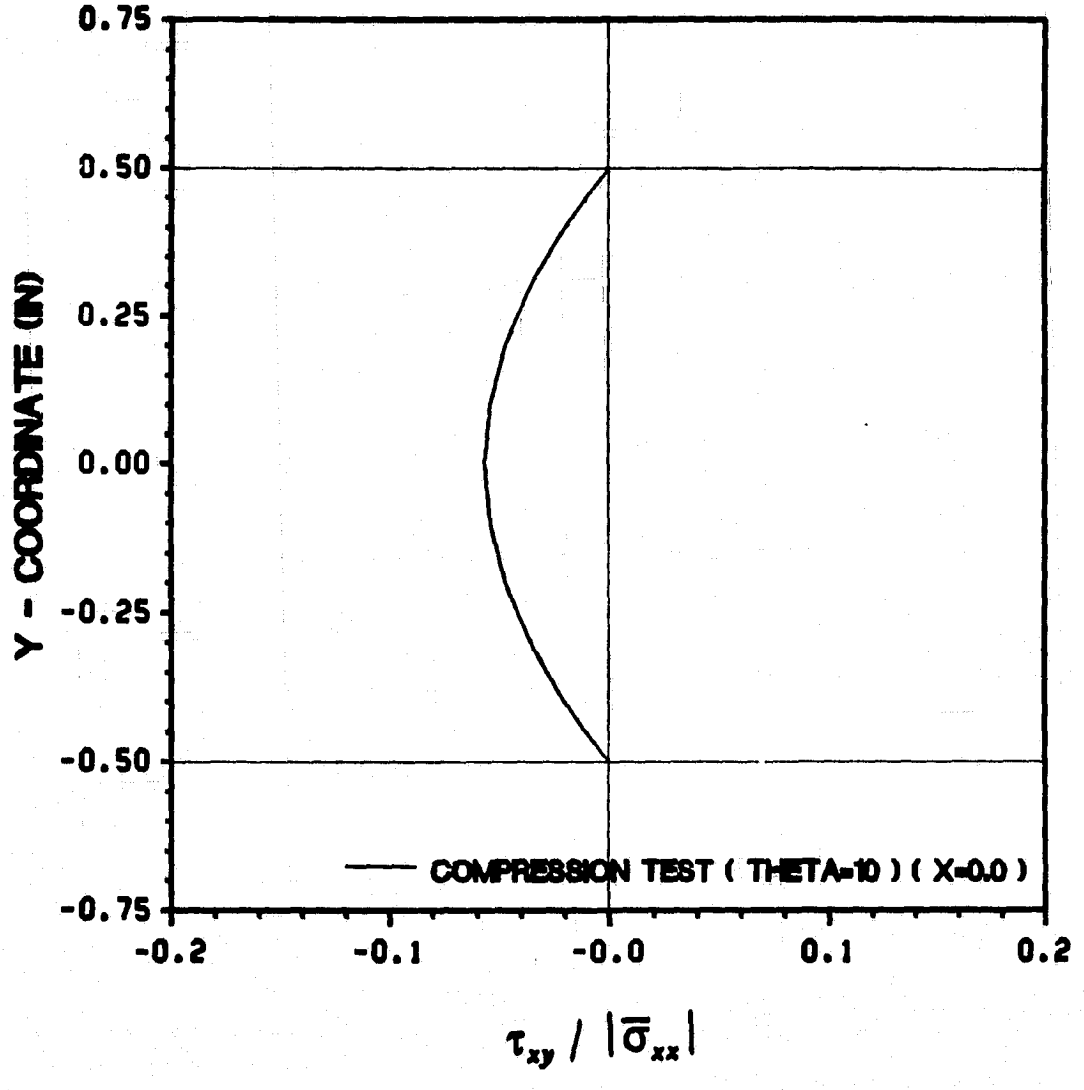

Figure 141. 10° Off-Axis Tests: (τ_{xy} / $|\bar{\sigma}_{xx}|$)

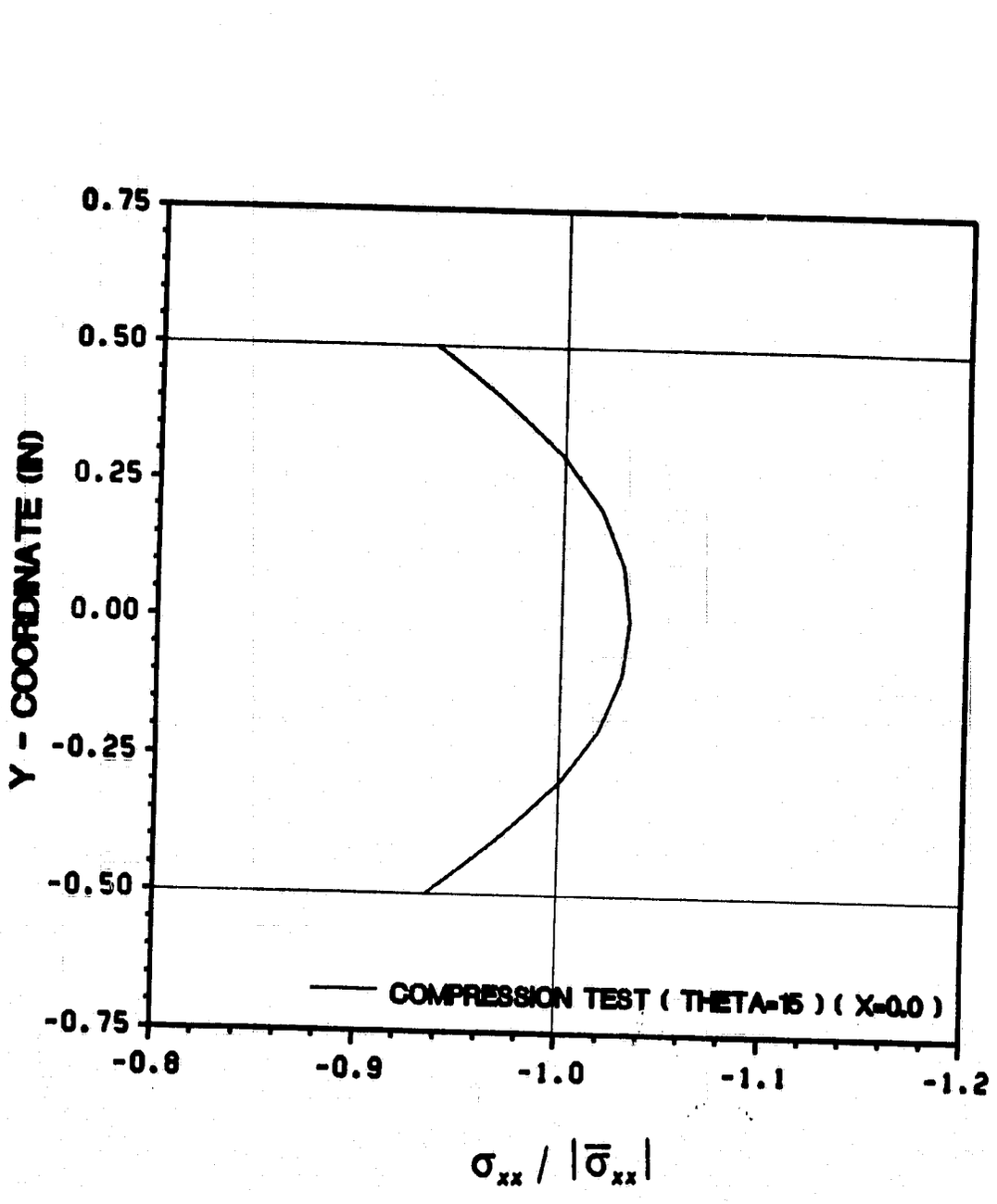

Figure 142. 15° Off-Axis Tests: (σ_{xx} / $|\bar{\sigma}_{xx}|$)

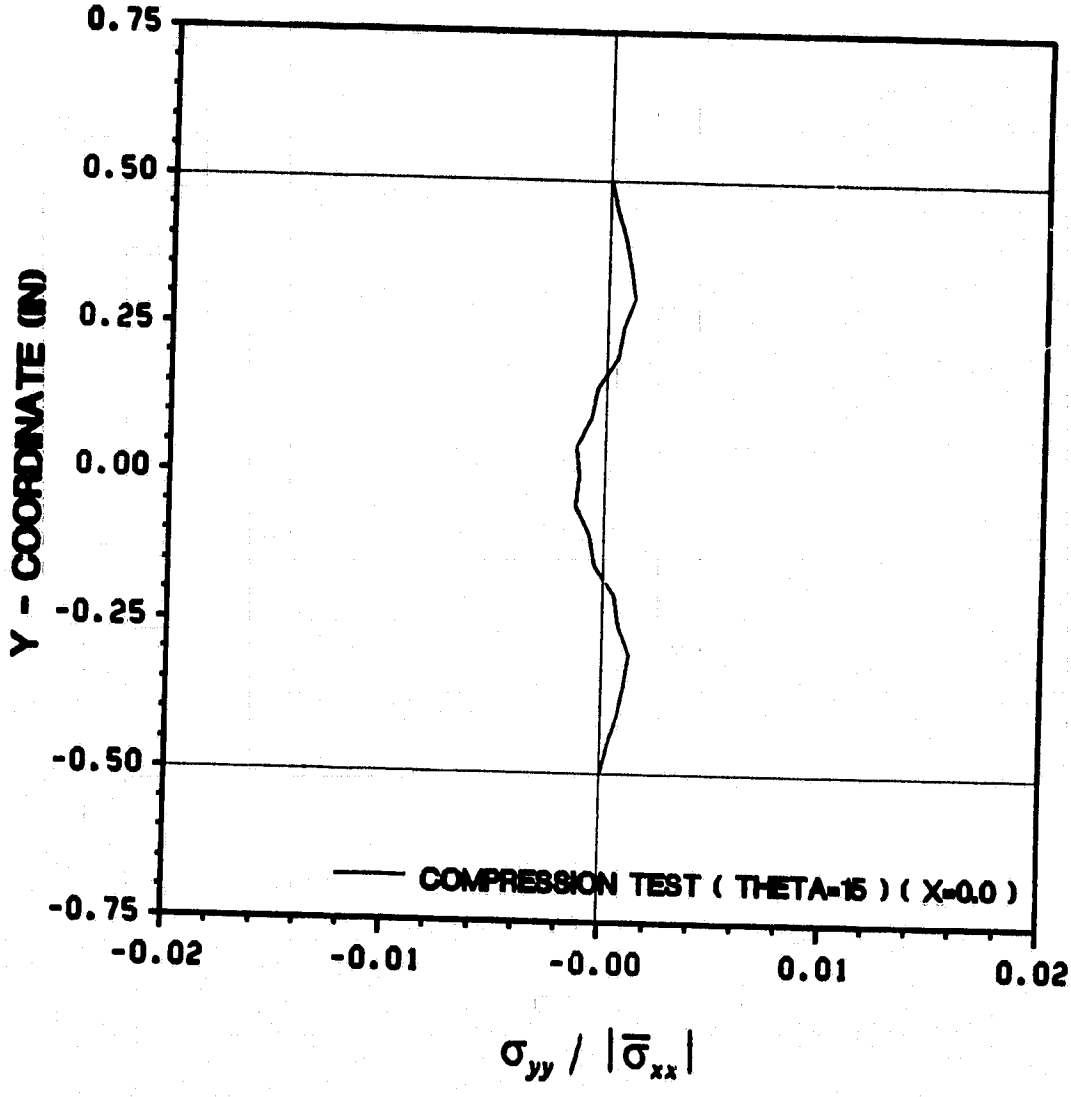

Figure 143. 15° Off-Axis Tests: (σ_{yy} / $|\bar{\sigma}_{xx}|$)

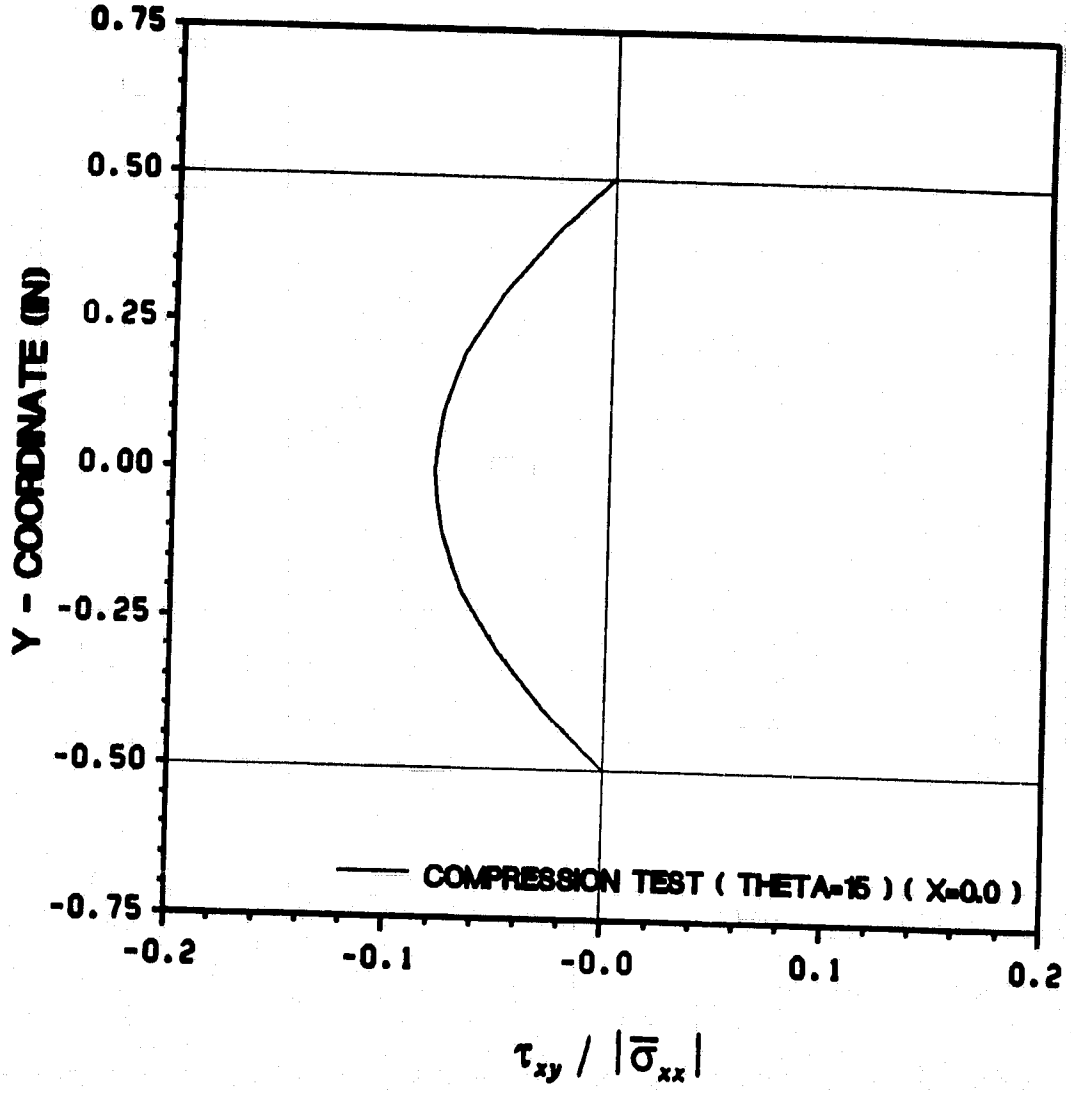

Figure 144. 15° Off-Axis Tests: ($\tau_{xy} / |\overline{\sigma}_{xx}|$)

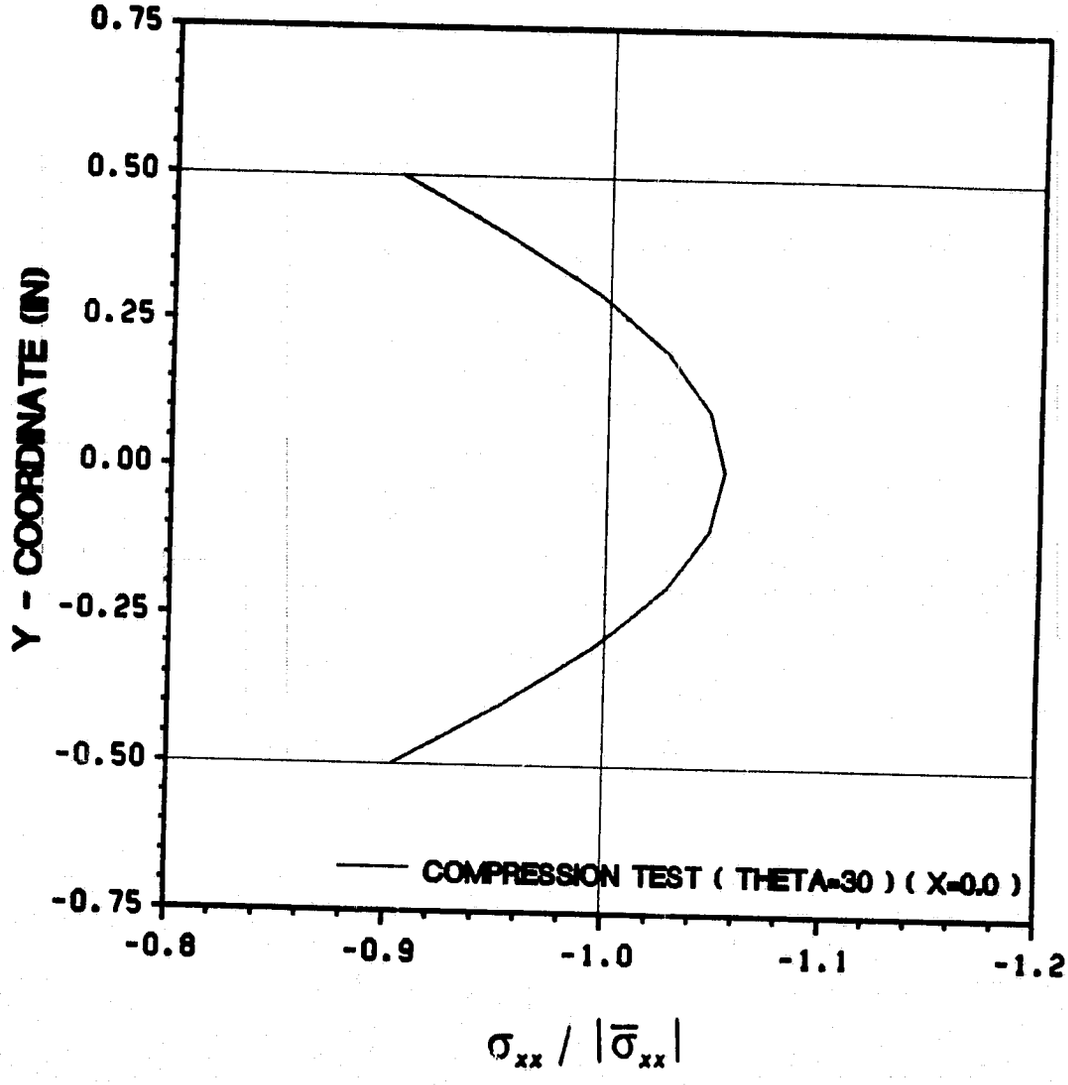

Figure 145. 30° Off-Axis Tests: (σ_{xx} / $|\bar{\sigma}_{xx}|$)

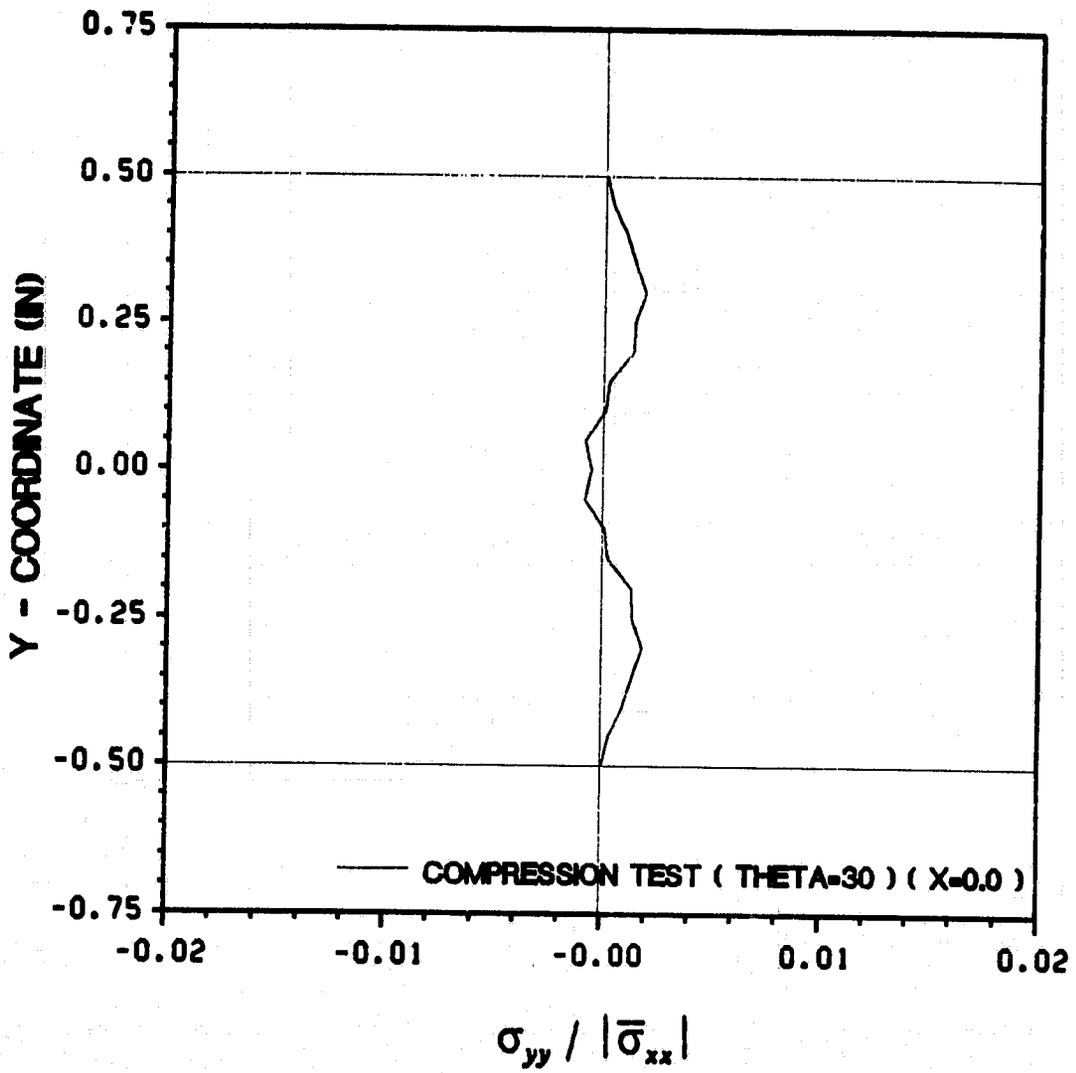

Figure 146. 30° Off-Axis Tests: (σ_{yy} / $|\bar{\sigma}_{xx}|$)

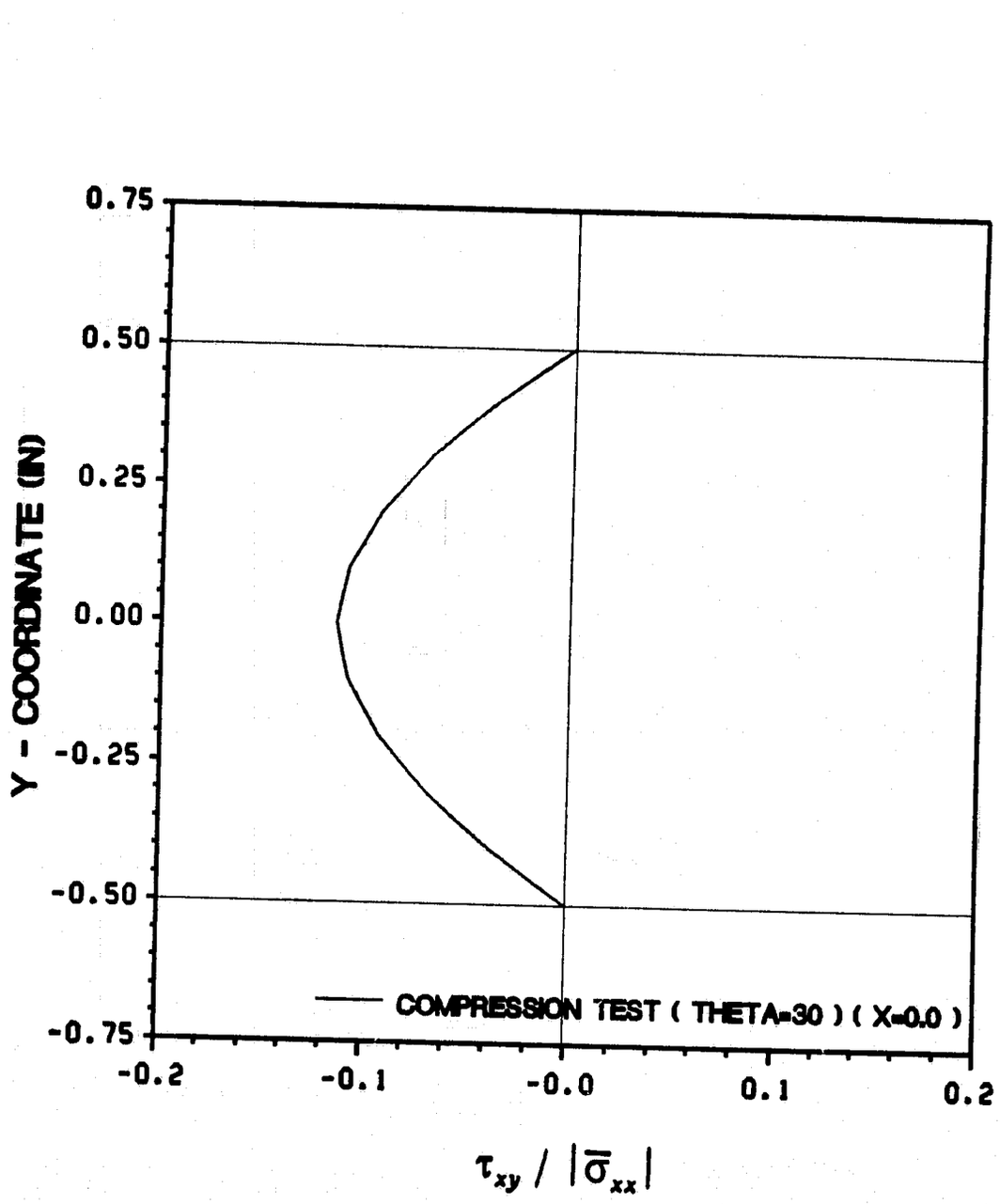

Figure 147. 30° Off-Axis Tests: ($\tau_{xy} / |\overline{\sigma}_{xx}|$)

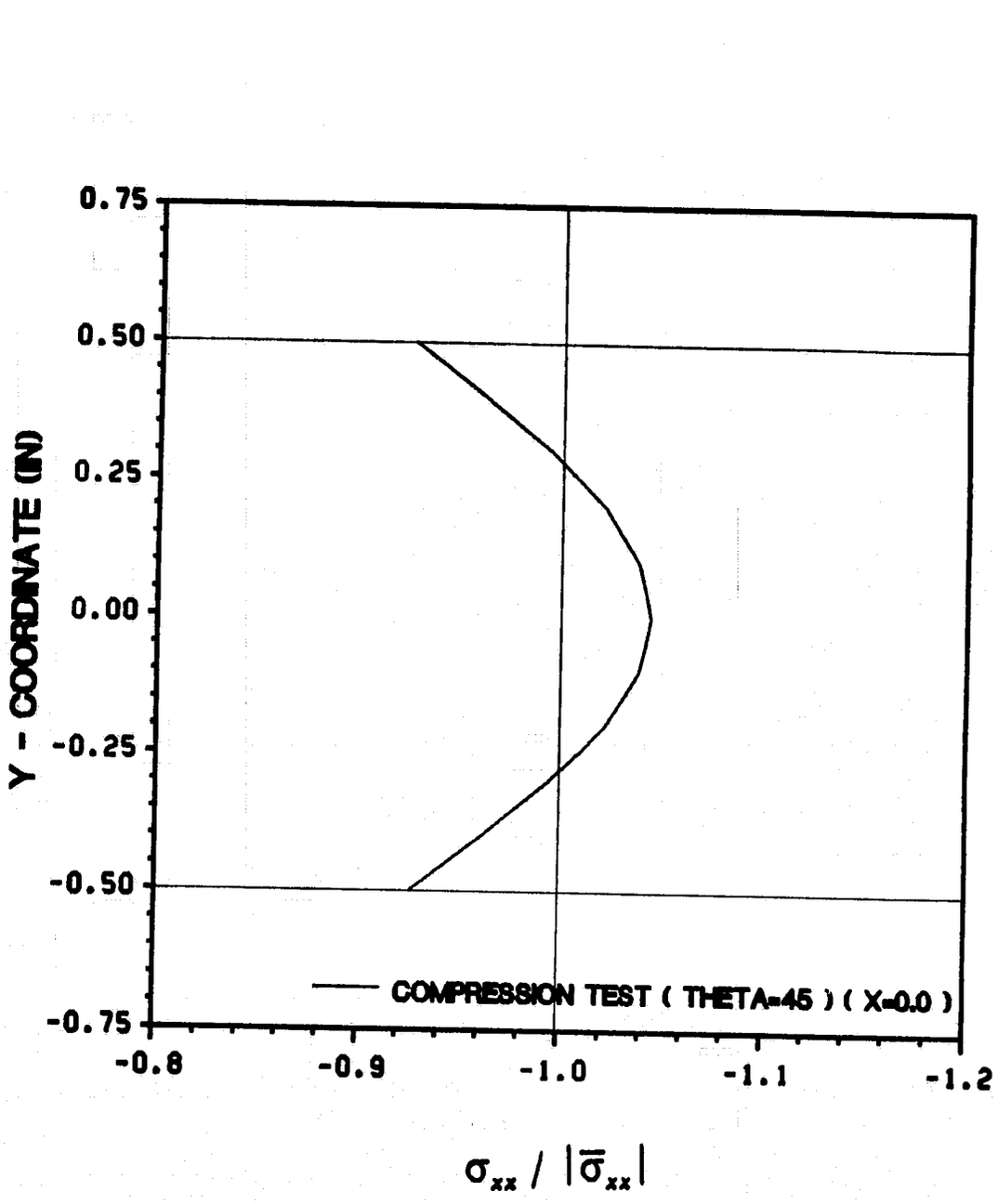

Figure 148. 45° Off-Axis Tests: (σ_{xx} / $|\bar{\sigma}_{xx}|$)

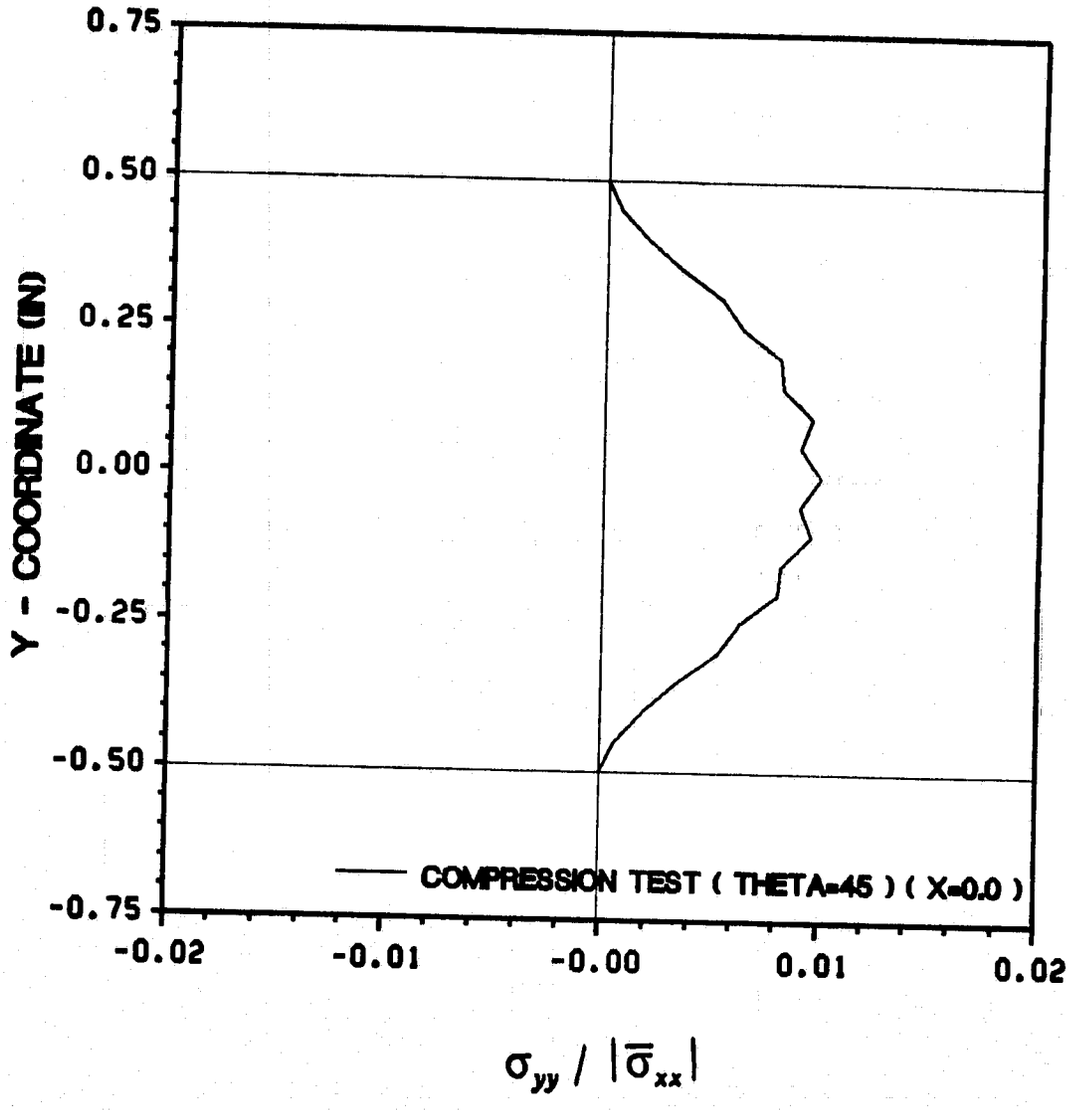

Figure 149. 45° Off-Axis Tests: (σ_{yy} / $|\overline{\sigma}_{xx}|$)

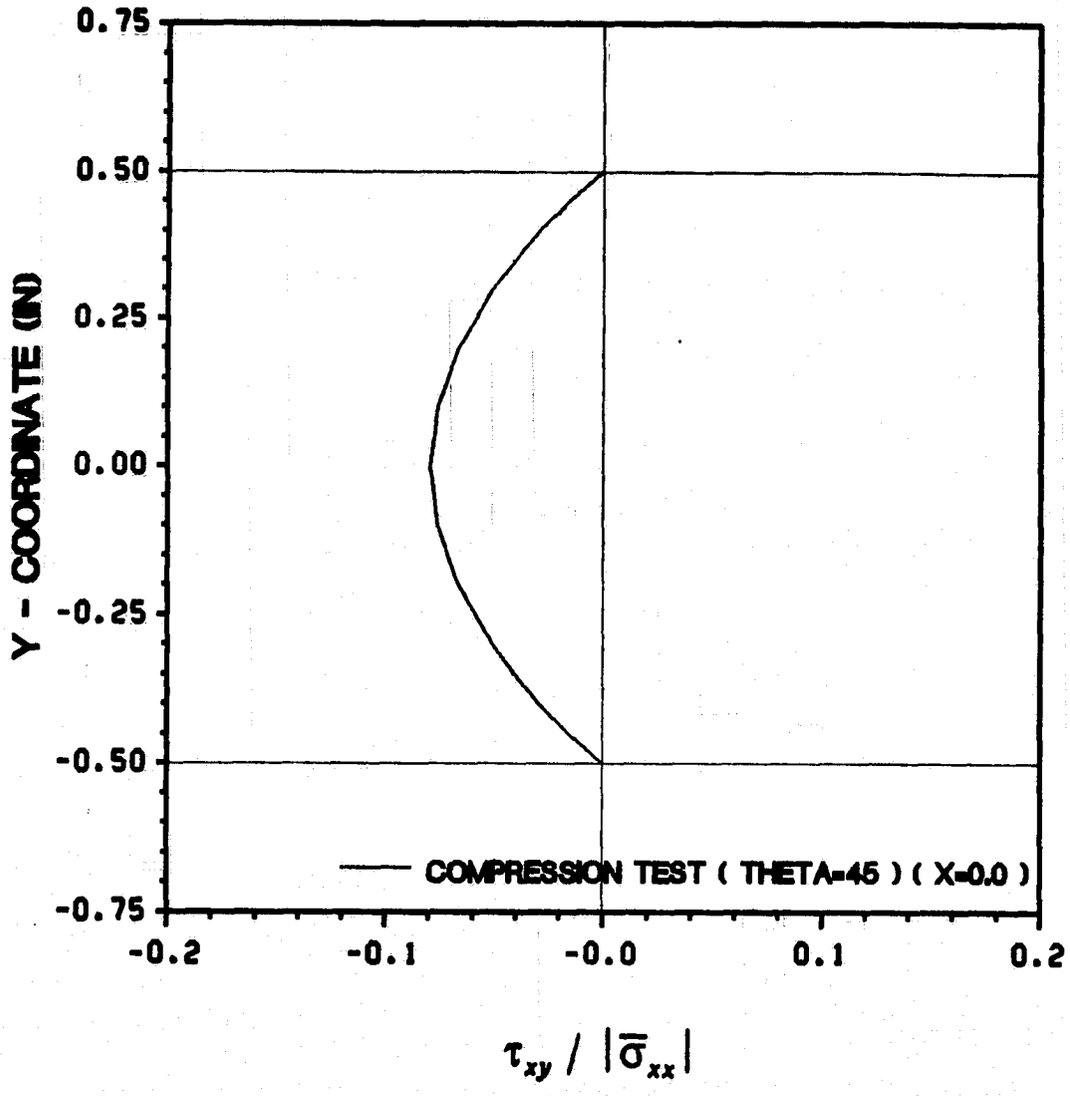

Figure 150. 45° Off-Axis Tests: ($\tau_{xy} / |\overline{\sigma}_{xx}|$)

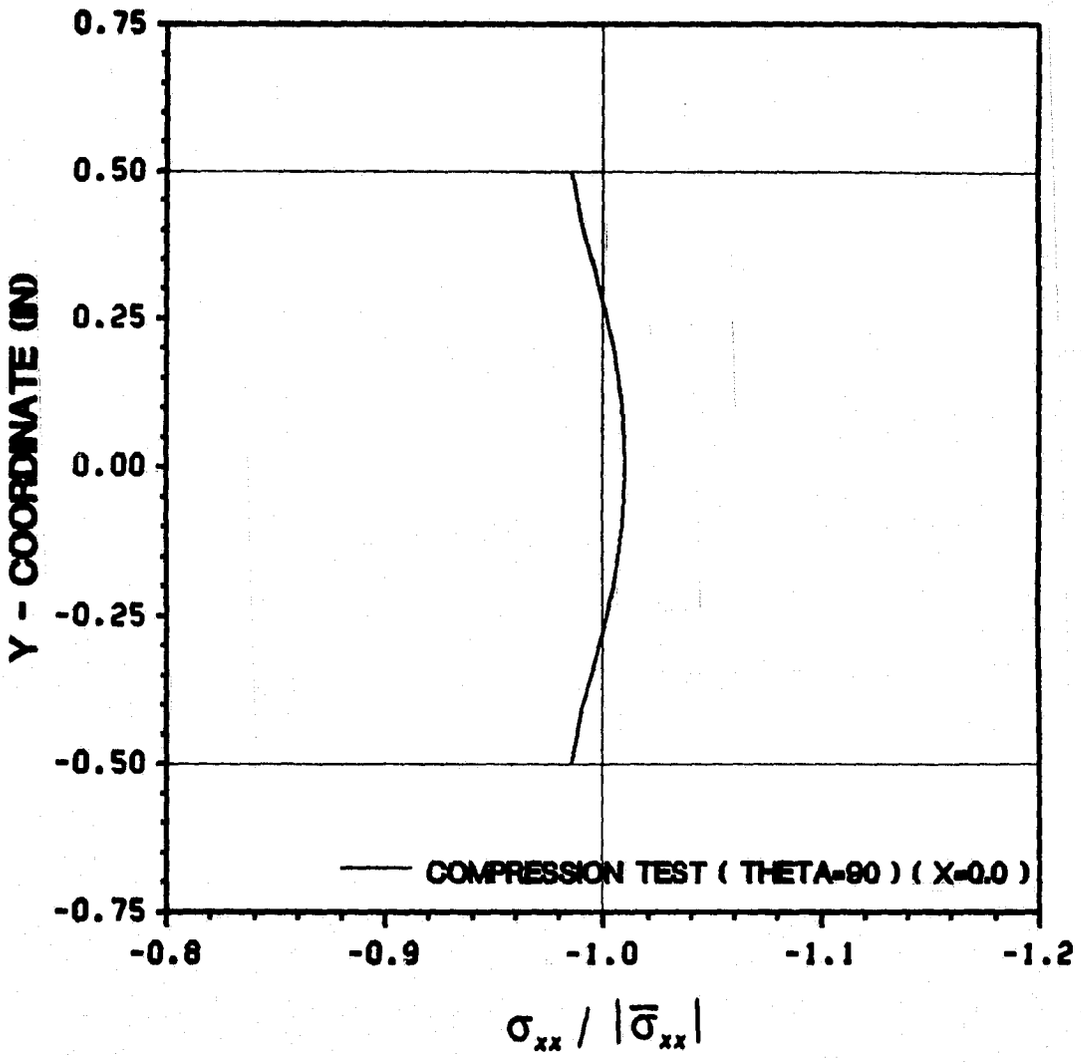

Figure 151. 90° On-Axis Tests: (σ_{xx} / $|\overline{\sigma}_{xx}|$)

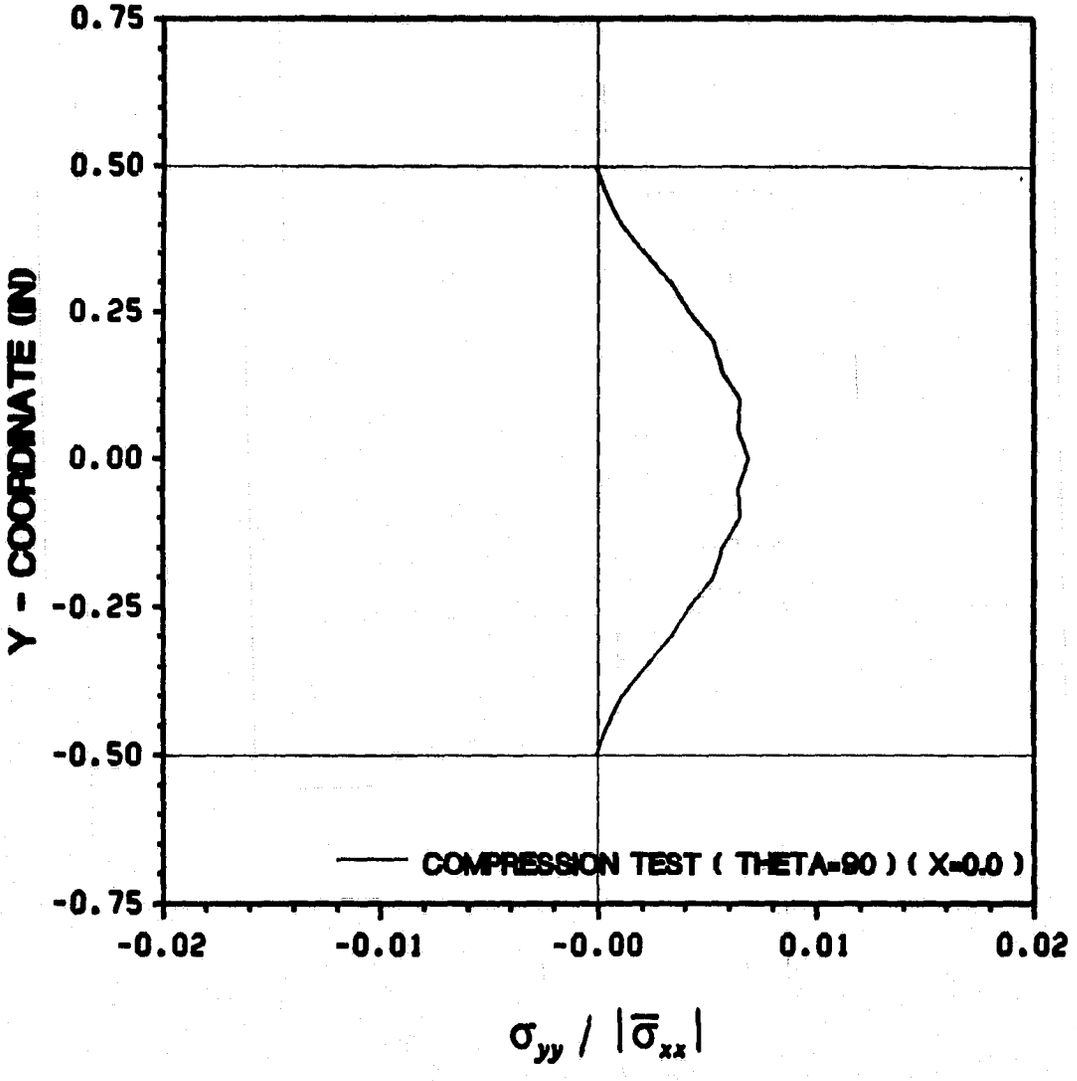

Figure 152. 90° On-Axis Tests: (σ_{yy} / $|\bar{\sigma}_{xx}|$)

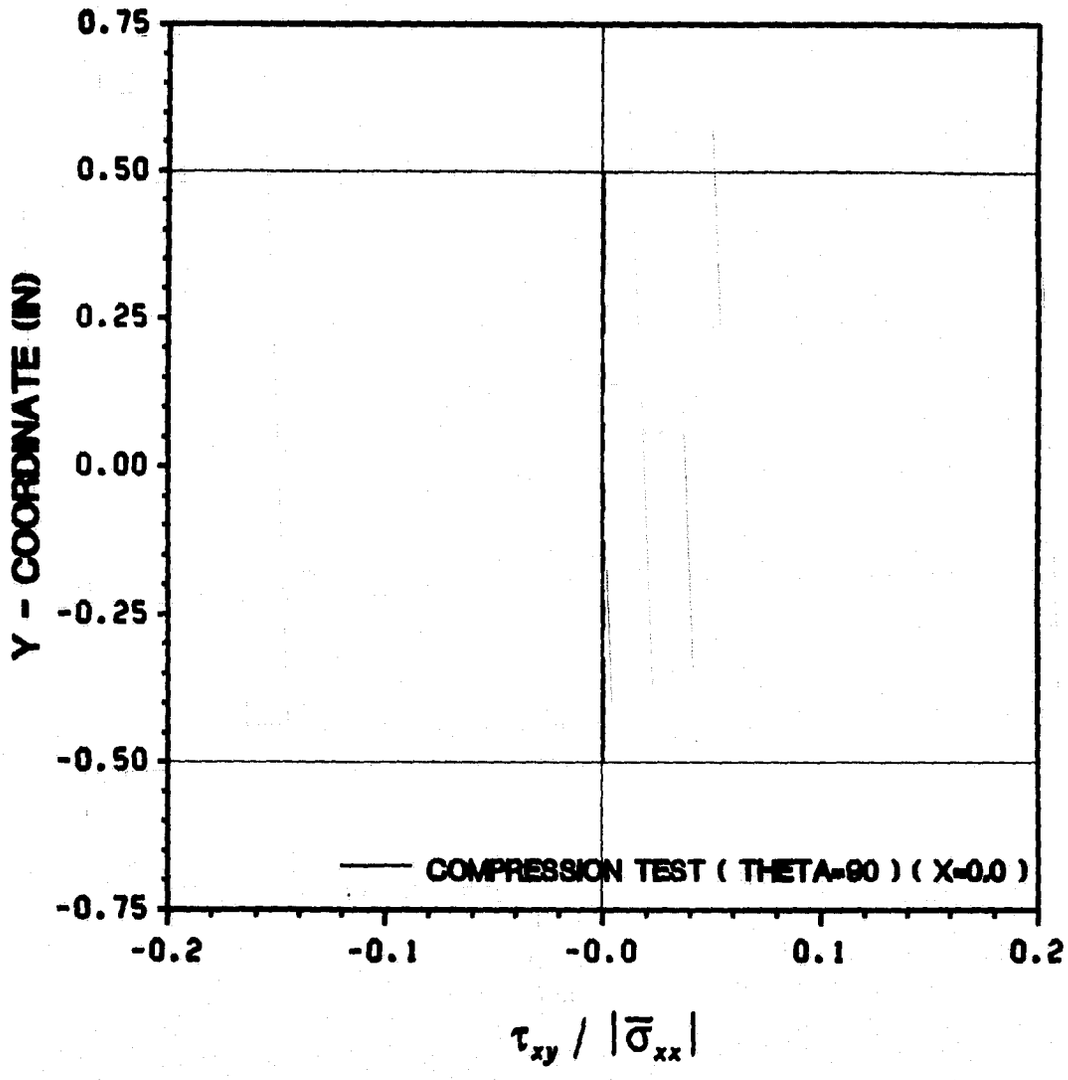

Figure 153. 90° On-Axis Tests: ($\tau_{xy} / |\bar{\sigma}_{xx}|$)

D.2 Boundary Condition #2 (one side node supported)

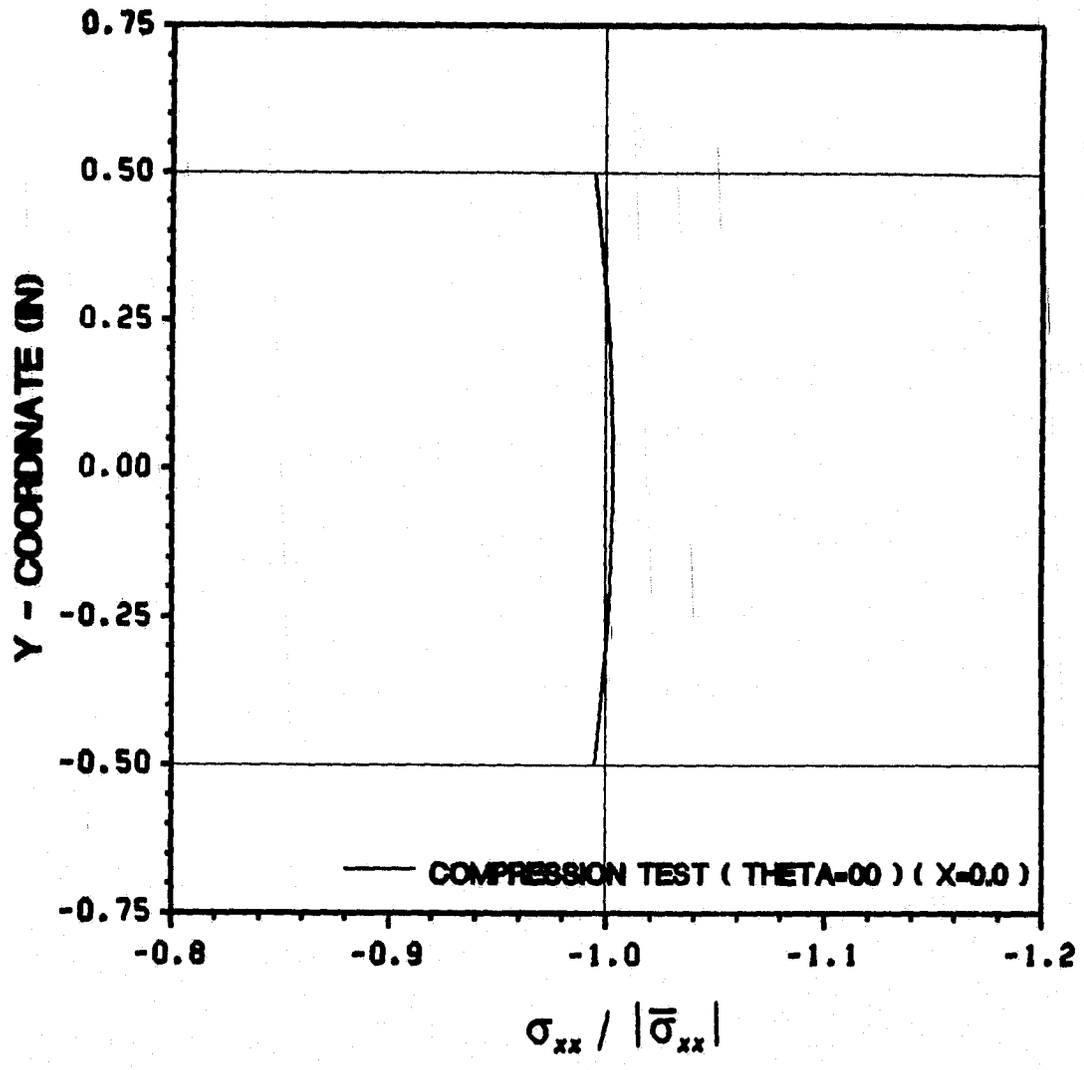

Figure 154. 0° On-Axis Tests: (σ_{xx} / $|\bar{\sigma}_{xx}|$)

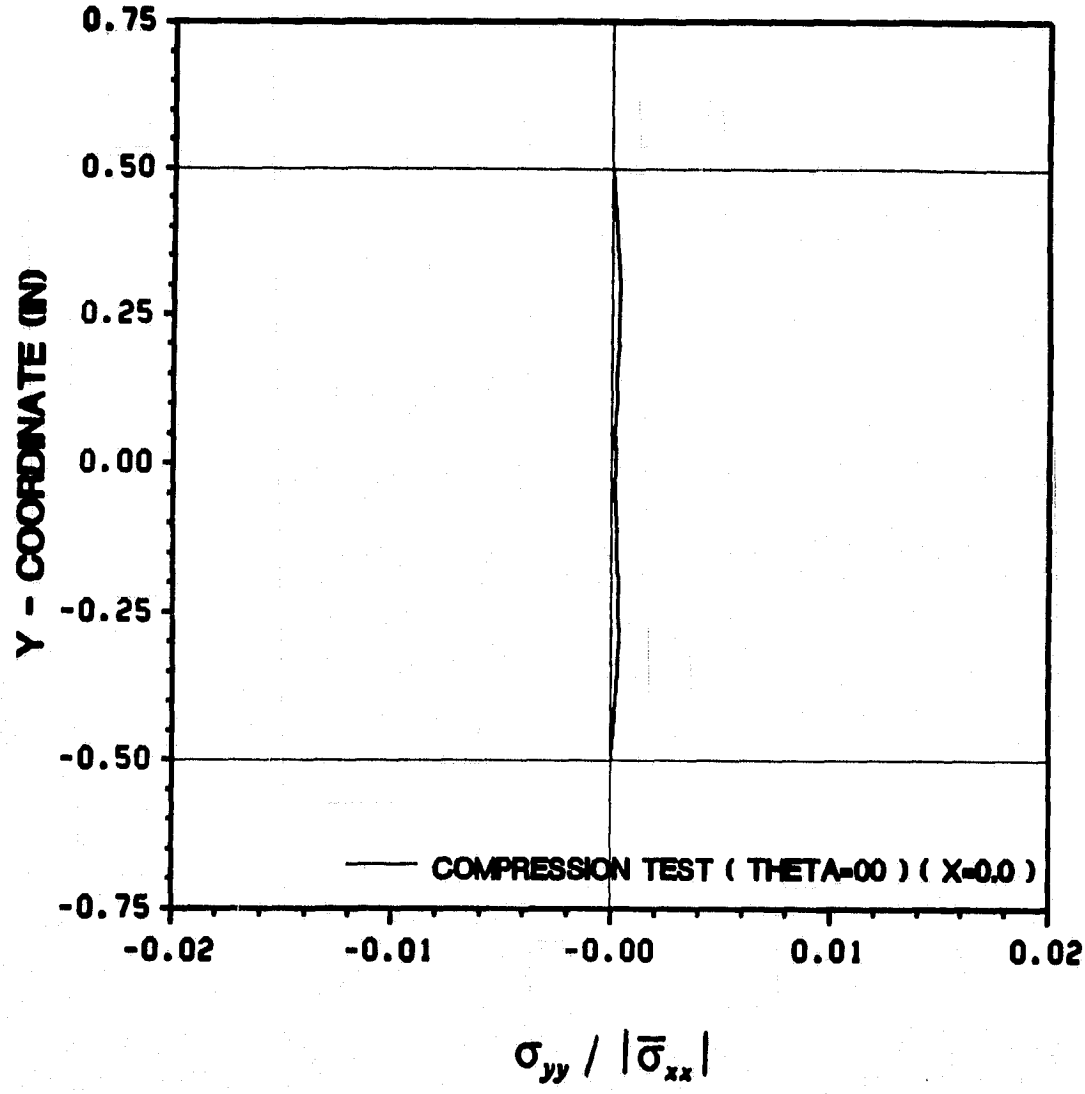

Figure 155. 0° On-Axis Tests: (σ_{yy} / $|\overline{\sigma}_{xx}|$)

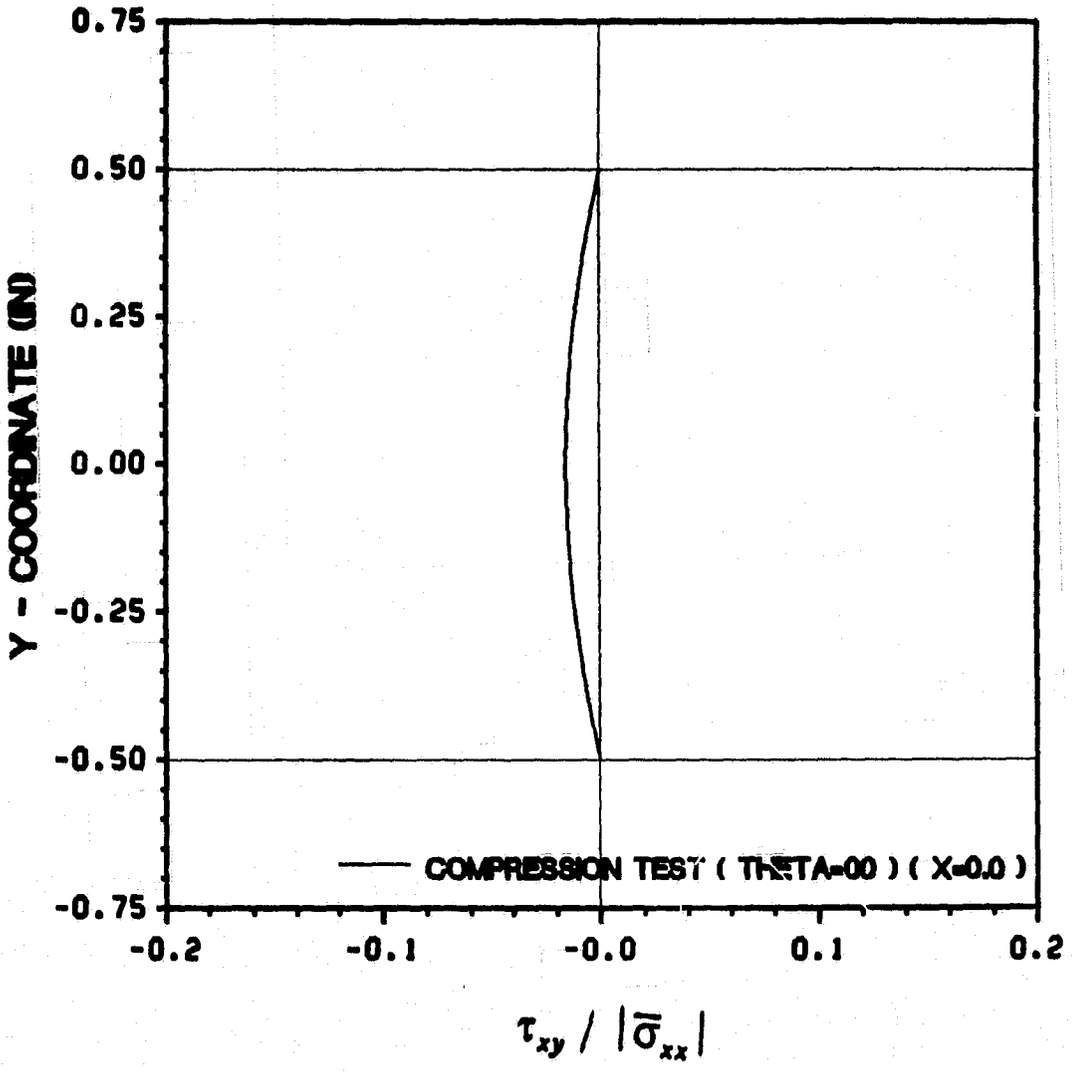

Figure 156. 0° On-Axis Tests: ($\tau_{xy} / |\bar{\sigma}_{xx}|$)

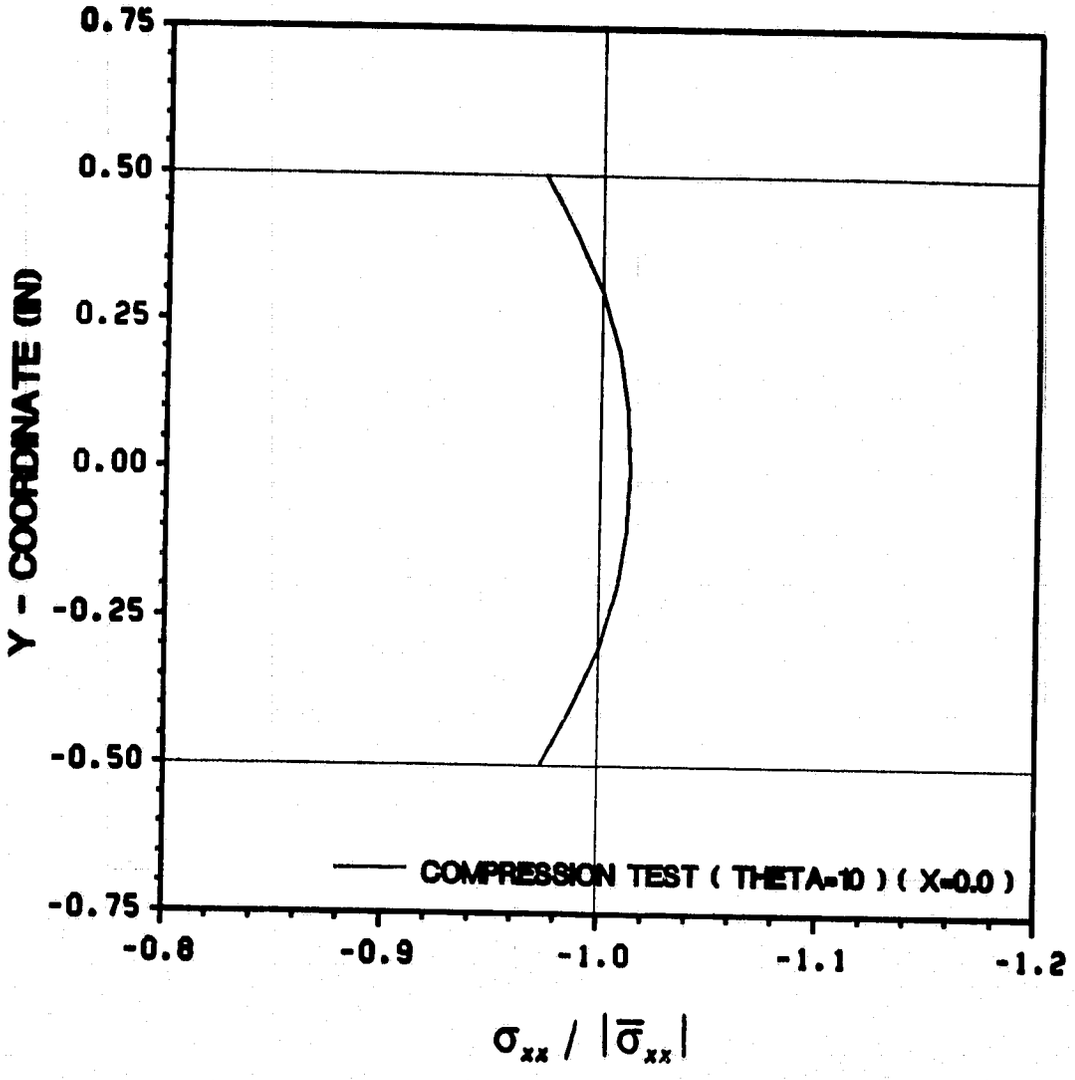

Figure 157. 10° Off-Axis Tests: (σ_{xx} / $|\bar{\sigma}_{xx}|$)

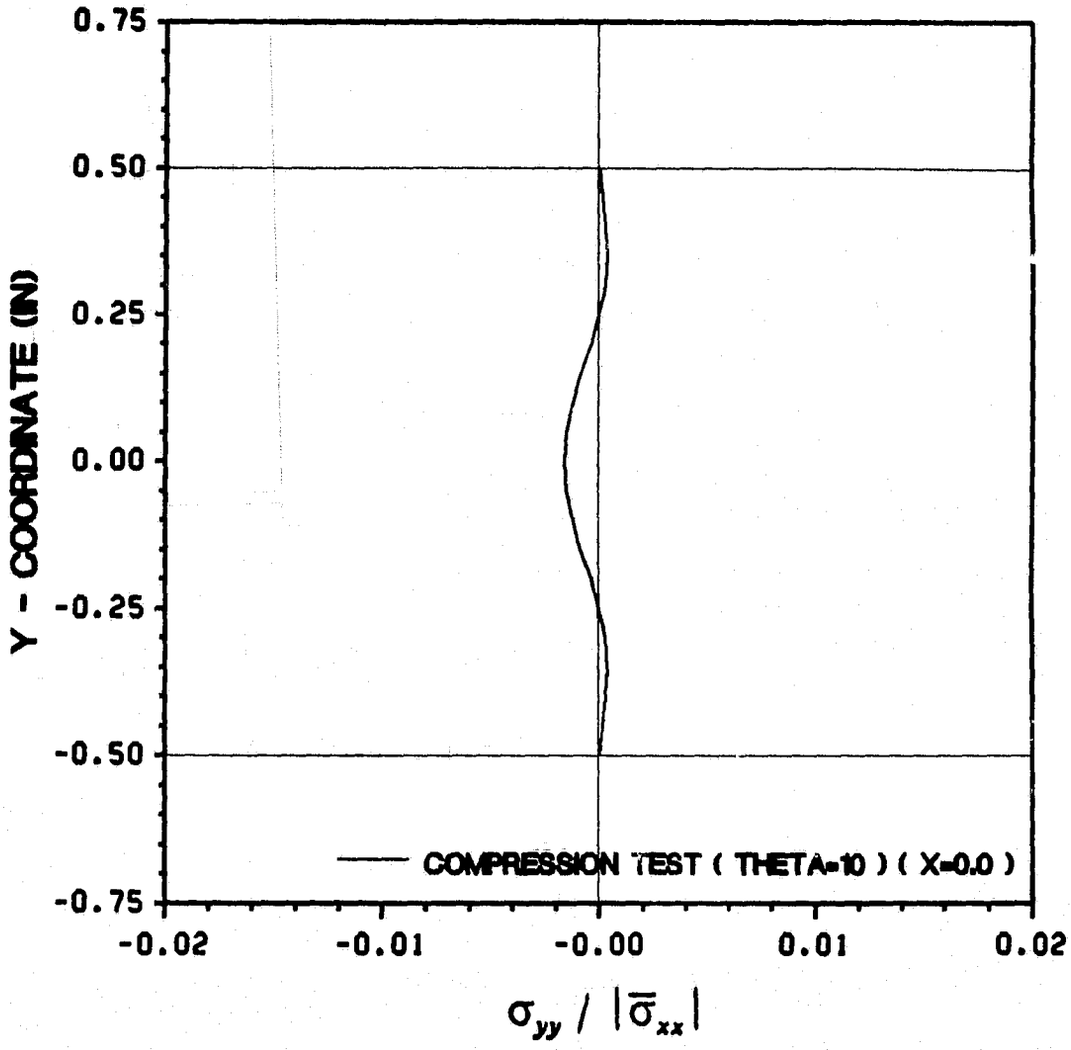

Figure 158. 10° Off-Axis Tests: (σ_{yy} / $|\bar{\sigma}_{xx}|$)

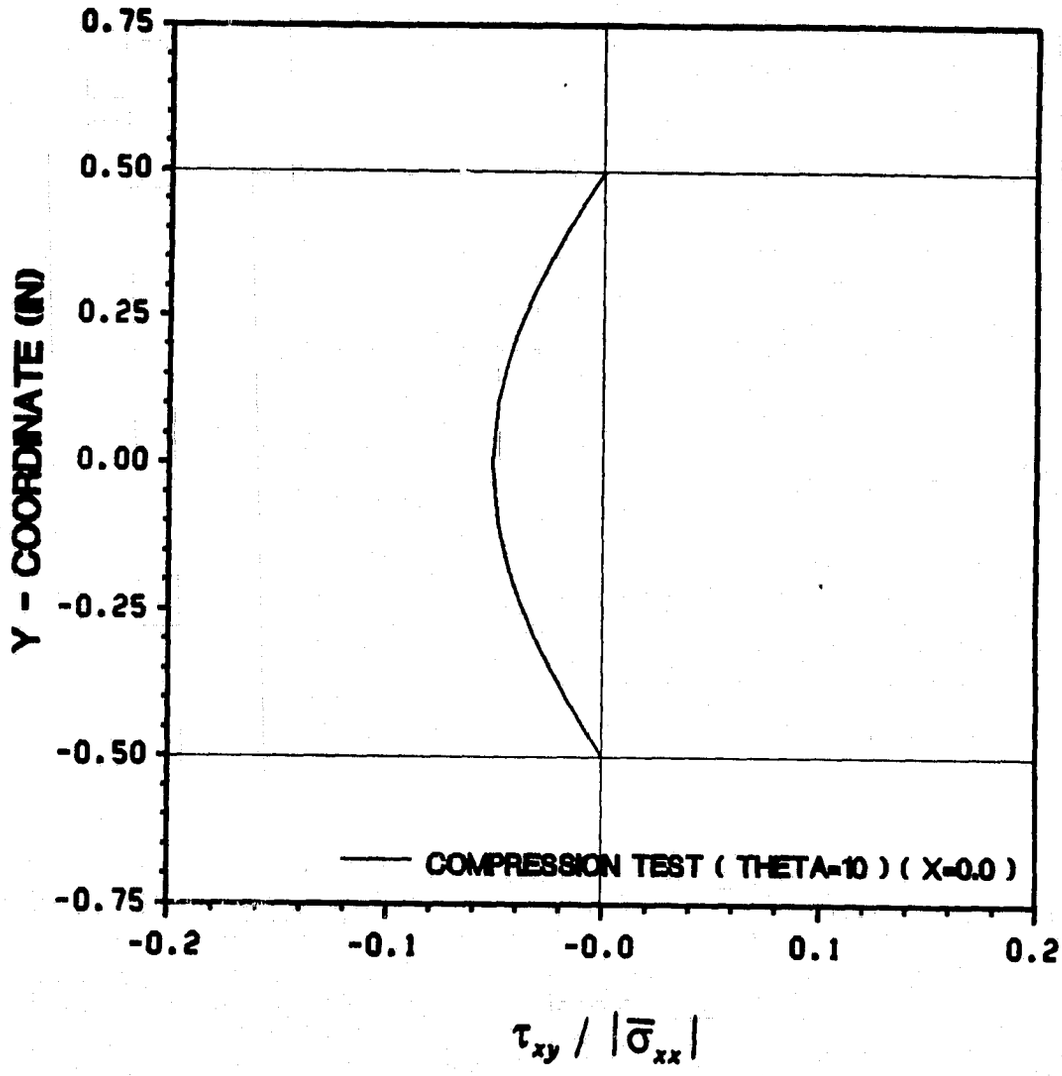

Figure 159. 10° Off-Axis Tests: ($\tau_{xy} / |\overline{\sigma}_{xx}|$)

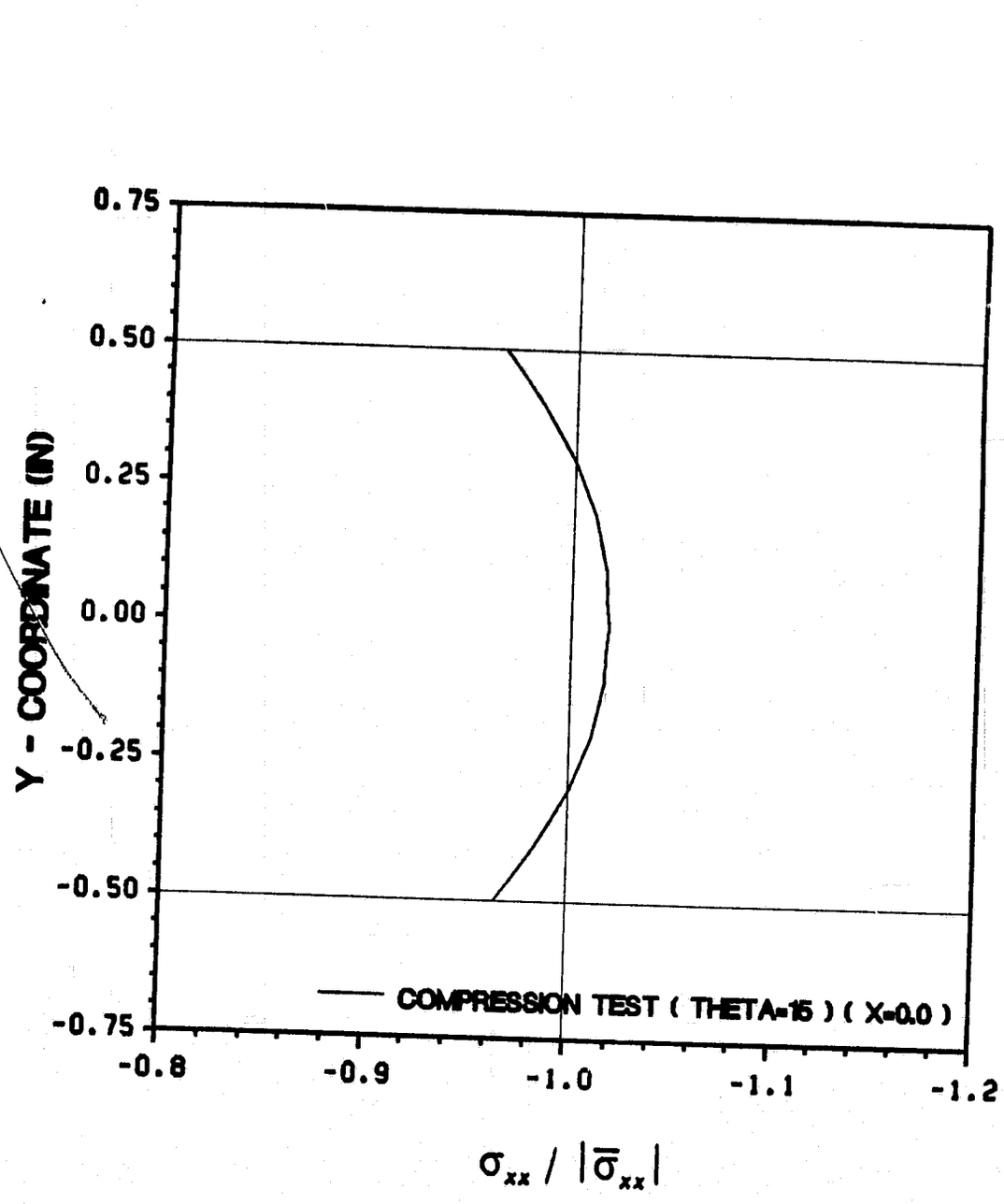

Figure 160. 15° Off-Axis Tests: (σ_{xx} / $|\bar{\sigma}_{xx}|$)

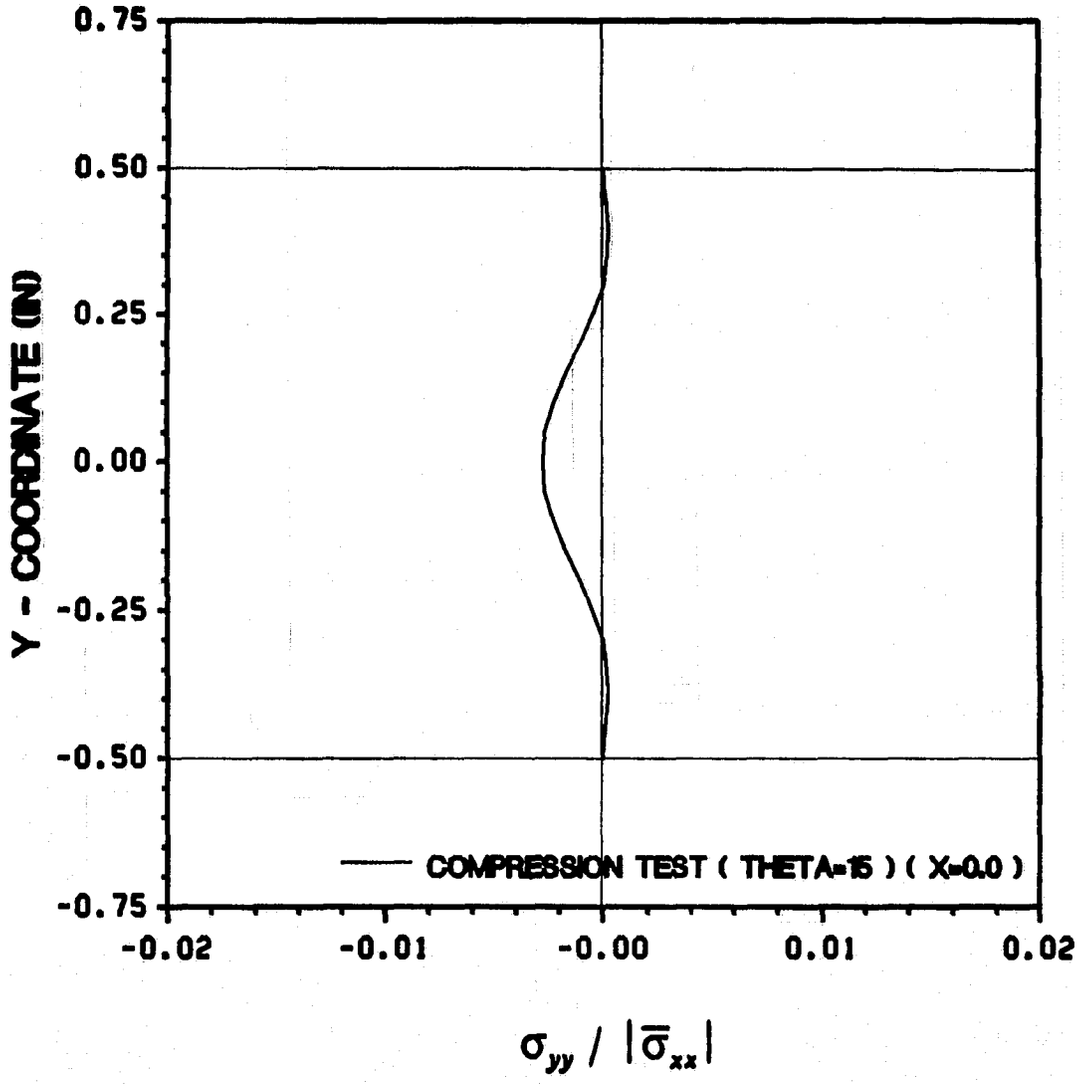

Figure 161. 15° Off-Axis Tests: (σ_{yy} / $|\bar{\sigma}_{xx}|$)

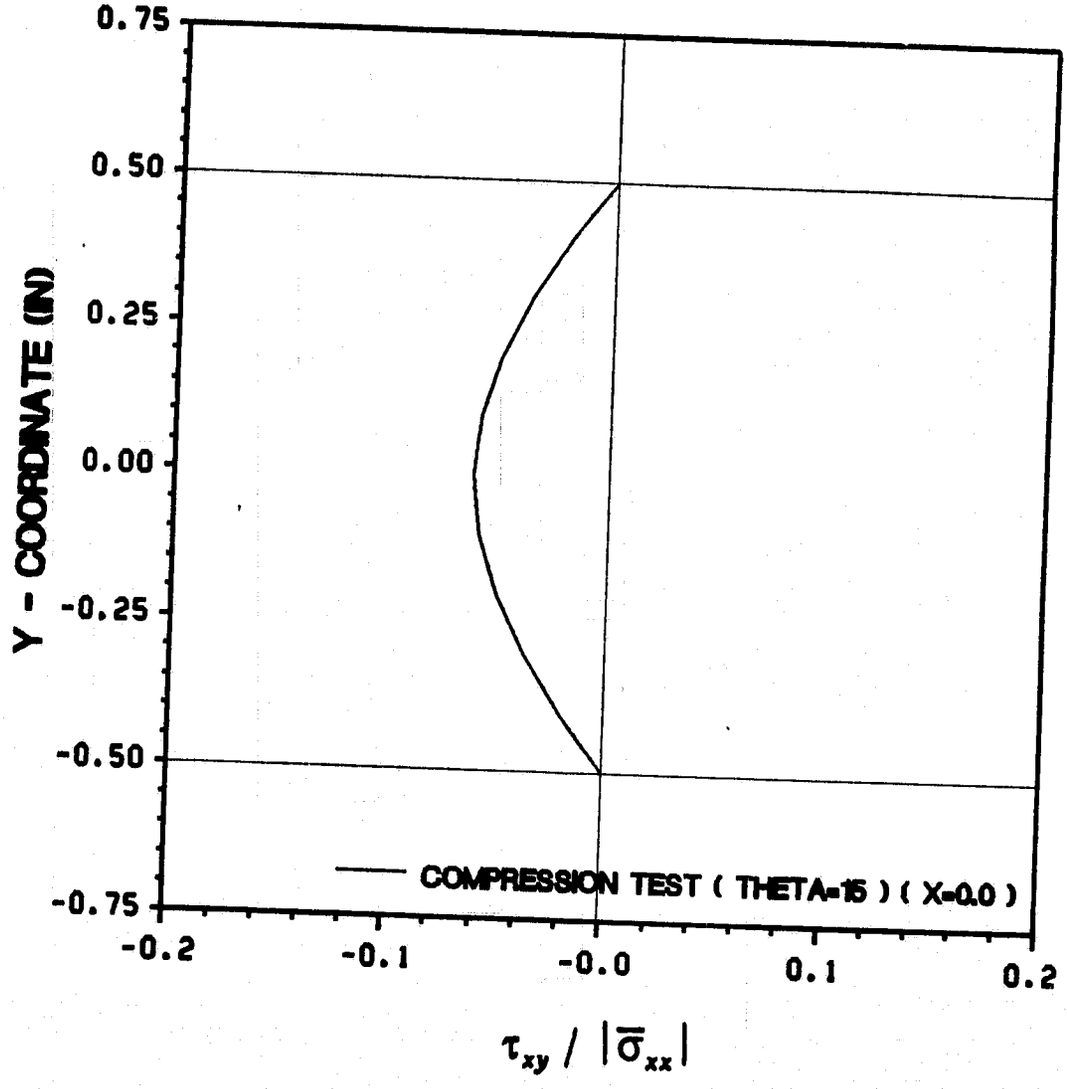

Figure 162. 15° Off-Axis Tests: (τ_{xy} / $|\overline{\sigma}_{xx}|$)

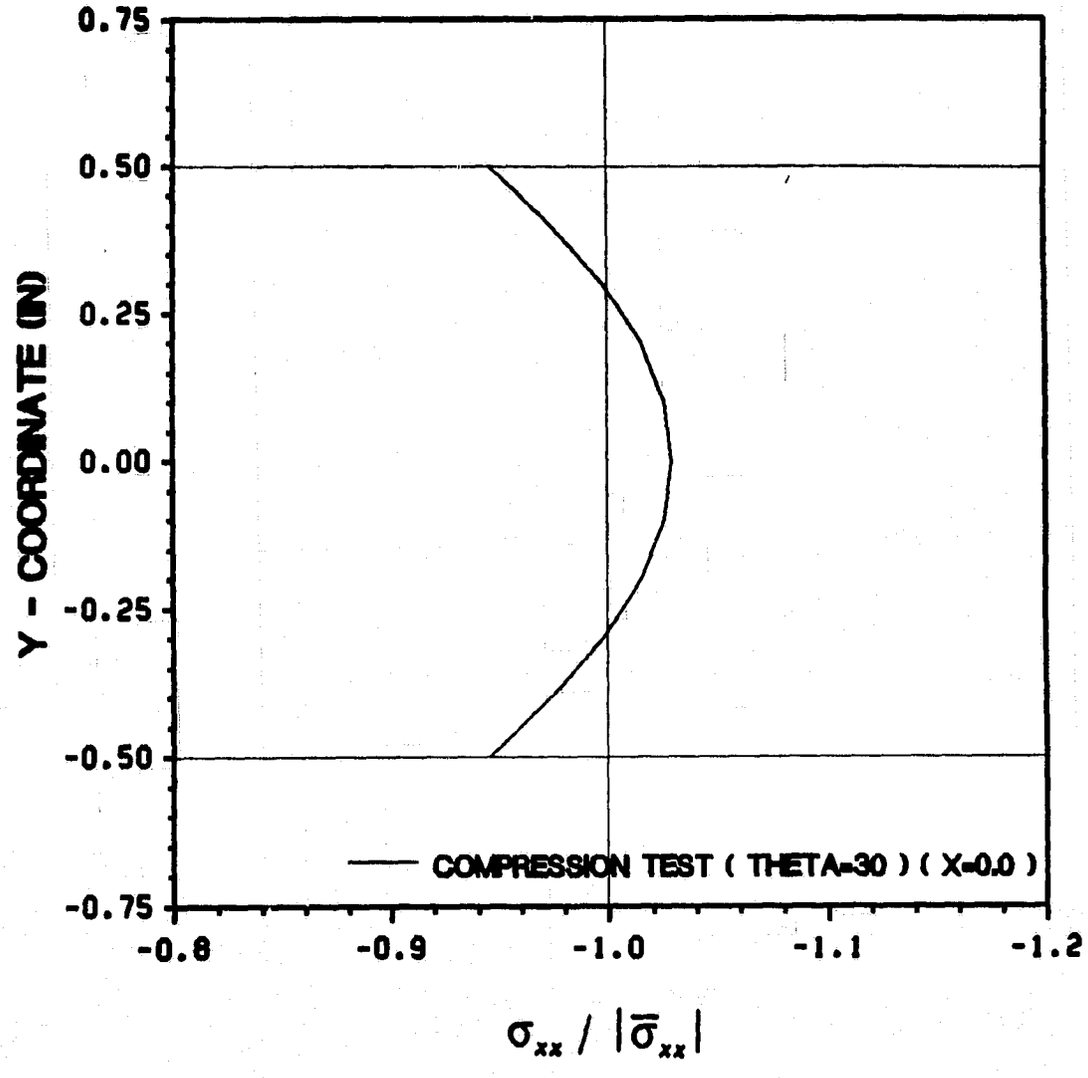

Figure 163. 30° Off-Axis Tests: (σ_{xx} / $|\bar{\sigma}_{xx}|$)

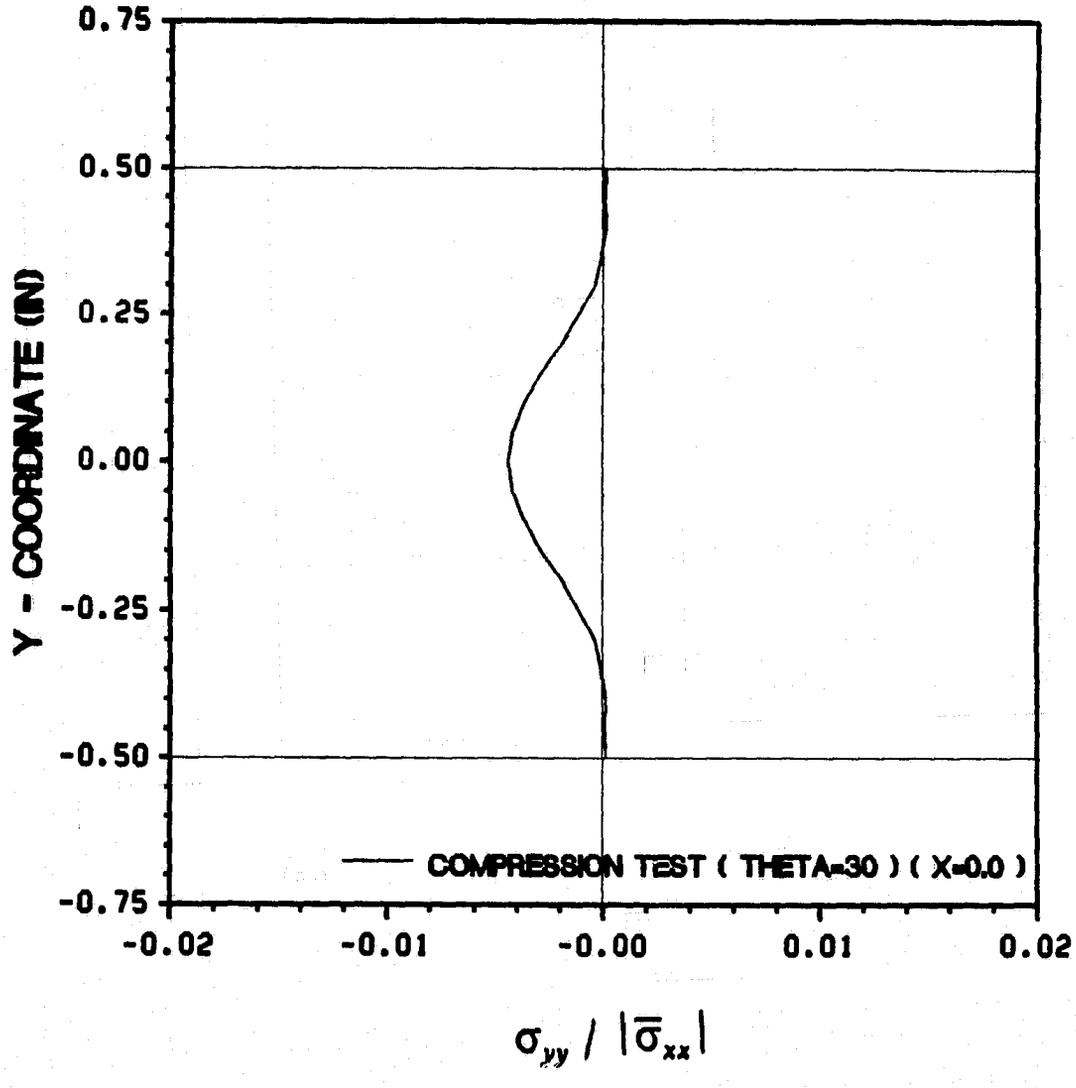

Figure 164. 30° Off-Axis Tests: (σ_{yy} / $|\bar{\sigma}_{xx}|$)

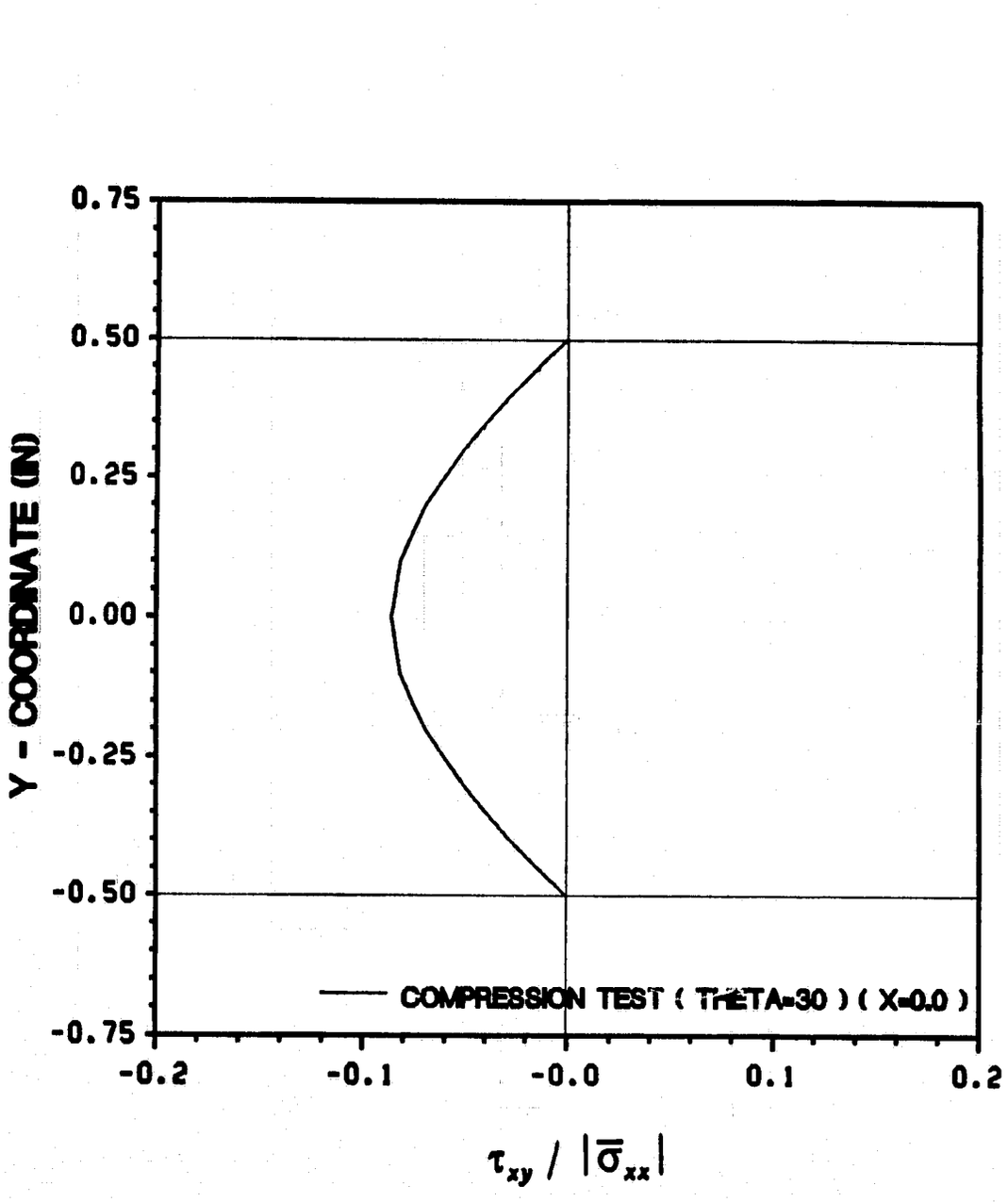

Figure 165. 30° Off-Axis Tests: ($\tau_{xy} / |\overline{\sigma}_{xx}|$)

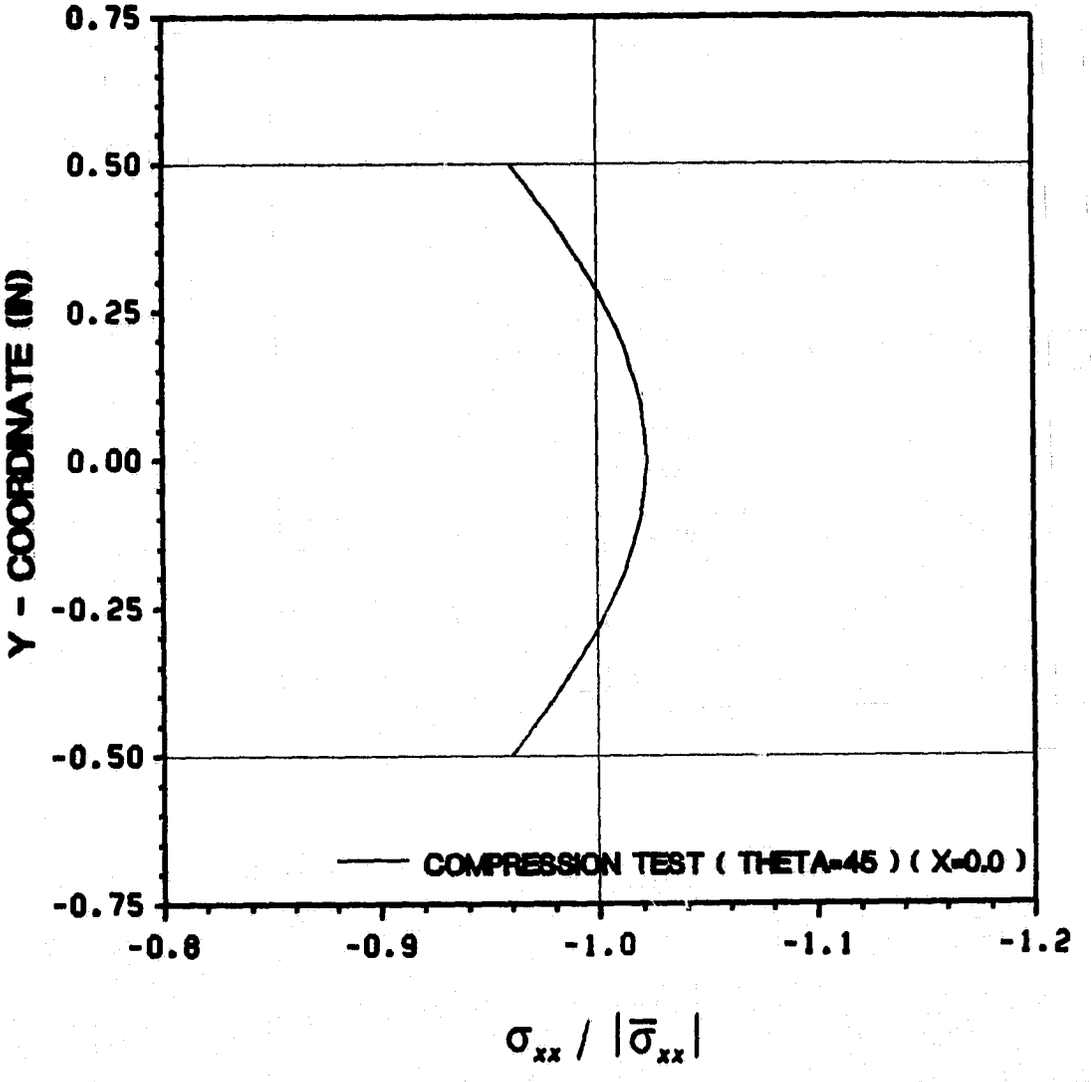

Figure 166. 45° Off-Axis Tests: (σ_{xx} / $|\bar{\sigma}_{xx}|$)

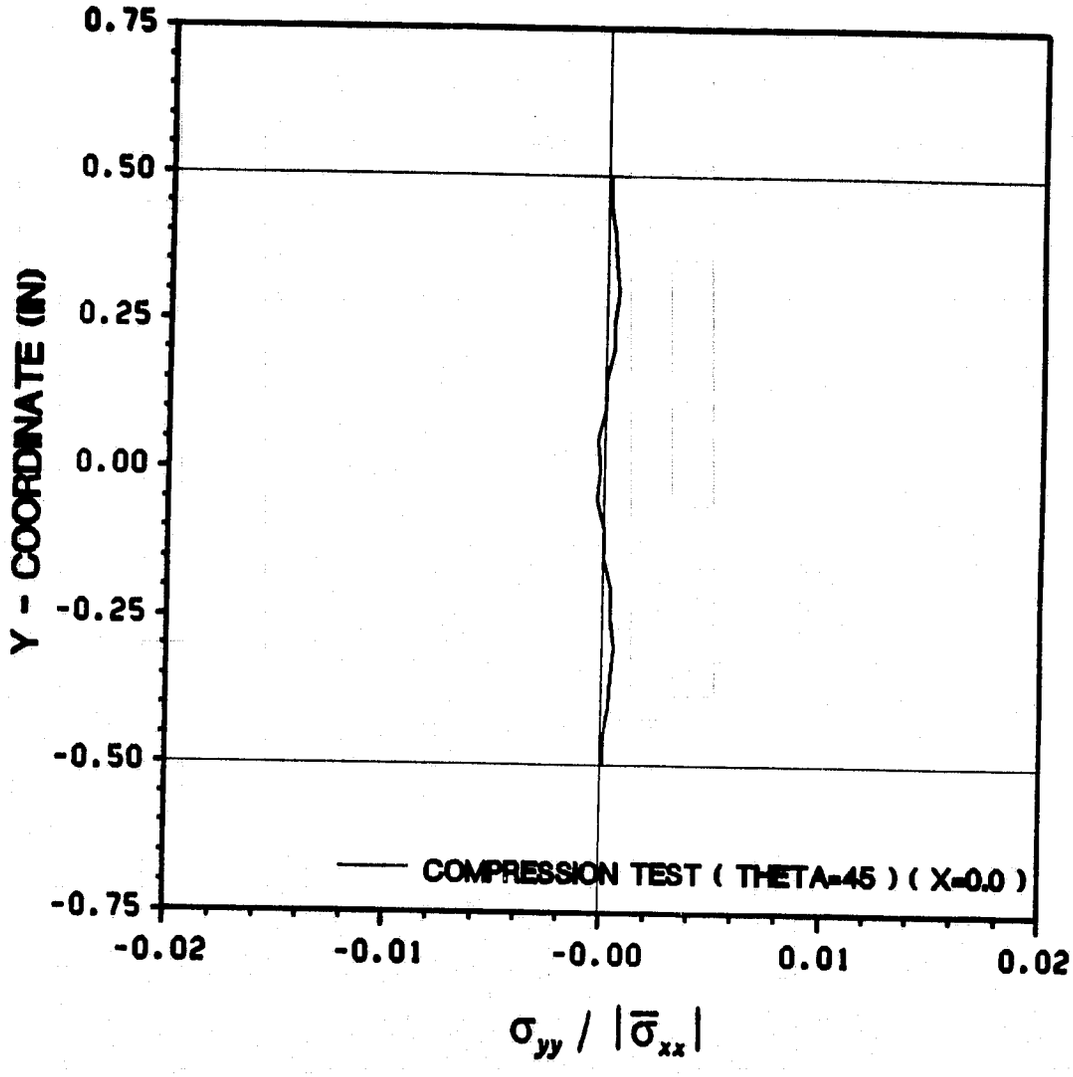

Figure 167. 45° Off-Axis Tests: ($\sigma_{yy} / |\overline{\sigma}_{xx}|$)

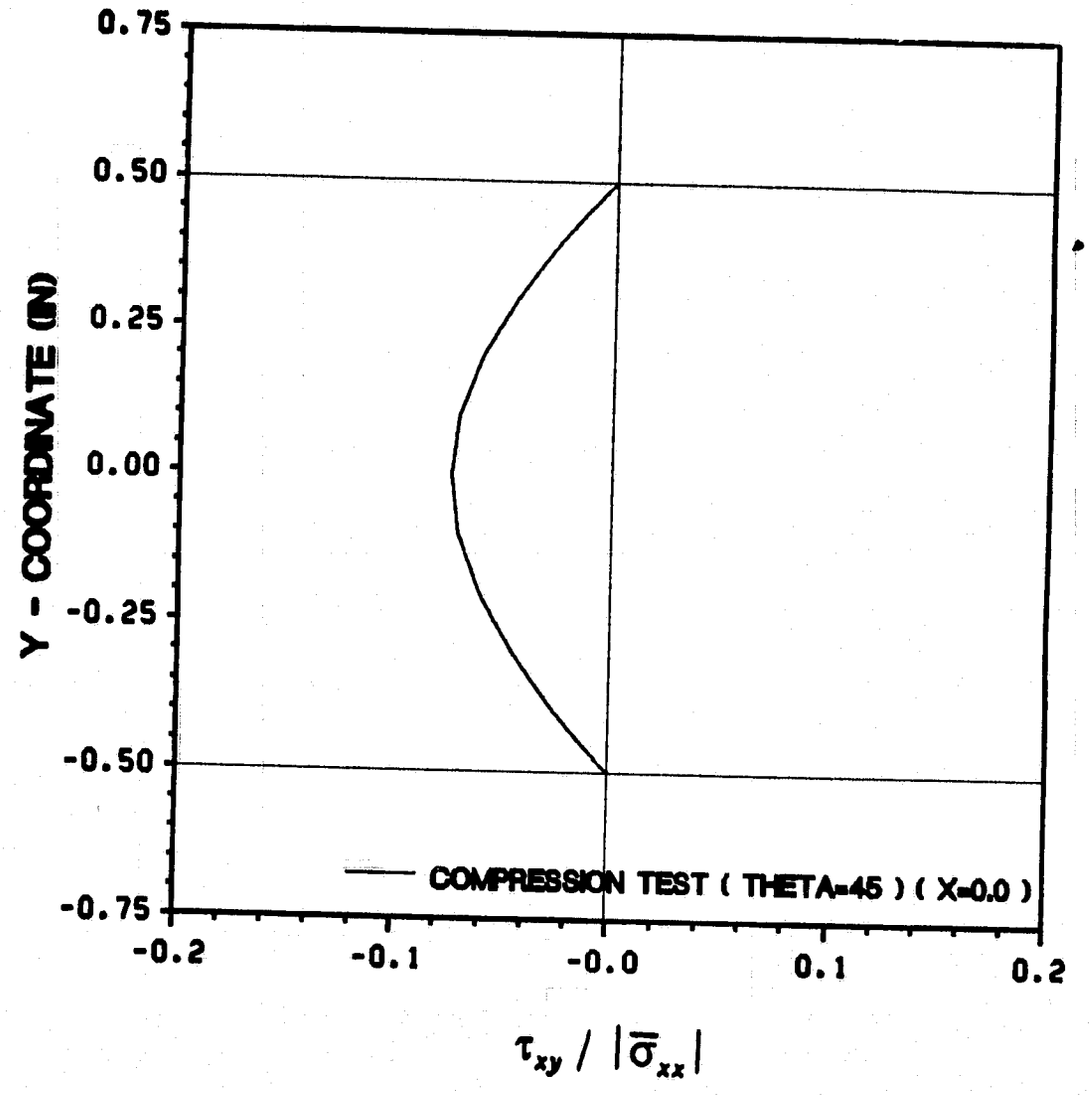

Figure 168. 45° Off-Axis Tests: ($\tau_{xy} / |\overline{\sigma}_{xx}|$)

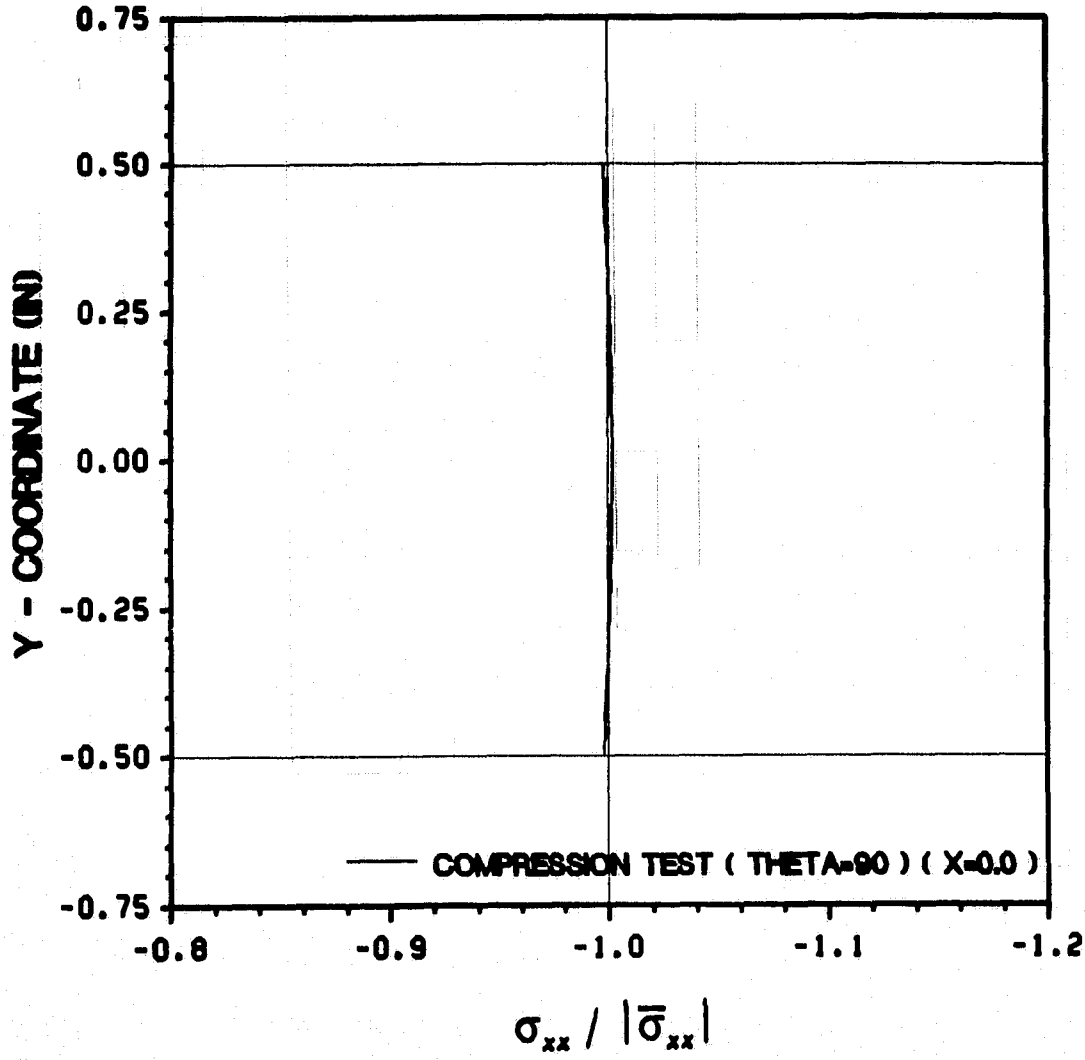

Figure 169. 90° On-Axis Tests: (σ_{xx} / $|\bar{\sigma}_{xx}|$)

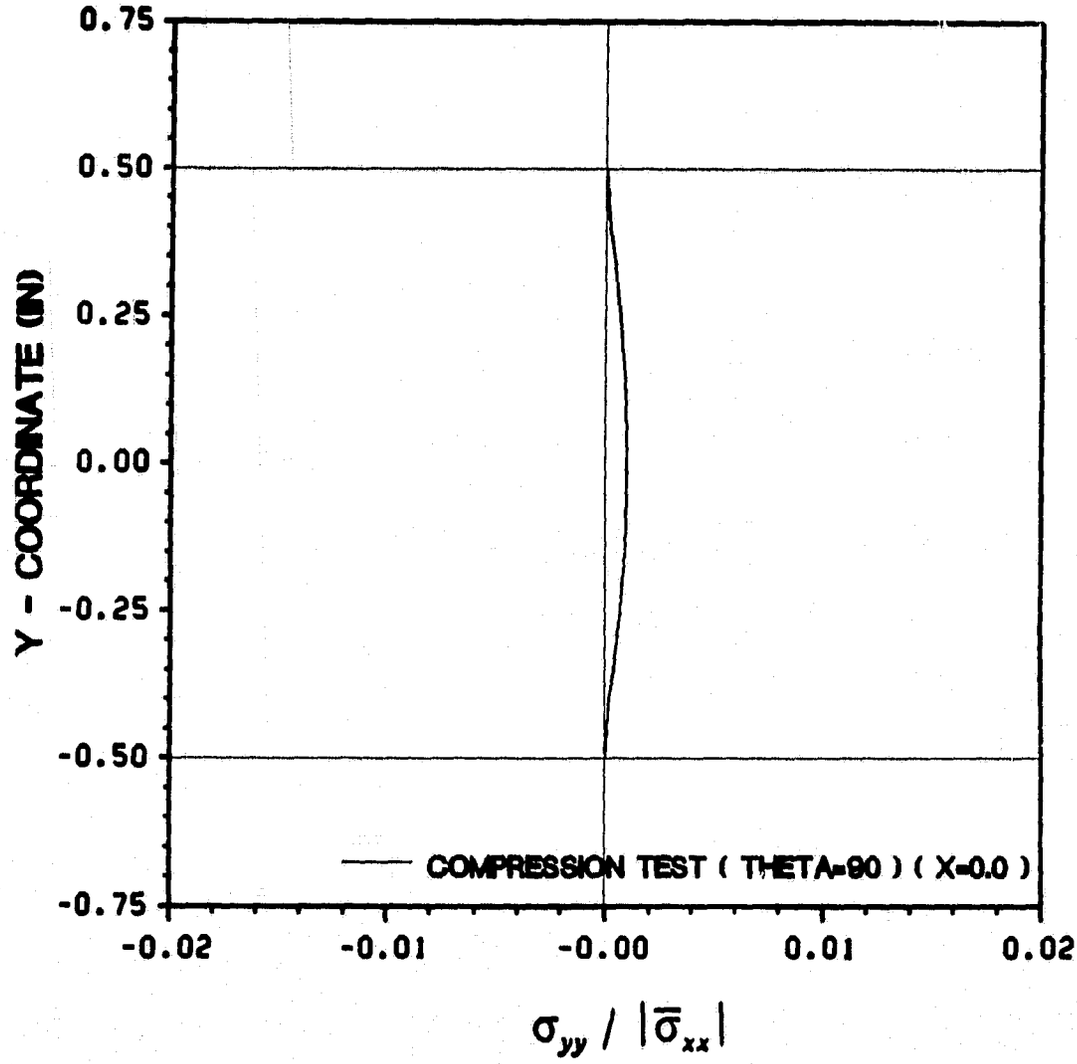

Figure 170. 90° On-Axis Tests: (σ_{yy} / $|\bar{\sigma}_{xx}|$)

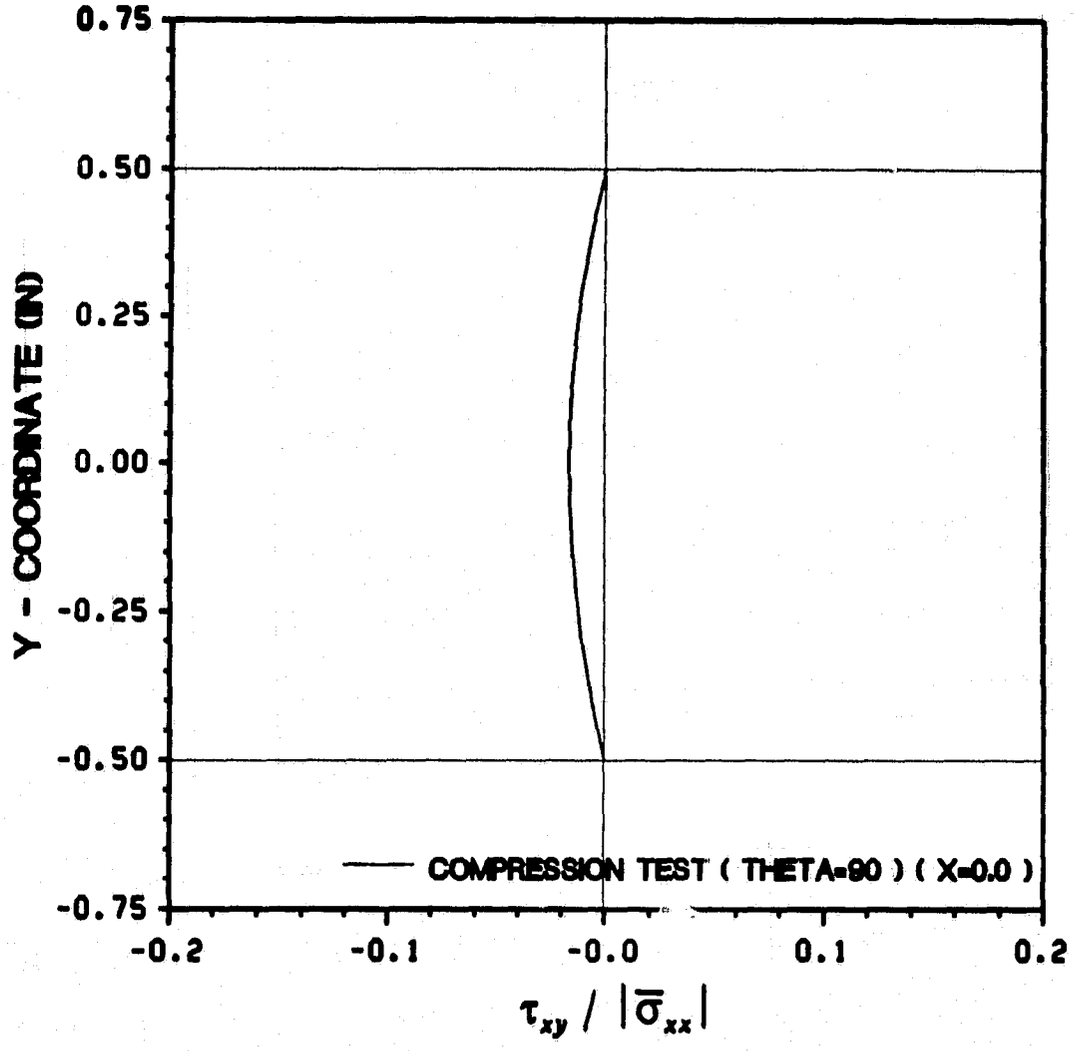

Figure 171. 90° On-Axis Tests: (τ_{xy} / $|\bar{\sigma}_{xx}|$)

Appendix E. Finite Element Results of a Iosipescu Shear Test Coupon

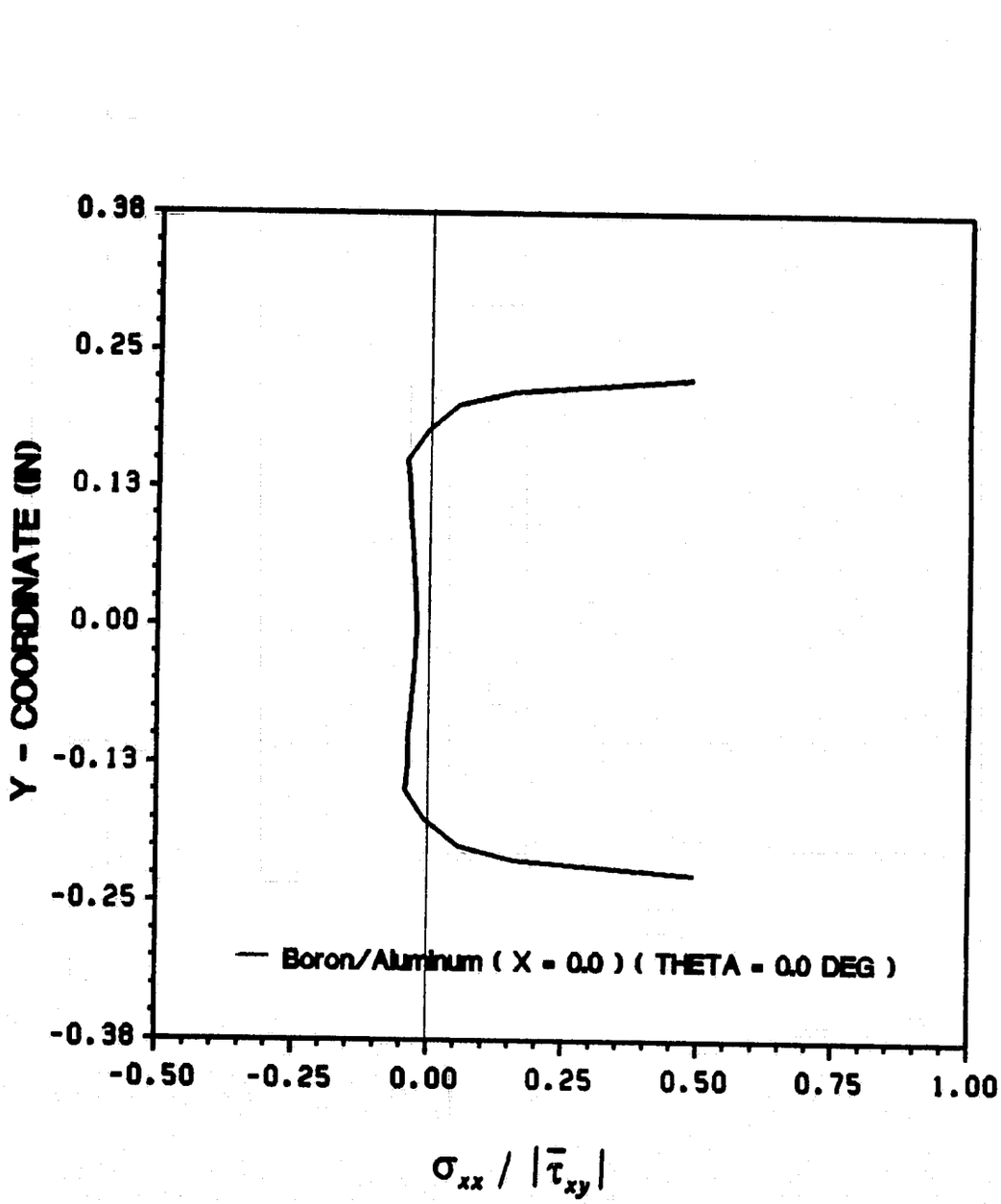

Figure 172. 0° On-Axis Tests: ($\sigma_{xx} / |\bar{\tau}_{xy}|$)

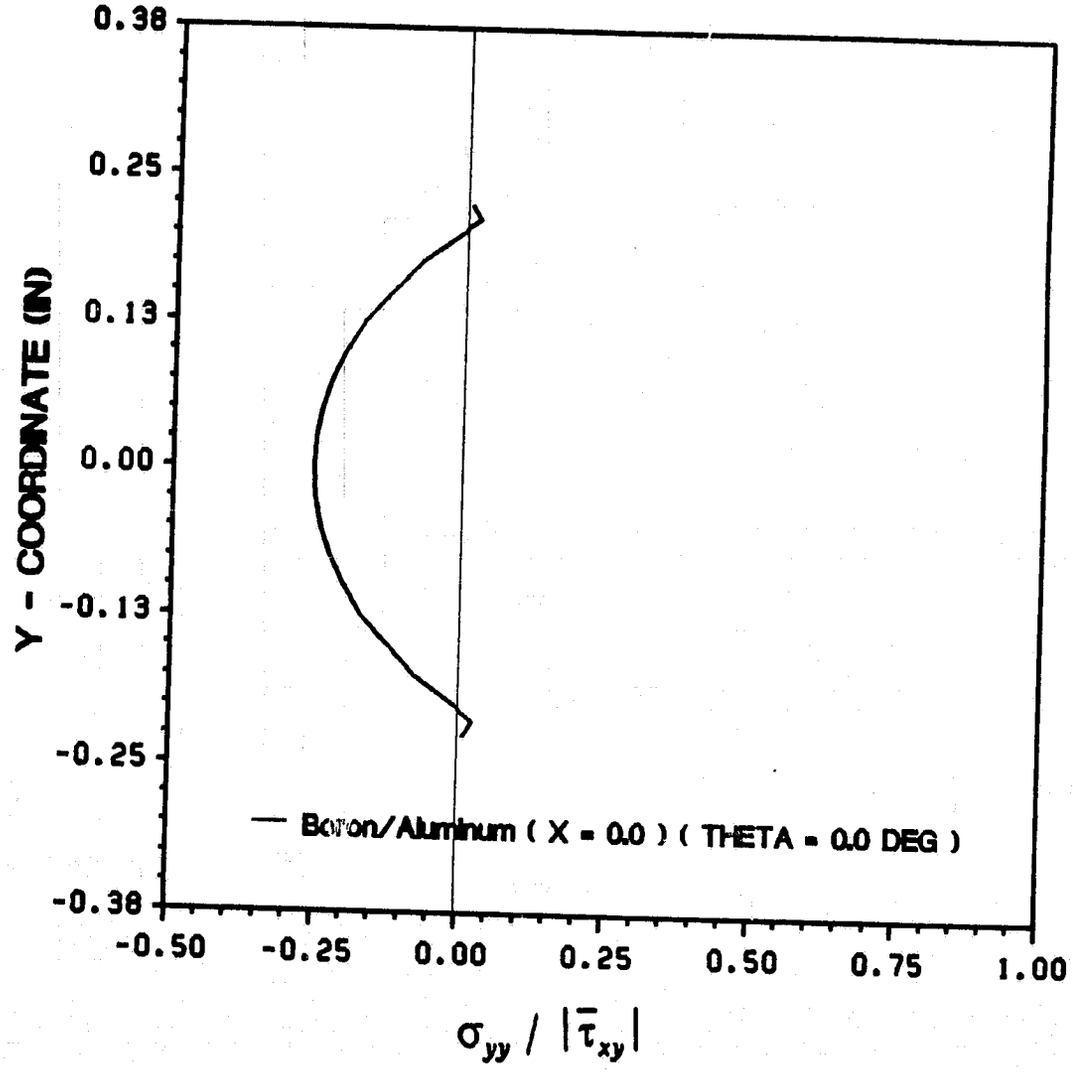

Figure 173. 0° On-Axis Tests: (σ_{yy} / $|\bar{\tau}_{xy}|$)

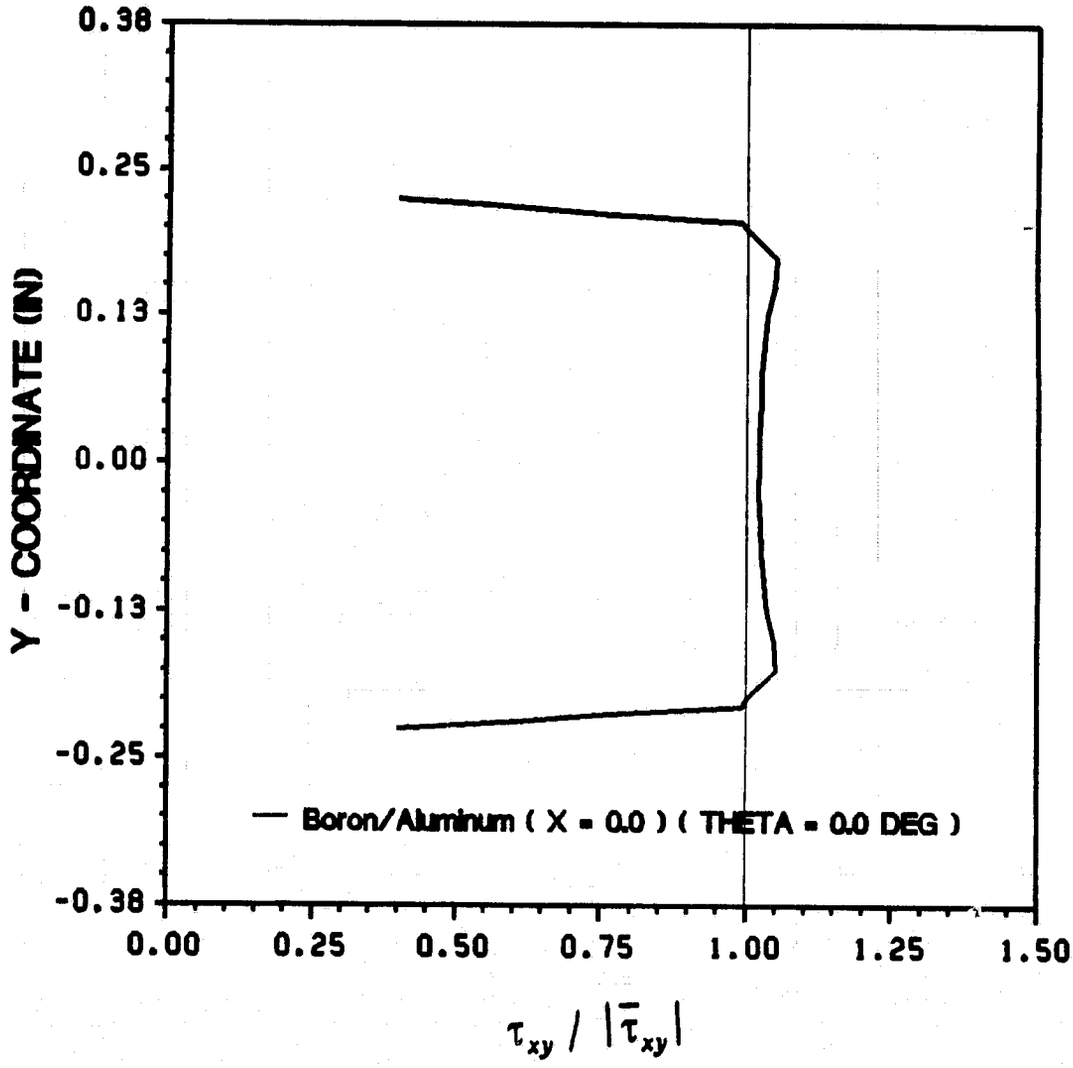

Figure 174. 0° On-Axis Tests: ($\tau_{xy} / |\bar{\tau}_{xy}|$)

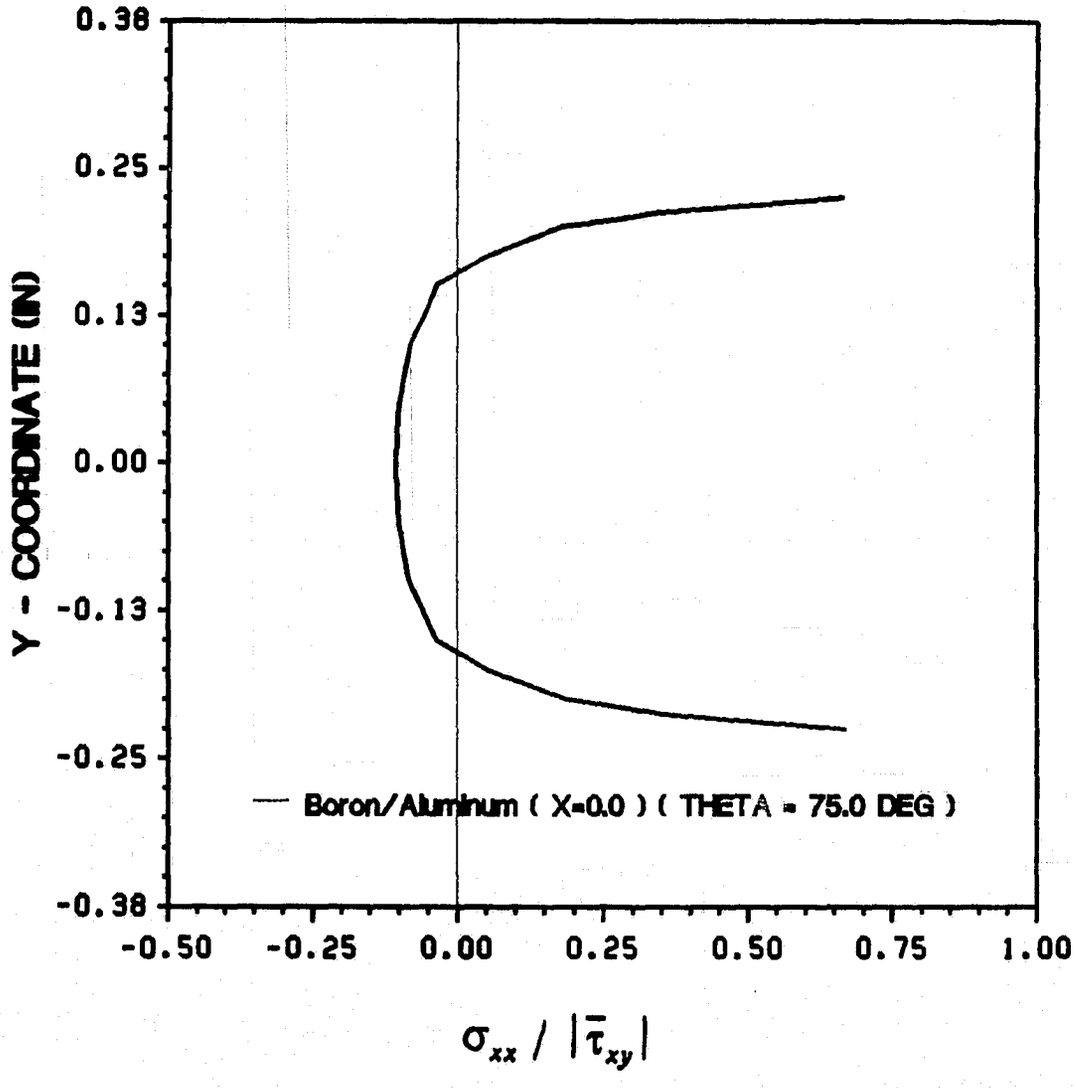

Figure 175. 75° Off-Axis Tests: ($\sigma_{xx} / |\bar{\tau}_{xy}|$)

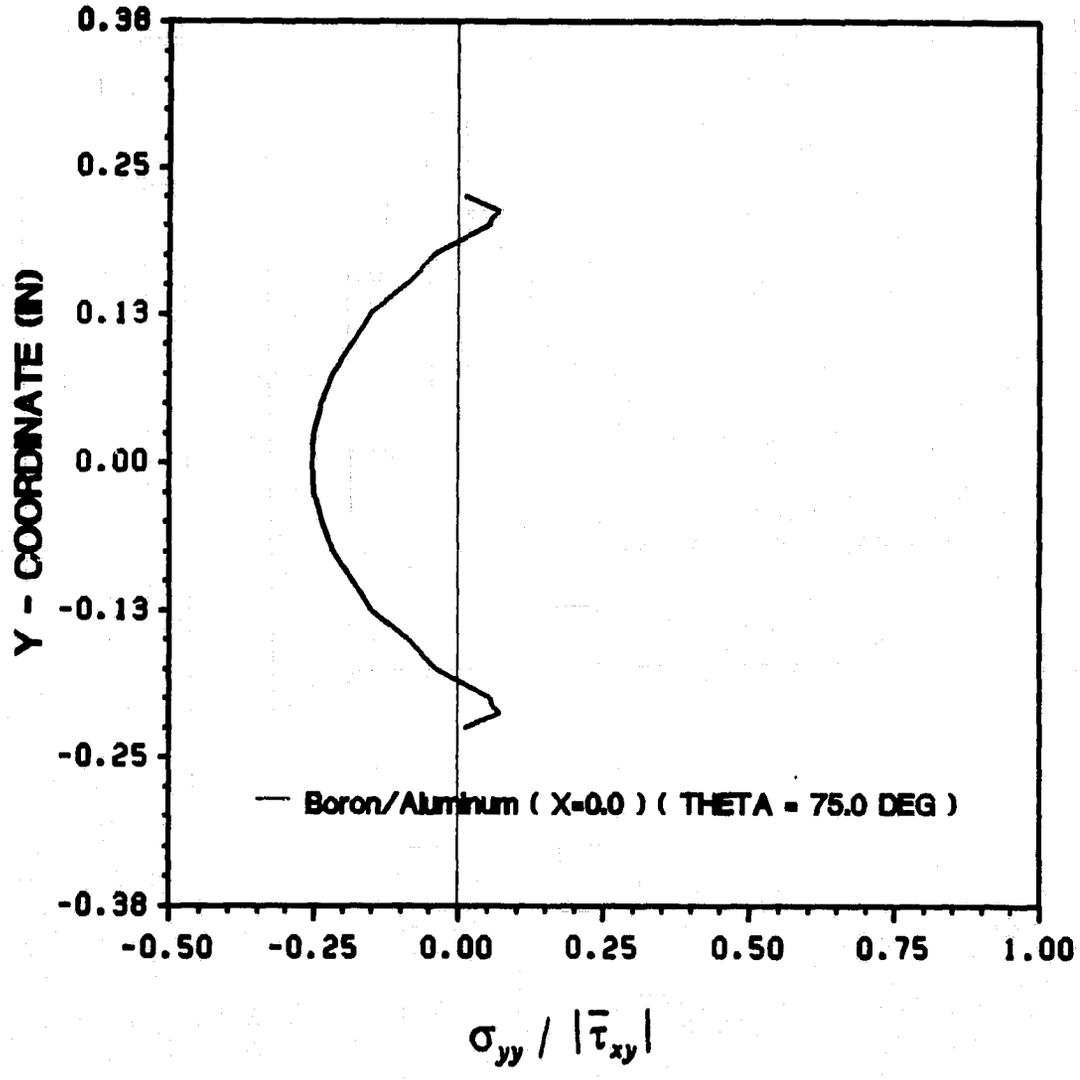

Figure 176. 75° Off-Axis Tests: (σ_{yy} / $|\bar{\tau}_{xy}|$)

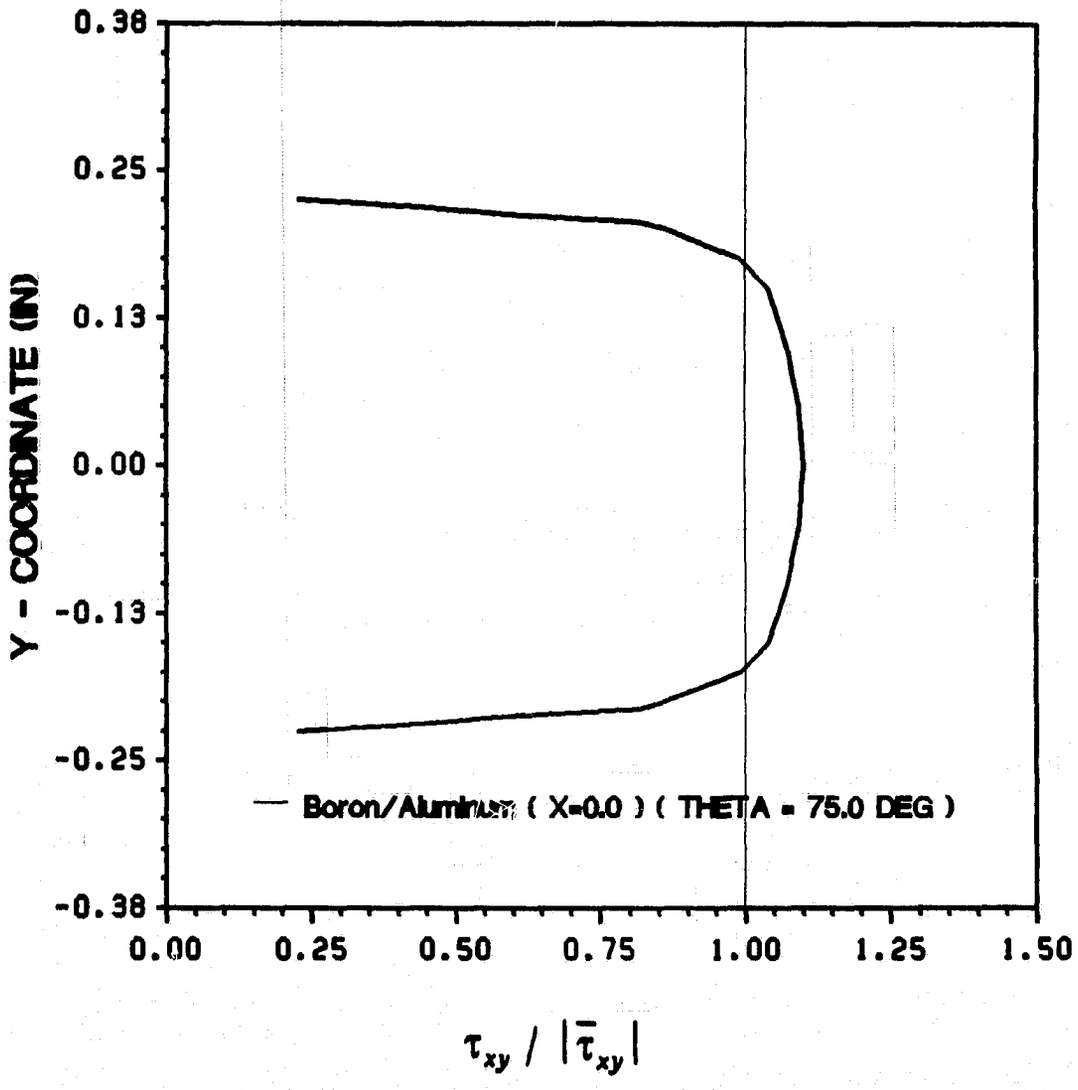

Figure 177. 75° Off-Axis Tests: ($\tau_{xy} / |\bar{\tau}_{xy}|$)

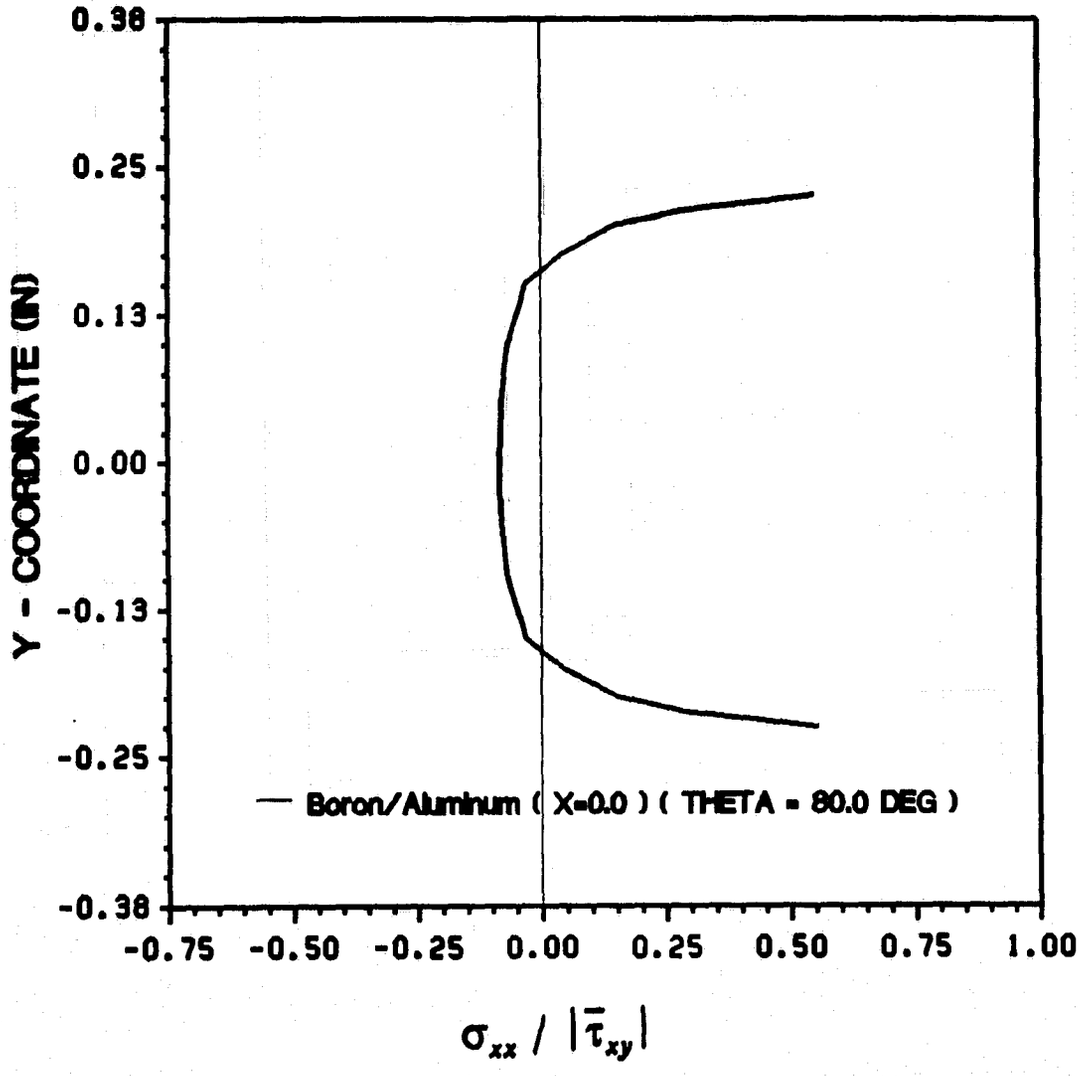

Figure 178. 80° Off-Axis Tests: ($\sigma_{xx} / |\bar{\tau}_{xy}|$)

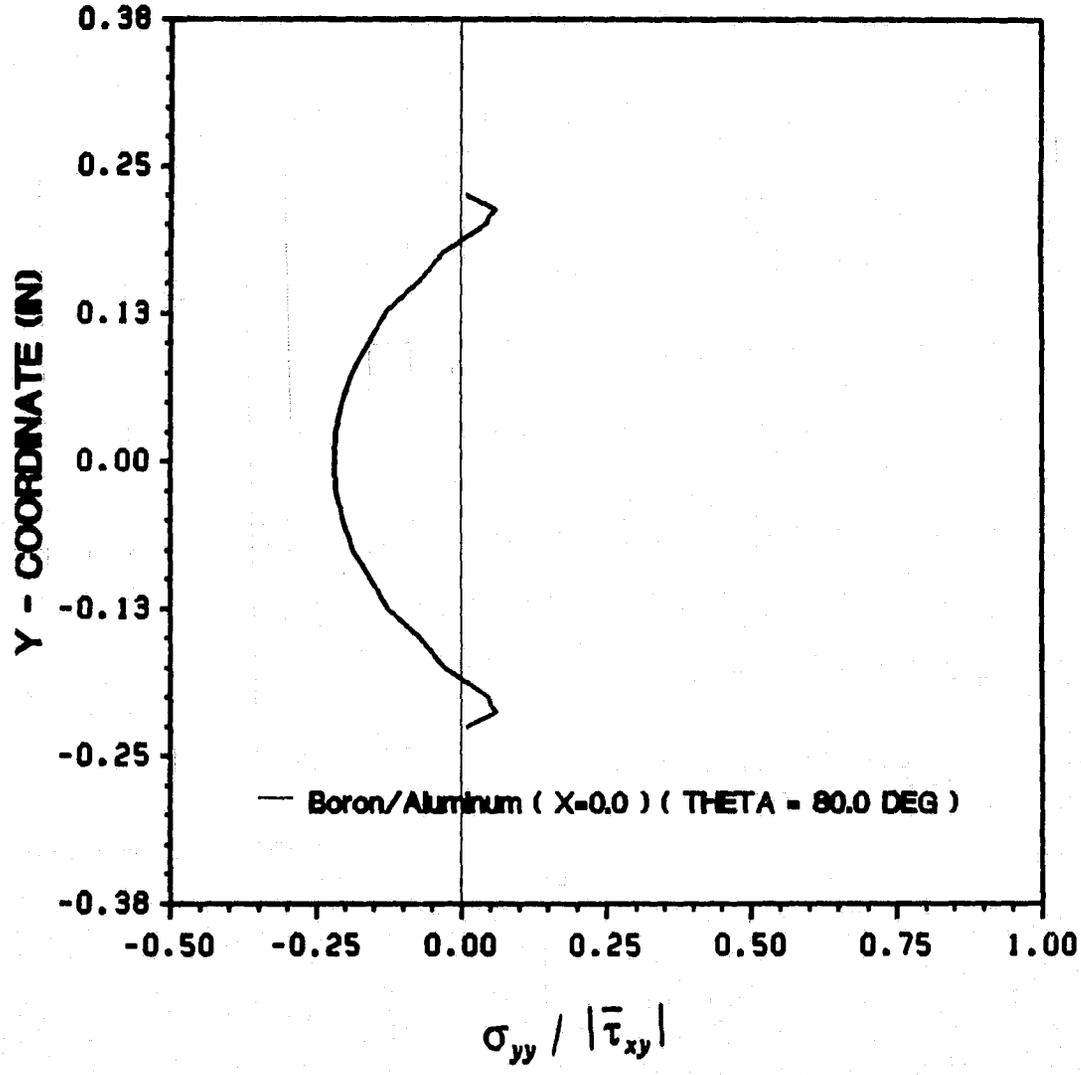

Figure 179. 80° Off-Axis Tests: (σ_{yy} / $|\bar{\tau}_{xy}|$)

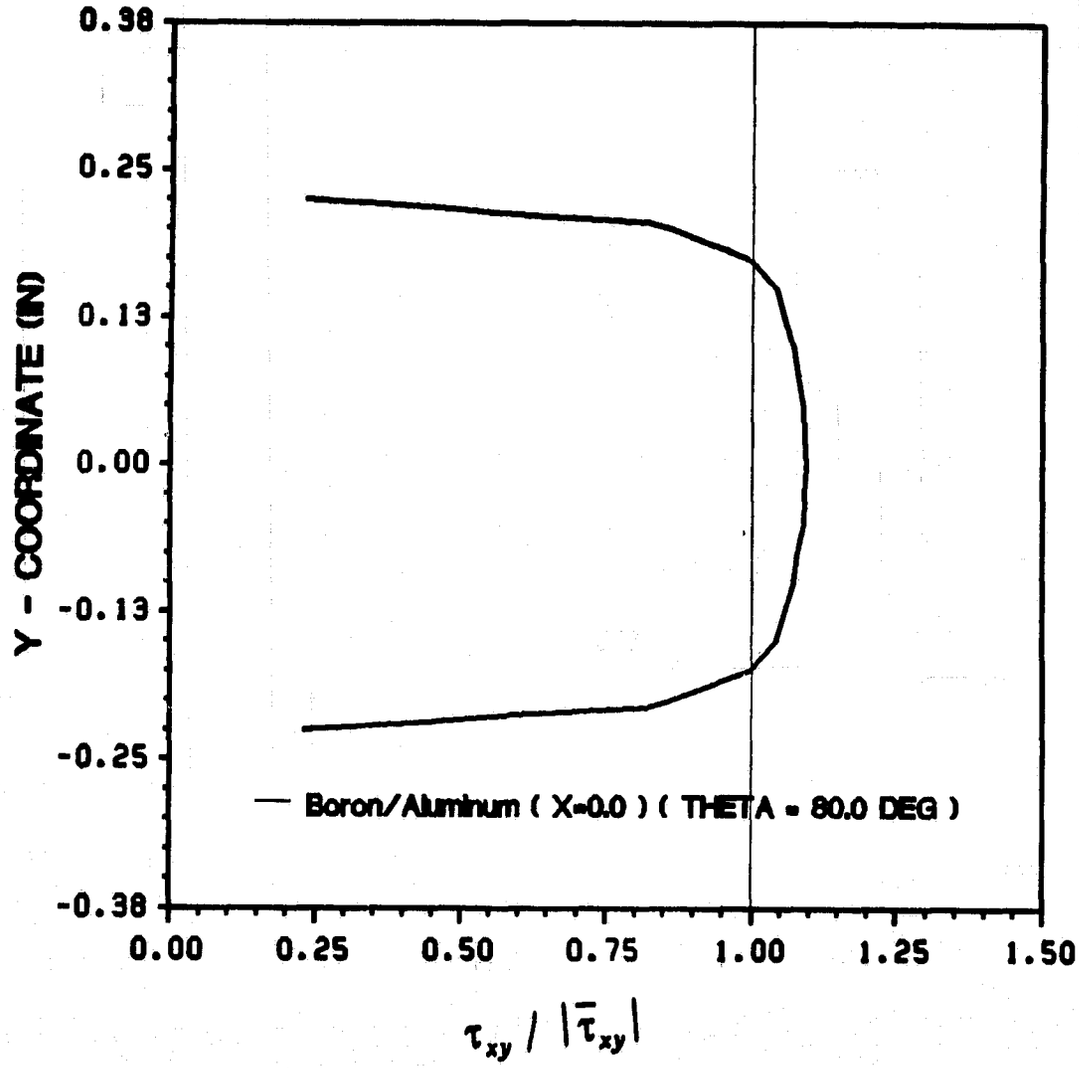

Figure 180. 80° Off-Axis Tests: ($\tau_{xy} / |\bar{\tau}_{xy}|$)

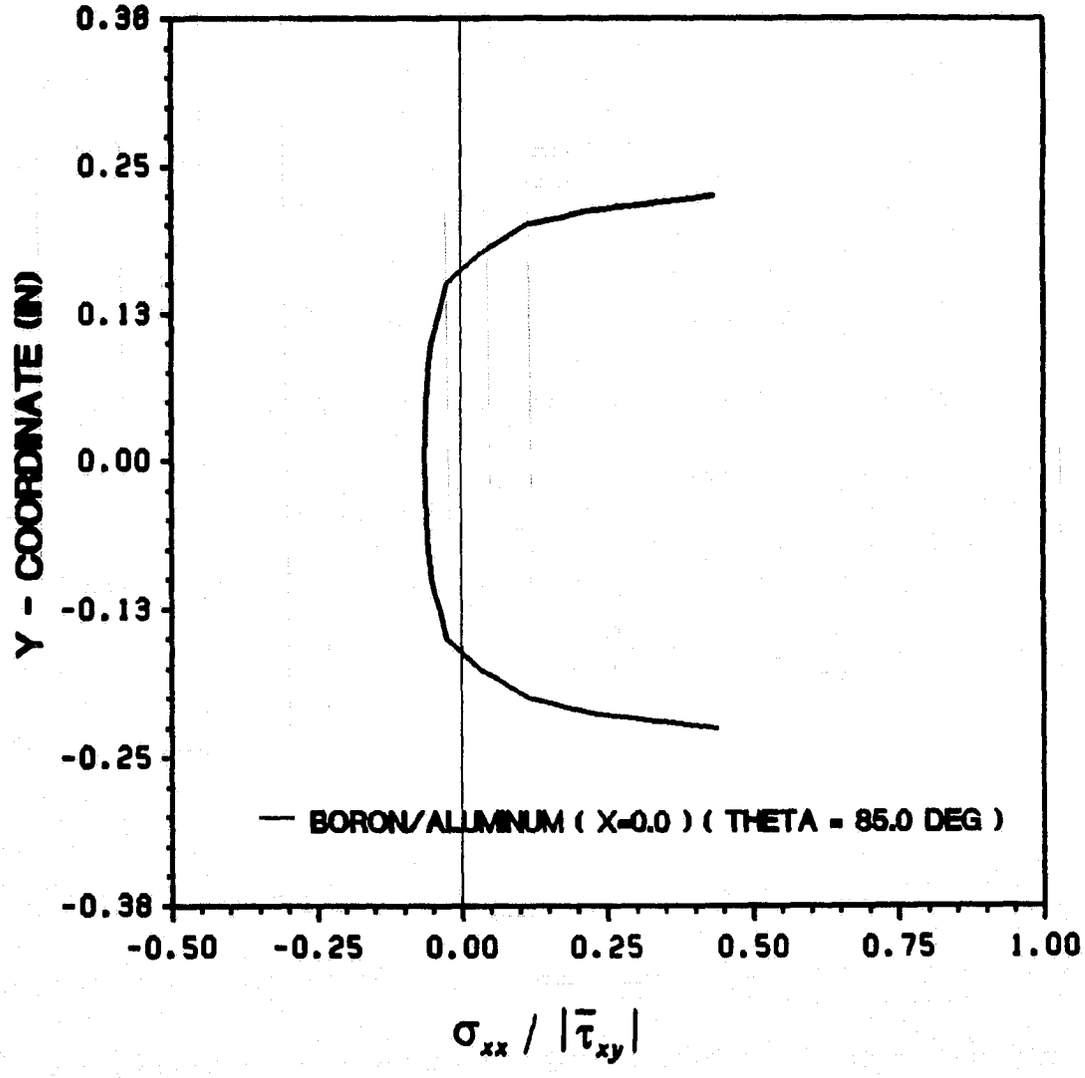

Figure 181. 85° Off-Axis Tests: (σ_{xx} / $|\bar{\tau}_{xy}|$)

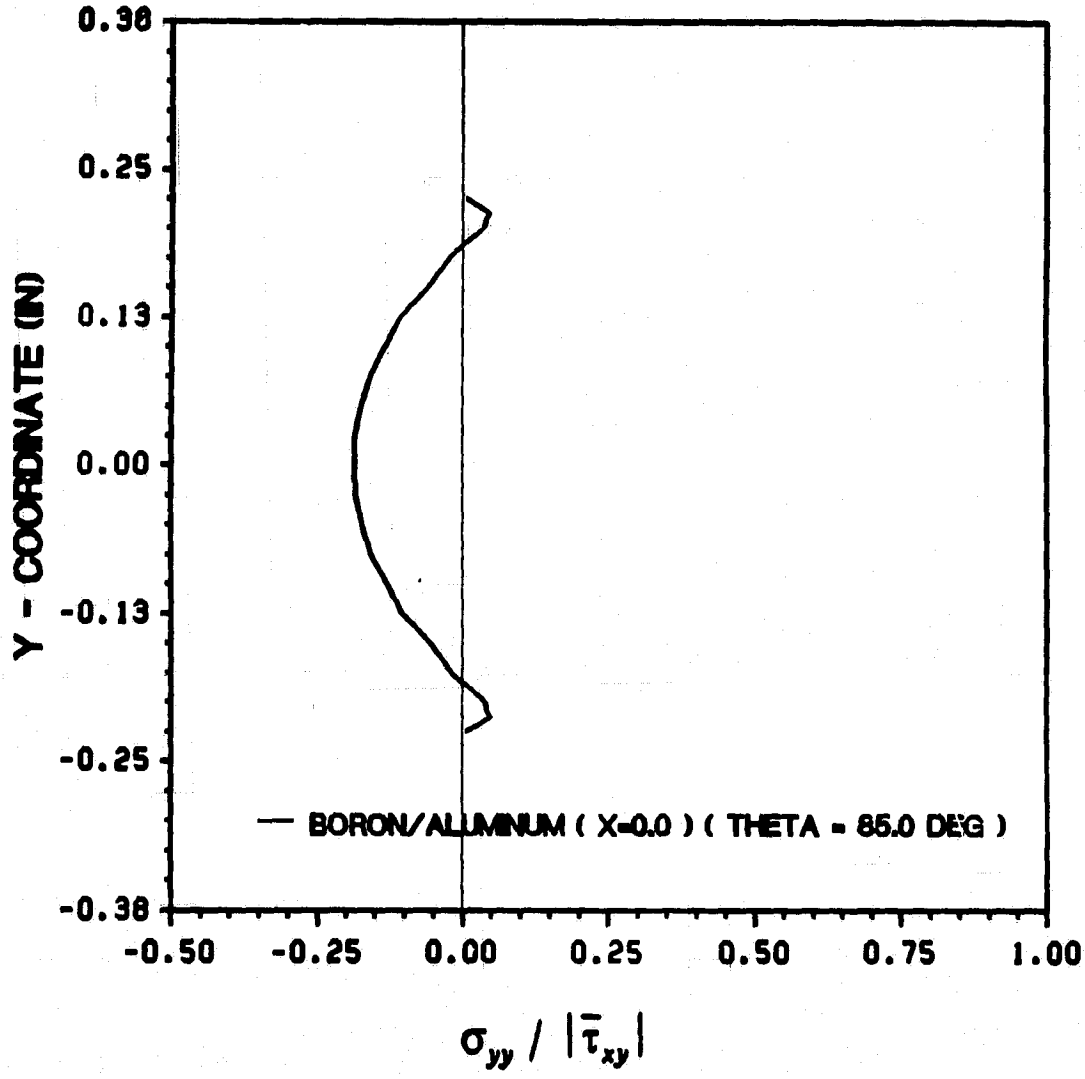

Figure 182. 85° Off-Axis Tests: (σ_{yy} / $|\bar{\tau}_{xy}|$)

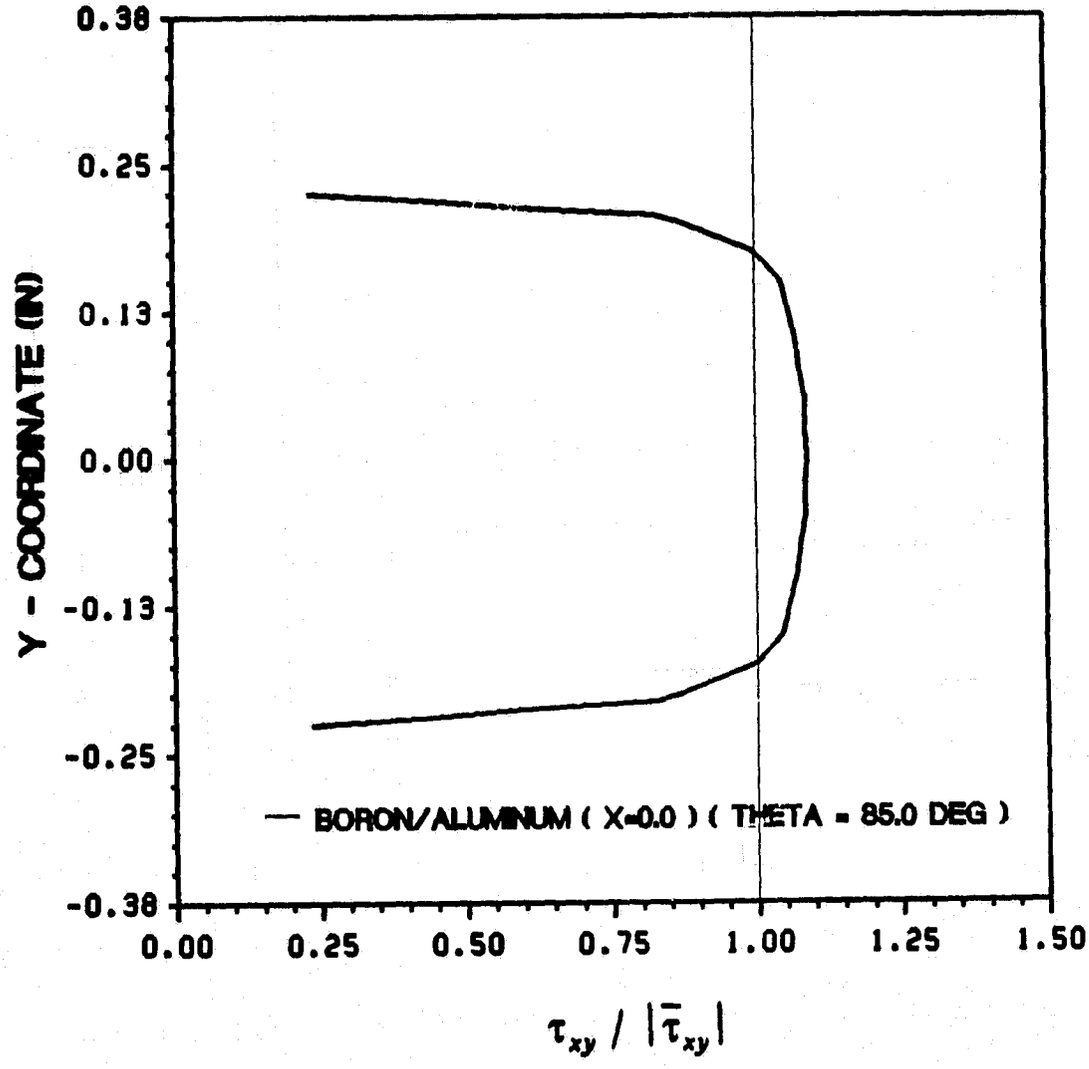

Figure 183. 85° Off-Axis Tests: ($\tau_{xy} / |\bar{\tau}_{xy}|$)

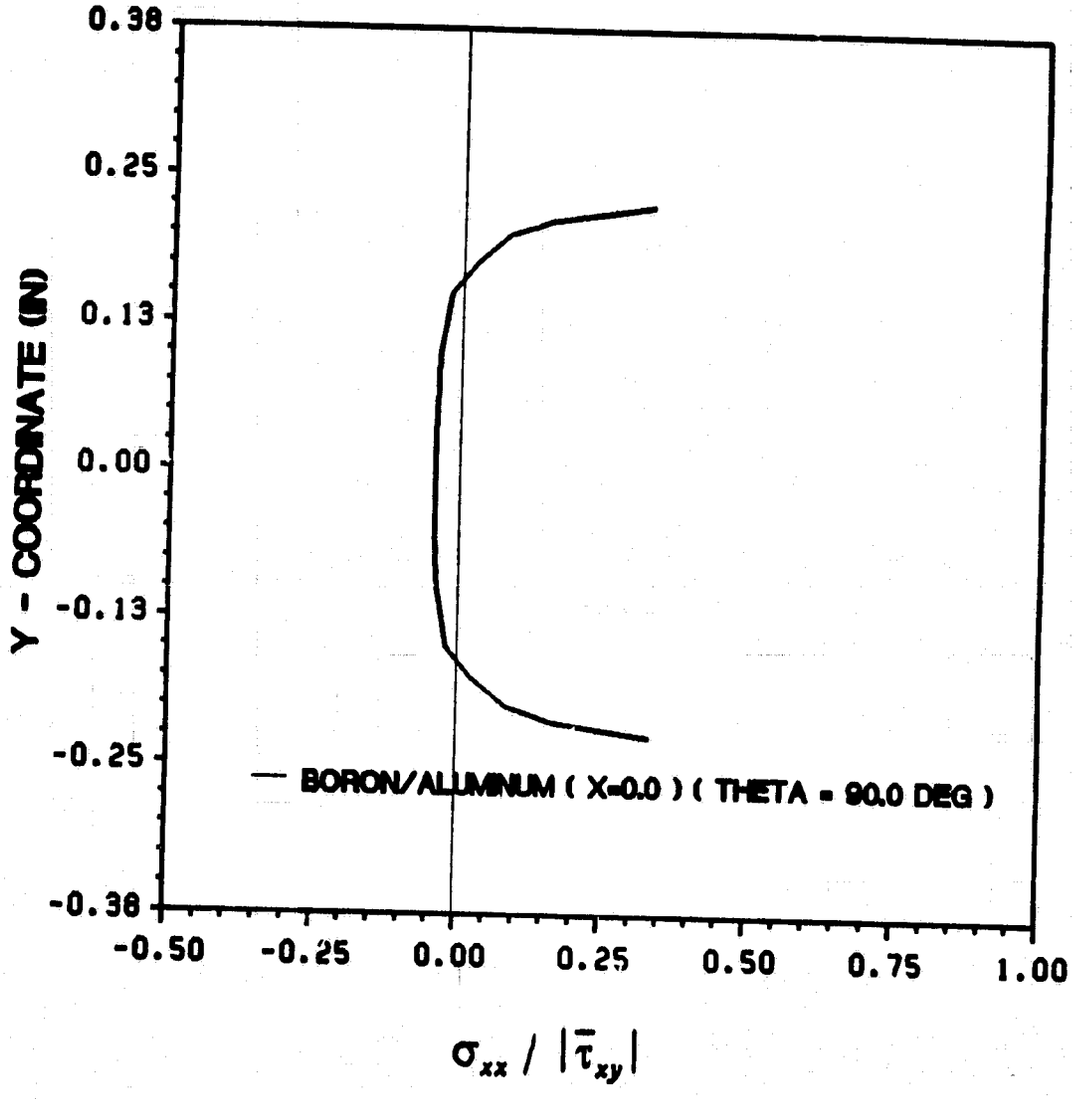

Figure 184. 90° On-Axis Tests: (σ_{xx} / $|\bar{\tau}_{xy}|$)

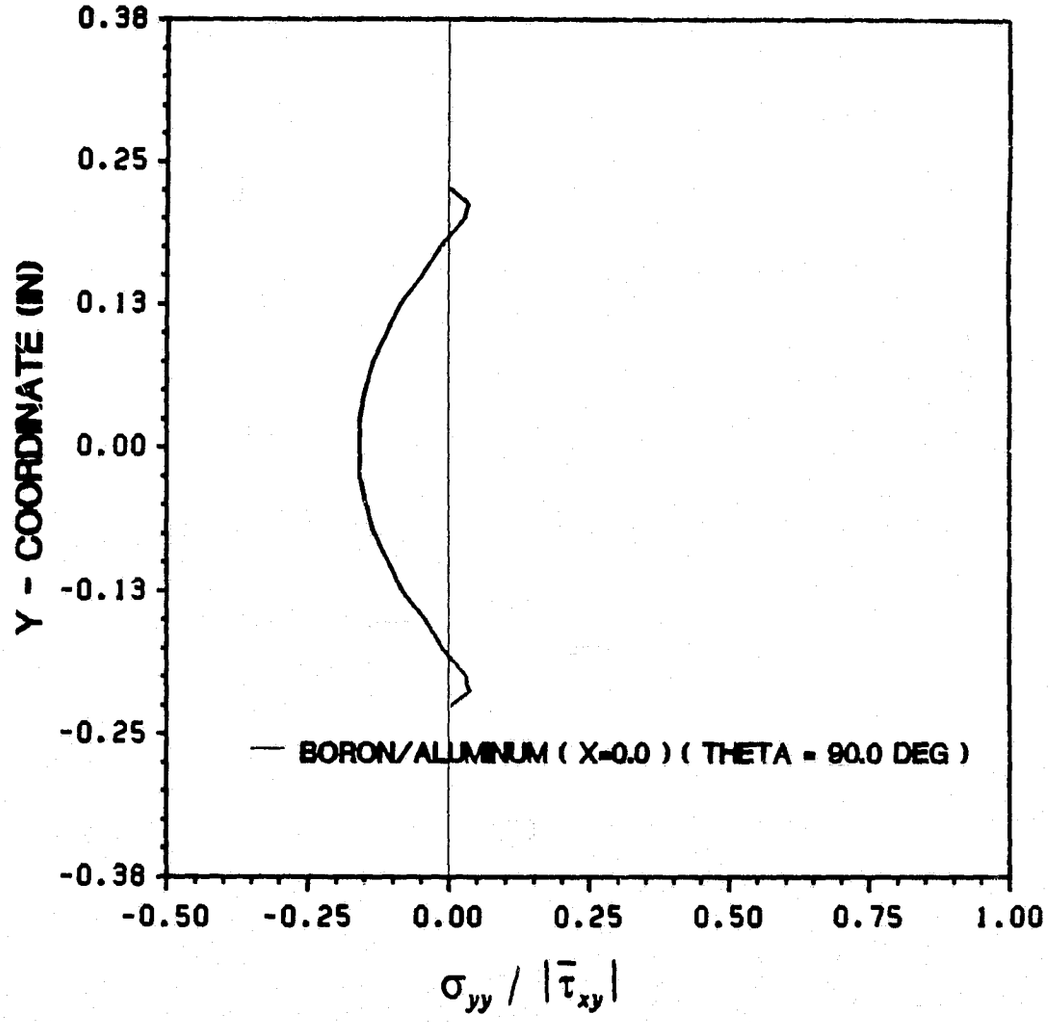

Figure 185. 90° On-Axis Tests: (σ_{yy} / $|\bar{\tau}_{xy}|$)

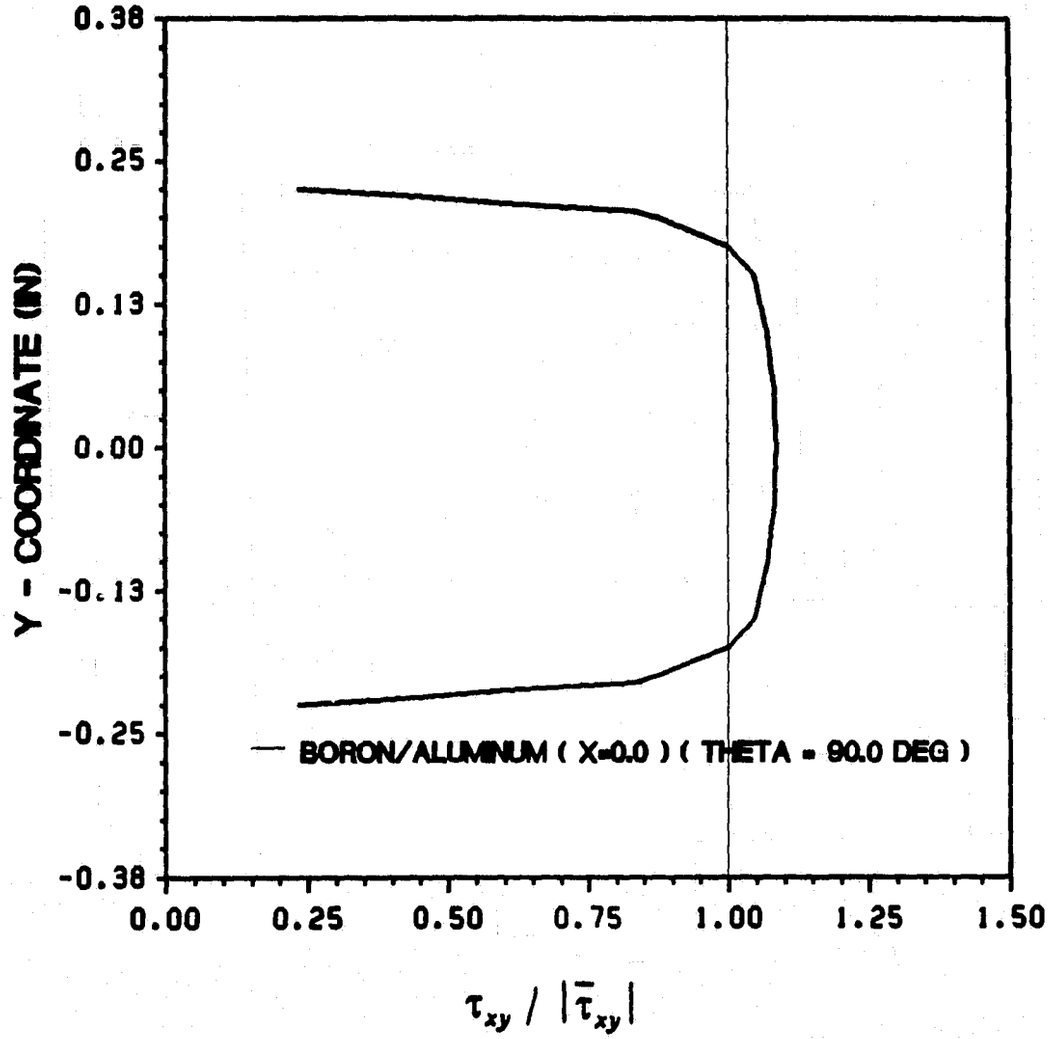

Figure 186. 90° On-Axis Tests: ($\tau_{xy} / |\bar{\tau}_{xy}|$)

Appendix F. Thermal Residual Stresses

The following results are based on a closed form elasticity solution. The composite is modeled as a cylinder as shown below. Fiber and matrix are assumed to be isotropic.

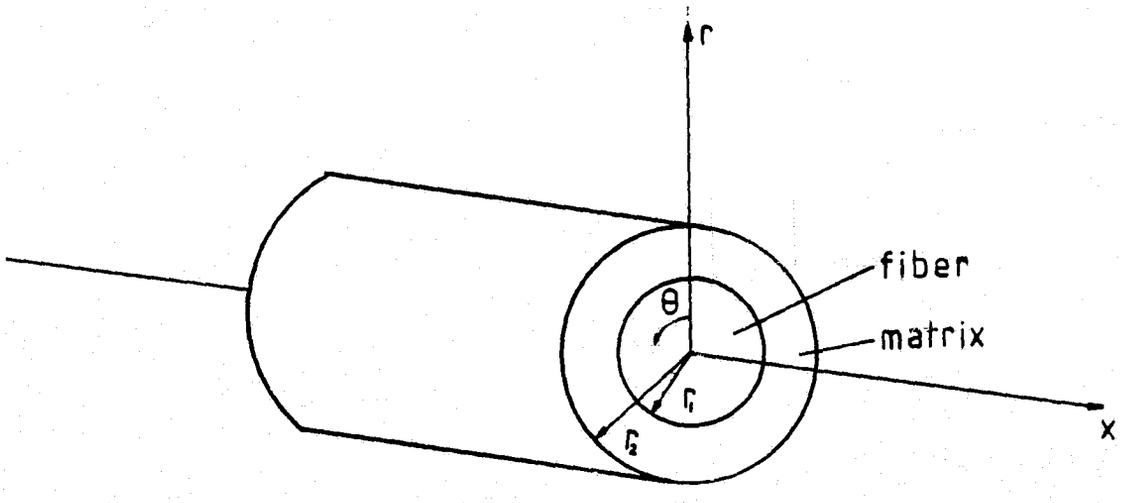

The input data are listed in the table below.

Table 17. Input Data for Elasticity Solution

Fiber Properties	Matrix Properties
E^f = 55.00 (msi) G^f = 22.92 (msi) ν^f = 0.20	E^m = 10.00 (msi) G^m = 3.75 (msi) ν^m = 0.31
Temperature Change	
ΔT = -100.0 °F	

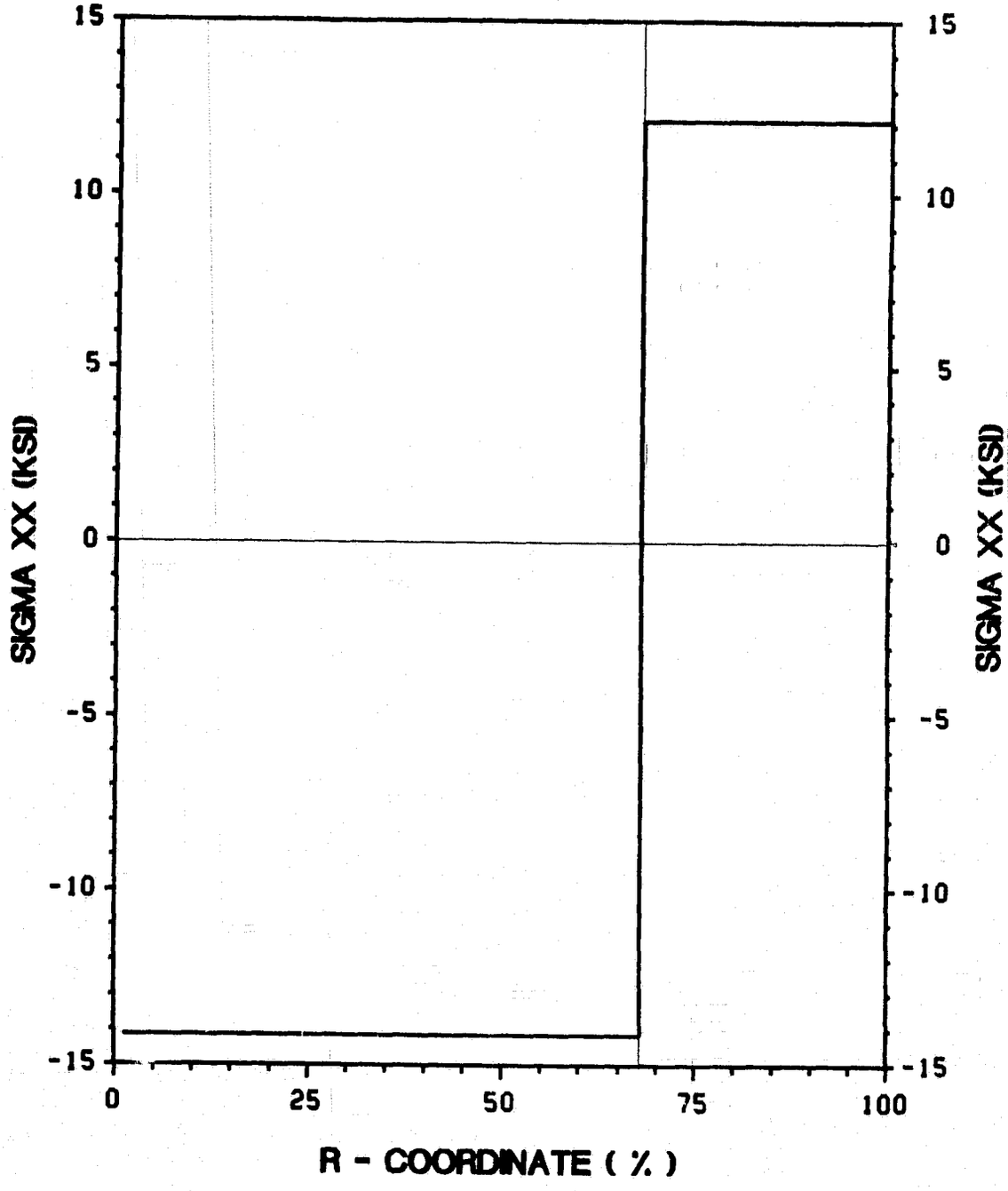

Figure 187. Longitudinal Residual Stress $\sigma_{xx}^{res.}$

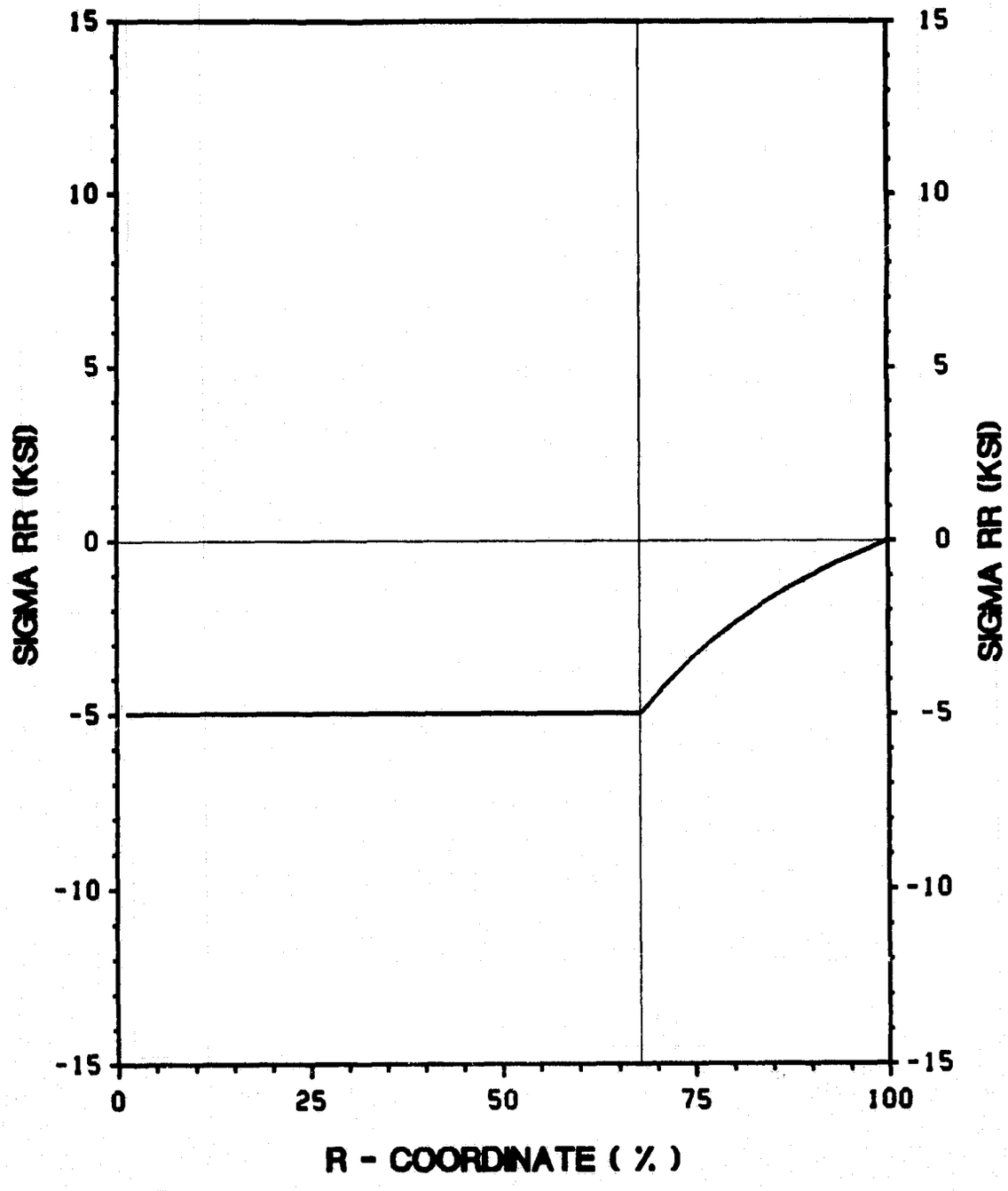

Figure 188. Radial Residual Stress σ_{rr}^{res}

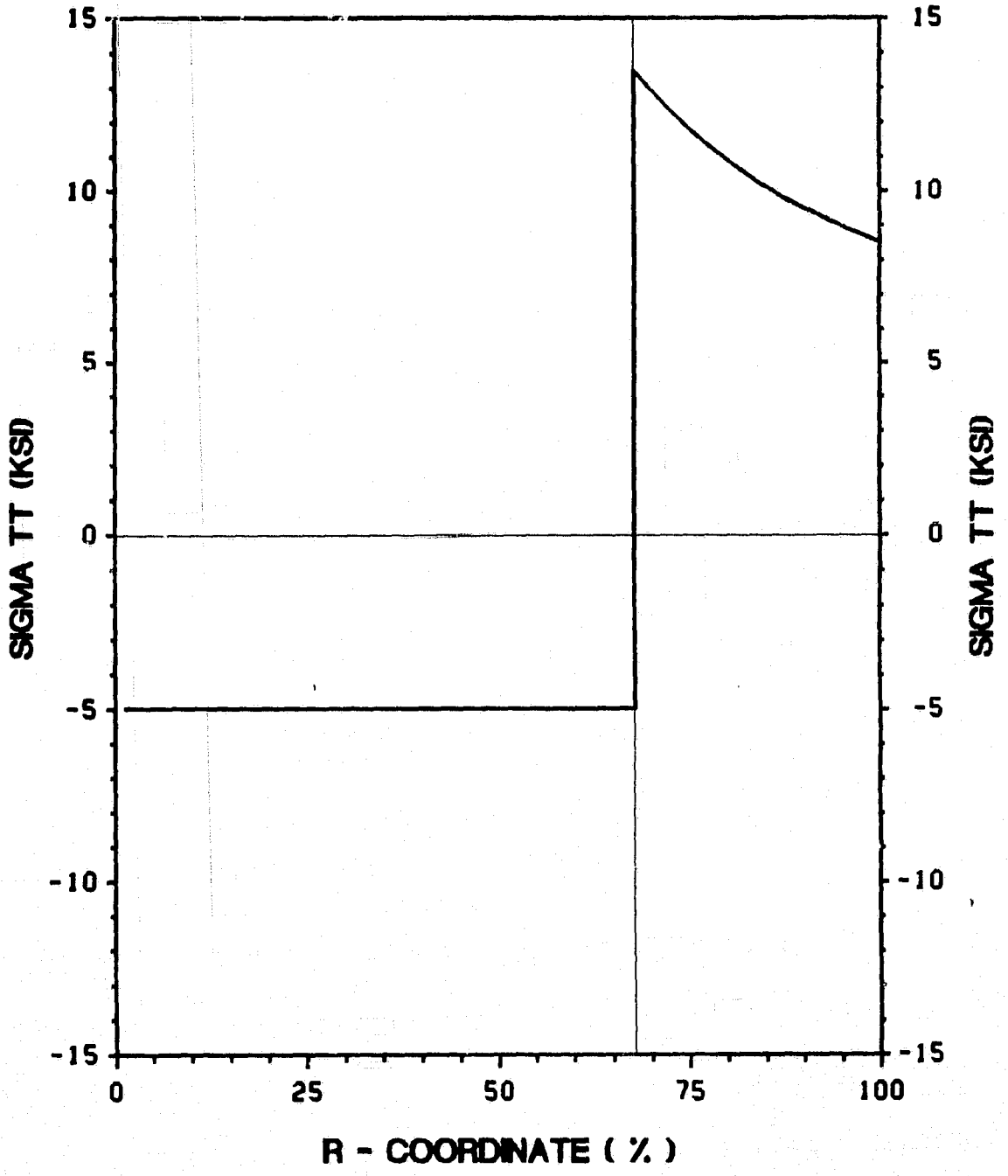

Figure 189. Circumferential Residual Stress $\sigma_{\theta\theta}$

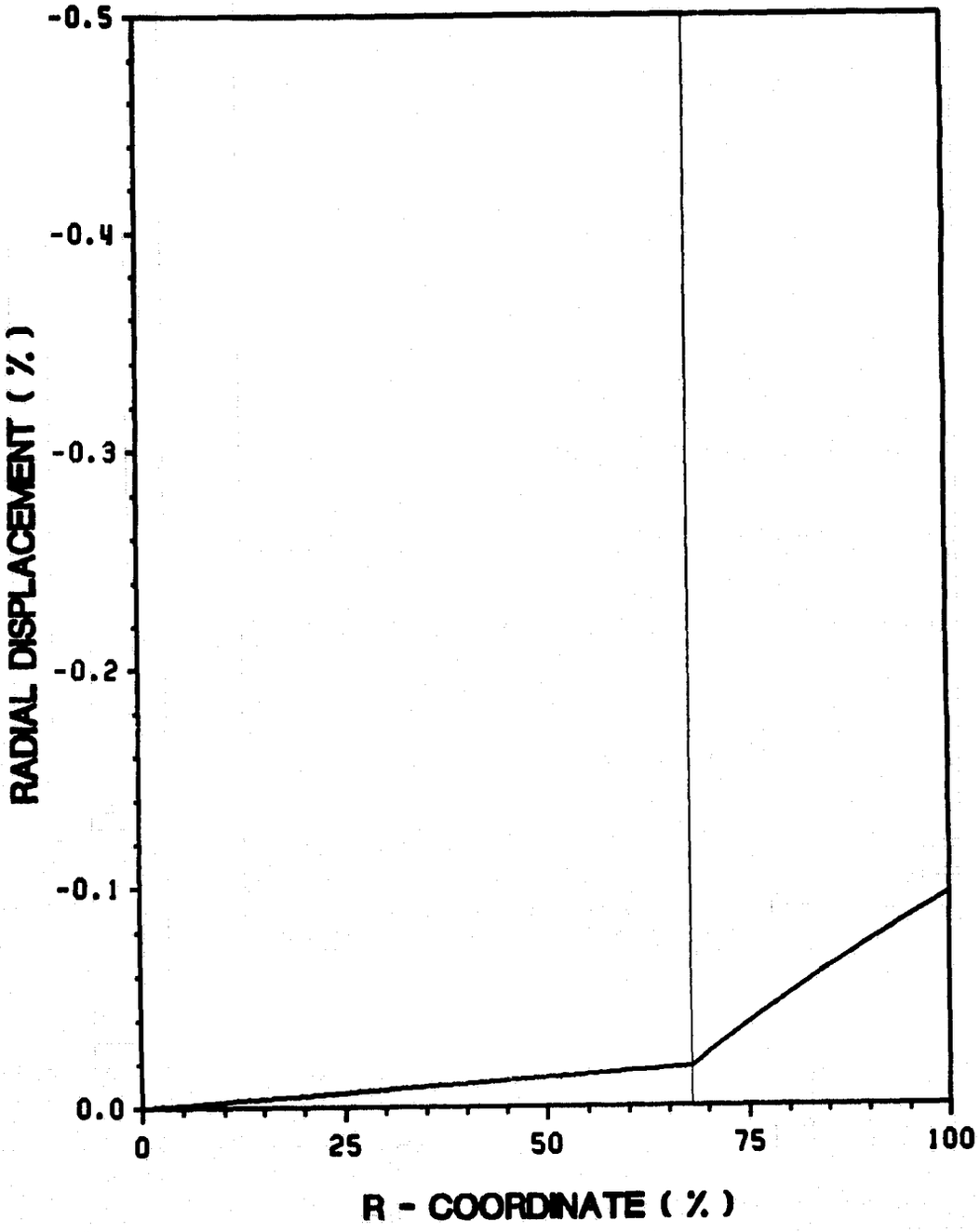

Figure 190. Radial Displacement w^{res}.

VIRGINIA TECH CENTER FOR COMPOSITE MATERIALS AND STRUCTURES

The Center for Composite Materials and Structures is a coordinating organization for research and educational activity at Virginia Tech. The Center was formed in 1982 to encourage and promote continued advances in composite materials and composite structures. Those advances will be made from the base of individual accomplishments of the forty members who represent ten different departments in two colleges.

The Center functions through an Administrative Board which is elected yearly and a Director who is elected for a three-year term. The general purposes of the Center include:

- collection and dissemination of information about composites activities at Virginia Tech,
- contact point for other organizations and individuals,
- mechanism for collective educational and research pursuits,
- forum and agency for internal interactions at Virginia Tech.

The Center for Composite Materials and Structures is supported by a vigorous program of activity at Virginia Tech that has developed since 1963. Research expenditures for investigation of composite materials and structures total well over seven million dollars with yearly expenditures presently approximating two million dollars.

Research is conducted in a wide variety of areas including design and analysis of composite materials and composite structures, chemistry of materials and surfaces, characterization of material properties, development of new material systems, and relations between damage and response of composites. Extensive laboratories are available for mechanical testing, nondestructive testing and evaluation, stress analysis, polymer synthesis and characterization, material surface characterization, component fabrication, and other specialties.

Educational activities include eight formal courses offered at the undergraduate and graduate levels dealing with the physics, chemistry, mechanics, and design of composite materials and structures. As of 1984, some 43 Doctoral and 53 Master's students have completed graduate programs and several hundred Bachelor-level students have been trained in various aspects of composite materials and structures. A significant number of graduates are now active in industry and government.

Various Center faculty are internationally recognized for their leadership in composite materials and composite structures through books, lectures, workshops, professional society activities, and research papers.

MEMBERS OF THE CENTER

Aerospace and Ocean Engineering
Raphael T. Haftka
William L. Hallauer, Jr.
Eric R. Johnson
Rakesh K. Kapania

Chemical Engineering
Donald G. Baird

Chemistry
James E. McGrath
Thomas C. Ward
James P. Wightman

Civil Engineering
R. M. Barker
Raymond H. Plaut

Electrical Engineering
Ioannis M. Besieris
Richard O. Claus

Enginering Science and Mechanics
Hal F. Brinson
Robert Czarnek
David Dillard
Norman E. Dowling
John C. Duke, Jr.
Daniel Frederick
O. Hayden Griffin, Jr.
Zafer Gurdal
Robert A. Heller
Edmund G. Henneke, II
Carl T. Herakovich
Robert M. Jones
Alfred C. Loos
Don H. Morris
Ali H. Nayfeh
Marek Pindera
Daniel Post
J. N. Reddy
Kenneth L. Reifsnider
C. W. Smith
Wayne W. Stinchcomb

Industrial Engineering and Operations Research
Joel A. Nachlas

Materials Engineering
David W. Dwight
D. P. H. Hasselman
Robert E. Swanson
W.J. van Ooij

Mathematics
Werner E. Kohler

Mechanical Engineering
Charles E. Knight
S. W. Zewari

Inquiries should be directed to:

Center for Composite Materials and Structures
College of Engineering
Virginia Tech
Blacksburg, VA 24061
Phone: (703) 961-4969